Dynamics of Active Magnetic and Non-Equilibrium Systems

Inauguraldissertation

zur

Erlangung des Doktorgrades

der Mathematisch-Naturwissenschaftlichen Fakultät

der Universität zu Köln

vorgelegt von

Dennis Christopher Hardt

aus Frechen

Köln 2025

Berichterstatter:	Prof. Dr. Achim Rosch
(Gutachter)	Prof. Dr. Matteo Rizzi
Vorsitzender der Prüfungskommission:	Prof. Dr. Joachim Hemberger

Tag der mündlichen Prüfung: 14.05.2025

Diese Dissertation wurde von der Mathematisch-Naturwissenschaftlichen Fakultät der Universität zu Köln im Jahr 2025 angenommen.

Die verarbeiteten Daten und Teile der Rohdaten können auf angemessene Anfrage zur Verfügung gestellt werden.

Science is the father of knowledge,
but opinion breeds ignorance.

—Hippocrates

Abstract

Many everyday phenomena, including climate patterns, traffic flow, and biological processes such as metabolic activity, are fundamentally out of equilibrium. The latter prevents the equilibration of an organism and makes life as we know it possible. Another instance is the relatively new field of 'active matter', which focuses on systems composed of self-propelled units that consume energy to generate motion and exhibit collective behaviours, often leading to complex and dynamic patterns. These examples, and many more, motivate the study of non-equilibrium phenomena.
Due to its complex systems, technological relevance, and emergent phenomena, condensed matter physics and magnetism, in particular, offer fertile ground for non-equilibrium research. In order to reach a non-equilibrium state in a material, some external force has to be applied to the system. This can be done, for example, by creating temperature gradients, applying external fields or mechanical stress, or using ultrafast laser pulses.
In this thesis, we investigate the model of a ferrimagnet driven out of equilibrium by an oscillating magnetic field. The model hosts ferromagnetic order in the z-direction and antiferromagnetic order in the xy-plane. We show that the oscillating magnetic field *activates* the rotational Goldstone mode, which describes a rotation of the magnetisation with constant speed ω_{rot} in the xy-plane. A crucial point of the construction is that the sign of the ferromagnetic component determines the direction of rotation. Necessarily, *dynamical frustration* builds up at a domain wall, where the different senses of rotation meet.
We first analyse the one-dimensional system. A direct consequence of the frustration is that a static domain wall is no longer stable. One way for the system to lift the frustration is via the active movement of the domain walls with a velocity proportional to the amplitude of the driving field. We observe this over a broad range of parameters. The direction of movement is thereby chosen by spontaneous symmetry breaking. This regime of actively moving domain walls has many similarities with active matter systems with regard to collective behaviour. Thus, we call it an active magnetic matter system. We find a strong hydrodynamic interaction, which, together with the movement of the domain walls, leads to a linear growth of the correlation length over time when the system is quenched into the ferrimagnetically ordered phase. The equilibrium growth is, in contrast, much slower. Moreover, the driven system is much more resilient to thermal fluctuations. We also discover another way to resolve the frustration for larger field amplitudes, the *localised* domain

wall. In this scenario, space-time vortices in the xy-order, accompanied by pulses in the ferromagnetic component, are released every rotation period.
In two dimensions, domain walls can move even in the non-driven system with a velocity proportional to their local curvature. We study the behaviour of the non-driven system after quenches to subcritical temperatures and use the Kibble-Zurek mechanism to confirm the Ising class exponents. For quenches to $T = 0$, the growth in correlation length is faster than in the Ising case due to the coupling to the xy-order. For the driven system, we find, again, linear growth of the correlation length. The resilience to thermal fluctuations manifests in a shift of the critical point of the phase transition to larger temperatures as the driving field is increased. A behaviour similar to the localised domain wall for larger fields from the one-dimensional discussion occurs. However, we do not find a truly localised domain wall. Instead, the domain walls move more slowly than the characteristic velocity, and vortices that are incommensurate with the rotation period are created.
We numerically analyse the phase transition of the driven system in three dimensions using the Binder cumulant. In contrast to recent analytical studies, we find signatures of a second-order transition with Ising class exponents.
We also study another non-equilibrium system given by a two-particle gas with particle number conservation. We successfully drive the system so that a steady-state current emerges. While the numerical implementation is very efficient for large system sizes, an analytical explanation remains to be found.

The thesis is structured as follows: In the first chapter, we introduce theoretical background on several concepts, from spin dynamics to non-equilibrium phase transitions. The first part is about the driven ferrimagnet and consists of four chapters. Ch. 2 explains, among others, the model, the activation of the Goldstone mode and the numerical methods used. The following three chapters discuss the results in increasing number of dimensions, Ch. 3 (one dimension), Ch. 4 (two dimensions), Ch. 5 (three dimensions). The second part consists of only one chapter, Ch. 6, which stands separately. It discusses the driven two-particle gas. Finally, we conclude our findings in the last chapter and give a brief outlook for future investigations.

Contents

List of Figures

1

Fundamentals

The study of magnetism has captivated human curiosity for centuries, dating back to ancient civilisations that first observed the magnetic properties of natural minerals, such as lodestone (magnetite, Fe_3O_4) and iron, which exhibit mutual attraction. Already Aristotle made a reference to permanent magnets around 350 B.C., see for example the translated version in [1]. A famous textbook example is the magnetic compass, whose first documented use for navigation is found in a Chinese text from around 1040. Thus, magnetism was first characterised as a long-distance interaction between ferromagnetic bodies. The question emerges: What is the actual element behind those interactions? The compass should be once again involved in a groundbreaking discovery. In 1819, Oersted discovered that a compass needle is deflected by a wire carrying an electric current, much like it would be by a permanent magnet. This discovery ultimately led to the idea that the magnetisation of permanent magnets is somehow caused by permanent currents. Later, the classical theory of electromagnetism was completed by Maxwell.

Even today, magnetism remains crucial in our lives and has everyday applications. Ranging from magnetic stripes on credit cards and hard drives to magnetic resonance imaging in medicine.

In this chapter, we will delve into some fundamental concepts related to magnetism that are relevant to this work. We cover topics from the dynamics of spin and exchange interactions to the Ginzburg-Landau paradigm and phase transitions. Of particular importance is the concept of Goldstone modes. Their activation forms a fundamental cornerstone of this thesis.

1.1 Spin Dynamics and the LLG Equation

We start by developing an understanding of the motion of magnetisation or spin. The corresponding dynamical equation was first introduced by Landau and Lifshitz in 1935 [2], known as the Landau-Lifshitz (LL) equation. Later, in 1955, Gilbert reformulated the equation by adjusting the damping term, allowing for reasonable dynamics even at large damping [3, 4]. This version is now known as the Landau-Lifshitz-Gilbert (LLG) equation and has been used to describe the magnetisation dynamics in a wide range of phenomena, such as skyrmions, domain walls and many more magnetic structures.

Let us briefly follow the phenomenological approach, which leads to the LLG equation based on [5]. The orbital motion of the spin of electrons is the main contribution to the magnetic properties of materials. Of course, quantum mechanical methods have to be used to describe electrons reasonably. Nevertheless, due to the large numbers involved in macroscopic magnetism, a classical or semi-classical description is still possible. One strong advantage of these approaches is the simpler visualisation. In this classical picture, we can think about an electron as a small current loop which we subject to a magnetic field $\boldsymbol{B}$. For now, this is just an applied external field that gets more intrinsic contributions once we extend it to multiple magnetic moments on a lattice. The torque $\boldsymbol{\tau}$ on the magnetic moment $\boldsymbol{m}$ is given by

$$\boldsymbol{\tau} = \boldsymbol{m} \times \boldsymbol{B}\,, \tag{1.1}$$

which can be rewritten as a differential equation for the magnetic moment using $\boldsymbol{\tau} = \dot{\boldsymbol{J}}$ and $\boldsymbol{m} = \gamma \boldsymbol{J}$ where $\boldsymbol{J}$ is the angular momentum. We get

$$\dot{\boldsymbol{m}} = \gamma \boldsymbol{m} \times \boldsymbol{B}\,, \tag{1.2}$$

with the gyromagnetic ratio $\gamma = \frac{gq}{2m_q}$ which is negative for a negative charge q and the Landé g-factor. Physically, this is equivalent to a force acting on the magnetic moment leading to precessional motion around the external magnetic field with the so-called Lamor frequency $\omega_L = |\gamma \boldsymbol{B}|$.

We can refer to the angular momentum as the spin $\boldsymbol{S}$ and thus rewrite the equation of motion by

$$\dot{\boldsymbol{S}} = \gamma \boldsymbol{S} \times \boldsymbol{B}\,, \tag{1.3}$$

which can be visualised as shown in Fig.1.1a).

We have already gained some understanding here, but there is one issue within this picture. The circular motion persists forever since the angle between the magnetic field and the spin stays the same. This contradicts our intuition as the spin relaxes

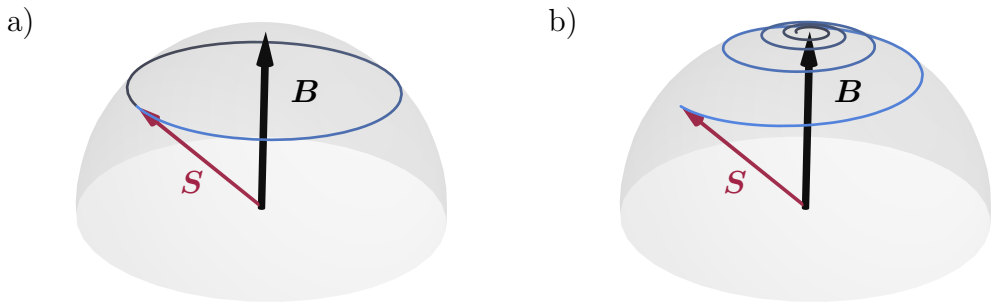

Figure 1.1: Visualisation of the trajectory of a single spin $\boldsymbol{S}$ subjected to a constant magnetic field $\boldsymbol{B} = (0, 0, 1)$ determined by the LLG Eq. (1.4). We assumed a negatively charged particle with $\gamma = -1$, resulting in an anti-clockwise direction. Notice that the rotational direction would be opposite, clockwise, for $\gamma > 0$. Panel a) is without damping $\alpha = 0$ and shows the constant precessional motion around the field. Panel b) shows the trajectory with phenomenological Gilbert damping of magnitude $\alpha = 0.1$ where the spin slowly aligns with the field.

in the direction of the applied magnetic field. Therefore, a dissipative contribution to the equation of motion is needed. This is where the phenomenological Gilbert damping term helps us out. We add it to Eq. (1.3) to get a more realistic equation of motion for a single spin subjected to a magnetic field,

$$\dot{\boldsymbol{S}} = \gamma \boldsymbol{S} \times \boldsymbol{B} - \alpha \, \mathrm{sign}(\gamma) \hat{\boldsymbol{S}} \times \dot{\boldsymbol{S}} \,, \tag{1.4}$$

where α is the dimensionless damping constant and $\hat{\boldsymbol{S}} = \frac{\boldsymbol{S}}{S}$ with $|\boldsymbol{S}| = S$, the normalised spin. The form stated here also allows for positive charges for which $\gamma > 0$ and the resulting motion is reversed. The prefactor $\mathrm{sign}(\gamma)$ in the second term takes this into account by also changing the sign of the dissipative contribution. Eq. (1.4) is the simplest form of the LLG equation for a single spin in the presence of an applied magnetic field.

As before, we can interpret the new contribution in the spirit of a force. This time, it is pointing perpendicular to the spin $\boldsymbol{S}$ and to its time derivative $\dot{\boldsymbol{S}}$, where the sign ensures that it points towards the applied magnetic field. As a result, the angle between $\boldsymbol{B}$ and $\boldsymbol{S}$ decreases. A visualisation of a trajectory following Eq. (1.4) is shown in Fig.1.1b).

Before extending the description to multiple spins, we can first compare the dissipative free part of Eq. (1.4) to the generalised canonical equation for the classical spin given by

$$\frac{d\boldsymbol{S}}{dt} = \{\boldsymbol{S}, H\} = -\boldsymbol{S} \times \frac{\partial H}{\partial \boldsymbol{S}} \,, \tag{1.5}$$

where H is some spin-dependent Hamiltonian and $\{\dots\}$ is the Poisson bracket [6]. This formula yields the same results as Eq. (1.4) for a Hamiltonian of the form $H = -\gamma \boldsymbol{S}\boldsymbol{B}$. As a side note, the same holds from a quantum mechanical perspective through the correspondence principle. In this case, the Poisson bracket is replaced by the commutator with $\{\boldsymbol{S}, H\} \to \frac{i}{\hbar}[\widehat{H}, \widehat{S}]$ where the hat $\widehat{\ }$ denotes quantum mechanical operators. For the rest of this thesis, we focus on classical spins.
With this at hand, we can simply extend the description above to a lattice of spins by small changes in notation, which yield

$$\dot{\hat{\boldsymbol{S}}}_i = \gamma \hat{\boldsymbol{S}}_i \times \boldsymbol{B}_{\text{eff}} + \alpha \hat{\boldsymbol{S}}_i \times \dot{\hat{\boldsymbol{S}}}_i \,, \tag{1.6}$$

where $\boldsymbol{B}_{\text{eff}} = -\frac{1}{\gamma}\frac{\partial H}{\partial \boldsymbol{S}_i}$ in agreement with the simple example of a constant external field. Notice that we already assumed $\text{sign}(\gamma) < 1$ for the electron. The effective field includes all magnetic influences on the single spin, such as exchange coupling between the spins (Sec. 1.2), anisotropy terms (Sec. 1.3), applied magnetic fields and demagnetisation fields. The index i is the label of the single spin on the lattice, e.g., for one spatial dimension $i \in [1, N]$ where N is the number of spins. In higher space dimensions, one can adjust the counting accordingly by replacing the index i with the lattice vector.
Additionally, we also want to introduce another contributing term to the LLG equation, a Gaussian noise field $\boldsymbol{\eta}_i$ arising from thermal fluctuations. This will become important for numerical simulations where we analyse the behaviour for $T > 0$, for example, in Sec. 3.5. The final, *stochastic* LLG equation has the following form

$$\dot{\hat{\boldsymbol{S}}}_i = -\hat{\boldsymbol{S}}_i \times \left(\frac{\partial H}{\partial \boldsymbol{S}_i} + \boldsymbol{\eta}_i \right) + \alpha \hat{\boldsymbol{S}}_i \times \dot{\hat{\boldsymbol{S}}}_i, \tag{1.7}$$

where $\langle \boldsymbol{\eta}_i \rangle = 0$ and $\langle \boldsymbol{\eta}_i \boldsymbol{\eta}_j(t') \rangle = 2C_\eta \delta_{i,j} \delta(t - t')$. The exact form of the noise strength C_η depends on the problem at hand. However, it is, in general, proportional to the damping α and temperature T. This is an imprint of the fluctuation-dissipation theorem.

1.2 Exchange Coupling

This section is mainly based on [7]. The most used interaction Hamiltonian in the field of magnetism is given by the Heisenberg model, which has the general form

$$H = \sum_{i \neq j} \frac{J_{ij}}{2} \boldsymbol{S}_i \boldsymbol{S}_j \,, \tag{1.8}$$

where the two sums run over the entire lattice each, and the factor of $\frac{1}{2}$ corrects double counting. $J_{ij} = J_{ji}$ are symmetric and called exchange constants or couplings. This exchange interaction has a quantum mechanical origin, resulting from Coulomb repulsion between electrons in combination with Pauli's exclusion principle. For this thesis and in many studies, the general form is broken down to just nearest-neighbour interactions. This turns out to be a reasonable assumption if the interaction decays fast with distance. Additionally, we assume that the exchange coupling is the same on all sites, i.e., $J_{ij} = J \; \forall i, j$. Thus, for $J < 0$, the energy is minimised for a parallel alignment of the spins, which describes ferromagnetism. For $J > 0$, antiparallel alignment is favoured, which describes antiferromagnetism.
The Heisenberg model is symmetric under the exchange of the three spin components and is thus also called isotropic. In the presence of spin-orbit coupling, exchange anisotropies arise, as well as magnetocrystalline anisotropy which is briefly discussed in Sec. 1.3. The XXZ model gives one example of an anisotropic exchange in uniaxial magnets with

$$H = \sum_{\langle i,j \rangle} \left[J_{x-y} \left(S_i^x S_j^x + S_i^y S_j^y \right) + J_z S_i^z S_j^z \right] \,, \tag{1.9}$$

where $\langle i, j \rangle$ denotes the sum over nearest neighbours and J_{x-y} and J_z are the two different coupling strengths.
In the limit $|J_{x-y}| \gg |J_z|$, we can neglect the contribution from J_z and arrive at the XY model

$$H = J_{x-y} \sum_{\langle i,j \rangle} \left[S_i^x S_j^x + S_i^y S_j^y \right] \,, \tag{1.10}$$

which we will shortly discuss later in Sec. 1.9.
In the opposite limit, $|J_{x-y}| \ll |J_z|$, where we can neglect the contributions from J_{x-y}, we obtain the Ising model

$$H = J_z \sum_{\langle i,j \rangle} S_i^z S_j^z \,. \tag{1.11}$$

All three variants possess different spin dimensions n. The generalisation is given by the n-vector model, also referred to as the $O(n)$ model. For the mentioned

examples, we have $n = 1$ for the Ising model, $n = 2$ for the XY model and $n = 3$ for the Heisenberg model.

1.3 Magnetocrystalline Anisotropy

This section draws upon insights from [5] and [8]. Magnetocrystalline anisotropy is one of the most common types of anisotropy. Its origin is spin-orbit coupling, which is the interaction between the spin and the orbital magnetic moment. In the case of a non-spherically symmetric orbit, the energy depends on the orbit's orientation with respect to the underlying crystal lattice. This leads to energetically preferred spin orientations along certain directions of the lattice structure. The orientation-dependent energy contribution is called magnetocrystalline anisotropy energy. Although these energies are often small compared to the exchange energy, they play a crucial role. Since the exchange energy mostly acts by means of parallel or antiparallel with the freedom of a global spin rotation, a small anisotropy term already gives rise to a particular direction.
Here, we want to consider uniaxial anisotropy. As the name suggests, this type of anisotropy is characterised by a single axis given either by a maximum or minimum in energy. The axis corresponding to the minimum is called the easy axis, and the maximum is the hard axis. Additionally, we use a phenomenological approach which considers the symmetries of the crystal. The assumption on the symmetries is that the crystal looks the same regardless of the direction we look along the easy or hard axis. Therefore, we expect only even powers in the spin or magnetisation. A form usually given in the literature is an expansion in $\sin(\theta_i)$ with

$$E_{a,i} = K_1 \sin^2(\theta_i) + K_2 \sin^4(\theta_i) + \mathcal{O}(\sin^6(\theta_i)) \,, \tag{1.12}$$

where K_1 and K_2 are the anisotropy constants and θ_i is the angle between the anisotropy axis and the spin $\boldsymbol{S}_i$. For simplicity, we align the anisotropy axis with the coordinate axis $\boldsymbol{e}_z$ and parametrise $S_i^z = \cos(\theta_i)$. As constant contributions can be neglected, we can rewrite the anisotropy part of the Hamiltonian as

$$H_a = \sum_i \tilde{K}_1 \, {S_i^z}^2 + \tilde{K}_2 \, {S_i^z}^4 + \mathcal{O}\left({S_i^z}^6\right) \,, \tag{1.13}$$

with scaled anisotropy constants $\tilde{K}_1$ and $\tilde{K}_2$. In terms of real materials, these constants are generally strongly temperature-dependent.

1.4 Equilibrium Phase Transitions

The following discussion is mainly based on [9]. Phenomenologically, following Landau [10], a phase transition can be described by an order parameter which typically takes a non-zero value in one phase but vanishes in the other. A phase transition often has a dramatic consequence for the material, e.g., for a liquid-gas system.
The classic example is the ferromagnetic transition in the Ising model. The order parameter is given by a scalar, which is the average magnetisation per site. Its transition goes from the ferromagnetic phase (ordered) to a paramagnetic phase (disordered). The control parameter is the temperature, and the transition occurs at the critical temperature T_c. The transition is characterised as second-order phase transition, also known by the term continuous phase transition, which is described by a continuous change in the order parameter from one phase to another. A discontinuous transition is referred to as a first-order transition, and the order parameter jumps at T_c.
One characterises a second-order transition using symmetries and their spontaneous breakdown. These transitions arise when a state with reduced symmetry emerges continuously from the disordered (high temperature) phase, which possesses the full symmetry. This is an imprint of spontaneous symmetry breaking, where the ordered state has a lower symmetry than the Hamiltonian. Long-range correlations are dynamically created, independent of whether the model only involves short-ranged interactions. In terms of the Ising model, the $\mathbb{Z}_2$ symmetry is broken, and one of the two states, up or down, gets spontaneously chosen through the transition. The build-up of the long-range correlations is characterised by a divergence in the correlation length in the vicinity of the transition with

$$\xi \sim |T - T_c|^{-\nu} \,, \tag{1.14}$$

where ν is a critical exponent. Alongside, further quantities show power-law divergences, such as the specific heat $C \sim |T - T_c|^{-\alpha}$ or the susceptibility $\chi \sim |T - T_c|^{-\gamma}$. Moreover, one can state the change of the order parameter for $T < T_c$ as proportional to $|T - T_c|^{\beta}$. All the exponents $\alpha, \beta, ...$ fall under the group of critical exponents. It turns out that due to the divergences, the precise microscopic details are not relevant, and the exponents are purely determined by the symmetries and dimensions of the model for short-range interacting equilibrium systems. This falls under the universality hypothesis, which was first clearly stated by Kadanoff [11]. It comprises a large number of critical phenomena to a small number of universality classes. For example, the liquid-gas critical phase transition falls under the Ising universality class. The universal behaviour at the transition also allows for a more

coarse-grained description of phase transitions, e.g., with the Ginzburg-Landau theory in Sec. 1.5.
In addition, we define the dynamical critical exponent z by

$$\tau \sim \xi^z \,, \tag{1.15}$$

which is a relation between the correlation length ξ and the relaxation time τ near the phase transition. It accounts for the critical slowing down of the dynamics close to a phase transition, which can be described by the given power-law divergence. A profound impact on the classification of classical equilibrium phase transitions has been made by Hohenberg and Halperin in [12].
In contrast, in the case of a first-order transition, the correlation length stays finite, and a universal behaviour like that for second-order transitions has not yet been found. At the transition, the free energies of the different states equalise. Thus, a state which is stable on one side of the transition becomes metastable on the other side. It follows that there is a coexistence regime of the phases. In most discussions, the interplay of only two states is discussed. However, in general, multiple states can be involved.

1.5 Ginzburg-Landau Theory

In Landau's first approach, only spatial homogeneous systems were considered. This was later generalised to inhomogeneous systems with the Ginzburg-Landau theory [13], first for superconductors. For this section, we follow [14].
Within this approach, the partition function takes the form of a functional integral

$$Z = \int \mathcal{D}m \, e^{-\beta F[m(x)]} \,, \tag{1.16}$$

with the order parameter $m(x)$. Here, the spatial variable x and the function m are continuous. This can be interpreted as a coarse-grained description of the discrete spins. The (effective) free energy $F[m(x)]$ is a functional of the order parameter. Using the interpretation of a thermal ensemble, we can state the probability of a given configuration of $m(x)$ via

$$p[m(x)] = \frac{e^{-\beta F[m(x)]}}{Z} \,. \tag{1.17}$$

A phenomenological approach is used to write down an explicit form of the free energy. As an example, we will use the Ising model on a square lattice. From the microscopic model, we can deduce constraints on the free energy:

- The model has local interactions, and thus, the free energy should be local

$$F[m(x)] = \int \mathrm{d}^d x \, f[m(x), \nabla m(x), \dots] \,, \tag{1.18}$$

  with a local function $f[m(x)]$, the free energy density, which depends on $m(x)$ and derivatives of $m(x)$.

- It carries a Z_2 symmetry if no external field is applied. Therefore, the free energy description should also be invariant under the following transformation

$$m(x) \to -m(x) \,. \tag{1.19}$$

- Additionally, it carries a discrete translation and rotation symmetry. In the limit of large distances, we expect the continuum version of these symmetries to emerge. Thus, the free energy should also be invariant under them.

- Furthermore, we assume that the free energy density is analytic in $m(x)$ and its derivatives.

Close to criticality, $m(x)$ becomes small, and a Taylor expansion is possible. Furthermore, we restrict the discussion to cases where $m(x)$ varies only slowly in space, which allows for a gradient expansion.
Keeping only the lowest order terms in the expansion yields

$$F[m(x)] = \int \mathrm{d}^d x \left[\frac{r}{2} m^2 + \frac{u}{4} m^4 + \frac{D}{2} (\nabla m)^2 + \dots \right] , \tag{1.20}$$

where r, u and D are unknown coefficients, which are, in general, dependent on temperature. The arguments leading to this expression are very general, and it turns out that the theory is able to describe the critical point correctly with the correct dependence of the critical exponents on the spatial dimension. This makes it a powerful tool.
Assuming that the path integral is dominated by configurations which minimise the free energy, we determine the Euler-Lagrange equations via a functional derivative,

$$\frac{\delta F}{\delta m(x)} = r m(x) + u m^3(x) - D \nabla^2 m(x) = 0 \,. \tag{1.21}$$

The equation is trivially fulfilled for constant $m(x) = m$, and we recover the result from Landau's theory. However, the equation also allows for spatially varying solutions, discussed in Sec. 1.6.

1.6 Domain Walls

The following discussion is based on [14]. For simplicity, we will limit this discussion to a one-dimensional problem.
We can think of a simple excitation in the ordered phase by connecting the two different domain values at $x = x_0$. Thus, there is a transient region from $m = -m_0$ to $m = +m_0$. This interpolation is called a domain wall. Due to the gradient term in the free energy, it cannot be instantaneous, but a smooth transition must be built. The solution to Eq. (1.21) for a smooth interpolation between the two domain values is given by

$$m_{\text{wall}} = m_0 \tanh\left(\frac{x - x_0}{\xi_0}\right), \quad \text{with} \quad \xi_0 = \sqrt{-\frac{2D}{r}}\,. \tag{1.22}$$

Here, ξ_0 is the width of the domain wall, which diverges at the critical point where $r = 0$. We now use this solution to calculate the energy cost of a domain wall in one dimension, which gives

$$\Delta F_{\text{wall}} = F(m_{\text{wall}}) - F(\pm m_0) \sim \sqrt{-\frac{Dr^3}{u^2}}\,. \tag{1.23}$$

Notice that the energy cost does not scale with the system size. Thus, the domain wall energy is always finite and thermal fluctuations destroy long-ranged order at any finite temperature.
This is very different in higher dimensions since the energy cost of a straight domain wall scales with the area of itself given by L^{d-1}. It follows that the ordered state for $d > 1$ is stable for small but finite temperatures.

1.7 Minimal Model for Moving Domain Walls in One Dimension

In this section, we want to investigate a simple model to describe moving domain walls. We will later encounter domain walls that move with a constant velocity due to an applied oscillating field where hydrodynamic interactions play an important role.
A simplified description neglects such interactions and models the domain walls as point particles with constant velocities $\pm v_0$. Upon collision, these particles annihilate, which effectively describes the shrinking of a domain until it vanishes. This model is also known as the 2-velocity or $\pm$ model and is well studied [15, 16]. It falls under the field of ballistic annihilation.
The long-time behaviour depends fundamentally on the initial velocity distribution,

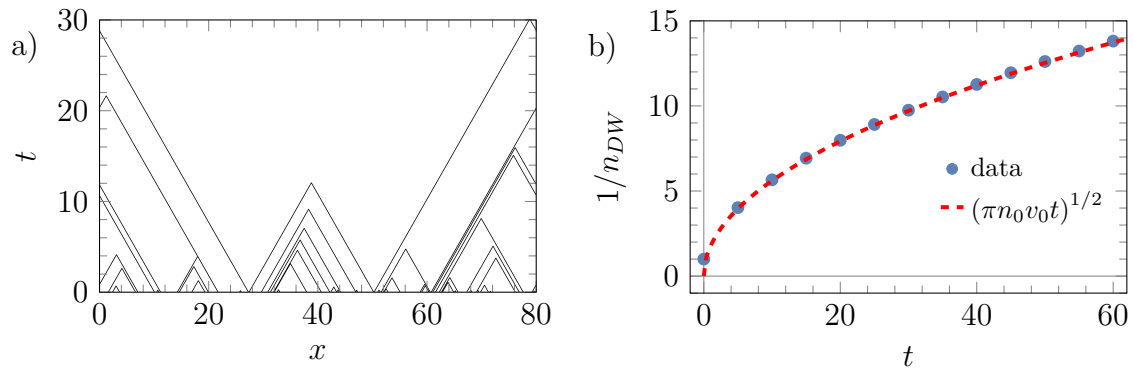

Figure 1.2: Panel a) shows worldlines for one realisation of a one-dimensional minimal domain wall model in space-time. The initial density is $n_0 = 1$ with an initial number of $N_0 = 80$ domain walls and a system of $L = 80$. Panel b) shows the comparison of the scaling of the inverse domain wall density with time against numerical data. The data was collected for a system of size $L = 20{,}000$, and initial density $n_0 = 1$ averaged over 200 initial conditions.

which is, in general, given by

$$P(v, t = t_0) = p_+\delta(v - v_0) + p_-\delta(v + v_0)\,, \tag{1.24}$$

with $p_+ + p_- = 1$. The spatial distribution turns out to have minimal influence on the kinetics. But an important requirement is that it is non-singular.
In the case where one of the probabilities is larger than the other, e.g., $p_+ > p_-$ the number of particles N_- with velocity v_- decays exponentially in time while N_+ quickly reaches its asymptotic limit.
For the interesting case where the probabilities are equal, $p_+ = 0.5 = p_-$, the particle (domain wall) density decays as

$$n_{\mathrm{DW}} \simeq (\pi n_0 v_0 t)^{-\frac{1}{2}} + \mathcal{O}(t^{-1})\,, \tag{1.25}$$

on long time scales where n_0 is the initial density. The decay is shown in Fig. 1.2b) together with data collected from simple simulations in `Mathematica` [17] averaged over 200 different initial configurations with periodic boundary conditions. The agreement of the numerical and analytical curves is excellent. Notice that for these simulations, it is not necessary to simulate in real-time and wait until all collisions have happened. We can calculate all possible collision times from the initial distribution and then sort them in a list to eliminate those that appear later with a particle that has already been annihilated. We have also used this trick to study a current-carrying non-equilibrium particle model in Ch. 6. A visualisation is shown in Fig. 1.2a) which displays the worldlines of one simulation. Particles that move in the same direction cannot annihilate since they have the same velocity, and due to

the annihilation process, particles never cross the trajectory of another. The initial positions are drawn from a uniform distribution, and the velocities according to Eq. (1.24) with $p_+ = 0.5 = p_-$.
While Eq. (1.25) has been derived analytically, we can additionally give a simpler argument for the algebraic decay using the central limit theorem and scaling [18]. We consider an initial number of $N = n_0 L$ particles, and the difference of left- and right-moving particles is of the order of $\Delta N = |N_+ - N_-| \sim \sqrt{N}$. At $t \to \infty$, all particles of the minority have been annihilated, and the final density is of the order of $n_{\text{final}} \sim \Delta N/L \sim \sqrt{n_0/L}$. Here, we assume a scaling form of $n \sim \sqrt{n_0/L} f(L/v_0 t)$ with unknown scaling function f. Following from the argument above, the function is constant for $t \to \infty$. In the other limit of shorter times, the density cannot depend on the system size, implying that $f(L/v_0 t) \propto \sqrt{L/v_0 t}$. Therefore, the same power law as in Eq. (1.25) follows.
For later purposes, see Sec. 3.4, we translate this back to the domain wall system. Here, the correlation length scales like the inverse density of domain walls and thus

$$\xi \sim \sqrt{v_0 t}\,, \tag{1.26}$$

has an algebraic growth as well.

1.8 Symmetry Breaking & Goldstone Modes

In the discussion about equilibrium phase transitions, we already used the term spontaneous symmetry breaking of a discrete symmetry. Here, we briefly elaborate on the general concept and focus, in particular, on the consequences of spontaneous symmetry breaking of a continuous symmetry. Within the discussion, we always refer to global symmetries. The information presented here is based on [19] and [14].
There are two different ways of symmetry breaking: explicit and spontaneous. For the explicit symmetry breaking, we can think again of the Ising model with a $\mathbb{Z}_2$ symmetry, $m \to -m$, as an example. If we apply a constant magnetic field h, we introduce a particular direction and a term of the form $h\,m$ is added to the Hamiltonian. This term breaks the $\mathbb{Z}_2$ symmetry, which we call an explicit symmetry breaking. Whenever we add a symmetry-breaking term to the Hamiltonian, it corresponds to an explicit breaking. Notice that we used the Hamiltonian description here. However, the arguments hold for a Lagrangian or action as well.
In the case of spontaneous symmetry breaking, no term is added to the Hamiltonian. It occurs when the Hamiltonian has a symmetry which is not respected by the ground state. The ground state is thus degenerate. An example with a dis-

crete symmetry is the already mentioned Ising model without an external applied magnetic field. When crossing the phase transition, one of the two ground states is spontaneously chosen, and the $\mathbb{Z}_2$ symmetry is broken. The Hamiltonian stays the same and still has the symmetry. But what happens with a continuous symmetry? For a spontaneously broken continuous symmetry, the ground state carries an infinite degeneracy, and thus, in contrast to the Ising model, there are not two choices but an infinite number of choices for the ground state. Here, we can use the example of the $O(n)$ model, which is then broken down into a residual $O(n-1)$ symmetry in the ground state. The space of ground states is given by the $n-1$ sphere, and each point on the sphere corresponds to one ground state, which all have the same energy.
This brings us to the point where we can state Goldstone's theorem, which was first proven in [20]. It states that the spontaneous breaking of a continuous symmetry gives rise to gapless excitations, the Goldstone modes. Gapless hereby means that the energy costs vanish in the infinite wavelength limit. In many condensed matter systems, low-temperature behaviour is dominated by gapless excitations since the exponential Boltzmann factor does not suppress them. For the example of the $O(n)$ model, the Goldstone manifold is given by $\frac{O(n)}{O(n-1)}$, which is the $n-1$ sphere. The dimension gives the number of generators, which is $n-1$. In case of a linear dispersion relation, e.g, an antiferromagnet, this corresponds to $n-1$ Goldstone modes. For a quadratic dispersion, e.g., a ferromagnet, there are $\frac{1}{2}(n-1)$ Goldstone modes.

1.9 XY Model and Kosterlitz-Thouless Transition

An interesting model which is a paradigm example for a topological phase transition is the two-dimensional XY model. We briefly discuss the model and sketch the idea of the phase transition based on [21]. It is possible to rewrite the Hamiltonian, Eq. (1.10), in terms of angles in the xy-plane with

$$H = -J \sum_{\langle i,j \rangle} \cos(\phi_i - \phi_j) \,, \tag{1.27}$$

where we now assume $J > 0$ for ferromagnetic coupling. Considering only small deviations between neighbouring angles, we can write down a continuous form in terms of a free energy by a Taylor expansion up to second order of the cosine and by switching the sum to an integral. This leaves us with

$$F - E_0 = \frac{J}{2} \int d\boldsymbol{r} \, (\nabla \phi)^2 \,, \tag{1.28}$$

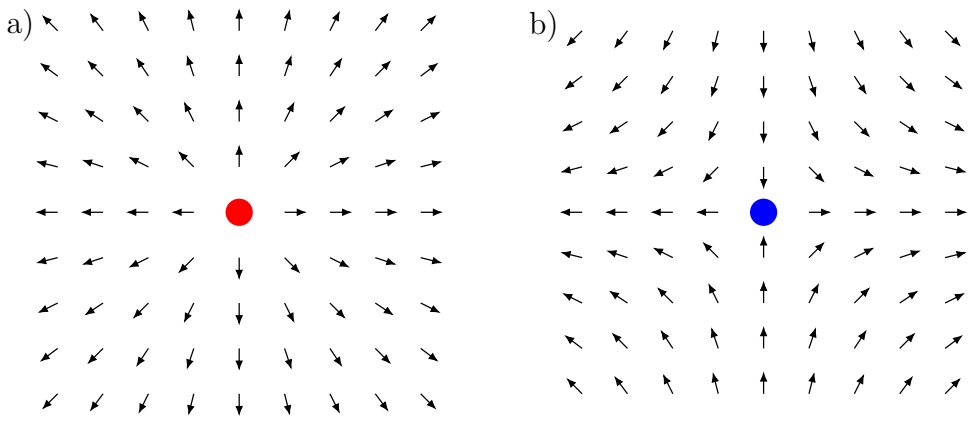

Figure 1.3: Two different spin configurations are visualised for the two-dimensional XY model. Panel a) displays a vortex structure with winding number +1, and panel b) an anti-vortex structure with winding number −1.

where $E_0 = 2JN$ is the fully aligned ground state with N spins in the system. Minimising the energy yields

$$\nabla^2 \phi = 0\,. \tag{1.29}$$

The trivial solution is given by ϕ =const., which is the ground state. However, stable defects exist in the form of vortices. Those defects are singular points which have to fulfil the following boundary conditions

$$\oint_{\boldsymbol{r}_0 \in C} d\boldsymbol{r} \nabla\phi = 2\pi n \quad \text{and} \quad \oint_{\boldsymbol{r}_0 \notin C} d\boldsymbol{r} \nabla\phi = 0\,, \tag{1.30}$$

where $n \in \mathbb{Z}$ denotes the vorticity or winding number of the vortex and $\boldsymbol{r}_0$ its location. Thus, if we enclose the vortex core with a closed loop, we expect a multiple of 2π. Fig. 1.3 shows two single vortices with vorticity +1 in panel a) and vorticity −1 in panel b). It is simple to check that the two images fulfil the above conditions. To estimate the energy of a single vortex, we can use the first boundary condition from which follows that $\nabla\phi = \frac{n}{\rho} e_\phi$ for a closed loop of radius ρ. Using this, we can determine the energy of a vortex state from Eq. (1.28) and get

$$F_{\text{vortex}} - E_0 = \pi n^2 J \ln\left(\frac{L}{a}\right)\,, \tag{1.31}$$

where L is the linear dimension of the system, and a is the lattice spacing. The energy shows a logarithmic divergence in the system size. At first glance, one might not expect a single vortex at any finite temperature. However, arguing with the entropy $S = 2k_B \ln\left(\frac{L}{a}\right)$ on a square lattice, which also diverges logarithmically with system size, one can estimate that for $T > \frac{\pi J}{2k_B} = T_{\text{KT}}$ the system favours the formation of vortices to lower the free energy. For low temperatures, $T < T_{\text{KT}}$, free

vortices do not exist, and quasi-long-range order shows up. This is described by an algebraic dependence of the spin-spin correlations on the distance given by $\sim \rho^{-\eta}$ where $\eta = \frac{T}{2\pi J}$. Notice that the exponent changes continuously with temperature.
Since the whole theory of the phase transition is not the goal of this section, let us only briefly discuss its phenomenology. For low temperatures below T_{KT}, only bound vortex-anti-vortex pairs can exist which are very close in distance. This does not disorder the system, and the low-temperature approximation above holds. Thus, correlations decay algebraically with distance. The average separation of the pairs increases with temperature until they finally unbind at T_{KT}. Free vortices move through the system, and the low-temperature approximation breaks down. The correlations decay exponentially with distance, and the system is disordered. Although there is a clear phase transition at T_{KT}, the rotational symmetry is not spontaneously broken, and there is no true long-range order. This last statement can be generalised to the Mermin-Wagner theorem [22, 23]. It states that continuous symmetries cannot undergo spontaneous breaking at finite temperatures in one- and two-dimensional systems with sufficiently short-range interactions.
The two-dimensional XY model is just one example where, in more general terms, a Berezinski-Kosterlitz-Thouless transition occurs [24, 25]. Similar to the continuous phase transitions, one can define it as a universality class and observe it in many systems.

1.10 Non-Equilibrium Phase Transitions

For the following discussion, we follow [9]. A strong and generalised treatment in terms of an equilibrium free energy is not known for non-equilibrium systems. A common way of treating a non-equilibrium system is starting directly from a general dynamical system, e.g., described by a Langevin equation. This should be interpreted as a coarse-grained description on a mesoscopic level. Its construction is done from symmetry arguments in the same way as the Ginzburg-Landau free energy [26].
Unlike in equilibrium systems, time is an important degree of freedom in non-equilibrium systems. In some cases, the system might relax to an equilibrium steady state. However, many non-equilibrium dynamics no longer follow detailed balance, allowing for a much richer behaviour in the steady states and the time-dependent relaxation process. One example is travelling states [27], just like the moving domain walls which we will encounter later, which cannot exist in equilibrium where any change in one direction is equally balanced in the other.
The large variety of steady states also allows for a wide range of non-equilibrium

phase transitions, active matter systems [28, 29] and fluid mechanics [30]. Similar to equilibrium systems, it is believed that universality and the notion of critical exponents can be applied to continuous non-equilibrium phase transitions as well. However, much less is known about the classification into universality classes, and each transition has to be studied individually.

Part I

Driven Ferrimagnet - Active Magnetic Matter

2

Ferrimagnet and Methods

This chapter is devoted to the model of a ferrimagnet and starts with its atomistic form using classical spins to explain the ground state behaviour. The model is a working example of an active magnetic matter model, and the last section of this chapter focuses on its terminology and relations to active matter from the literature. The first essential concept for this is the *activation of the Goldstone mode*, here, with an oscillating magnetic field. Even a tiny driving field can strongly influence the dynamical properties. This rotational mode in the xy-plane and its direction dependence on the sign of the z-component of the spin play a crucial role in the active behaviour and are discussed in Sec. 2.2.
Furthermore, in Sec. 2.4, we explain the implementation in Mumax3 in the spirit of a micromagnetic approach and connect it to the spin model, particularly how the different parameters are related and which choice of units are made. In addition, we introduce an effective description that is valid for smooth profiles, which will be used later to explain and understand the results. The numerical implementation of this model is briefly discussed.
The chapter concludes by giving a brief notion for *dynamical frustration*, which is the second essential concept for this work, as well as an overview of active matter.

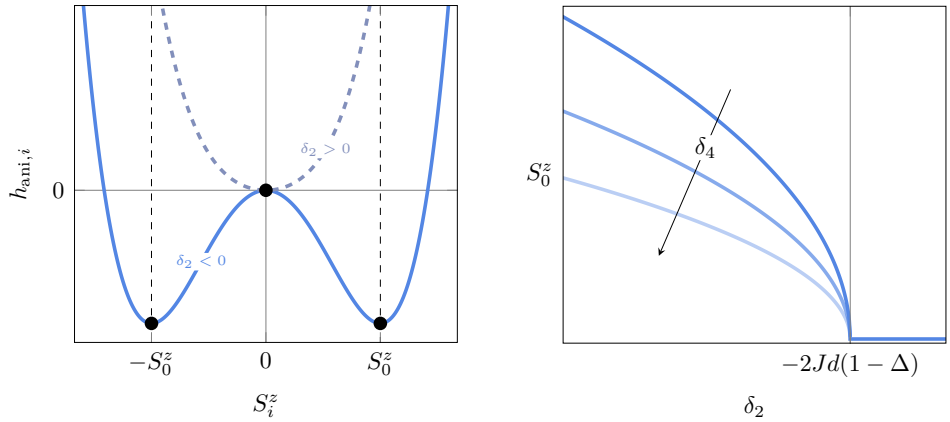

Figure 2.1: Panel a) shows the shape of the anisotropy potential without the correction from the interaction with two minima for $\delta_2 < 0$ and one minimum at $S_i^z = 0$ for $\delta_2 > 0$. Panel b) shows the ground state value of S_i^z as function of the control parameter, including the effects of the XXZ-interaction, $H = H_0 + H_{\mathrm{ani}}$, for three different values of δ_4.

2.1 Equilibrium Spin Model and Ground State

This section discusses the underlying spin model and its ground state properties. The building block is an XXZ-Heisenberg interaction of the following form

$$H_0 = J \sum_{\langle i,j \rangle} \left[S_i^x S_j^x + S_i^y S_j^y - \Delta S_i^z S_j^z \right], \tag{2.1}$$

with $J, \Delta > 0$, i.e., the coupling in the xy-plane favours antiferromagnetic order, while the coupling in z-direction (minus sign in front of Δ in Eq. (2.1)) favours ferromagnetic order. Here we use classical spins $\boldsymbol{S}_i = (S_i^x, S_i^y, S_i^z)$, and the summation $\langle i, j \rangle$ goes over nearest neighbours. Our lattice of choice is a d-dimensional hypercube, e.g., a spin chain in one dimension with $\sum_{\langle i,j \rangle} \to \sum_i$ and $j \to i + 1$. Additionally, we will use normalised spins with $|\boldsymbol{S}_i| = 1$. Notice that this is equivalent to a rescaling of the time by the length of the spin $t \to t_s = St$ in the LLG equation, which will become important later in Sec. 2.4 to compare to the micromagnetic simulations.
Furthermore, we impose local uniaxial anisotropy terms inspired by the Ginzburg Landau theory of the following form

$$H_{\mathrm{ani}} = \sum_i h_{\mathrm{ani},i} = \sum_i \frac{\delta_2}{2} \left(S_i^z\right)^2 + \frac{\delta_4}{4} \left(S_i^z\right)^4, \tag{2.2}$$

where we use $\delta_4 > 0$ and δ_2 as a control parameter. For $\delta_2 > 0$, $h_{\mathrm{ani},i}$ has one minimum exactly at $S_i^z = 0$, whereas for $\delta_2 < 0$, there are two minima at $S_i^z = \pm\sqrt{\frac{-\delta_2}{\delta_4}}$, see Fig. 2.1a).

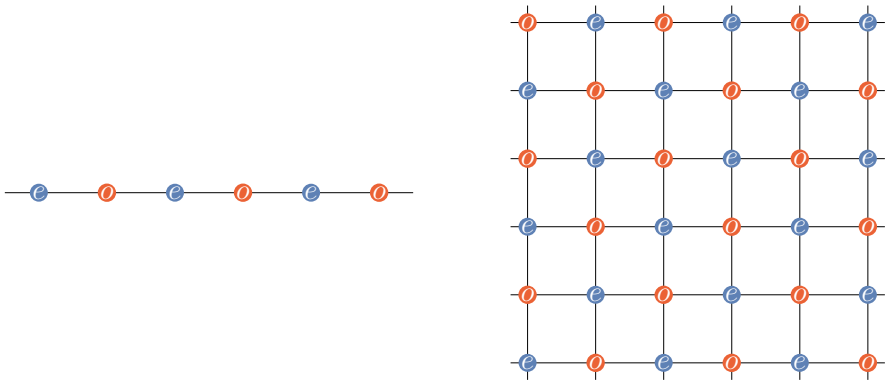

Figure 2.2: Illustration of the used spin chain and square lattice. The two sublattices are denoted by e and o for even and odd, respectively which are required due to the antiferromagnetic coupling in the xy-plane. The number of neighbouring spins on a d-dimensional hypercube is given by $2d$, i.e., two for the chain and four for the square lattice.

How does that influence the ground state in the full Hamiltonian $H = H_0 + H_{\text{ani}}$? The first thing to notice is that the Hamiltonian is translationally invariant by two lattice sites, i.e., $\boldsymbol{S}_i = \boldsymbol{S}_{i+2}$, due to the antiferromagnetic coupling. Therefore, it is sufficient to consider only the two sublattices, $\boldsymbol{S}_e$ and $\boldsymbol{S}_o$, for even and odd sites, respectively. The resulting structure for a spin chain and a square lattice is illustrated in Fig. 2.2. For the calculation, the only effective change with dimension is the number of neighbouring sites. For a d-dimensional hypercube, each site has $2d$ neighbours.

A direct consequence is that, e.g., in one dimension, a simulation of two sites can describe the relevant physics of the ground state. Naturally, this breaks down once the state is not translationally invariant, e.g, for a domain wall.

We use the following parametrisation for the spin, which will also become handy in later calculations

$$\boldsymbol{S}^{\text{param}}(\theta,\phi) = \begin{pmatrix} \sin(\theta)\cos(\phi) \\ \sin(\theta)\sin(\phi) \\ \cos(\theta) \end{pmatrix}, \tag{2.3}$$

where $\theta \in [0,\pi]$, $\phi \in [0,2\pi)$. For the calculation here, we use $\boldsymbol{S}^{(0)}_{e/o} = \boldsymbol{S}^{\text{param}}(\theta^{(0)}_{e/o}, \phi^{(0)}_{e/o})$ where the superscript denotes the order in applied magnetic field and will become helpful in the next section where we add a time-dependent magnetic driving field to the Hamiltonian. Inserting Eq. (2.3) into the Hamiltonian and minimising the energy with respect to the fields, $\theta^{(0)}_{e/o}, \phi^{(0)}_{e/o}$), by means of Euler-Lagrange equations, yields

$$\begin{aligned} \left(S^z_{e/o}\right)^{(0)} = \cos\left(\theta^{(0)}_{e/o}\right) &= \pm\sqrt{\frac{-\delta_2 - 2Jd(1-\Delta)}{\delta_4}}\,, \\ \phi^{(0)}_e = \tilde{\phi} &= \phi^{(0)}_o + \pi\,. \end{aligned} \tag{2.4}$$

For convenience, we will denote $\theta_{e/o}^{(0)}$ by θ_0 and the spin in z-direction $\left(S_{e/o}^z\right)^{(0)}$ by S_0^z in the following.
It turns out that the transition in S_0^z is at $\delta_2 = -2Jd(1-\Delta)$, which means that $S_i^z = 0\ \forall i$ above this value for the ground state. For $\delta_2 < -2Jd(1-\Delta)$ the z-component of the spins take one of the values given by Eq. (2.4). This gives an Ising-like transition with respect to the control parameter δ_2, see Fig. 2.1b). We will also call it the Ising mode for this reason. For the angle in the xy-plane, any value $\tilde{\phi} \in [0, 2\pi)$ can be chosen, which is an imprint of spontaneous symmetry breaking of the global U(1) symmetry of the full Hamiltonian, i.e., rotations of all spins around the S^z-axis. In fact, this is the Goldstone mode that we will activate in the next section. We also call this mode the *staggered* xy-order, i.e., ϕ=$(\phi_e, \phi_o + \pi)$, due to the π-shift caused by the antiferromagnetic nature.

2.2 Goldstone Mode Activation

Previously, we learned about the ground state of the ferrimagnet and that it has a rotational Goldstone mode given by the staggered xy-order. This section is about one simple way of activating this mode to study the consequences on the dynamics. The general mechanism is referred to as *Goldstone mode activation* and has been used for other systems, e.g., driven chiral magnets [31, 32] and driven skyrmions [33]. An advantage of driving the Goldstone mode is that arbitrarily small driving fields are sufficient to drive the system out of equilibrium.
In this thesis, we use the following driving term in the Hamiltonian

$$H_{\text{driv}} = -\sum_{i\in\text{even}} g_e B_z S_i^z - \sum_{i\in\text{odd}} g_o B_z S_i^z \quad \text{with} \quad B_z(t) = b_0 \cos(\omega t)\,, \tag{2.5}$$

where $g_{e,o}$ are (different) g-factors (coupling strength to the magnetic field) corresponding to each sublattice, b_0 is the field strength and ω is the frequency of the drive. This is a simple way of driving the system and activating the rotational mode. It turns out that using $g_e = g_o$ does *not* lead to a rotation of the spins, and thus for this protocol, a finite difference between the two is necessary.
To show the activation of rotation, we calculate the responses via an expansion in orders of the driving strength b_0 up to second order around the ground state of the ferrimagnet, Eq. (2.4). The expansion is justified for $J \gg b_0$. First, we can reuse the parametrisation Eq. (2.6) via

$$\boldsymbol{S}_{e/o} = \boldsymbol{S}^{\text{param}}\left(\theta_0 + \theta_{e/o}^{(1)} + \theta_{e/o}^{(2)} + \mathcal{O}(b_0^3), \phi_{e/o}^{(0)} + \phi_{e/o}^{(1)} + \phi_{e/o}^{(2)} + \mathcal{O}(b_0^3)\right)\,, \tag{2.6}$$

where the superscript becomes useful, with θ_0 and $\phi^{(0)}_{e/o}$ now being the equilibrium solution, Eq. (2.4). Now, we can insert this expression into the LLG Eq. (1.7) with $\boldsymbol{\xi}_i = 0$. Additionally, we project the vector-valued equation onto the vectors $\frac{\partial \boldsymbol{S}_{e,o}}{\partial \theta_{e,o}}$ and $\frac{\partial \boldsymbol{S}_{e,o}}{\partial \phi_{e,o}}$ orthogonal to $\boldsymbol{S}_{e,o}$ to arrive at four coupled equations in $\theta^{(n)}_{e,o}$ and $\phi^{(n)}_{e,o}$ with all orders of b_0^n.
Next, we can solve the equations order by order, starting with the first-order contributions given by

$$\begin{aligned}
0 &= -2Jd\sin(\theta_0)\left(\phi^{(1)}_{e/o} - \phi^{(1)}_{o/e}\right) + \dot{\theta}^{(1)}_{e/o} + \alpha\sin(\theta_0)\dot{\phi}^{(1)}_{e/o}\,, \\
0 &= 4Jd\left(\Delta - (\Delta-1)\cos^2(\theta_0)\right)\theta^{(1)}_{e/o} \\
&\quad + \left(2Jd(-1-\Delta) + (2Jd(1-\Delta) + 2\delta_2 + \delta_4)\cos(2\theta_0) + \delta_4\cos(4\theta_0)\right)\theta^{(1)}_{o/e} \\
&\quad + 2\alpha\dot{\theta}^{(1)}_{o/e} - 2\sin(\theta_0)\left(b_0 g_{e/o}\cos(\omega t) + \dot{\phi}^{(1)}_{o/e}\right).
\end{aligned} \tag{2.7}$$

Notice that, as expected for a linear response, the source term is given by $\sim \cos(\omega t)$, so that the following ansatz describing oscillations around the equilibrium value with respect to the frequency of the drive is suitable to solve the equations

$$\begin{aligned}
\phi^{(1)}_{e/o} &= \phi^{(1)}_{e/o,\omega}e^{i\omega t} + \phi^{(1)}_{e/o,-\omega}e^{-i\omega t}\,, \\
\theta^{(1)}_{e/o} &= \theta^{(1)}_{e/o,\omega}e^{i\omega t} + \theta^{(1)}_{e/o,-\omega}e^{-i\omega t}\,.
\end{aligned} \tag{2.8}$$

We can solve for the coefficients by comparing the terms in front of $e^{\pm i\omega t}$. As these are larger expressions, they are given in App. A. $\theta^{(1)}_{e/o}$ and $\phi^{(1)}_{e/o}$ are real-valued, i.e., the coefficients $\theta^{(1)}_{e/o,-\omega}$, $\phi^{(1)}_{e/o,-\omega}$ are the complex conjugates of $\theta^{(1)}_{e/o,\omega}$, $\phi^{(1)}_{e/o,\omega}$. Hence, it is enough to state only the $+\omega$ coefficients.
With full knowledge of the linear response, we can go to the second and final order in driving strength for this analysis. The much more lengthy equations read

$$\begin{aligned}
0 &= -2Jds_1\left(s_1\left(\phi^{(2)}_{e/o} - \phi^{(2)}_{o/e}\right) + c_1\left(\theta^{(1)}_{e/o} + \theta^{(1)}_{o/e}\right)\left(\phi^{(1)}_{e/o} - \phi^{(1)}_{o/e}\right)\right) \\
&\quad + \alpha s_2\theta^{(1)}_{e/o}\dot{\phi}^{(1)}_{e/o} + s_1\dot{\theta}^{(2)}_{e/o} + c_1\theta^{(1)}_{e/o}\dot{\theta}^{(1)}_{e/o} + \alpha s_1^2\dot{\phi}^{(2)}_{e/o}\,, \\
0 &= 2c_1\theta^{(1)}_{e,o}\left(2(\Delta-1)Jds_1\theta^{(1)}_{o,e} - \dot{\phi}^{(1)}_{e,o} - b_0 g_{o,e}\cos(\omega t)\right) + c_2\Big(-2(\Delta-1)Jd\theta^{(2)}_{o,e} \\
&\quad + (\delta_2 + \delta_4 s_1^2)\theta^{(2)}_{e,o}\Big) + c_4\delta_4\theta^{(2)}_{e,o} - Jds_2\left(\left(\phi^{(1)}_{e,o} - \phi^{(1)}_{o,e}\right)^2 - (\Delta-1)\theta^{(1)}_{o,e}\theta^{(1)}_{o,e}\right) \\
&\quad - 2(\Delta+1)Jd\left(\theta^{(2)}_{e,o} - \theta^{(2)}_{o,e}\right) + s_2\theta^{(1)}_{e,o}\theta^{(1)}_{e,o}(15(1-\Delta)Jd + 3(2\delta_2+\delta_4)) - 2s_1\dot{\phi}^{(2)}_{e,o} \\
&\quad + 2\alpha\dot{\theta}^{(2)}_{e,o}\,,
\end{aligned} \tag{2.9}$$

where we used $c_n = \cos(n\theta_0)$ and $s_n = \sin(n\theta_0)$ to shorten the expressions.
Three different types of terms lead to a second-order contribution. The first is the driving term paired with a first-order field, the second is pairs of first-order fields, and

the last is the second-order fields themselves. To find the right ansatz for the latter ones, we can look at the first two types, which give equivalent combinations. The simplest ones are the oscillatory terms in both fields with $e^{\pm 2i\omega t}$. But, in contrast to before, $e^{\pm i\omega t}$ paired with $e^{\mp i\omega t}$ leads to a constant contribution. The crucial point here comes from the first equation of Eq. (2.9), where the only term able to compensate for a constant contribution is $\dot{\phi}^{(2)}_{e/o}$, i.e., $\phi^{(2)}_{e/o}$ has a linear in t contribution. This is precisely the rotation in the xy-plane we want to activate. Notice that $\theta^{(2)}_{e,o}$ cannot be used in the same way since it is a bound quantity by the anisotropy. A similar argument applies to the second equation, with the difference that we get a different constant which cannot be equally compensated by $\dot{\phi}^{(2)}_{e/o}$. The way out is given by $\theta^{(2)}_{e,o}$, which we can allow to have a small but constant contribution. Putting this all together leads to the following ansatz

$$\begin{aligned} \phi^{(2)}_{e/o} &= \phi^{(2)}_{e/o,\omega} e^{2i\omega t} + \phi^{(2)}_{e/o,-\omega} e^{-2i\omega t} + \omega_{\mathrm{rot},e/o}\, t\,, \\ \theta^{(2)}_{e/o} &= \theta^{(2)}_{e/o,0} + \theta^{(2)}_{e/o,\omega} e^{2i\omega t} + \theta^{(2)}_{e/o,-\omega} e^{-2i\omega t}\,. \end{aligned} \tag{2.10}$$

It turns out that $\omega_{\mathrm{rot},e} = \omega_{\mathrm{rot}} = \omega_{\mathrm{rot},o} = \langle \dot{\phi}^{(2)}_{e/o} \rangle_{T_\omega}$ which is the speed of rotation in the xy-plane. $\langle \dots \rangle_{T_\omega}$ denotes the average over a period $T_\omega = \frac{2\pi}{\omega}$ of the driving field B. The full expression with all parameter dependencies is given in App. A. A shorter way of writing it directly in terms of the first-order fields is given by

$$\omega_{\mathrm{rot}} = i\omega \frac{\cos\big(\theta^{(0)}\big)}{\sin(\theta^{(0)})} \left(\theta^{(1)}_{e,\omega}\phi^{(1)}_{e,-\omega} - \theta^{(1)}_{e,-\omega}\phi^{(1)}_{e,\omega} + \theta^{(1)}_{o,\omega}\phi^{(1)}_{o,-\omega} - \theta^{(1)}_{o,-\omega}\phi^{(1)}_{o,\omega} \right) = \iota S^z_0\,. \tag{2.11}$$

Note that the sign of the spin-z-component $S^z_0 = \cos(\theta_0)$ from the ground state defines the direction of rotation, where we absorbed all other dependencies into ι, with $0 < \iota \sim b_0^2 (g_e - g_o)^2$. In particular, it means that a spin pointing down, $S^z_0 < 0$, rotates clockwise, $\langle \dot{\phi} \rangle_{T_\omega} < 0$, and a spin pointing up, $S^z_0 > 0$, rotates anti-clockwise, $\langle \dot{\phi} \rangle_{T_\omega} > 0$. We call this driven rotation of the Goldstone mode its *activation*.
The resonance frequency of ω_{rot} is

$$\omega_{\mathrm{res}} = \left[\frac{2Jd}{1+\alpha^2} \left(4J(1+\Delta) - (2\delta_2 + \delta_4)\cos(2\theta_0) - \delta_4 \cos(4\theta_0) \right) \right]^{1/2}, \tag{2.12}$$

which reduces to a simpler form at the critical point $\delta_2 = 2J(\Delta - 1)$ given by

$$\omega_{\mathrm{res,crit}} = 4Jd \left[\frac{\Delta}{1+\alpha^2} \right]^{1/2} \overset{\alpha \ll 1}{\approx} 4J\sqrt{\Delta}\,. \tag{2.13}$$

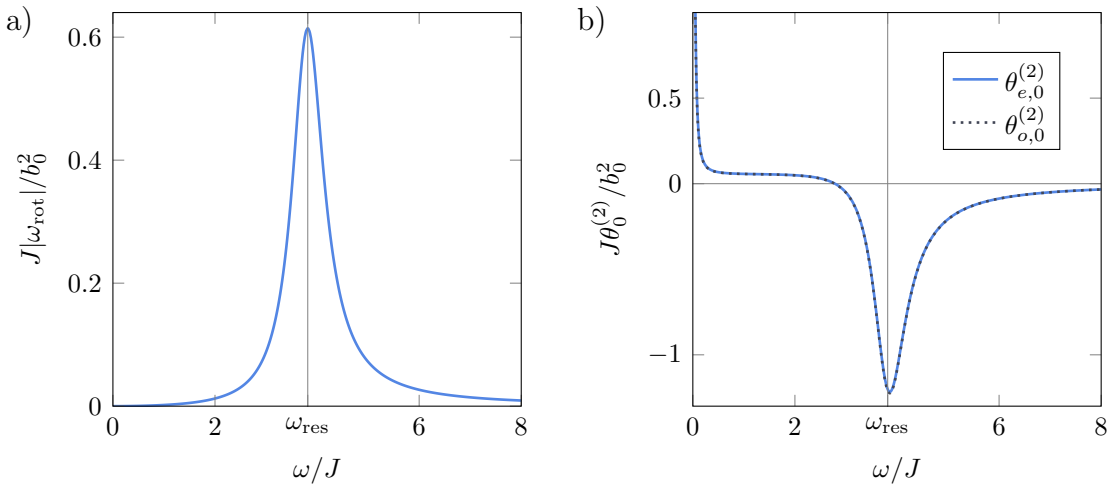

Figure 2.3: The rotational frequency (panel a)) and the constant second-order correction in $\theta_{e,o}$ (panel b)) are shown as a function of the driving frequency. For values of ω near the resonance frequency ω_{res}, driving leads to an enhancement of the S^z-component. Notice that we zoomed in on the resonance frequency. At $\omega = 0$ the value of $\theta_{e/o,0}^{(2)}$ remains finite. Parameters are $d = 1, J = 1, \Delta = 0.8, \delta_2 = -0.6, \delta_4 = 1, \alpha = 0.1, g_e = 1, g_o = 0.1, b_0 = 0.1$.

At resonance, the expression for ω_{rot} reduces to a shorter expression,

$$\omega_{\text{rot}} \overset{\omega\to\omega_{\text{res}}}{=} \frac{4b_0^2 Jd\cos(\theta_0)\,(g_e - g_o)^2}{\alpha^2\left(\delta_4\cos(4\theta_0) + (2\delta_2+\delta_4)\cos(2\theta_0) - 4(\Delta+3)Jd\right)^2}, \tag{2.14}$$

which scales with the inverse of the square of the damping α.
Fig. 2.3a) shows ω_{rot} as a function of the driving frequency, additionally displaying the value of the resonance frequency determined by Eq. (2.12). The knowledge of the resonance frequency becomes important for the simulations that follow. ω_{rot} shows a narrow peak, and we thus want to stay close but not at resonance to get a reasonable number of rotations that does not scale with the inverse of the square of the damping.
While ω_{rot} is the same for even and odd sites, the constant shifts $\theta_{e/o,0}^{(2)}$ differ in leading order by a term proportional to the square of the damping $\sim \alpha^2$, see App. A for the full expression. However, on the scale shown in Fig. 2.3b), the difference ($\sim 10^{-3}$) is not visible. Nevertheless, we can see that in a regime around the resonance frequency, the static spin-z-value $\cos(\theta_0)$ is enhanced to $\cos\left(\theta_0 + \theta_{e/o,0}^{(2)}\right)$ due to the driving field. While this is negligible for small driving strength, it will become visible at higher driving strength. We will see this, for example, in Sec. 3.7 about the localised domain wall in the regime far away from the domain wall.

2.3 Rotation of the Goldstone Mode from Conservation Laws

Another way of calculating ω_{rot} also exists, which uses the perspective of conservation laws. This approach, valid for values close to the critical point, can be found in [34]. Here, we want to extend this to general values of $\delta_2 < -2Jd(1-\Delta)$ and re-derive the result from the previous section.
The quantity of interest is the total spin in the z-direction $\Sigma_z = \sum_i S_i^z$. Its time derivative, given by the z-component of the LLG, is

$$\dot{\Sigma}_z = \sum_i \alpha \left(\boldsymbol{S}_i \times \dot{\boldsymbol{S}}_i \right)_z = \alpha \sum_i \sin^2(\theta_i)\dot{\phi}_i = \alpha \sum_i \left(1 - (S_i^z)^2\right) \dot{\phi}_i \,, \tag{2.15}$$

where we used again the usual parametrisation of spins from Eq. (2.3). The denomination might now seem misleading since Σ_z is not conserved for finite damping, $\alpha > 0$. However, this is exactly the main ingredient of this calculation. Σ_z is periodic in the driving period T_ω and thus $\langle \dot{\Sigma}_z \rangle_{T_\omega} = 0$ so that

$$0 = \langle \dot{\Sigma}_z \rangle_{T_\omega} = \alpha \sum_i \langle \left(1 - (S_i^z)^2\right) \dot{\phi}_i \rangle_{T_\omega} = N\alpha \langle \left(1 - (S_i^z)^2\right) \dot{\phi}_i \rangle_{T_\omega, N} \,, \tag{2.16}$$

where the additional subscript N in the last step denotes an average over all N sites. Notice that this is different for ϕ_i, which can change from one period to another. As averaging is a linear operation, we can separate it and rewrite the expression in the following way

$$\langle \dot{\phi}_i \rangle_{T_\omega, N} = \langle (S_i^z)^2 \, \dot{\phi}_i \rangle_{T_\omega, N} \,. \tag{2.17}$$

Notice that the prefactors α and N dropped out.
We know that linear response terms oscillate at the driving frequency and thus will average out to zero. So, the first non-zero contribution comes from the second order in the driving field. This should not be so surprising, as it mirrors the full calculation in the previous section.
Taking only the second-order contributions from Eq. (2.17), we get

$$\langle \dot{\phi}_i^{(2)} \rangle_{T_\omega, N} = 2 \langle S_i^{z\,(1)} \, \dot{\phi}_i^{(1)} \rangle_{T_\omega, N} S_0^z + \langle \dot{\phi}_i^{(2)} \rangle_{T_\omega, N} \left(S_0^z\right)^2 \,, \tag{2.18}$$

which we can recast to

$$\omega_{\text{rot}} = \langle \dot{\phi}_i^{(2)} \rangle_{T_\omega, N} = -2 \frac{\cos(\theta_0)}{\sin(\theta_0)} \langle \theta_i^{(1)} \dot{\phi}_i^{(1)} \rangle_{T_\omega, N}. \tag{2.19}$$

Where we used that $S^{z\,(1)} = -\sin(\theta_0)\theta^{(1)}$. This gives us the same result as we obtained previously, compare to Eq (2.11). For a parameter-dependent expression, one still needs to insert the first-order expressions, see App. A.
Close to the critical point, as in [34], we can focus on only the leading order in S_0^z. This is equivalent to neglecting the last term in Eq. (2.18), giving

$$\omega_{\mathrm{rot}} \approx -2\sin(\theta_0)\cos(\theta_0)\langle\theta_i^{(1)}\dot{\phi}_i^{(1)}\rangle_{T_\omega,N}. \tag{2.20}$$

2.4 Mumax3 Implementation and Conversion

To study the spin Hamiltonian numerically, we use *Mumax3* [35], an open-source software for micromagnetic simulations running on GPUs. Micromagnetism is a continuum theory where instead of the discrete spin $\boldsymbol{S}_i$, a continuous magnetisation field $\boldsymbol{M}(\boldsymbol{x})$ is used. The software solves the LLG equation and generates the time- and space-dependent magnetisation. The efficient parallelisation on graphics cards gives rise to high performance and, thus, large-scale simulations. As it is written in Go and CUDA, an Nvidia GPU, in addition to one of the three operating systems, Linux, Windows or Mac, is required. Furthermore, it contains predefined functions, e.g., for ferromagnetic Heisenberg coupling, various anisotropy fields and a thermally fluctuating field, which we will utilise. On the other hand, an XXZ-interaction with antiferromagnetic couplings, as in our Hamiltonian Eq. (2.1), is not predefined. Mumax3 also allows the user to define custom energy density terms, which we need to add our interaction term. Moreover, external, time-dependent fields can be added, and we use this to include the driving field.
The implementation in Mumax3 was done within the Master's thesis of Reza Doostani [36]. This section aims to explain how the interaction term is included and how the parameters used for the discrete Hamiltonian translate to the ones used in the simulations. While we name the most important used predefined functions and the concept, we refer to the Mumax3 webpage [37] for more details, where all functions are explained and examples are shown.
The first step is to approximate the discrete Hamiltonian with a continuous free energy description. This is done to stick to the same units and representation as chosen in [35] to match the one in Mumax3. However, at the end we discretise and match to the spin model. In Sec. 2.2, we used normalised spins. Instead of setting $S = 1$, this can be viewed as a rescaling of the time in the LLG equation with $t \to t_s = St$. Here, we want to start from the time t with spins of arbitrary length S. For all quadratic terms in spin length, interaction and anisotropy, this is trivial, e.g., with $H = J\sum_i \boldsymbol{S}_i\boldsymbol{S}_{i+1}$ the LLG equation is $\frac{d\hat{\boldsymbol{S}}_i}{dt} = -JS\hat{\boldsymbol{S}}_i \times \left(\hat{\boldsymbol{S}}_{i+1} + \hat{\boldsymbol{S}}_{i-1}\right)$ which be-

comes $\frac{d\hat{\boldsymbol{S}}_i}{dt_s} = -J\hat{\boldsymbol{S}}_i \times \left(\hat{\boldsymbol{S}}_{i+1} + \hat{\boldsymbol{S}}_{i-1}\right)$ under the time rescaling and is now in the form used in the previous sections. For the driving field, we used $\frac{d\hat{\boldsymbol{S}}_i}{dt_s} = g_{e,o}B_z(t)\hat{\boldsymbol{S}}_i \times \hat{e}_z$ which is $\frac{d\hat{\boldsymbol{S}}_i}{dt} = g_{e,o}B_z(t)S\hat{\boldsymbol{S}}_i \times \hat{e}_z$ in the time t. Since the only non-local term is the interaction term, we discuss this one in more detail.
For simplicity, we use a one-dimensional chain where the XXZ-interaction part of Eq. (2.1) can be written in the following form

$$H_0 = \frac{J}{2}\sum_i \left[S_i^x\left(S_{i+1}^x + S_{i-1}^x\right) + S_i^y\left(S_{i+1}^y + S_{i-1}^y\right) - \Delta S_i^z\left(S_{i+1}^z + S_{i-1}^z\right)\right] . \tag{2.21}$$

Each individual term has the same form, up to prefactors, and we can use a single index to describe the three spin-space directions $\mu = x, y, z$. We expand the value of the neighbours of spin $\boldsymbol{S}_i$ via

$$S_{i\pm1}^\mu \approx S^\mu(x) \pm a\partial_x S^\mu(x) + \frac{a^2}{2}\partial_x^2 S^\mu(x) + \mathcal{O}(a^3) , \tag{2.22}$$

where we switched to continuous spin variables $S^\mu(x)$, which are assumed to be smooth in space and fulfil $S^\mu(x = x_i) = S_i^\mu$ for a spin at site i.
Mumax3 uses SI units. Thus, we change to the magnetisation per unit volume, defined via

$$\boldsymbol{M}(x) = \frac{\gamma \boldsymbol{S}(x)}{a^3} . \tag{2.23}$$

Notice that for electrons with $\gamma < 1$, spin and magnetisation point in opposite directions. This form encodes that the magnetisation is given per cell of volume a^3 for each spin. With this replacement and the Taylor expansions, we can rewrite Eq. (2.21) to a free energy functional by additionally transforming the sum to an integral,

$$\begin{aligned} F = \int \frac{dx}{a}\frac{Ja^6 M_0^2}{\gamma^2}\Big[\frac{a^2}{2}\left(\hat{M}^x\partial_x^2\hat{M}^x + \hat{M}^y\partial_x^2\hat{M}^y - \Delta\hat{M}^z\partial_x^2\hat{M}^z\right) \\ - (1+\Delta)\left(\hat{M}^z\right)^2\Big] . \end{aligned} \tag{2.24}$$

All units are comprised in the prefactor in front, and a simple check shows that this free energy has units of energy (Joule) as it should. Furthermore, we introduced the normalised magnetisation per unit volume defined by $\hat{\boldsymbol{M}} = \frac{\boldsymbol{M}}{M_0}$ with $M_0 = |\boldsymbol{M}|$. The additional contribution to $\left(\hat{M}^z\right)^2$ arises as we absorbed the quadratic terms of $\hat{M}^x$ and $\hat{M}^y$ from the Taylor expansions into a term $\sim \hat{\boldsymbol{M}}^2$. Since this is just a constant shift to the free energy landscape, we dropped it from the description.
With this free energy, we can now calculate the corresponding effective field. To get a feeling for possible correction factors, we use the simple example of a constant

external field with spin Hamiltonian $H = -\sum_i \gamma \boldsymbol{S}_i \boldsymbol{B}$ similar to Sec. 1.1. Changing to the magnetisation per unit volume using Eq. (2.23) and approximating the sum by an integral yields $F = -\int d^d x a^{3-d} \boldsymbol{M}\boldsymbol{B}$, where we stated the free energy for arbitrary space dimensions d. From this, we can now deduce the effective field for free energies in our convention to be $\boldsymbol{B}_{\text{eff}} = -a^{d-3}\frac{\delta F}{\delta \boldsymbol{M}}$.
Thus, we can state the effective field for the free energy in Eq. (2.24) with $d = 1$ as

$$\begin{aligned}\boldsymbol{B}_{\text{eff}} = \tilde{J}\Bigg[&- a^2\left(\partial_x^2 \hat{M}^x \hat{e}_x + \partial_x^2 \hat{M}^y \hat{e}_y - \Delta \partial_x^2 \hat{M}^z \hat{e}_z\right) + \left(-\frac{\delta_2}{J} + 2(1+\Delta)\right)\hat{M}^z \hat{e}_z \\ &- \frac{\delta_4}{J}\left(\hat{M}^z\right)^3 \hat{e}_z + \frac{g_{e,o} B_z}{J}\hat{e}_z\Bigg] = \tilde{J}\tilde{\boldsymbol{B}}_{\text{eff}}\,,\end{aligned} \tag{2.25}$$

where we added the remaining local terms. $\tilde{J} = \frac{J a^3 M_0}{\gamma^2}$ is again the unit carrying factor in the front. The LLG equation is rewritten to

$$\dot{\hat{\boldsymbol{M}}} = \gamma \hat{\boldsymbol{M}} \times \boldsymbol{B}_{\text{eff}} + \alpha \hat{\boldsymbol{M}} \times \dot{\hat{\boldsymbol{M}}}\,. \tag{2.26}$$

Mumax3 uses a similar form to this where just one time derivative term enters, also often referred to as Landau-Lifshitz (LL) equation. However, the parameters entering the equations are the same as in the LLG equation, so that we can keep the form above for convenience. To keep our life simple, we absorb the factor $\tilde{J}$ into the time variable with $t \to \tilde{t} = \tilde{J}t$. This allows us to stick to the unit-free field $\tilde{\boldsymbol{B}}_{\text{eff}}$ from Eq. (2.25) and we define all fields in the following with respect to this time.
For the anisotropy contributions, we can use a predefined function in Mumax3 with a uniaxial anisotropy field. This is given in the following form

$$\boldsymbol{B}_{\text{ani}} = \frac{2K_{u1}}{M_0}\left(\boldsymbol{u}\hat{\boldsymbol{M}}\right)\boldsymbol{u} + \frac{4K_{u2}}{M_0}\left(\boldsymbol{u}\hat{\boldsymbol{M}}\right)^3 \boldsymbol{u}\,, \tag{2.27}$$

where $\boldsymbol{u}$ is the anisotropy direction, in our case $\hat{e}_z$, and K_{u1}, K_{u2} are the parameters of the anisotropy. Comparing to the anisotropy contributions in the effective field given above, Eq. (2.25), we can identify the two parameters as

$$\begin{aligned}K_{u1} &= \frac{M_0}{2J}\left(2J(1+\Delta) - \delta_2\right)\,, \\ K_{u2} &= -\frac{\delta_4 M_0}{4J}\,.\end{aligned} \tag{2.28}$$

These can be added directly to the predefined parameters *Ku1* and *Ku2*. The object *anisU* is used to define the anisotropy axis $\boldsymbol{u}$. In higher dimensions the first term in the brackets of K_{u1} gets an extra factor d to account for the dimension, i.e., $K_{u1} = \frac{M_0}{2J}\left(2dJ(1+\Delta) - \delta_2\right)$.

For the ferrimagnetic interaction, we have to build our own custom term, since the implemented Heisenberg interaction allows *only* a ferromagnetic coupling strength. Antiferromagnetic couplings in terms of compensated antiferromagnetic interfaces have been realised within Mumax3 [38] using multiple layers. As we are not concerned with different layers, we want to take a different route by defining a custom field $\boldsymbol{B}_{\text{int}}$ and its corresponding energy density E_{dens}. $\boldsymbol{B}_{\text{int}}$ can be read off from Eq. (2.25), however, we have to use a discrete derivative $\tilde{\partial}_x^2 M^\mu = \frac{M_{i+1}^\mu + M_{i-1}^\mu - 2M_i^\mu}{a^2}$ for the implementation, which yields

$$\boldsymbol{B}_{\text{int}} = -a^2 \left(\tilde{\partial}_x^2 \hat{M}^x \hat{e}_x + \tilde{\partial}_x^2 \hat{M}^y \hat{e}_y - \Delta \tilde{\partial}_x^2 \hat{M}^z \hat{e}_z \right) . \tag{2.29}$$

Following the usual implementation of the energy density of an interaction term within Mumax3, we get $E_{\text{dens}} = -\frac{1}{2} \boldsymbol{B}_{\text{int}} \boldsymbol{M}$. These two are added via *AddFieldTerm* and *AddEdensTerm*, respectively. For higher dimensions, we get the same contribution, but one for each spatial direction.

The driving field has to be treated separately, as well. The amplitude of the drive in time $\tilde{t}$ is given by $\frac{b_0 S}{\tilde{J}} = \frac{b_0}{J}$, where the appearance of S was explained at the beginning of this section. Without the staggered g-factors of the field, we could simply add it to the externally applied field $\boldsymbol{B}_{\text{ext}} = \frac{b_0}{J} \cos\big(\tilde{\omega}\tilde{t}\big) \hat{e}_z$ which is automatically updated for each time step in the simulations. However, Mumax3 allows to define *regions* in each of which the field can have a different value. This is done with the *DefRegionCell* function for each site individually, and we define a region for the even sites and a region for the odd sites. We can then set $\boldsymbol{B}_{\text{ext}} = \frac{g_e b_0}{J} \cos\big(\tilde{\omega}\tilde{t}\big) \hat{e}_z$ for all even sites and $\boldsymbol{B}_{\text{ext}} = \frac{g_o b_0}{J} \cos\big(\tilde{\omega}\tilde{t}\big) \hat{e}_z$ for all odd sites with the function *SetRegion*. Notice that since we rescaled the time, the frequency must also be rescaled with the inverse.

This, in total, allows us to simulate the model in Mumax3 with the time measured in $\tilde{t}$. Later, we want to refer only to the units from the discrete Hamiltonian. Within that description, we scaled the time by $t_s = St$. Therefore, the relation is given by

$$t_s = \frac{S}{\tilde{J}} \tilde{t} = \frac{|\gamma|}{J} \tilde{t} \, , \tag{2.30}$$

and all time-dependent quantities will be shown in the unit t_s for all simulations following. Furthermore, we will display the parameters in the scheme of the spin Hamiltonian in time t_s for all simulations. The parameters for the two different choices of times are summarised in Tab. 2.1, including their SI units.

Mumax3 also includes a method to model thermal fluctuations developed in [39]. To correctly account for thermal fluctuations, a stochastic thermal field $\boldsymbol{B}_{\text{therm}}$ is added to the effective field in the LLG equation. This field acts like a vector-valued

Table 2.1: Summary of the main parameters and their units in the two different pictures. The left side shows the values used in the simulations with Mumax3 and the right side displays the units in the spin model used in the discussion about the Goldstone mode activation. To convert the times between each other, we can use Eq. (2.30) where γ has the units $\mathrm{T}^{-1}s^{-1}$.

in Mumax3		in Spin Model	
Parameters	Units	Parameters	Units
$\tilde{t} = \tilde{J}t$	Ts	$t_s = St$	Js^2
$K_{u1} = \frac{M_0}{2J}(2J(1+\Delta) - \delta_2)$	Am^{-1}	δ_2	$\mathrm{J}^{-1}\mathrm{s}^{-2}$
$K_{u2} = -\frac{\delta_4 M_0}{4J}$	Am^{-1}	δ_4	$\mathrm{J}^{-1}\mathrm{s}^{-2}$
1	-	J	$\mathrm{J}^{-1}\mathrm{s}^{-2}$
Δ	-	Δ	-
$b_{\mathrm{ext}} = \frac{b_0}{J}$	-	b_0	$\mathrm{J}^{-1}\mathrm{s}^{-2}$
M_0	Am^{-1}	S	Js

Gaussian white noise with zero mean and variance given by

$$\langle B_{\mathrm{therm},i,\mu}(\tilde{t}) B_{\mathrm{therm},j,\nu}(\tilde{t}')\rangle = C_{\mathrm{therm}}\delta_{i,j}\delta(\tilde{t}-\tilde{t}')\delta_{\mu,\nu} \text{ with } C_{\mathrm{therm}} = \frac{2\alpha T}{|\gamma| M_0 a^3}\,, \quad (2.31)$$

where the indices i and j are the lattice site indices and $\mu, \nu = x, y, z$ describe the field components. Here, we already denoted the time to the rescaled time $\tilde{t}$, which we use in the simulations. Furthermore, we measure temperature in units of energy, i.e., a possible k_B prefactor in front of T was absorbed into the temperature.
For all simulations used in this thesis, we set $M_0 = 1$ and $a = 1$ which simplifies the conversion rules. For most of the data shown, we will use stroboscopic data, i.e., data which is multiples of T_ω apart. Thus, if not stated otherwise, plots from the microscopic simulations include only stroboscopic data. This is sufficient to explain most of the findings and conclusions and saves a lot of memory and averaging.

2.5 Continuous Description and Domain Wall

The description used in Mumax3 serves very well for numerical calculations upon discretising. However, in cases of a fully analytic description, the staggered driving field demands careful consideration. One way to incorporate it while recovering the same first-order responses and rotational frequency as in the discrete case is to build on two sublattices, one for even and one for odd sites. Each of these has its

own continuous counterpart. Thus, we can express the Hamiltonian density for the XXZ-interaction term as

$$\begin{aligned}\mathcal{H}_0 = \frac{J}{2a}\sum_{h=\pm a}\big(&S_e^x(x)S_o^x(x+h) + S_e^y(x)S_o^y(x+h) \\ &- \Delta S_e^z(x)S_o^z(x+h)\big) + (e \leftrightarrow o)\,,\end{aligned} \tag{2.32}$$

which corresponds to the Hamiltonian Eq. (2.1) via $H_0 = \int dx \mathcal{H}_0$. We again reuse the parametrisation Eq. (2.3) to describe the spins, with $\boldsymbol{S}_e(x) = \boldsymbol{S}^{\text{param}}(\theta_e(x), \phi_e(x))$ and $\boldsymbol{S}_o(x) = \boldsymbol{S}^{\text{param}}(\theta_o(x), \pi + \phi_o(x))$. At this stage, we perform a Taylor expansion $f(x \pm a) = f(x) \pm af'(x) + \frac{a^2}{2}f''(x) + \mathcal{O}(a^3)$, where f serves as a placeholder for the four angle fields $\theta_{e/o}$ and $\phi_{e/o}$. Inserting this into the Hamiltonian density above and keeping only terms up to and including second order in a yields

$$\begin{aligned}\mathcal{H}_0 = \frac{J}{a}\Bigg[&- 2\left(s_e s_o \cos(\phi_e - \phi_o) + \Delta c_e c_o\right) + \frac{1}{2}a^2\Bigg(s_e s_o \sin(\phi_e - \phi_o)(\phi_e'' - \phi_o'') \\ &+ s_e s_o \cos(\phi_e - \phi_o)\left((\phi_o')^2 + (\phi_e')^2\right) + 2\sin(\phi_e - \phi_o)\left(c_e s_o \theta_e' \phi_e' - c_o s_e \theta_o' \phi_o'\right) \\ &+ \left(s_e s_o \cos(\phi_e - \phi_o) + \Delta c_e c_o\right)\left((\theta_e')^2 + (\theta_o')^2\right) + \left(\Delta c_o s_e - c_e s_o \cos(\phi_e - \phi_o)\right)\theta_e'' \\ &+ \left(\Delta c_e s_o - c_o s_e \cos(\phi_e - \phi_o)\right)\theta_o''\Bigg) + \mathcal{O}(a^3)\Bigg],\end{aligned} \tag{2.33}$$

where we used $c_{e/o} = \cos\big(\theta_{e/o}\big)$ and $s_{e/o} = \sin\big(\theta_{e/o}\big)$ to shorten the expression. This approximation is reasonable when the fields change on length scales much larger than the lattice spacing a. The local terms such as anisotropies and the driving term stay the same, i.e., $\mathcal{H}_{\text{ani}} = \frac{\delta_2}{2a}\left(c_e^2 + c_o^2\right) + \frac{\delta_4}{4a}\left(c_e^4 + c_o^4\right)$ and $\mathcal{H}_{\text{driv}} = -\frac{b_0}{a}\cos(\omega t)\left(g_e c_e + g_o c_o\right)$. Clearly, the driving term takes a simple form within this choice of continuous variables with two sublattices.

Two simple checks can be conducted to verify the correctness of the derived continuous form. We state them here for completeness. One is the limit of no driving field, where the difference between even and odd sites vanishes. The constant solution is the same as the ground state solution from before, Eq. (2.4). Another limit is the ferrimagnetic domain with driving field. All spatial derivatives vanish, and we indeed recover the same response as for the discrete model.

We proceed by using the just-derived continuous description to derive the domain wall solution at zero driving field where the even and odd fields are the same, i.e., $\phi_e = \phi_{\text{wall}} = \phi_o$ and $\theta_e = \theta_{\text{wall}} = \theta_o$. Using the Euler-Lagrange formalism for the density $\mathcal{H}_0 + \mathcal{H}_{\text{ani}}$, we get two equations of motion. One of them is trivially solved

by ϕ being constant. The other one has the following form

$$\begin{aligned} 0 = &\sin(\theta_{\text{wall}})\cos(\theta_{\text{wall}})\left(2J\left(\Delta-1\right)-\delta_2-\delta_4\cos^2(\theta_{\text{wall}})\right) \\ &- a^2 J(\theta''_{\text{wall}}\left(\Delta\sin^2(\theta_{\text{wall}})+\cos^2(\theta_{\text{wall}})\right) \\ &+ (\theta'_{\text{wall}})^2\sin(\theta_{\text{wall}})\cos(\theta_{\text{wall}})\left(\Delta-1\right)). \end{aligned} \tag{2.34}$$

From Sec. 1.6, we know that a domain wall given by $S^z_{\text{wall}}(x)$ scales with S^z_0 and each derivative of it gives another factor of S^z_0. Therefore, we first switch from the θ-angle description to the S^z one via $S^z_{\text{wall}} = \cos(\theta)$, and then perform a scaling of $S^z_{\text{wall}}(x) = S^z_0 \cdot g_{\text{wall}}(\tilde{x})$, where we also scaled the position by $\tilde{x} = S^z_0 x$. Additionally, we replace $\delta_2 = -2J + 2J\Delta - \left(S^z_0\right)^2\delta_4$ and get

$$0 = g_{\text{wall}} - g^3_{\text{wall}} + \frac{Ja^2\Delta}{\delta_4} g''_{\text{wall}} + \mathcal{O}\left((S^z_0)^2\right). \tag{2.35}$$

Comparing to Sec. 1.6 the solution is given by

$$S^z_{\text{wall}}(x) = S^z_0 g_{\text{wall}}(\tilde{x}) = S^z_0 \tanh\left(\frac{\tilde{x}}{\tilde{\xi}_0}\right) = S^z_0 \tanh\left(\frac{x}{\xi_0}\right), \tag{2.36}$$

with $\tilde{\xi}_0 = S^z_0\xi_0$ and $\xi_0 = \frac{a}{S^z_0}\sqrt{\frac{2J\Delta}{\delta_4}}$ as the domain wall width. We assume that the width is not strongly affected by small driving strength and that the general profile persists. The domain wall is (maybe not by surprise) an allowed solution of the ferrimagnet. We will examine the effects of driving the system in the next chapter.

2.6 Effective Model

The Hamiltonian Eq. (2.33) given in the previous section is rather lengthy, and the corresponding equations of motion consist of even more terms. In addition, averages of oscillatory terms and their combinations must be considered. This section aims to introduce an effective description following the Ginzburg Landau paradigm, Sec. 1.5, which covers only the most relevant terms. One advantage is that it will help us to get a more intuitive understanding of the long-time dynamics. Furthermore, as the equations are based on symmetry considerations, this theory might also be able to describe other microscopic systems on large scales, with the exact length scales depending on the problem at hand.

Inspired by the Goldstone mode activation, we want to use the magnetisation in z-direction m^z, denoted by m in the following to simplify notation, and the xy-order ϕ to describe the dynamics. We first discuss the non-driven setting. Generally, there are now two transitions in the system. One is the Ising-like transition in

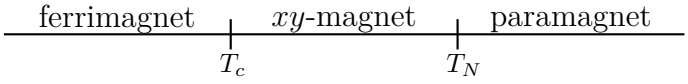

Figure 2.4: Illustration of the phases for the equilibrium ferrimagnet. We assume that the transition of the xy-order ϕ occurring at T_N is at higher temperatures than the transition in the ferromagnetic component m, which occurs at T_c. In the driven scenario, the latter transition is modified into a transition without rotation to one with rotation in the xy-plane.

the ferromagnetic component m at the critical temperature T_c. The other is the spontaneous ordering in ϕ for temperatures $T < T_N$. For our discussion, we assume that $T_c < T_N$. Thus, when starting in an xy-ordered state with approximately constant ϕ, the phase starts to rotate when crossing T_c. This is visualised in Fig. 2.4. Close to the phase transition T_c, i.e., small m, and in the limit of large wavelength, we can expand in orders of fields and derivatives with respect to the symmetries. Those are given by the continuous $U(1)$-symmetry of the Goldstone mode

$$\phi \to \phi + p\,, \tag{2.37}$$

and the discrete $\mathbb{Z}_2$ symmetry

$$\phi \to -\phi \text{ and } m \to -m\,. \tag{2.38}$$

A direct result from the first symmetry is that the field ϕ can only appear with a spatial derivative. From the $\mathbb{Z}_2$-symmetry, it follows that m, as in the Ginzburg Landau theory, and ϕ occur only in even powers in the free energy expansion. Keeping only the lowest orders, we get a free energy of the form

$$F[m(x),\phi(x)] = \int \mathrm{d}^d x \left[\frac{r}{2}m^2 + \frac{u}{4}m^4 + \frac{D_m}{2}\left(\nabla m\right)^2 + \frac{D_\phi}{2}\left(\nabla\phi\right)^2 + \dots\right], \tag{2.39}$$

with the usual Ginzburg-Landau potential in m, where $r \sim T - T_c$ is the control parameter. From this free energy, we can determine the equations of motion from functional derivatives to get

$$\begin{aligned} \alpha\dot{\phi} &= D_\phi\nabla^2\phi + \dot{m} + \eta_\phi\,, \\ \alpha\dot{m} &= -rm - um^3 + D_m\nabla^2 m - \dot{\phi} + \eta_m\,. \end{aligned} \tag{2.40}$$

Notice that we sneaked in $\dot{m}$ and $-\dot{\phi}$ into the equations, respectively. This comes due to the fact that the magnetisation in z-direction is the generator of spin rotations, and thus m and ϕ are conjugate variables. It is also derived in Sec. 2.6.1. Additionally, we have added the two Gaussian white noise fields η_m and η_ϕ. The exact

relation of the noise fields and their variances will be discussed in Sec. 2.6.2. Furthermore, the damping turns out to be the same for both quantities, see Sec. 2.6.1. Eq. (2.40) is the lowest order assumption in derivatives and fields in the non-driven ferrimagnet. However, we wish to bring it out of equilibrium by activating the Goldstone mode rotation. From the response calculation, Eq. (2.11), we know that $\omega_{\mathrm{rot}} = -\iota m$ (including that magnetisation points in the opposite direction to the spin). We can add this term in a phenomenological way to our equations,

$$\begin{aligned} \alpha\dot{\phi} &= -\alpha\iota m + D_\phi \nabla^2 \phi + \dot{m} + \eta_\phi \,, \\ \alpha\dot{m} &= -rm - um^3 + D_m \nabla^2 m - \dot{\phi} + \eta_m \,. \end{aligned} \tag{2.41}$$

Here, we neglect non-local terms with memory effects, i.e., assume that the dynamics remain Markovian. This is reasonable in the case of a rapidly oscillating driving field, as fulfilled by our setting.
In principle, further non-equilibrium terms that do not result from a free energy description but fulfil the above-mentioned symmetries could arise. One example is $\nabla^2\phi$ in the second equation of Eq. (2.41). However, we assume that the prefactors of those terms are small since we operate mostly at low driving amplitudes and that $\omega_{\mathrm{rot}} = -\iota m$ in the first equations of Eq. (2.41) is the most relevant term.
An additional remark should be made at this point: Assuming a stationary state with a constant m-profile and spatially constant ϕ without thermal fluctuations, we obtain

$$\begin{aligned} \alpha\dot{\phi} &= -\alpha\iota m \,, \\ 0 &= -rm - um^3 - \dot{\phi} \,. \end{aligned} \tag{2.42}$$

And it follows directly that $m = \pm\sqrt{\frac{-r+\iota}{u}}$. However, this is incompatible with the microscopic model, where the domain value gets only a small correction due to the drive. The correction is tiny compared to ι for small driving amplitudes, compare to $\theta^{(2)}$ in Sec. 2.2. In order to compensate for that, we can add a shift in r, and thus

$$\begin{aligned} \alpha\dot{\phi} &= -\alpha\iota m + D_\phi \nabla^2 \phi + \dot{m} + \eta_\phi \,, \\ \alpha\dot{m} &= -(r+\iota)m - um^3 + D_m \nabla^2 m - \dot{\phi} + \eta_m \,, \end{aligned} \tag{2.43}$$

should be used for comparisons with the microscopic ferrimagnet. In later sections we perform several numerical comparisons with good agreement.

2.6.1 Connection to the Microscopic Model

To numerically compare the two models (effective theory and the microscopic version used in Mumax3), we need to convert the microscopic parameters to the effective

parameters. We will define those rules within this subsection. While the values of r and u could, in principle, be read off from the domain value, this is not so simple for the other parameters. Since we assume a small driving amplitude and thus only small corrections to the parameters, we can use the non-driven model to define the relations. We start from the LLG Eq. (2.26), by inserting the effective field, Eq. (2.25), and switching from the time $\tilde{t}$ to t_s, Eq. (2.30). Additionally, we go back to a discrete description and get

$$\dot{\hat{\boldsymbol{M}}}_i = \hat{\boldsymbol{M}}_i \times \left(J\boldsymbol{D}_\Delta(\hat{\boldsymbol{M}}_{i+1} + \hat{\boldsymbol{M}}_{i-1}) + \delta_2 \hat{M}_i^{\,z} + \delta_4 \left(\hat{M}_i^{\,z}\right)^3 \right) + \alpha \hat{\boldsymbol{M}}_i \times \dot{\hat{\boldsymbol{M}}}_i \,, \quad (2.44)$$

where we used the diagonal matrix $\boldsymbol{D}_\Delta = \mathrm{diag}\,(1, 1, -\Delta)$ to shorten the expression. The term $-2\hat{\boldsymbol{M}}_i$ vanishes due to the cross product with itself. Again, we use a Taylor expansion to get a continuous description, but this time we also use that every second spin is shifted by π in the xy-plane. However, this time we directly expand the magnetisation in z-direction, $m = \cos(\theta)$, instead of the angle $\theta(x)$. Since we are dealing with normalised magnetisation, we can again use the same parametrisation as before, with $\hat{\boldsymbol{M}}(m(x), \phi(x)) = \boldsymbol{S}^{\mathrm{param}}(\arccos(m(x)), \phi(x))$. Projecting the vector-valued Eq. (2.44) onto $\frac{\partial \hat{\boldsymbol{M}}}{\partial m(x)}$ and $\frac{\partial \hat{\boldsymbol{M}}}{\partial \phi(x)}$, we obtain two scalar equations

$$\begin{aligned} \alpha\dot{\phi} &= (1+m^2)\dot{m} + Ja^2\phi'' \,, \\ \alpha\dot{m} &= -(1-m^2)\dot{\phi} - (\delta_2 + 2J(1-\Delta))m - (\delta_4 - \delta_2 - 2J(1-\Delta))m^3 \\ &\quad + Ja^2\Delta m'' + Ja^2 m(\phi')^2 \,, \end{aligned} \quad (2.45)$$

where we additionally expanded in powers of m and derivatives of both fields and kept only terms up to third order in both together. Keeping only the leading order derivative terms and dropping $-\delta_2 - 2J(1-\Delta) = m_0^2\delta_4$ in front of m^3 as it is small compared to δ_4, gives us the final equations

$$\begin{aligned} \alpha\dot{\phi} &= Ja^2\phi'' + \dot{m} \,, \\ \alpha\dot{m} &= -(\delta_2 + 2J(1-\Delta))m - \delta_4 m^3 + Ja^2\Delta m'' - \dot{\phi} \,. \end{aligned} \quad (2.46)$$

By comparing this to the effective model without drive and thermal fluctuations, Eq. (2.40), we can read off the following conversion rules

$$r \to \delta_2 + 2J(1-\Delta), \quad u \to \delta_4, \quad D_m \to Ja^2\Delta, \quad D_\phi \to Ja^2 \,. \quad (2.47)$$

This also has the correct domain value with $m_0 = \pm\sqrt{\frac{-r}{u}}$.
However, it still remains open how these rules have to be adjusted in case of higher spatial dimensionality on a hypercube. In fact, the only term which is dependent on

the lattice dimension is the interaction term. For each higher dimension, we have to perform one more Taylor expansion in the new spatial direction. It turns out that the only change is in the control parameter with

$$r \to \delta_2 + 2Jd(1-\Delta)\,, \tag{2.48}$$

where d denotes the dimension.
In Sec. C.3 in the appendix, we compare the two models numerically via the example of a shrinking circle. The agreement turns out to be very good for small m and still qualitative for larger m. Similarly, we get qualitative agreement for the velocity of one domain wall in one dimension, comparing Fig. 3.2 and Fig. 3.5. There is one more limiting factor, which is that the effective model gives a good description only in the regime of small driving amplitude. Above a certain critical field, which depends on the parameters, localised (non-moving) domain walls with very different vortex dynamics show up. This will be briefly discussed in Sec. 3.7. Thus, as long as unpaired vortices do not exist, the effective model is able to describe the dynamics. This discussion referred exclusively to the non-driven case. Nevertheless, the assumption that we can neglect corrections in the limit of small driving amplitudes gives convincing results, i.e., Eq. (2.43) is a good qualitative description in the limiting cases described above.

2.6.2 Validating the Noise-Strength Scaling

In this subsection, we want to investigate the dependencies of the two thermal noise fields η_ϕ and η_m, or more specifically, their variances with respect to the damping constant and temperature. One way to do this is by comparing to the stochastic LLG equation with just thermal and damping contributions, where the damping contribution is kept as a reference point for the final equations. Writing the discrete equation in the time scale set by t_s gives

$$\dot{\hat{\boldsymbol{M}}}_i = \hat{\boldsymbol{M}}_i \times \left(-J\boldsymbol{B}_{\mathrm{therm},i} + \alpha\dot{\hat{\boldsymbol{M}}}_i\right)\,. \tag{2.49}$$

The variance of the thermal field, from Eq. (2.31), is given by

$$C_{\mathrm{therm}} = \frac{2\alpha T}{JM_0a^3}. \tag{2.50}$$

Where $|\gamma|$ in the denominator vanished and J appeared since we switched from $\tilde{t}$ to t_s. As before, we project the vector-valued equation onto $\frac{d\hat{\boldsymbol{M}}_i}{d\phi}$ and $\frac{d\hat{\boldsymbol{M}}_i}{d\theta}$ to arrive at

the following two scalar equations

$$\begin{aligned} 0 &= \sin(\theta)\left(-cJ\eta_x\sin(\phi) + cJ\eta_y\cos(\phi) + \alpha\sin(\theta)\dot{\phi} + \dot{\theta}\right), \\ 0 &= cJ\sin(\theta)\cos(\theta)\Big(\eta_y\sin(\phi) + \eta_x\cos(\phi)\Big) - cJ\eta_z\sin^2(\theta) \\ &\quad + \alpha\sin(\theta)\dot{\theta} - \sin^2(\theta)\dot{\phi}\,, \end{aligned} \tag{2.51}$$

where we used $c = \sqrt{C_{\text{therm}}}$ for readability and $B_{\text{therm},\mu} = \sqrt{c}\eta_\mu$, where $\mu = x, y, z$ is the index for the component and $\langle\eta_\mu\rangle = 0, \langle\eta_\mu\eta_\nu\rangle = \delta_{\mu\nu}$.
We can identify three independent random contributions in Eq. (2.51), given by

$$\begin{aligned} X_1 &= -Jc\sin(\theta)\left(\eta_x\sin(\phi) - \eta_y\cos(\phi)\right), \\ X_2 &= -Jc\sin(\theta)\cos(\theta)\Big(\eta_y\sin(\phi) + \eta_x\cos(\phi)\Big), \\ X_3 &= -Jc\eta_z\sin^2(\theta)\,. \end{aligned} \tag{2.52}$$

The relation $\langle X_i\rangle = 0$ is trivially fulfilled. For the variances, a small calculation is needed, which yields

$$\begin{aligned} \langle X_1^2\rangle &= J^2c^2\sin^2(\theta)\left(\langle\eta_x^2\rangle\sin^2(\phi) + \langle\eta_y^2\rangle\cos^2(\phi)\right) = J^2c^2\sin^2(\theta), \\ \langle X_2^2\rangle &= J^2c^2\sin^2(\theta)\cos^2(\theta)\Big(\langle\eta_y^2\rangle\sin^2(\phi) + \langle\eta_x^2\rangle\cos^2(\phi)\Big) = J^2c^2\sin^2(\theta)\cos^2(\theta), \\ \langle X_3^2\rangle &= J^2\langle\eta_z^2\rangle c^2\sin^4(\theta) = J^2c^2\sin^4(\theta), \end{aligned} \tag{2.53}$$

where we used that the noise fields are orthogonal to each other, $\langle\eta_\mu\eta_\nu\rangle = \delta_{\mu\nu}$.
From these expressions, we can now read off the variances of η_ϕ and η_m,

$$\begin{aligned} \langle\eta_\phi^2\rangle &= \langle X_1^2\rangle = J^2C_{\text{therm}}\sin^2(\theta) \sim J^2C_{\text{therm}}\,, \\ \langle\eta_m^2\rangle &= \langle X_2^2\rangle + \langle X_3^2\rangle = J^2C_{\text{therm}}\sin^2(\theta)(\sin^2(\theta) + \cos^2(\theta)) \sim J^2C_{\text{therm}}\,. \end{aligned} \tag{2.54}$$

In the last step, we used that in the spirit of the effective model, Sec. 2.6, higher orders in m are neglected, which means that $\sin(\theta) \sim 1$. Thus, the variance of both is approximately $\frac{2J\alpha T}{M_0a^3}$. Notice that even without the last approximation, the variances of the two noise strengths are *exactly* the same.

2.6.3 Implementation of the Effective Model

After discussing the effective model and understanding the connection to the parameters of the microscopic model, we can now explain its numerical implementation. Without thermal fluctuations, the equations are purely deterministic. However, including Gaussian white noise requires more careful consideration. Since Eq. (2.43)

and Eq. (2.41) differ only by the shift in r we use the latter for simplicity. The two equations are coupled and have time derivatives on each side. The usual framework of solving differential equations numerically consists of a discretisation in space and time. The subsequent time step is thereby calculated from the previous one, and thus, we seek an expression where only a single time derivative term exists in each equation. Thus, we first add and subtract the two coupled equations so that one consists solely of $\dot{\phi}$, and the other solely of $\dot{m}$. This gives us

$$\begin{aligned}(1+\alpha^2)\dot{\phi} =& -(r+\iota\alpha^2)m + \alpha D_\phi \nabla^2\phi - um^3 \\ &+ D_m\nabla^2 m + \alpha\eta_\phi + \eta_m\,, \\ (1+\alpha^2)\dot{m} =& (\iota - r)\alpha m - u\alpha m^3 - D_\phi\nabla^2\phi \\ &+ \alpha D_m\nabla^2 m + \alpha\eta_m - \eta_\phi\,,\end{aligned} \tag{2.55}$$

where $(1+\alpha^2)$ was kept on the LHS to avoid notation clutter, although we move it to the RHS in the implementation. The discretisation of the local terms is straightforward. For the spatial derivatives of m, we use the central finite difference, which takes the form

$$\partial_i^2 m_i \approx \frac{m_{i+a} + m_{i-a} - 2m_i}{a^2}\,, \tag{2.56}$$

in one spatial dimension. In higher dimensions, we obtain such a term for each dimension. For the phase ϕ, we use the lattice finite difference inspired by the XY model [40], given by

$$\partial_i^2 \phi_i \approx \frac{\sin(\phi_{i+a} - \phi_i) + \sin(\phi_{i-a} - \phi_i)}{a^2}\,, \tag{2.57}$$

which naturally takes jumps of 2π into account.
With this at hand, we can now write each equation in the general form given by

$$\dot{X}_{\epsilon,i} = f_{\epsilon,i}(\boldsymbol{X}) + \sum_{\beta,k} g_{\epsilon\beta,ik}(\boldsymbol{X})\eta_{\beta,k}\,, \tag{2.58}$$

where $\boldsymbol{X} = (X_{\phi,1}, ..., X_{\phi,n}, X_{m,1}, ..., X_{m,n})$ are the dynamical variables ϕ or m, labelled by ϵ, β, evaluated on each site, labelled by i, k. $f_{\epsilon,i}$ consists of the corresponding deterministic parts, and the last term includes the noise terms. We denote the noise properties by $\langle\eta_{\beta,k}\rangle = 0$ and $\langle\eta_{\beta,k}(t)\eta_{\epsilon,l}(t')\rangle = T_{\text{eff}}\delta_{kl}\delta_{\beta\epsilon}\delta(t-t')$, where T_{eff} was given at the end of the previous subsection.
As a solver, we use Heun's method [41, 42], which is also used by Mumax3 in case of simulations with thermal fluctuations. This is a predictor-corrector method con-

sisting of two main steps: The predictor step is an Euler integration given by

$$\tilde{X}_{\epsilon,i}(t+\Delta t) = X_{\epsilon,i}(t) + \Delta t f_{\epsilon,i}(\boldsymbol{X}(t)) + \sum_{\beta,k} g_{\epsilon\beta,ik}(\boldsymbol{X}(t))\Delta\eta_{\beta,k}\,, \tag{2.59}$$

where $\Delta\eta_{\epsilon,k} = \int_t^{t+\Delta t} \Delta\eta_{\epsilon,k}(s)\mathrm{d}s$ are still Gaussian random numbers, i.e, $\langle\Delta\eta_{\beta,k}\rangle = 0$ and $\langle\Delta\eta_{\beta,k}\Delta\eta_{\epsilon,l}\rangle = T_{\text{eff}}\Delta t\delta_{kl}\delta_{\beta\epsilon}$, and Δt is the discretisation interval in time. This is followed by the corrector step

$$\begin{aligned} X_{\epsilon,i}(t+\Delta t) = X_{\epsilon,i}(t) &+ \frac{\Delta t}{2}\left[f_{\epsilon,i}(\tilde{\boldsymbol{X}}(t+\Delta t)) + f_{\epsilon,i}(\boldsymbol{X}(t))\right] \\ &+ \frac{1}{2}\sum_{\beta,k}\left[g_{\epsilon\beta,ik}(\tilde{\boldsymbol{X}}(t+\Delta t)) + g_{\epsilon\beta,ik}(\boldsymbol{X}(t))\right]\Delta\eta_{\beta,k}\,, \end{aligned} \tag{2.60}$$

which represents the final value of $X_{\epsilon,i}$ at time $t+\Delta t$. Notice that the same noise realisation is used in both steps. Heun's method is of order $\mathcal{O}(\Delta t^2)$ for deterministic equations and of order $\mathcal{O}(\Delta t)$ for stochastic equations. We will use $\Delta t = 0.1$ in the absence of thermal fluctuations and $\Delta t = 0.05$ in the presence of thermal fluctuations. For the latter, we compromised a higher error to simulate larger system sizes for longer times.

In the context of this approach, we have chosen a particular stochastic calculus. There are two widely used types, Itô [43] and Stratonovich [44], which differ with respect to the stochastic integral used. In case of Itô, apparent in the Euler step Eq. (2.59), the prefactor is evaluated at time t while in the case of Stratonovich, shown in the corrector step Eq. (2.60), an averaged value is formed between the value at t and $t+\Delta t$. Both are suitable, depending on the problem. While Itô is generally used in financial contexts such as modelling stock prices, Stratonovich is more common in the physical sciences. This is because physical systems can have a finite but small correlation time. Thus, the noise autocorrelation is sharply peaked but with a finite width, where the delta function is only an approximation. With this approximation, the result of the integral converges to the Stratonovich interpretation for the correlation time going to zero, which makes it preferable for physical applications (implicitly used in, e.g., Kubo [45] and Brown [46]).

In principle, this would also apply to our equations. However, our equations consist of additive noise, and thus $g_{\epsilon\beta,ik}$ is independent of $\boldsymbol{X}$ and does not change in time. The exact values are given by $g_{\phi\phi,ik} = \alpha\delta_{ik}, g_{\phi m,ik} = \delta_{ik}, g_{mm,ik} = \alpha\delta_{ik}$ and $g_{m\phi,ik} = -\delta_{ik}$. Within this limit, the two stochastic integrals give the same result.

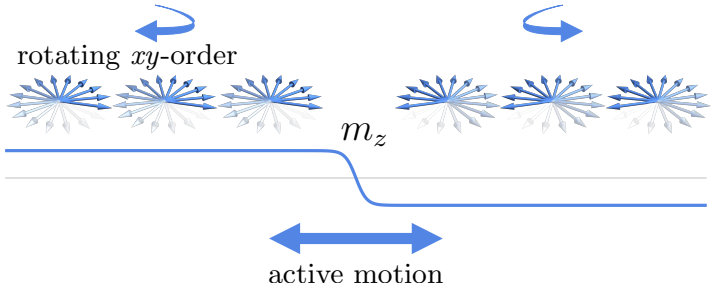

Figure 2.5: Illustration of a domain wall in the ferromagnetic component m. Dynamical frustration builds up due to the opposite sense of rotation of the xy-order ϕ on the left and right sides of the wall. One potential solution is the continuous movement of the domain wall.

2.7 Dynamical Frustration

In the previous sections, we set the stage for the driven ferrimagnet and the activation of the Goldstone mode, which leads to a rotation where the orientation is dependent on the magnetisation in the z-direction. This is a crucial point for the project, and we would like to stress one important concept in this section.
Consider an excitation on top of the constant ferrimagnetic state. The simplest stable solitonic excitation one can think of is a domain wall in the ferromagnetic component m. The rotational directions are opposite in the driven system, far away from the domain wall. This raises the question of what happens at the domain wall, where the two opposite rotational directions meet. There is an increasing tension throughout one period of rotation, and it is evident that it cannot continue to accumulate indefinitely. We call this *dynamical frustration*. This is the second important building block, in addition to the Goldstone mode activation. An immediate consequence is that a single stationary domain wall, as found in equilibrium, can no longer exist.
Fig. 2.5 shows a visualisation of this setup and illustrates the first of the two main mechanisms that we find which resolve the dynamical frustration. In an extensive range of parameters, we find that domain walls move with a constant velocity actively propelled by the driven rotation in the xy-plane, see Fig. 3.2.
The second mechanism occurs at larger driving amplitudes and results in a localised domain wall, which sends out pulses in m and creates, overall, one topological defect per side of the domain wall per rotation period of the Goldstone mode. In particular, the topological defects are space-time vortices in one dimension, see Sec. 3.7.
The two concepts together, Goldstone mode activation and dynamical frustration, give rise to novel types of collective behaviour that show remarkable similarities to active matter. For this reason, we want to draw the connection and briefly introduce

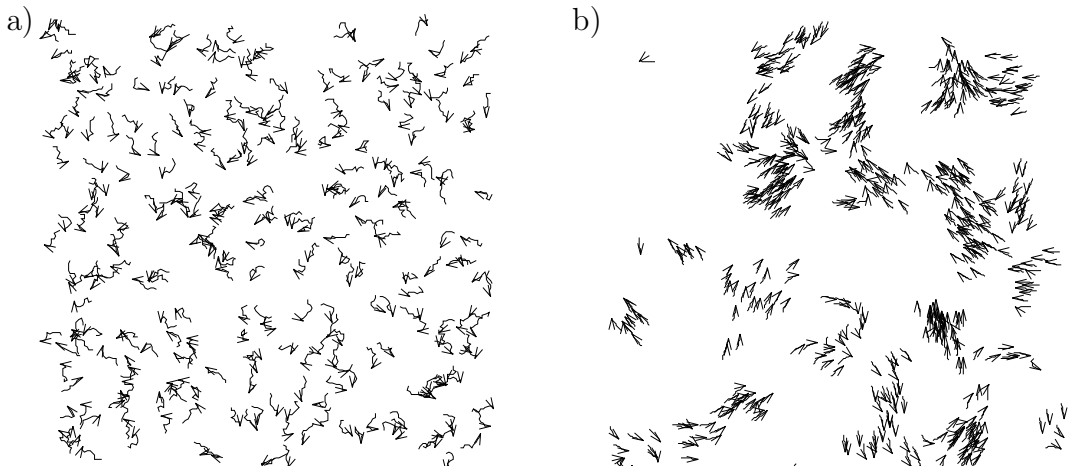

Figure 2.6: Snapshots from simulations of the Vicsek model for two different noise strengths. Panel a) shows the system at a higher noise level, where the system possesses a disordered state. Panel b) displays the system at a lower noise level, where patches with the same orientation form and an order is visible. Images taken from [50].

active matter in the next section.
As a last remark about dynamical frustration, we want to mention that it can already be identified in another published work. In [47], the influence of an electron microscope on a lattice of magnetic skyrmions is studied. Torques from the imaging processes break the lattice into domains with relative rotation. This, in turn, creates dynamical frustration, which induces collective behaviour of dislocations. Although it has not been explicitly referred to as dynamical frustration, it follows the same principles as in our case, where frustration accumulates at the interfaces of differing rotational directions.

2.8 Brief Excursus on Active Matter

Active matter [48] encompasses a broad range of systems, both living and non-living, where each microscopic constituent consumes energy to drive, e.g., motion or apply mechanical forces. Some prominent examples of active matter systems are schools of fish and flocks of birds [29, 49, 50], traffic [51], self-propelling bacteria [52], cytoskeleton components [53] and synthetic microswimmers [54] or other artificial self-propelled particles [55, 56]. Because detailed balance is broken, these systems are intrinsically out of thermal equilibrium and can display novel collective behaviours which cannot exist under equilibrium conditions. One of the best examples is the Vicsek model, which stands out as one of the field's first and most extensively studied models [50]. Vicsek et al. introduced the model to describe flocking birds via their orientation angle in two dimensions. They found sponta-

neous symmetry breaking of the rotational symmetry at small noise strength in two dimensions. Fig. 2.6 shows snapshots from simulations, which nicely show that for smaller noise levels, order builds up and the 'birds' move in flocks. Shortly after, it was confirmed by Toner and Tu [57] within a hydrodynamic formulation. While such behaviour is usually ruled out by the Mermin-Wagner theorem in equilibrium, this is not true for the active non-equilibrium system where the theorem can be broken. Another model concerned with flocking is the active Ising model [58, 59] which discussed actively moving particles with spin.

We want to bring this into a solid-state context by showing that our driven ferrimagnet can show active behaviour analogous to active matter. While we study a specific example, we believe that the general conclusions are primarily based on the broader concepts of Goldstone mode activation and dynamical frustration, which lead to domain walls that are propelled by the rotation of the xy-order. In terms of the spin interpretation, each spin rotates either to the left or to the right, which breaks detailed balance on a local level. Additionally, the domain walls move either to the left or to the right, and we will later find interactions over large distances which cannot be explained solely from local interactions.

However, these statements are only true for the continuously driven ferrimagnet. Once the oscillating field is turned off, after a short lag time, the rotation stops, and detailed balance is recovered. This contradicts common biological active matter systems, e.g., animals which have an energy storage and thus do not need a continuous energy intake. As a result, one might question whether 'active matter' is the appropriate terminology. To give an answer, we can make use of a recent metareview [48], 'review of reviews', which gives a great overview of the field. Besides many others, we also find the category of artificial active matter. One topic here is the light-driven propulsion of active particles [56], which follows mostly from the fact that the light creates an anisotropic distribution of, e.g., temperature or electric flow, which causes a movement of the particles. A particular example are $BiVO_4$ microparticles [60, 61]. In the absence of irradiation, the particles perform Brownian motion, whereas in the presence of irradiation, a gradient forms and propels the microparticles.

These arguments, together with the explanation of the driven ferrimagnet, lead us to conclude that the term *active magnetic matter* is appropriate for our model and findings.

3

Active Domain Walls in One Dimension

After setting the stage for the active ferrimagnet in the previous chapter, we can start to analyse the influence of the driving and understand in more detail how dynamical frustration leads to the active movement of domain walls in the ferrimagnet. We start in one dimension by studying a single domain wall. It turns out that, similar to the light-driven microswimmers, a gradient in the xy-order leads to the propulsion of the domain wall. We also state an approximate formula for the velocity of a domain wall. Afterwards, we extend the analysis to multiple domain walls and their interaction using instantaneous quenches to zero temperature. This reveals the build-up of a long-time hydrodynamic interaction between domain walls, which leads to a fast ordering, i.e., linear growth of correlations with time. The ordering is very fast compared to the non-driven system and the minimal model, Sec. 1.7.
Furthermore, we investigate the influence of thermal fluctuations and find that the driven system possesses very effective mechanisms to heal defects that could destroy the ordered phase. Thus, the driven system is more resilient to noise. Using space-time correlations of the stationary state, we estimate the enhancement in velocity due to thermal fluctuations and confirm the linear scaling of the correlations with time.
Finally, we turn to the regime of larger field amplitudes, where the domain wall becomes localised, and space-time vortices, in combination with pulses, are the process observed to lift dynamical frustration.
Many of the results presented in this chapter were published in a collaborative work with Reza Doostani, Sebastian Diehl, Nina del Ser and Achim Rosch [62].

3.1 The Moving Domain Wall - First Insight

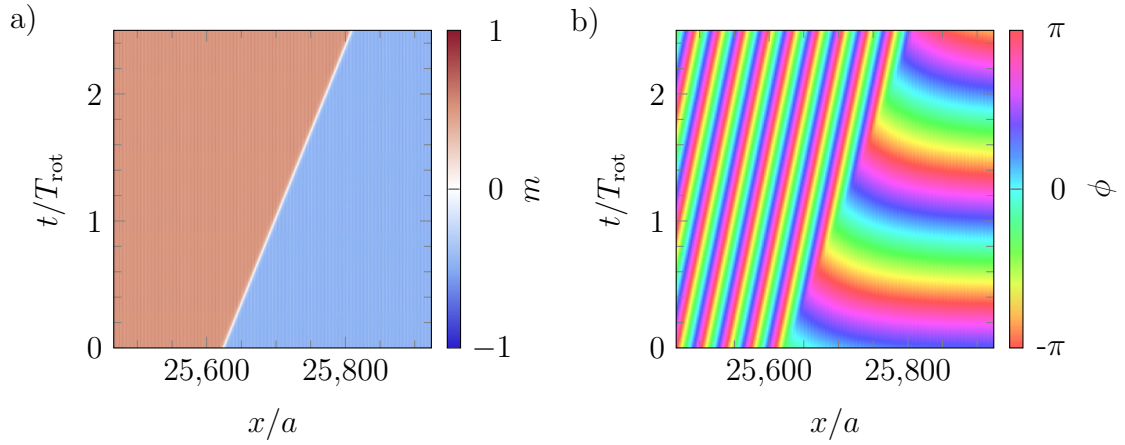

Figure 3.1: Mircoscopic simulation with 40,000 spins showing a zoom onto a right-moving up-down domain wall. Its velocity is approximately given by $v \approx 0.1226$ determined from the gradient of the $m = 0$ worldline. Panel a) displays the magnetisation in z-direction m and panel b) the staggered angle in the xy-plane ϕ. The domain wall exhibits a constant velocity and accumulates a gradient in ϕ behind it. Parameters are $J = 1, \Delta = 0.8, \delta_2 = -0.6, \delta_4 = 1, g_e = 1, g_o = 0.1, \alpha = 0.1, b_0 = 0.15, \omega = 3.6$ which results in $T_{\mathrm{rot}} = \frac{2\pi}{\omega_{\mathrm{rot}}} \approx 612$ for the rotational period

In this section, we aim to gain first insights into the moving domain wall as a mechanism to lift dynamical frustration at its centre where the two different senses of rotation meet. The results of a numerical simulation of a right-moving up-down domain wall are shown in Fig. 3.1 where we display the magnetisation in z-direction, for simplicity denoted by m, in panel a) and the staggered xy-order ϕ in panel b). The wall exhibits a constant velocity and carries a constant slope $\partial_x \phi = \phi'$ behind itself. We find that the direction of motion, either to the left or right, is dependent on small fluctuations in the angle ϕ in the initial state.

To get an initial understanding of the moving domain wall, let us consider the zero damping limit, $\alpha \to 0$, and simplified equations. In the limit of $\alpha = 0$ the magnetisation m is conserved, and we can formulate a continuity equation with

$$\dot{m} + j_s' = 0\,, \tag{3.1}$$

where the spin current is proportional to the gradient in ϕ, $j_s = \rho_s \phi'$ [63–65], and $\rho_s \approx Ja^2(1 - m^2)$ is the spin stiffness. Motivated by the numerical simulations, we use the following ansatz

$$\begin{aligned} m(x,t) &\to m(x - vt)\,, \\ \phi(x,t) &\to \phi(x - vt) + At\,, \end{aligned} \tag{3.2}$$

of a moving m and ϕ profile with constant velocity v. The constant A compensates for the difference between ω_{rot} and the moving slope ϕ', which creates a rotational contribution. Therefore, $A = \omega_{\mathrm{rot}}$ for a constant ϕ profile, i.e., vanishing slope. For a symmetric shape around the domain wall, with opposite slopes on the left and right sides, $A = 0$. Next, we shift to the moving frame of reference with $x \to x + vt$. Using the continuity equation and the knowledge about the rotating Goldstone mode $\dot{\phi} = \omega_{\mathrm{rot}}$, we get

$$\begin{aligned} vm' &= j_s' \,, \\ -v\phi' + A &= \omega_{\mathrm{rot}} \,. \end{aligned} \tag{3.3}$$

As both sides of the first equation consist of a spatial derivative, a natural way to proceed is by integrating in space, which yields

$$v\,[m]_L^R = [j_s]_L^R = \rho_s\,[\phi']_L^R \,. \tag{3.4}$$

We choose the integral limits in such a way that the integral goes from one constant domain to the other. Without loss of generality, we follow the example in Fig. 3.1, and define the left side as the up-domain with $m_L = m_0$ and $\omega_{\mathrm{rot}} = -|\omega_{\mathrm{rot}}|$ and the right side with opposite signs. It follows from the second line in Eq. (3.3) that $v\phi_L' = A + |\omega_{\mathrm{rot}}|$ and $v\phi_R' = A - |\omega_{\mathrm{rot}}|$. Inserting this into the integrated expression yields

$$-2vm_0 = \rho_s\,(\phi_R' - \phi_L') = -2\rho_s \frac{|\omega_{\mathrm{rot}}|}{v} \,. \tag{3.5}$$

We can conclude that the velocity of a domain wall is given by

$$v = \pm\sqrt{\frac{\rho_s|\omega_{\mathrm{rot}}|}{m_0}} \,, \tag{3.6}$$

in the limit of $\alpha \to 0$. Notice that the actual shape of the domain wall did not enter and the derivation is only based on the knowledge of the rotating Goldstone mode and the continuity equation for m. In the following sections, we will improve our understanding of the influence of the drive on the shape of the domain wall.

The result supports the numerical finding that the velocity for both up-down or down-up domain walls can be *positive* or *negative*. As the sign does not depend on the parameters, we conclude that it is determined by spontaneous symmetry breaking.

Another important point is that the velocity scales fast with the driving field. As the rotational frequency is proportional to the square of the field amplitude, $\omega_{\mathrm{rot}} \propto b_0^2$, the derived velocity scales with $v \propto b_0$. As a consequence, it is very large compared to intrinsic velocity scales, e.g., $\omega_{\mathrm{rot}}\xi_0$ for small b_0 where ξ_0 is the width of a domain wall

at equilibrium, see Sec. 2.5. In other projects based on Goldstone mode activated motion, e.g., the Archimedean screw [31] and the driven skyrmion [33], the velocity scaled comparably slower, with a quadratic dependence on the driving field(s).
Eq. (3.6) is valid in the limit of $\alpha \to 0$. In the case of finite damping, the calculation is more complicated and several approximations have to be made, see appendix in [62]. We will show the approach for the effective model in the next section, Sec. 3.2. Here, we briefly give the approximate result for the microscopic model,

$$v \approx \pm \left(\sqrt{\left(\frac{\alpha \rho_s}{\xi_0 \eta} \right)^2 + \frac{\rho_s |\omega_{\mathrm{rot}}|}{m_0}} - \frac{\alpha \rho_s}{\xi_0 \eta} \right) , \tag{3.7}$$

where η is a dimensionless factor given by

$$\eta = 2(1 - m_0^2) + \sqrt{1 - m_0^2} \left(1 + \frac{m_0^2 (1 - \Delta)}{2\Delta} \right) . \tag{3.8}$$

η interpolates smoothly between $\eta = 0$ for $m_0 \to 1$ and $\eta = 3$ for $m_0 \to 0$. A first simple check that we can do is taking two limits of the velocity formula Eq. (3.7). Each consists of the assumption that one of the two terms under the square root dominates the other. This gives us the following two expressions

$$v \approx \pm \begin{cases} \sqrt{\dfrac{\rho_s |\omega_{\mathrm{rot}}|}{m_0}} & \text{for } \dfrac{|\omega_{\mathrm{rot}}|}{m_0} \gg \alpha^2 \dfrac{\rho_s}{\xi_0^2} , \\ \dfrac{\xi_0 \eta |\omega_{\mathrm{rot}}|}{2\alpha m_0} & \text{for } \dfrac{|\omega_{\mathrm{rot}}|}{m_0} \ll \alpha^2 \dfrac{\rho_s}{\xi_0^2} . \end{cases} \tag{3.9}$$

For $\frac{|\omega_{\mathrm{rot}}|}{m_0} \gg \alpha^2 \frac{\rho_s}{\xi_0^2}$ the dependence on damping drops out and we recover the velocity derived at the beginning of this section, Eq. (3.6), with a linear dependence on b_0. In the opposite limit, we get a quadratic dependence on the driving field and an inverse dependence on damping. For typical values of $\alpha \ll 1$ and $m_0 < 1$, the domain wall moves still a large distance of $\frac{\pi \eta \xi_0}{\alpha m_0^z} \gg \xi_0$ during each rotation. A similar expression to the velocity in this limit has been derived for rare-earth transition-metal ferrimagnets, which are driven by a field rotating in the xy-plane [66]. An important difference to our setup is that the direction of motion is given externally and is not chosen spontaneously.
Fig. 3.2 shows the comparison of numerical simulations performed with Mumax3 to the approximate velocity formula given by Eq. (3.7). Due to numerical limitations, we were not able to reach stationary, moving solutions for values below $\frac{b_0}{J} = 0.1$.
The simulations were performed by initialising the system with one up-down domain wall in the magnetisation profile, see Fig. 3.1a), with position x_0 roughly at a quarter of the system of $N = 40,000$ spins. We used open boundary conditions and an initial

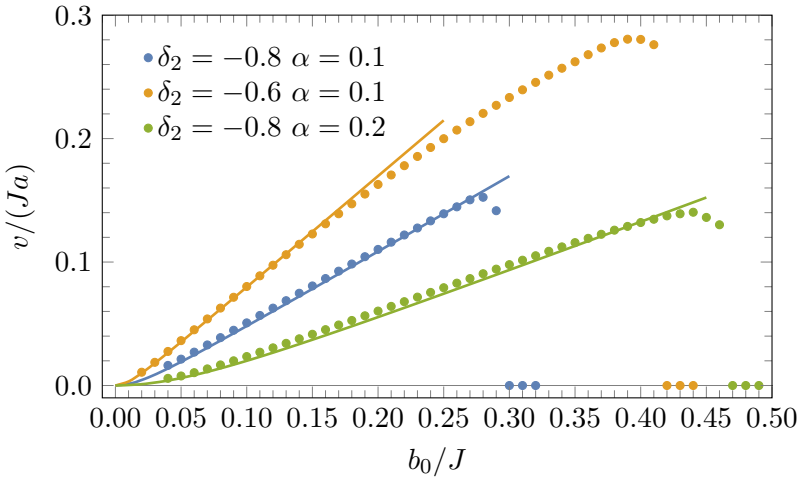

Figure 3.2: Points show the velocity of one domain wall conducted from simulations as shown in Fig. 3.1 as a function of the amplitude of the driving field b_0, shown for different values of anisotropy δ_2 and damping α. The initialisation is discussed in the text. Beyond very small field values, we observe linear behaviour of v with b_0 over a long interval in agreement with $\sqrt{|\omega_{\text{rot}}|}$ and Eq. (3.6). The lines are generated from Eq. (3.7) using the parameters: $J = 1, \Delta = 0.8, \delta_2 = -0.6$ and -0.8, $\delta_4 = 1, g_1 = 1, g_2 = 0.1, \alpha = 0.1$ and $0.2, \omega = 3.6$ for a system of 40,000 sites with open boundary conditions. Errors turn out to be smaller than the point size and are, therefore, omitted.

angle profile with $\phi'(x < x_0) = \phi'_L = \frac{2|\omega_{\text{rot}}|}{v}$ and $\phi'(x > x_0) = \phi'_R = 0$ similar to Fig. 3.1b) and inspired by Eq. (3.5). The analytical curves of v are determined by Eq. (3.7), where we choose the positive solution. Thus, we initialised right-moving up-down domain walls with roughly the correct velocity. We then simulated long enough to reach stationary motion and measured the value of the velocity by tracking the zero crossing, $m = 0$, over time.

There are two motivations for this method. One is that due to the finite system, it is beneficial to have a domain wall moving in the direction of the farther boundary. Another one is that the build-up of the needed slope in the angle takes longer simulation time the smaller b_0 is and with this, the smaller the rotational frequency is. Therefore, one should read the figure as showing the maximum range in b_0 up to which a moving domain wall can exist for the given parameters.

The last sentence already gives a slight hint that the moving solution does not exist for arbitrarily high field amplitudes. All of the three different parameter sets displayed in Fig. 3.2 show a drop at sufficiently high but different driving strengths. This might not come as a surprise since in many driven domain wall systems, such a breakdown of the steady domain wall motion exists, e.g., the Walker breakdown [67]. However, we are investigating a system with dynamical frustration which asks for a new process to lift the frustration. Numerically, we identify it and call it the localised domain wall. It sends out pulses in m and creates space-time vortices in

ϕ to dissipate the frustration. We analyse this further in Sec. 3.7. The last three points of each data curve in Fig. 3.2 show this solution.
Below a critical field value, the agreement with the approximate velocity formula Eq. (3.7) is very good. In particular, we highlight the fact that no fitting parameter is needed, and we can calculate the velocity directly from input parameters. For larger damping, the deviation increases slightly. This might be caused by renormalisation effects that have not been taken into account.

3.2 Domain Wall Velocity Derivation

This section is devoted to deriving the approximate velocity formula in the framework of the effective model. Since we want an expression comparable to the microscopic model, we use the expression with the additional shift in the control parameter, Eq. (2.43). The one-dimensional form without thermal fluctuations is given by

$$\begin{aligned} \alpha\dot{\phi} &= -\alpha\iota m + D_\phi \phi'' + \dot{m}\,, \\ \alpha\dot{m} &= -(r+\iota)m - u m^3 + D_m m'' - \dot{\phi}\,. \end{aligned} \tag{3.10}$$

This approach follows the strategy developed by Nina del Ser, presented in the appendix of [62]. It consists of solving the equations step by step by slowly increasing the degree of complexity. The focus here is on the moving solution, i.e., we use a moving ansatz and the moving frame of reference once the driving is turned on. However, we first start with the non-driven stationary solution. We linearise the fields around it and re-derive the non-damped solution in the driven case. Afterwards, we adjust the ansatz to include damping and evaluate the equations far away from the domain wall, which serves as a well-understood limiting case. This allows us to estimate corrections to the non-damped solution. One important finding is that these corrections arise close to the domain wall in the direction of movement. Finally, we can tackle the area around the centre of the domain wall, which leads to an approximate expression for the velocity at finite α. Hereby, we make several assumptions which mainly rely on small velocities and small driving strengths.

3.2.1 Stationary Domain Wall Solution

For the stationary state without driving, i.e., $\iota = 0$, all time derivatives drop out, and the equations have the following form

$$0 = D_\phi \phi''_{\text{stat}}, \quad 0 = -r m_{\text{stat}} - u m^3_{\text{stat}} + D_m m''_{\text{stat}}\,. \tag{3.11}$$

The two equations decouple in this limit, and the ϕ-equation becomes trivial. The general solution allows for a constant slope in ϕ_{stat}. For simplicity, we choose the slope to be zero, with $\phi'_{\text{stat}} = 0$.
The m-equation is simple as well, it has the form of the standard domain wall equation with the solution

$$m_{\text{stat}} = m_0 \tanh\left(\frac{x - x_{\text{DW}}}{\xi_0}\right), \tag{3.12}$$

where $m_0 = \pm\sqrt{\frac{-r}{u}}$, as before, is the magnetisation in the domain far away from the domain wall and $\xi_0 = \sqrt{\frac{-2D_m}{r}}$ is its width. Notice that the width is the same as the one in Sec. 2.5 using the translation rules from Sec. 2.6.1. For notational convenience and without affecting any of the results, we assume the domain wall to be at $x_{\text{DW}} = 0$. This is the stationary, non-driven solution around which we want to expand in the next subsections. Within this picture, the general ansatz motivated by the numerical simulations can expressed as

$$\begin{aligned} m(x,t) &\to m_{\text{stat}}(x - vt) + \delta m(x - vt)\,, \\ \phi(x,t) &\to \delta\phi(x - vt) + At\,, \end{aligned} \tag{3.13}$$

where A is the compensation between the moving slope and the full rotational speed ιm_{stat} deep in the domain far away from the domain wall, as before at the beginning of Sec. 3.1. δm and $\delta\phi$ are not yet identified corrections which we keep general for now. We will determine the different corrections, which are dependent on the limits discussed in the following subsections.
The corresponding linearised equations, from Eq. (3.10), in the moving frame of reference $x \to x + vt$ can be written in the following form

$$\begin{aligned} \alpha\left[A + \iota(m_{\text{stat}} + \delta m) - v\delta\phi'\right] &= D_\phi\delta\phi'' - v\left(m'_{\text{stat}} + \delta m'\right)\,, \\ \alpha v\left(m'_{\text{stat}} + \delta m'\right) + v\delta\phi' + D_m\delta m'' &= \delta m\left(\iota + \left(3m_{\text{stat}}^2 - m_0^2\right)u\right) \\ &\quad + A + \iota m_{\text{stat}}\,, \end{aligned} \tag{3.14}$$

where we used Eq. (3.11) to eliminate several terms with m_{stat}. We will use this equation in the following with different expressions for δm and $\delta\phi$ to solve it in each limiting case.

3.2.2 Driven Solution in the Absence of Damping

Here, we want to re-derive the result in the absence of damping, including a short look at the influence of the corrections. Setting $\alpha = 0$ simplifies the first equation

of Eq. (3.14) to

$$0 = D_\phi \delta\phi''_{\alpha=0} - v\,(m'_{\text{stat}} + \delta m'_{\alpha=0})\ . \tag{3.15}$$

Similarly, we can look at the second equation of Eq. (3.14) and evaluate it deep in the domain, far away from the domain wall. $\delta m_{\alpha=0}$ and its derivatives vanish in this limit, leaving us with

$$0 = -\iota m_{\text{stat}} + v\delta\phi'_{\alpha=0} - A\,. \tag{3.16}$$

Integrating Eq. (3.15) and comparing it to the expression above far away from the domain wall to fix the integration constant. To do so, we compare the m_{stat}-dependent and m_{stat}-independent terms, which yields

$$0 = D_\phi \delta\phi'_{\alpha=0} - \frac{D_\phi A}{v} - v\,(m_{\text{stat}} + \delta m_{\alpha=0})\ . \tag{3.17}$$

Additionally, we can balance the m_{stat} dependent terms of the two equations, which gives us the expression for the velocity

$$v^2 = D_\phi \iota\,, \tag{3.18}$$

as before, compare to Eq. (3.6) with $\iota = \frac{|\omega_{\text{rot}}|}{m_0}$ and $D_\phi \approx \rho_s$ for small m.
For later purposes, it is useful to state the m-equation, given by

$$\frac{v^2}{D_\phi}(m_{\text{stat}} + \delta m_{\alpha=0}) + D_m \delta m''_{\alpha=0} = m_{\text{stat}}\iota + \delta m_{\alpha=0}(\iota + u(3m_{\text{stat}}^2 - m_0^2))\,, \tag{3.19}$$

where we used Eq. (3.17) to replace the $\sim \delta\phi'$-term in Eq. (3.14) and arrive at an equation solely for $\delta m_{\alpha=0}$. This equation will help us in later calculations, see the paragraph above Eq. (3.28).

3.2.3 Driven Solution with Finite Damping Deep in the Domain

Now, we are ready to evaluate the second equation of Eq. (3.14) deep in the domain where the stationary magnetisation is constant, $m_{\text{stat}} = m_0$, which should hold for $|x| \gtrsim \xi_0$. This serves as a last step before we can finally tackle the expression for the velocity. In this limit, Eq. (3.14) reduces to

$$\begin{aligned} 0 &= -\alpha A - \alpha\iota(m_0 + \delta m) - v\delta m' + v\alpha\delta\phi' + D_\phi\delta\phi''\,, \\ 0 &= -A - \iota(m_0 + \delta m) - 2m_0^2 u\delta m + v(\alpha\delta m' + \delta\phi') + D_m\delta m''\,. \end{aligned} \tag{3.20}$$

From the previous subsection, we know that the slope of the angle is given by Eq. (3.16) deep in the domain in the absence of damping. Comparing to the first

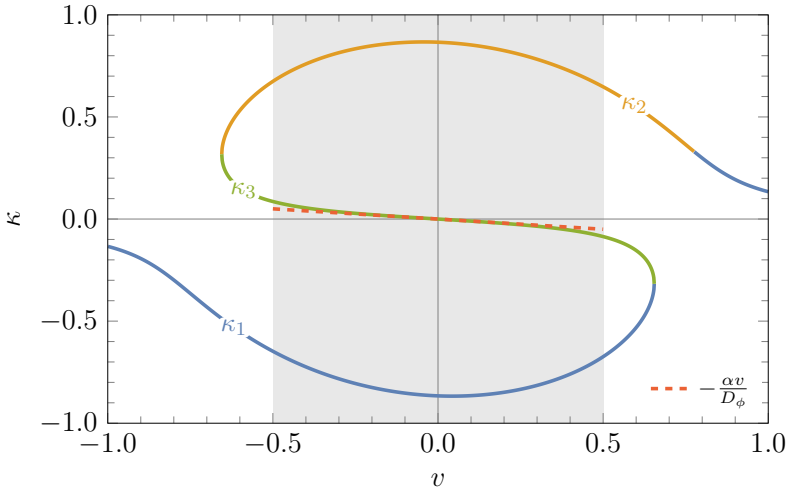

Figure 3.3: Non-trivial solutions of Eq. (3.22) shown with $\iota = 0$ for illustrational purposes. Only κ_3 gives meaningful values for small velocities. The gray area serves as a guide to the eye where the linear approximation, shown as a dashed line on top, is reasonable. Parameters: $D_m = 0.8, D_\phi = 1, \alpha = 0.1, r = -0.3, \iota = 0$.

equation of Eq. (3.20) in the same limit, where $\delta m, \delta m', \delta\phi'' = 0$, it turns out that the constant is exactly given by the same expression. This motivates us to use the following ansatz with exponentials to solve the equations

$$\begin{aligned} \delta\phi' &= \frac{A + \iota m_0}{v} + \phi_{\text{exp}} e^{\kappa x} \,, \\ \delta m &= m_{\text{exp}} e^{\kappa x} \,. \end{aligned} \tag{3.21}$$

The constant correction also balances the constant terms in the second equation, i.e., all constant terms drop out, and only terms proportional to the exponentials remain. Thus, we can write down two coupled equations for ϕ_{exp} and m_{exp},

$$\begin{aligned} 0 &= (\alpha\iota + v\kappa) m_{\text{exp}} - (v\alpha + D_\phi \kappa)\phi_{\text{exp}} \,, \\ 0 &= (2m_0^2 u + \iota - \kappa(v\alpha + D_m\kappa)) m_{\text{exp}} - v\phi_{\text{exp}} \,, \end{aligned} \tag{3.22}$$

where κ is a constant, which we need to choose in such a way that the expression vanishes far away from the domain wall.
For now, we neglect the $\sim \alpha\iota$-term in the first equation, motivated by the fact that small velocities correspond to small driving strength and that we usually operate at small α. Next, we can cast Eq. (3.22) into a matrix equation and know that for non-trivial solutions, the determinant of that matrix has to be zero. This can be used to determine an expression for κ. As it is a cubic equation in κ, we get three solutions, shown in Fig. 3.3 for $\iota = 0$. The graph does not change qualitatively for small values of ι and just serves as illustration. Two of the roots are $|\kappa_1|, |\kappa_2|$

are of the order of the inverse domain wall width, and thus decay too fast and are irrelevant for $|x| \gtrsim \xi_0$. Only $\kappa_3 \ll \frac{1}{\xi_0}$ so that

$$\kappa = \kappa_3 = -\frac{\alpha v}{D_\phi} + \mathcal{O}(v^3)\,, \tag{3.23}$$

is the correct choice to fulfil the requirements. It has an approximately linear dependence on the velocity. The grey area in Fig. 3.3 serves as a guide to the eye where this assumption is reasonable.
This means that the exponent is linear in velocity and dependent on the sign of it, in particular $\mathrm{sign}(\kappa) = -\mathrm{sign}(v)$. As we need an exponential decay in space for $\delta\phi'$ and δm in order to fulfil the requirements far away from the domain wall, the exponential decay turns out to be only on the side of the domain wall in which it moves, for $|x| \gtrsim \xi_0$. This condition is imposed on m_{exp} and ϕ_{exp} and becomes relevant in the next subsection.
But we can get even more out of Eq. (3.22) by using Eq. (3.23). Taking the second equation and keeping only the leading order terms in velocity leads to

$$v\phi_{\mathrm{exp}} = \left(2m_0^2 u + \iota + \mathcal{O}(v^2)\right) m_{\mathrm{exp}}\,, \tag{3.24}$$

which means that $m_{\mathrm{exp}} \propto v\phi_{\mathrm{exp}}$ in the limit of small velocities.

3.2.4 Driven Solution with Finite Damping Velocity

Our journey of increasing complexity is reaching its end. To describe the region close to the domain wall $|x| \lesssim \xi_0$, we modify our ansatz to

$$\begin{aligned} \delta\phi' &= \frac{A + m_{\mathrm{stat}}\iota}{v} + \frac{v}{D_\phi}\delta m_{\alpha=0} + \phi_{\mathrm{exp}}(x)e^{\kappa x}\,, \\ \delta m &= \delta m_{\alpha=0} + m_{\mathrm{exp}}(x)e^{\kappa x}\,, \end{aligned} \tag{3.25}$$

where $m_{\mathrm{exp}}(x)$ and $\phi_{\mathrm{exp}}(x)$ are now space-dependent functions given by the following expressions far away from the domain wall

$$m_{\mathrm{exp}}(|x| \gtrsim \xi_0) = \begin{cases} m_{\mathrm{exp}}, & \kappa x < 0 \\ 0, & \kappa x > 0 \end{cases}, \quad \phi_{\mathrm{exp}}(|x| \gtrsim \xi_0) = \begin{cases} \phi_{\mathrm{exp}}, & \kappa x < 0 \\ 0, & \kappa x > 0 \end{cases}. \tag{3.26}$$

Within this definition, the exponential decay is on the correct side of the domain. The ansatz also fulfils the other requirements, as for $\alpha = 0$ it recovers Eq. (3.17), furthermore, $\delta m_{\alpha=0}$ vanishes and $m_{\mathrm{stat}} = m_0$ for $|x| \gtrsim \xi_0$ which gives the same as Eq. (3.21).

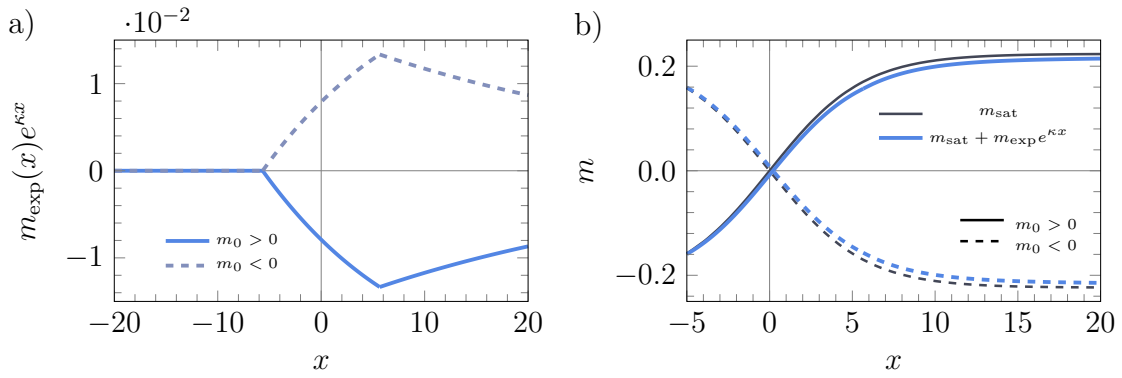

Figure 3.4: Illustration of the impact of the exponential corrections on the domain wall. Panel a) shows the exponential correction to m where the prefactor in the range close to the domain wall is approximated via a straight line, see Eq. (3.27). We show it for a right-moving down-up and an up-down domain wall. Notice the small values of the order of 10^{-2} for a velocity of $v = 0.3$. Panel b) shows the influence of the exponential correction on m_{sat}. Again, we show the two possible right-moving domain walls. The main influence happens in the direction of movement, roughly around the boundary between close and far-field at $x \sim \xi_0$. Parameters: $D_m = 0.8, D_\phi = 1, \alpha = 0.1, r = -0.05, u = 1, v = 0.3$.

An open question is what form $m_{\mathrm{exp}}(x)$ and $\phi_{\mathrm{exp}}(x)$ take in the intermediate regime $|x| \lesssim \xi_0$. We make the simple approximation of straight lines with

$$\phi_{\mathrm{exp}}(x) = \frac{\phi_{\mathrm{exp}}}{2}\left(1 + \mathrm{sign}(v)\frac{x}{\xi_0}\right), \quad m_{\mathrm{exp}}(x) = \frac{m_{\mathrm{exp}}}{2}\left(1 + \mathrm{sign}(v)\frac{x}{\xi_0}\right). \tag{3.27}$$

This is solely motivated by its simplicity. Fig. 3.4 shows the space-dependent exponential part of the correction in m around a right-moving domain wall in panel a), and its influence on m_{stat} in panel b). Both show an up-down and a down-up domain wall scenario. It is clearly visible that the contribution vanishes far away from the domain wall. Although the correction in m is of the order of 10^{-2} for a larger velocity of $v = 0.3$, it is a key ingredient in this velocity derivation.
To proceed, we first insert the modified ansatz into the second line of Eq. (3.14) and use Eq. (3.19), which eliminates terms without proportionality constant α and $\delta m_{\alpha=0}$ dependence. Additionally, we evaluate the resulting equation at the domain wall, $x = 0$, where $m_{\mathrm{stat}} = 0$. This leaves us with

$$\begin{aligned} 0 = \Bigg[& m_{\mathrm{exp}}\left(m_0^2 u - \iota + D_m\kappa^2 + \frac{2D_m \mathrm{sign}(v)\kappa}{\xi}\right) + v\phi_{\mathrm{exp}} \\ & + \alpha\left(m_{\mathrm{exp}}\left(v\kappa + \frac{\mathrm{sign}(v)v}{\xi}\right) + 2v(m'_{\mathrm{stat}} + \delta m'_{\alpha=0})\right)\Bigg]_{x=0}. \end{aligned} \tag{3.28}$$

We use Eq. (3.24) to replace all m_{exp}, which allows us to estimate which terms can be neglected. Furthermore, one, yet unknown, term is $\delta m'_{\alpha=0}$. To determine an approximate expression, we use, again, Eq. (3.19) and take its derivative to solve for

$$\delta m'_{\alpha=0}(x=0) = \frac{(v^2 - D_\phi \iota)}{D_\phi r - v^2 + D_\phi \iota} m'_{\text{stat}}(x=0)\,, \tag{3.29}$$

where we neglected $\delta m'''_{\alpha=0}$ as it is of higher order in derivatives and evaluated the whole equation at $x = 0$. Notice that the numerator cancels out exactly in the $\alpha = 0$ case, compare to Eq. (3.18). Therefore, we assume the correction in the finite but small damping case to be small and neglect $\delta m'_{\alpha=0}$ in Eq. (3.28).
Using Eq. (3.23) to replace κ in Eq. (3.28), while keeping only the terms of leading order in velocity, gives

$$0 = \left(\frac{3m_0^2 u}{2m_0^2 u + \iota} v + \mathcal{O}(v^2) \right) \phi_{\text{exp}} + 2\alpha v \frac{m_0}{\xi_0}\,. \tag{3.30}$$

For the last term, m'_{stat} was evaluated at $x = 0$.
Here, we see that in the limit of small velocities, ϕ_{exp} is independent of v. Solving for it assuming small driving strength yields

$$\phi_{\text{exp}} = -\frac{4m_0\alpha}{3\xi_0} + \mathcal{O}(\alpha\iota, v^2)\,. \tag{3.31}$$

Now, we have an expression for κ and ϕ_{exp}, and due to the relation Eq. (3.24) also for m_{exp} in the limit of small driving strength and velocity. Thus, the only unknown quantity left is the velocity itself, for which we can solve now. Luckily, we have not used the ϕ-equation close to the domain wall yet. Substituting in the full ansatz above into the first line of Eq. (3.20) and integrating over the domain wall from $-\xi_0$ to ξ_0 yields

$$\begin{aligned}
&-2m_0 v + \frac{2D_\phi m_0 \iota}{v} \\
&= m_{\text{exp}} \Bigg(\left(v + \frac{\alpha\iota}{\kappa} \right) \text{sign}(v) \cosh(\kappa\xi_0) \\
&\qquad + \left(v + \frac{\alpha\iota}{\kappa} - \frac{\text{sign}(v)\alpha\iota}{\kappa^2 \xi_0} \right) \sinh(\kappa\xi_0) \Bigg) \\
&+ \phi_{\text{exp}} \Bigg(- \left(D_\phi + \frac{v\alpha}{\kappa} \right) \text{sign}(v) \cosh(\kappa\xi_0) \\
&\qquad - \left(D_\phi + \frac{v\alpha}{\kappa} - \frac{\text{sign}(v) v\alpha}{\kappa} \right) \sinh(\kappa\xi_0) \Bigg).
\end{aligned} \tag{3.32}$$

This equation consists of infinitely many orders in $\kappa \propto v$ due to the trigonometric functions. Therefore, following our previous approximations, we can expand $\cosh(\kappa\xi_0) \approx 1 + \mathcal{O}(v^2)$ and $\sinh(\kappa\xi_0) \approx \kappa\xi_0 + \mathcal{O}(v^3)$ to leading order in κ to get a

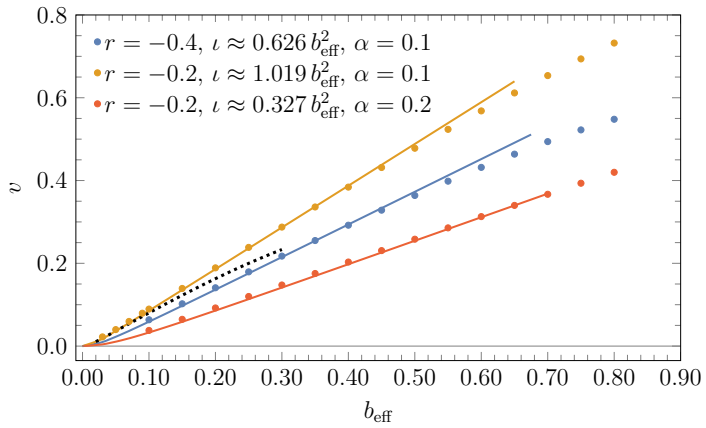

Figure 3.5: The points show the velocity of a single domain wall conducted from simulations with 20,000 sites with the effective model, Eq. (2.43). For a comparable plot, we identify an effective driving-field amplitude from $\iota \propto b_{\text{eff}}^2$ where the prefactor is determined from the microscopic model using the conversion rules, Eq. (2.47), and shown in the legend. The initial state is a domain wall with approximately correct height in m and slightly varying ϕ. Thus, we do not impose an initial direction and velocity in contrast to the microscopic simulations. The solid lines display the theoretical prediction from Eq. (3.35), which agrees well with the data points over a large range of effective field amplitudes and throughout the three parameter sets. The first two sets shown correspond to the first two in Fig. 3.2. For the second set, we show the data from the microscopic model as a dashed black line. The curves coincide for small field amplitudes but differ for larger values, $b_{\text{eff}} \gtrsim 0.2$. The microscopic model possesses zero velocity from $b_{\text{eff}} \geq 0.42$ due to the localised domain wall, which uses space-time vortices to lift the dynamical frustration. This mechanism does not exist in the effective model, which explains why the curves stretch out over a larger range. Parameters: $u = 1, D_m = 0.8, D_\phi = 1, \alpha = 0.1$, others in the legend.

simplified expression, given by

$$\begin{aligned} &-2m_0 v + \frac{2D_\phi m_0 \iota}{v} \\ &= m_{\text{exp}}(\text{sign}(v)v + \alpha\iota\xi_0 + v\kappa\xi_0) - \phi_{\text{exp}}((v\alpha + D_\phi\kappa)\xi_0 + D_\phi \text{sign}(v)). \end{aligned} \tag{3.33}$$

The first part of the second term on the RHS cancels directly due to $\kappa D_\phi \approx -v\alpha + \mathcal{O}(v^3)$ in the limit of small velocities. Additionally, we follow the strategy from before and use Eq. (3.24) to replace m_{exp} by ϕ_{exp} and keep only the leading order terms. This leads to

$$-2m_0 v + \frac{2D_\phi m_0 \iota}{v} = \phi_{\text{exp}} \left(D_\phi \text{sign}(v) + \mathcal{O}(v^2, \alpha\iota v)\right). \tag{3.34}$$

Next, we insert our expression for ϕ_{exp} from Eq. (3.31) and finally solve for the velocity. Due to the sign(v), we get four velocities out of this equation. Only two of them are physical, i.e., they are zero for zero driving strength. The expressions

of the two are

$$v = \pm \left(\sqrt{\left(\frac{D_\phi \alpha}{3\xi_0} \right)^2 + D_\phi \iota} - \frac{D_\phi \alpha}{3\xi_0} \right) . \tag{3.35}$$

This formula fits very well with our numerical simulations at small driving strength and damping of the effective model. Fig. 3.5 shows the result of three parameter sets, with the velocity predicted by Eq. 3.35 displayed as solid lines on top. Furthermore, we have an expression which supports the finding that the domain walls can move to the left or to the right for the same parameters, and the direction is chosen from small fluctuations in the initial conditions.
Additionally, this expression is equal to the one from the microscopic theory, see Eq. (3.7), with $\iota = \frac{|\omega_{\mathrm{rot}}|}{m_0}$ for small values of m where $D_\phi \approx \rho_s$ and $\eta \approx 3$.
Therefore, it is consistent that it shows qualitatively the same behaviour as the microscopic model, compare to Fig. 3.1. However, in contrast to the microscopic model, the velocity does not drop to zero for large field amplitudes for the shown parameters. This comes because the vortices from localised domain walls are not captured in the same way. Essentially, m is not bound to stay smaller than or equal to one. The localised domain wall in the microscopic model is discussed in Sec. 3.7.

3.3 Domain Wall Velocity - Green's Function

For this approach, we start with the ansatz used at the beginning of the section about the first insights on the moving domain wall, Sec. 3.1. Inserting this into the equations of motion, Eq. (3.10), and shifting to the moving frame of reference, with $x \to x + vt$, gives

$$\begin{aligned} D_\phi \phi'' + \alpha v \phi' = \alpha A + \alpha \iota m + v m' = S(x) \,, \\ A - v\phi' = -rm - um^3 + D_m m'' + \alpha v m' \,, \end{aligned} \tag{3.36}$$

where we identify the RHS of the first line as a source function $S(x)$ for ϕ'. This allows solving the equation using the Green's function formalism. The Green's function is the solution of the differential equation where the delta function replaces the source function. The full solution can then be calculated via the convolution

$$\phi'(x) = \int \mathrm{d}x' G(x - x') S(x'), \text{ with } G(x) = \mathrm{sign}(v) \mathcal{H}(\mathrm{sign}(v) x) \frac{\mathrm{e}^{-\frac{v\alpha}{D_\phi} x}}{D_\phi} . \tag{3.37}$$

Here, $\mathcal{H}$ is the Heavyside step function. Notice that within this approach, the exponential correction, $e^{\kappa x}$, used in the previous section with $\kappa = -\frac{v\alpha}{D_\phi}$ shows up naturally in the derivative of the phase. In fact, this served as an inspiration for the

ansatz in the previous section.
To solve this integral with m and m' in the source function, approximations are needed, since the exact form is unknown. But first, we take care of the constant part with A in it, which yields

$$\phi'|_{m,m'\to 0} = \frac{A}{v}\,. \tag{3.38}$$

Thus, the temporal shift A drops out in both equations, and we can work with $A = 0$ from now on. It follows that the velocity does not depend on A.
We can shortly recall what it means to have $A = 0$. In this case, the moving slope of ϕ is exactly the rotational speed ($\pm\omega_{\mathrm{rot}}$) on both sides of the domain wall, i.e., equal and opposite.
To make it easier to perform approximations, we first use partial integration to transform the m'-term under the integral to an m-term and get

$$\phi'(x) = \frac{v}{D_\phi} m(x) - \operatorname{sign}(v)\alpha \int \mathrm{d}x' \mathcal{H}\left[\operatorname{sign}(v)(x-x')\right] \frac{\mathrm{e}^{-\frac{v\alpha}{D_\phi}(x-x')}}{D_\phi} \left(\frac{v^2}{D_\phi} - \iota\right) m(x')\,, \tag{3.39}$$

where the first term arises from the boundary term.
The main contributions under the integral are the exponential and m. We can compare the two corresponding length scales, $\frac{\alpha v}{D_\phi}$ as an inverse length scale from the exponential term and ξ_0 as the width of the domain wall encoded in m. Assuming that $\left(\frac{\alpha v}{D_\phi}\right)^{-1} \gg \xi_0$ means that the exponential term changes on a large scale compared to the domain wall, and thus $m(x) \approx m_0 \operatorname{sign}(x)$ is a reasonable approximation to use under the integral, which should not introduce a large error. This should be fulfilled within the limits of small velocities and damping. The integral becomes feasible under this assumption, and we get

$$\phi'(x) = \frac{v}{D_\phi} m(x) - \frac{m_0(-v^2 + D_\phi\iota)\left(-\operatorname{sign}(x) + \mathrm{e}^{-\frac{v\alpha}{D_\phi}x}(\operatorname{sign}(v) + \operatorname{sign}(x))\right)}{D_\phi v}. \tag{3.40}$$

We now reverse the replacement, with $m_0 \operatorname{sign}(x) \approx m(x)$, to arrive at the final expression for the slope in ϕ,

$$\phi'(x) = \frac{\iota}{v} m(x) + \frac{\mathrm{e}^{-\frac{v\alpha}{D_\phi}x}(v^2 - D_\phi\iota)}{D_\phi v}\left(m(x) + \operatorname{sign}(v) m_0\right)\,. \tag{3.41}$$

Therefore, we recover the contribution coming from the rotation with the first term in the expression. The second term comes from the moving domain wall.
A comparison of Eq. (3.41), evaluated using numerical data of m, to the correspond-

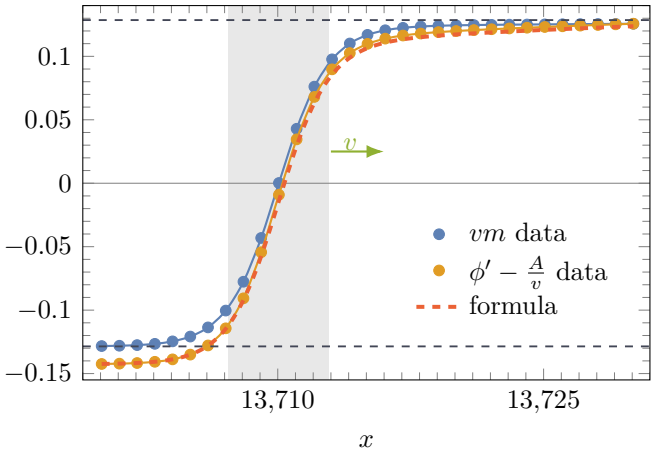

Figure 3.6: Comparison of numerical data to the approximate Eq. (3.41) (formula) for a right-moving up-down domain wall with velocity $v \approx 0.2875$, estimated from the zero crossing in m. The lines of the data curves serve as a guide to the eye. The simulation was conducted with open boundaries and 20,000 sites, and thus $A \neq 0$. Therefore, the ϕ' data has to be shifted according to Eq. (3.38). We estimate $A \approx 0.041$ by shifting data curves of ϕ' from two different times onto each other. The agreement with Eq. (3.41) is very good, with only a small deviation in the movement direction. Additionally, the data of m used to evaluate Eq. (3.41) is shown. The horizontal dashed lines indicate the value of m_0. The horizontal dashed lines indicate the value of m_0, clearly demonstrating that m also carries an exponential correction in the direction of movement, as the convergence to m_0 is slower on that side. The grey background highlights the area where $|x| \lesssim \xi_0$. Parameters: $r = -0.2, u = 1, D_m = 0.8, D_\phi = 1, \iota = 0.09171, \alpha = 0.1$.

ing data of ϕ' shows very good agreement, see Fig. 3.6. We estimate $v \approx 0.2875$ and $A \approx 0.041$ from the temporal data and shift the numerical data of ϕ' accordingly, compare Eq. (3.38). This allows a comparison with Eq. (3.41). Furthermore, we display the data of m and its asymptotes m_0. It is clearly visible that the left side of the domain converges faster than the right side. Thus, m carries an exponential correction as well.

Far away from the domain wall, the second part, in particular $(m(x) + \mathrm{sign}(v)m_0)$, is either zero or $2m_0$, depending on the direction of the velocity and the type of domain wall, i.e., up-down or down-up. It takes care of smoothly adding the exponential in the area around the domain wall. This has significant similarity with an ansatz from the previous section, in particular with $\phi_{\mathrm{exp}}(x)$. Expanding $m(x)$ in the second term around the position of the domain wall gives $m(x) \approx \frac{m_0 x}{\xi_0} + \mathcal{O}(x^3)$ which is a straight line as used for the approximation of $\phi_{\mathrm{exp}}(x)$ around the domain wall. This turns out to be a good approximation in the area $x \leq \xi_0$, compare to the grey area in Fig. 3.6.

However, one drawback is that the prefactor of the exponential correction includes $v^2 - D_\phi \iota$ and is seemingly not independent of the velocity. Comparing to the final equation from the previous section, Eq. (3.34), we see that the prefactor in Eq. (3.41)

is directly proportional to ϕ_{exp} with

$$\frac{v^2 - D_\phi \iota}{D_\phi v} = -\frac{\phi_{\text{exp}} \text{sign}(v)}{2m_0} \left(1 + \mathcal{O}(v^2, \alpha\iota v)\right), \tag{3.42}$$

for small velocities. Inserting this into Eq. (3.41) yields approximately the same ansatz as for $\phi_{\text{exp}}(x)$.
While we are not able to predict any reasonable velocity value from the Green's function approach with the approximations used, it effectively provides additional informations about the approximation made in the previous section. It also provides the possibility to compare directly to numerical simulations which strengthens the line of arguments and approximations made.

3.4 Memory Effect & Domain Wall Interactions

After studying the behaviour of a single domain wall, we can also study the more general scenario of many domain walls. To do so, we use an instantaneous quench of the microscopic model from an xy-ordered state to the ferrimagnet at $T = 0$. This will also give insights into the ordering dynamics of the system. We initialise the system in a staggered xy-ordered state with random z-components and periodic boundary conditions. In particular, we use m_i drawn from a uniform distribution in the interval of $(-0.1, 0.1)$ and $\phi_e = 0,\ \phi_o = \pi$. Additionally, we stay in the regime of the moving domain wall solution by choosing a small field amplitude of $b_0 = 0.15\, J$. This procedure ensures that we cross only one transition, see Fig. 2.4, from xy-order to ferrimagnetic order.
Fig. 3.7 shows an example of a simulation performed with these initial conditions at the same parameters as the moving solution in Fig. 3.1. Panel a) of Fig. 3.7 displays the m-profile as an orientation for the up or down nature of each domain. Already this quantity depicts that interaction effects play an important role in the dynamics. Main changes come from collisions of domain walls, either due to opposite moving domain walls or parallel moving ones, which come closer over time. A good example of the influence of interactions is at $x \approx 36{,}750\, a$ where a left-moving up-down domain wall changes its direction at roughly $t \approx 12\, T_{\text{rot}}$. This reversal in direction cannot show up in the single domain wall picture and is thus to be an interaction effect.
To understand the cause behind this, we can remind ourselves about a single moving domain wall, where we found that a domain wall builds up a finite phase gradient behind itself, see Fig. 3.1. During an annihilation event opposite, moving domain walls and with that opposite ϕ gradients meet at a collision point (x_a, t_a). In terms

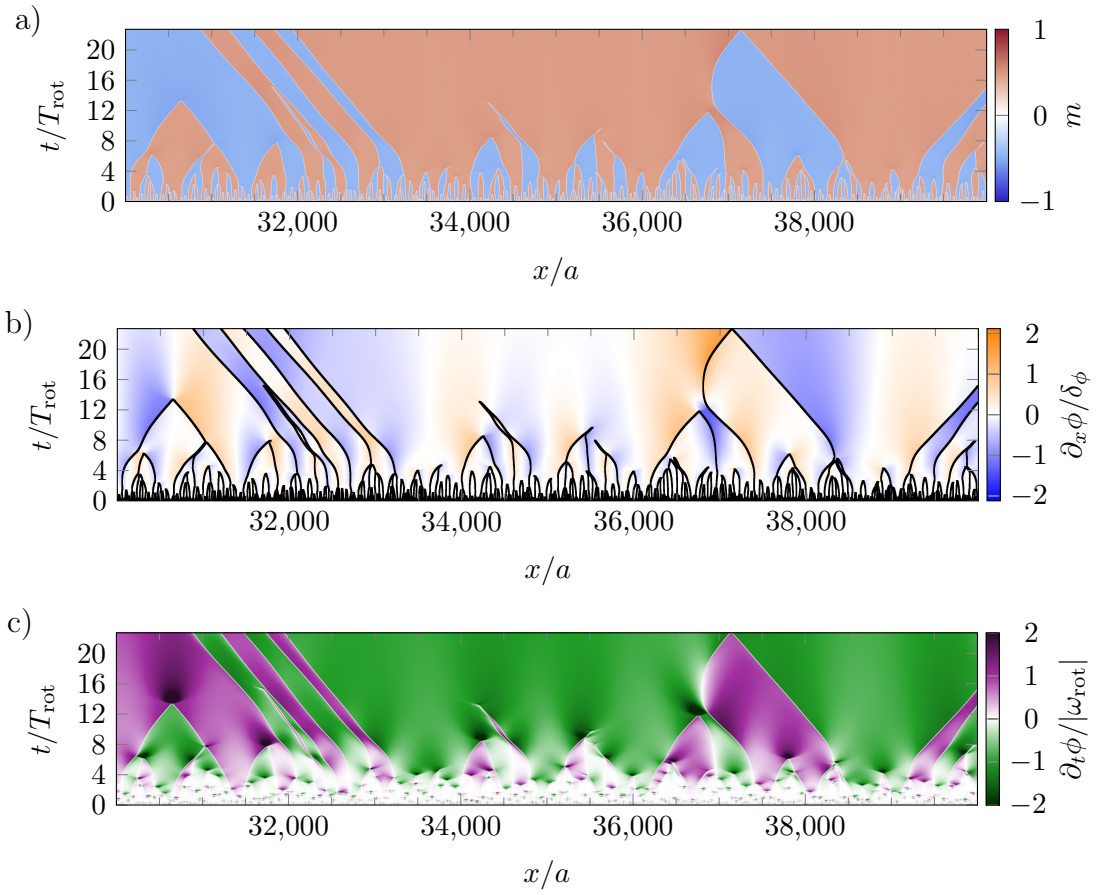

Figure 3.7: Data of an instantaneous quench from an xy-ordered state into the ferrimagnetic phase at $T = 0$ with a field amplitude of $b_0 = 0.15\,J$, which lies in the regime well described by the approximate velocity expression, Eq. (3.7), compare Fig. 3.2. Panel a) shows the magnetisation data for more than $\sim$ 20 rotations. Domains shrink and vanish either due to collisions of two opposite moving domain walls or by two parallel moving domain walls, with a slight mismatch in the velocities. Panel b) shows the gradient of the phase normalised by the difference in the phase across a single moving domain $\delta_\phi = \partial_x\phi^{\mathrm{left}} - \partial_x\phi^{\mathrm{right}} \approx 0.176$, evaluated from Fig. 3.1b). We show the domain wall position determined from $m = 0$ as black lines. The motion of the domain walls is strongly influenced by a long-range hydrodynamic interaction governed by $\partial_x\phi$. This can be seen, e.g., at $x \approx 36{,}750a$ and $t \approx 12T_{\mathrm{rot}}$. Panel c) displays the current corresponding to the approximately conserved quantity $\partial_x\phi$ normalised by the rotation period. It can be expressed in terms of $\partial_t\phi$. Deep inside a domain far away from any collision events, we thus expect it to be ± 1. At a collision event, the current accumulates and decays slowly. Parameters: same as in Fig. 3.1 for a system of 40,000 sites and periodic boundary conditions.

of magnetisation, it is equivalent to a shrinking domain, i.e., the magnetisation recovers a uniform domain shortly after t_a. This is very different for the build-up phase gradient, which can be seen in Fig. 3.7b), where we show the phase gradient scaled by the numerical value of the difference of the phase gradients for a single domain wall, $\delta_\phi \approx 0.176$. It is very visible that the accumulated phase gradient decays very slowly compared to other processes in the system, e.g., the rotational mode or the movement of domain walls. We will now quantify this observation, again using the effective theory.

Similar to the single domain wall, vortices do not show up in the regime of small amplitudes, and ϕ is smooth in space and time. Therefore, we can interpret $\partial_x \phi$ as a conserved quantity (due to periodic boundary conditions) and define the corresponding topological charge density via

$$\rho_{\text{top}} = \frac{\partial_x \phi}{2\pi}\,, \tag{3.43}$$

which encodes how often ϕ winds in the xy-plane via the associated topological charge $Q_{\text{top}} = \int \rho_{\text{top}}\, dx$. The conservation of ρ_{top} can then be stated into a continuity equation with

$$\partial_t \rho_{\text{top}} + \partial_x j_{\text{top}} = 0\,, \tag{3.44}$$

where the topological current can be identified from the first line of Eq. (3.10) by performing an additional derivative in space. This gives

$$j_{\text{top}} = \frac{\iota m}{2\pi} - \frac{D_\phi}{\alpha}\partial_x \rho_{\text{top}} - \frac{\dot{m}}{2\pi\alpha}\,. \tag{3.45}$$

For a description without thermal fluctuations, $\eta_\varphi = 0$. Another way of writing the topological current is by $j_{\text{top}} = \frac{\partial_t \phi}{2\pi}$. Thus, deep inside a domain, we expect only a contribution from the first term, i.e., $\frac{\iota m}{2\pi} = \frac{|\omega_{\text{rot}}|}{2\pi}$. Therefore, we normalise the topological current by $\frac{\omega_{\text{rot}}}{2\pi}$ when presenting it in Fig. 3.7c) within the same spatial and temporal range as the magnetisation and phase gradient above.

With this at hand, we can focus back on the process after an annihilation event. As the magnetisation is uniform, the first and last contribution of j_{top} drops out of the equation, and we arrive at a diffusion equation for the topological charge density

$$\left(\partial_t - \frac{D_\phi}{\alpha}\partial_x^2\right)\rho_{\text{top}} = 0\,. \tag{3.46}$$

This confirms our previous observation that the accumulated phase gradient decays slowly. In particular, it decays diffusively with $t \sim \frac{\alpha x^2}{D_\phi}$. Therefore, we can estimate the average time needed for the accumulated topological charge to decay after an

annihilation event by $T_d \sim \frac{\alpha L_d^2}{D_\phi}$ where L_d is the average size of a domain. At later times where $L_d \gg \frac{D_\phi}{\alpha v}$, we find that $T_d \gg \frac{L_d}{v}$ which is the average time for nearby domain walls to arrive at the annihilation point (x_a, t_a). While ρ_{top} does not have an influence on the speed of domain walls, spatial derivatives $\partial_x \rho_{\text{top}}$ do. This arises due to the fact that the change in spin current is dependent on $\partial_x^2 \phi \propto \partial_x \rho_{\text{top}}$, see, e.g., the argument under Eq. (3.1). In particular, a negative topological charge gradient $\partial_x \rho_{\text{top}} < 0$ leads to a local increase in magnetisation $\dot{m} > 0$. This local additional magnetisation will then suppress incoming negative magnetisation, i.e., an incoming down-domain is slowed down, or even reversed, as in the example at $x \approx 36{,}750\, a$ discussed at the beginning of this section. Thus, the primary source of interaction between domain walls turns out to be given by gradients in topological charge, which are produced in annihilation processes.

This is different to the minimal model explained in Sec. 1.7, where domain walls are treated like particles and interact *only* at collision events. We recall that the correlation length in this model scales in time via $\xi \propto \sqrt{t}$. Similarly, we can study the correlation data of instantaneous quenches to the ferrimagnetic phase for our microscopic ferrimagnet. The previous findings regarding the interactions over long time scales are already a hint that we will find a drastic difference for the driven ferrimagnet compared to the simple model and the non-driven system.

Since we are still in the noise-free regime, we can once again count the number of domain walls and define a correlation length as the inverse of the domain wall density n_{DW}, i.e., $\xi = 1/n_{\text{DW}}$. Fig. 3.8a) displays this correlation length, with the inset zooming in on the short-term dynamics. Each point of the driven data is averaged over 20 different initial states in a system with 500,000 sites with the same quench scenario as before, compare to Fig. 3.7. At initial times, the non-driven and driven points follow roughly the same curve. However, after a few rotations, the correlation length in the driven system grows rapidly in time. This second regime can be divided into two regions. The first and smaller one grows roughly with $\xi \approx vt$, where $v \approx 0.1226$ is indicated by a red dashed line and is nicely visible in the inset. For the longer times, we can observe the second region, from approximately $t \gtrsim 20\, T_{\text{rot}}$. The separations into these two regions can be explained by the time it needs until the domain walls have the correct velocity value. To support this claim, we show the velocity distribution at different times in Fig. B.1 in the appendix. At early times, the distribution is centred around $v = 0$, but for later times, it is centred around the correct velocity values given by Eq. (3.7). For the second region, we find a linear growth in the correlation length, which can be

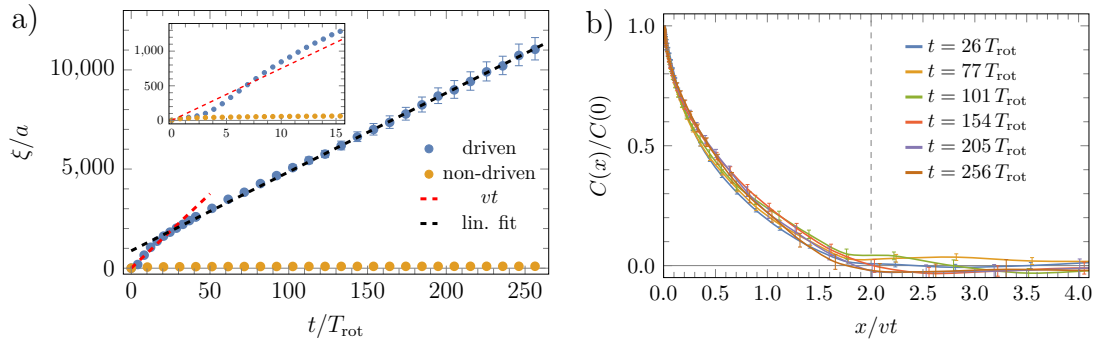

Figure 3.8: Emergence of correlations in m after an instantaneous quench from an xy-ordered state into the ferrimagnetic phase at $T = 0$, similar to Fig. 3.7. Panel a) displays the correlation length in m, defined by the inverse of the domain wall density, $\xi = 1/n_{\mathrm{DW}}$, as a function of time after the quench for both the driven and the non-driven system. At short times, the evolution of the two is identical, compare in the inset of panel a). However, after a few rotations, the driven system exhibits a rapid growth in the correlation length. This is again divided into two regimes: a short, intermediate interval where correlations grow roughly proportional to vt, shown as a red dashed line (where $v \approx 0.1226$ is the velocity of a single domain wall, e.g., Fig. 3.1), and the long-time limit where ξ grows approximately as $0.53vt$. Panel b) shows the normalised m-correlations of the same data in space, where the x-axis is scaled by vt, for six different times in the linear regime associated with the black dashed line in panel a). The data collapses nicely on the same curve, up to error bars. This confirms the linear growth of the correlation length with time. The point where the curves hit zero is approximately at $x = 2vt$, marked with a vertical dashed line. We can identify this as the maximum relative velocity in the system. The initial conditions and parameters are the same as in Fig. 3.7, but larger system sizes of 500,000 sites have been used. Each data point is averaged over 20 initial states for the driven and 15 for the non-driven data points, and the errors are the standard deviation of the mean.

related to the single domain wall velocity via

$$\xi \approx \mu\, vt \quad \text{for} \quad t \gtrsim 20\, T_{\mathrm{rot}}\,, \tag{3.47}$$

where $\mu \approx 0.53$ is a fitting parameter. This describes a much more efficient ordering than the simple model without long-range interactions of the domain walls. Thus, the strong growth of the correlation length has to emerge from the interactions, which we found to be mediated by phase gradients at the beginning of this section. The linear growth in correlation length has also been found in active matter systems of self-propelled particles [68, 69].

To support this claim, we can use a simple argument: Inside a domain, the angle changes linearly in time with $\phi \approx \omega_{\mathrm{rot}} t$. If we assume an average domain size of L_d, we can estimate the average phase gradient with

$$|\partial_x \phi| \sim \frac{2\omega_{\mathrm{rot}} t}{L_d}\,. \tag{3.48}$$

Since the phase gradient is a bounded quantity, the expression above must stay finite in the $t \to \infty$ limit. A simple expression to achieve this is the linear time dependence of the average domain size, $L_d \propto t$. Since the correlation length is proportional to the average domain size, we can deduce that it grows linearly in time as well, $\xi \propto t$. This is just a rough estimate and not a rigorous proof. However, it gives us some intuition about the emerging linear growth in correlation length.
We additionally show the equal-time correlations of the magnetisation calculated via

$$C(x) = \langle m_i m_{i+x/a} \rangle \,, \tag{3.49}$$

normalised by the value at $x = 0$ in space at different times in Fig. 3.8b). The brackets $\langle \dots \rangle$ stand for an average over all even, or equivalently, all odd sites. The $x-$axis is normalised by the distance vt, which a single domain wall moves over in time t. By this choice, the shown curves of the correlation, which are more than 200 rotation periods apart, fall nicely on top of each other with respect to the error bars. The first point where zero correlation is reached is at approximately $x = 2vt$ for all times shown. This is related to two domain walls moving in opposite directions, i.e., the relative maximum velocity of $2v$. This confirms the linear scaling of the correlation length and validates the domain wall velocity for the single-moving domain wall. In the next section, we study the influence of thermal fluctuations.

3.5 Resilience to Thermal Fluctuations

So far, we have studied the system in the limit of zero temperature and found actively moving domain walls. Two upcoming questions are whether this observation is stable at finite temperatures, in one dimension, and what effect it has on the stability of the ordered phase in comparison to its equilibrium counterpart without actively moving domains.
Within this section, we want to give an answer to these questions by exploring the finite temperature regime. It turns out that the active movement is stable at the studied temperatures and the ordered phase is more stable against thermal fluctuations. This is the first point in this thesis where the stochastic part of the LLG Eq. (1.7) in the form of a randomly fluctuating field plays a role.
In equilibrium, for one dimension, the cost of a domain wall does not scale with system size, and thus domain walls can proliferate the ground state at finite temperature. Consider a constant negative domain, for which large enough fluctuations can locally alter the value to a positive domain. As the temperature increases, the frequency of these events rises, leading to a loss of the ordered phase. A useful guidance is the average domain wall distance, which scales with the ratio of temper-

ature and domain wall energy at zero temperature, here denoted by E_{DW}, via the Boltzmann factor with

$$\xi_{\mathrm{th}} \sim e^{E_{\mathrm{DW}}/T}\,, \tag{3.50}$$

where T is measured in units of energy. We, therefore, display the temperature in units of E_{DW}, which gives a feeling of the change of the average domain wall distance with temperature in equilibrium. For the parameters chosen in this section, we determined its value numerically as $E_{\mathrm{DW}} = 0.076$. This can be done by initialising the system with and without a domain wall at $T = 0$. The difference between the two yields the domain wall energy.

Figs. 3.9a) and b) show the magnetisation in space and time for the driven system at two different temperatures. We used the same quench protocol as described in Sec. 3.4, which goes from an xy-ordered state to a ferrimagnetic state, but now at finite temperature. The relative temperature difference of the two simulations is about 4.5%. Nevertheless, we observe a significant difference between them. At lower temperatures, large domains are rarely proliferated by domain creation events. In contrast, at higher temperatures, this process occurs frequently. However, we still observe moving domain walls in the latter case. We can estimate the speed of domain walls from the picture for $T \approx 0.349\,E_{\mathrm{DW}}$ as approximately 10% larger compared to the $T = 0$ case. This is just a rough estimate, and we will later confirm it by analysing the stationary-state space-time correlations, see Sec. 3.5.1.

Additionally, we compare this briefly to the equilibrium system. Fig. 3.9c) displays at the top and centre the final time-step from Figs. 3.9a) and b), respectively, and at the bottom, an equilibrium simulation at the lower temperature of $T \approx 0.334\,E_{\mathrm{DW}}$. The dashed lines represent the domain value at $T = 0$ as a guide to the eye. The thin solid lines represent $m = 0$ for the corresponding curve. For the lowest temperature, it is almost one domain for the entire section shown. There are still rare events where the magnetisation switches to the opposite side, but it is not able to fully grow into a bigger domain. For the higher temperature, we do observe these branches of domains of the order of 100 sites inside the large domain displayed. In contrast, the equilibrium curve shows a very different behaviour. The magnetisation switches between the two domain values on a very short length scale of less than 20 sites, and the ordered state is lost. Notice that local fluctuations are roughly of the same order of magnitude in all three curves, but swaps to the other domain value have a very different frequency. Later, in Sec. 3.5.2, we analyse possible healing mechanisms which distinguish the driven system from the non-driven system.

The main finding of this analysis is that the driven system is significantly more *resilient* to thermal fluctuations compared to the equilibrium system. In the following, we want to quantify this observation by studying the equal-time correlation

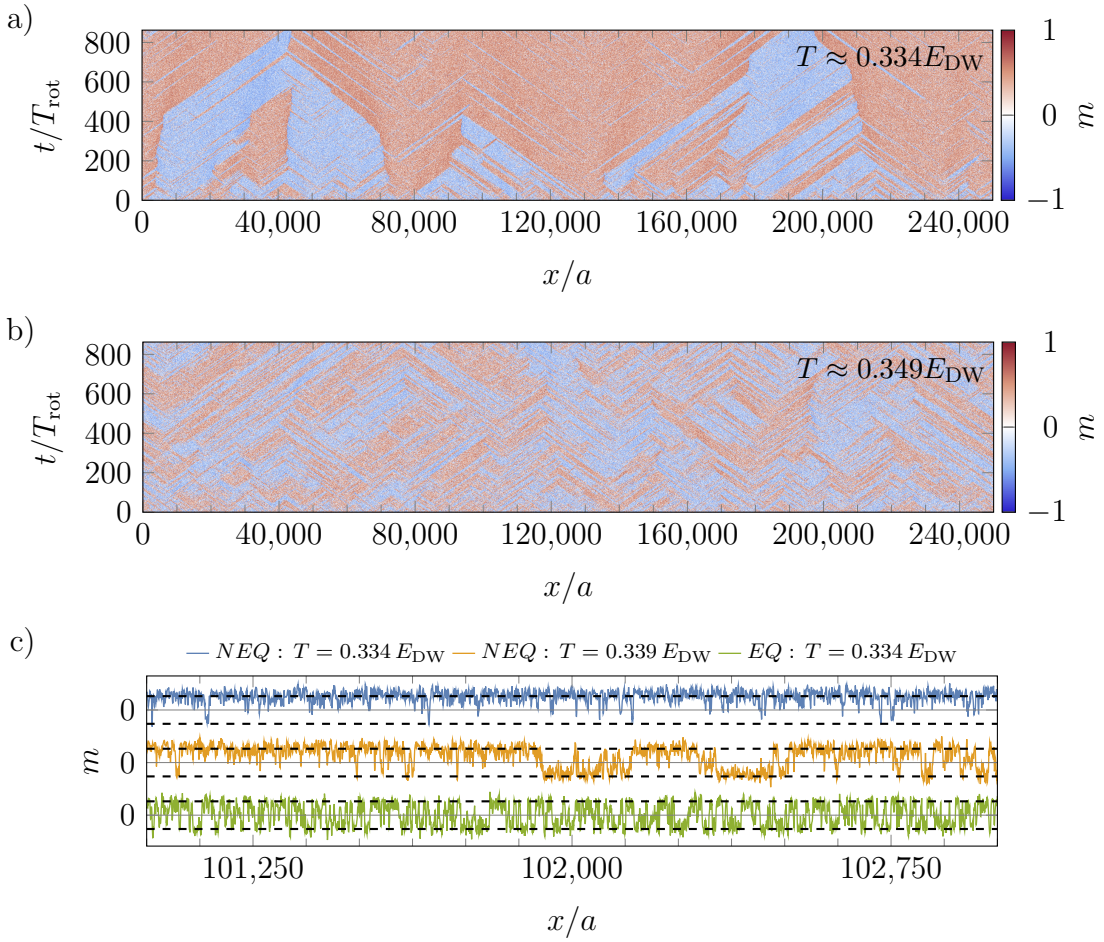

Figure 3.9: Simulations of an instantaneous quench from an xy-ordered state to a ferrimagnetic state at finite temperature. Panels a) and b) show the magnetisation as a function of space and time after the quench for two marginally different temperatures, i.e., different noise levels. The temperatures are given in terms of the energy of a domain wall in the non-driven system estimated from a numerical simulation. We show the total system simulated, consisting of 250,000 sites with the same parameters as before, Fig. 3.1. Panel c) displays the final time step of the two simulations shown in panels a) and b) for a small interval of 2,000 sites, the curves in the top and the centre. The bottom curve shows data from an equilibrium simulation at the lower temperature. We use NEQ for the (non-equilibrium) driven simulations and EQ for the (equilibrium) non-driven simulations. The correlation length is significantly lower in the non-driven system compared to the driven system for the same temperature. Even from the bare data, the driven system appears much more stable against thermal fluctuations. Furthermore, we observe moving domain walls with constant velocity at both temperatures with roughly 10% higher velocity compared to that of a single domain wall.

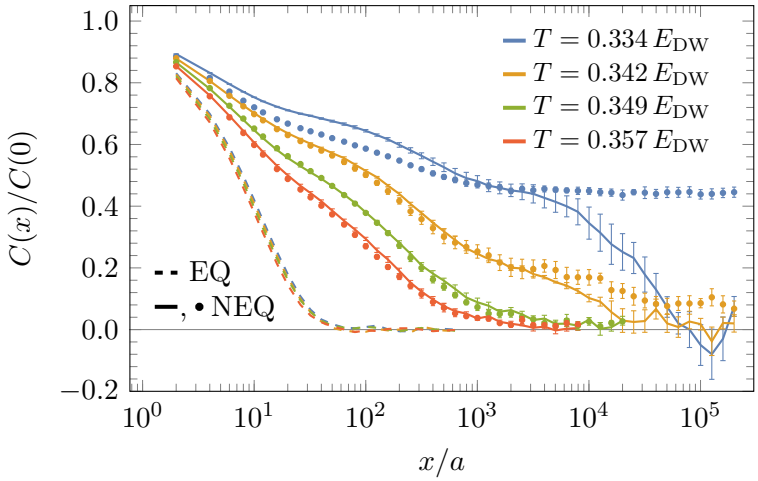

Figure 3.10: Equal-time correlations in m calculated via Eq. (3.49) for systems of 250,000 sites in the presence of thermal fluctuations. The data is taken at approximately $t \approx 850\,T_{\mathrm{rot}}$ after an instantaneous quench from an xy-ordered state (solid and dashed lines) to a ferrimagnetic state at finite temperature. For the data displayed as points, we used a quench from a ferrimagnetic state as a simple test to verify whether the stationary state was reached. For a shorter notation, the legend denotes the non-driven (equilibrium) system with EQ and the driven (non-equilibrium) system with NEQ. Apart from the curve for the lowest temperature, the system attained a stationary state at that point, visible from the fact that the two curves from the two different initial states fall roughly on top of each other. The dashed lines are for the non-driven system, showing only a marginal scaling with temperature in the range shown. In contrast, the curves from the driven scenario show a broad distribution of domain sizes with approximately linear shapes on linear-log scale. The correlation length is many orders of magnitude larger compared to the equilibrium system. Parameters as in Fig. 3.1. The error bars denote the standard deviation of the mean averaged over four runs. The error of the equilibrium simulations is omitted since it is smaller than the line width.

function for different temperatures and give an estimate for the correlation length. We calculate this quantity via Eq. (3.49).

One difficulty is that the more robust and, with this, the more ordered the system is, the longer it takes to reach the stationary state. As a simple estimate to test if the final stationary state is reached, we perform simulations from the xy-ordered state as for Fig. 3.9 but additionally from an ordered state in the ferrimagnetic phase corresponding to the chosen parameters. Once these two distinct states, one with finite average z-magnetization and one with zero, reach the same state within error bars, we can conclude that the final stationary state has been achieved. The correlations extracted from the two opposite initial states, ferrimagnetic with dots and xy-ordered with solid lines, are shown in Fig. 3.10, where each is averaged over four different simulations. Notice that it is on a linear-log axis. Additionally, we show the equilibrium correlations at the same temperatures with dashed lines. We can see directly that the equilibrium system has much shorter correlations and changes

Table 3.1: Estimate for the correlation length for the solid lines, quench from xy-order, in Fig. 3.10 for all four temperatures shown. The second and fourth columns show the lower and upper bounds. The third column shows the estimated value. For the lowest temperature, we give only a very rough estimate since the stationary state was not fully reached, hence the infinite upper bound. The corresponding plot is shown in Fig. 3.11.

T/E_{DW}	$\xi^{<}_{\mathrm{max}}/a$	ξ_{max}/a	$\xi^{>}_{\mathrm{max}}/a$
0.334	45,200	475,000	∞
0.342	10,400	18,100	108,000
0.349	800	1,800	13,600
0.357	400	700	5,900

only a little with temperature on the scale shown. This is drastically different in the driven system. All but the lowest temperature reached the stationary state according to our simple test, i.e., the curves from the different initial conditions lie on top of each other within error bars. Furthermore, the correlations increase rapidly with temperature, as already anticipated from the raw magnetisation data, see Fig. 3.9. Additionally, we observe a very slow decay over many length scales roughly described by

$$C(x) \approx C(0) \left(1 - \ln\left[\frac{x}{a}\right] / \ln\left[\frac{\xi_{\mathrm{max}}}{a}\right]\right) , \tag{3.51}$$

which corresponds to a very broad distribution of domain sizes. In Fig. 3.10 with linear-log axis, the curve Eq. (3.51) corresponds to a straight line which hits zero at ξ_{max}. Thus, ξ_{max} is a measure for the largest correlation length in the system. Because of the slow decay in space, an often used definition of the half-width $\xi_{1/2}$, defined by $C(\xi_{1/2}) = \frac{1}{2}C(0)$, does not serve as a sufficient measure for the domain sizes. We can confirm this by going back to Fig. 3.9b), which shows the magnetisation data for $T = 0.349\, E_{\mathrm{DW}}$, and compare the bare observation to its half-width estimate. From Fig. 3.10 we can read off a half-width of $\xi_{1/2} \approx 35$. This is at least one order of magnitude lower than the actual correlations roughly extracted from the domain sizes shown. For the lower temperature $T = 0.334\, E_{\mathrm{DW}}$, due to the not fully equilibrated correlation function, we can only give a very rough estimate of $\xi_{1/2} \approx 615$. However, this also turns out to be orders of magnitude lower than the true correlations of the displayed magnetisation data.

Therefore, we choose a different route and use ξ_{max} as a measure, which we determine by a fit to Eq. (3.51). We use the data from the xy-ordered initial state, solid lines in Fig. 3.10, and apply the fit on the values up to $x/a \leq$ 8,000, 20,000, 1,000 and 300 for $T = 0.334, 0.342, 0.349$ and $0.357\, E_{\mathrm{DW}}$, respectively. The low value for the lowest temperature results from the fact that it is not fully in the stationary state and is only equilibrated on short distances up to roughly this point. To compensate for

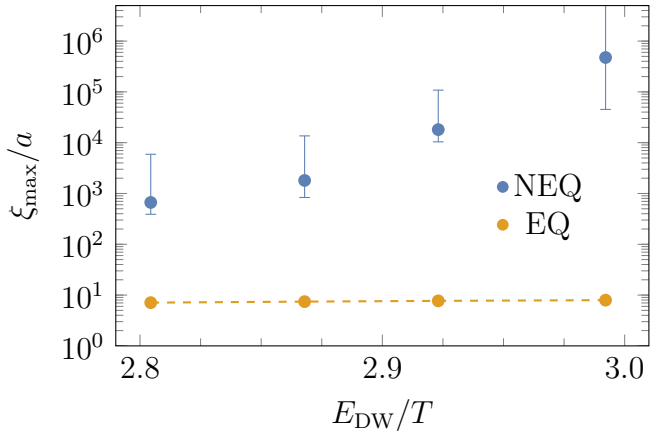

Figure 3.11: $\xi_{\max}$ extracted from Fig. 3.10 and summarised in Tab. 3.1, shown as a function of the inverse temperature. The estimate is described in the text. Additionally, we show the equilibrium values at the same temperatures, evaluated via the half-width. The maximal correlation length in the driven system grows faster than exponential. Hence, a thermal process cannot be the cause. The growth of the equilibrium points is tiny on the scale shown. This confirms that the driven system is more resilient to thermal fluctuations.

the crudeness of the fit, we choose generous error bars derived in the following way: for the lower bound $\xi^{<}_{\max}$, we use $C(\xi^{<}_{\max}) = 0.1\,C(0)$, while for the upper bound $\xi^{>}_{\max}$, we choose the first point where $C(x) \approx 0$ with respect to the error bars. For the lowest temperature curve, we cannot assign an upper bound using this method since it is not equilibrated on these length scales. However, the fitted value exceeds the system size, and thus, the only reasonable choice for the error is infinity. The values are summarised in Tab. 3.1. We show these values in Fig. 3.11. The growth of $\xi_{\max}$ with $1/T$ is much faster than exponential, and thus, a purely thermal process can be excluded as a source. Additionally, we show the values from the equilibrium simulations. For this data, we use the usual definition of the half-width, which gives reasonable results in the absence of driving. Since two different methods are used, the exact values are not directly comparable. However, any reasonable definition of the equilibrium correlation length is at least one order of magnitude smaller than the value of the driven system for the lowest temperature. Furthermore, the scaling with temperature of the equilibrium simulations is tiny on the shown scale. This underlines the previous statement that the driven system has a significant increase in correlation length by several orders of magnitude.

For completeness, we show the correlations in the xy-order in Fig. B.2 in the appendix. In contrast to the correlations in m, these show short correlation lengths of $\lesssim 30$ sites for all temperature values. Furthermore, we compare it to the non-driven system at the same temperatures, which shows more extensive correlation lengths and exponential decay in space.

This concludes the extended answer to the two questions at the beginning of the sec-

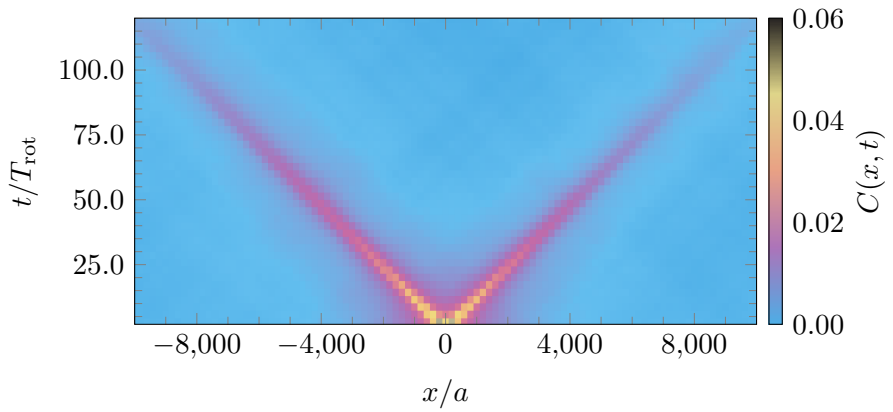

Figure 3.12: Steady-state space-time correlations calculated via Eq. (3.52) for the driven ferrimagnet as in Fig. 3.9b) ($T = 0.349\,E_{\mathrm{DW}}$) and 250,000 sites averaged over five runs and several t_0 values. The two slowly decaying lines associated with the domain wall speed $v \approx \pm 0.135$ are clearly visible as distinguished directions. Different cuts through this plot are shown in Fig. 3.13.

tion. In summary, the rotation due to the driving and the actively moving domain walls are stable at the finite temperatures studied. The ordered phase is more stable against thermal fluctuations, resulting in large values for the correlation length. Before moving to a possible explanation for the enhanced resilience, we first study space-time correlation in the stationary state.

3.5.1 Space-Time Correlations

After studying the equal-time correlation functions, both for the stationary state and throughout a quench, we can now turn to the space-time correlations. This quantity can be reasonably defined in simulations with thermal fluctuations where a steady state is reached. We calculate it via

$$C(x,t) = \left\langle m_i(t_0) m_{i+x/a}(t_0+t) \right\rangle , \tag{3.52}$$

which compares the z-magnetisation not only with spatial separation x/a, but also temporal separation t. As before, we average over all even sites denoted by $\langle \dots \rangle$. We highlight that we use stroboscopic time values in terms of the driving period to eliminate contributions from oscillations, as in all previous discussions.
We show the space-time correlation from data with an initial xy-order for temperature $T = 0.349\,E_{\mathrm{DW}}$ in Fig. 3.12. Two peaks with $x = \pm vt$ carrying a linear velocity of $v \approx 0.135$ are clearly visible due to the very slow decay compared to most other directions. The dominating effect leading to these peaks is the moving domain walls. Comparing to Fig. 3.9b), which shows raw magnetisation data for the chosen temperature, we can confirm this claim. For example, if we choose $+v$ and move on

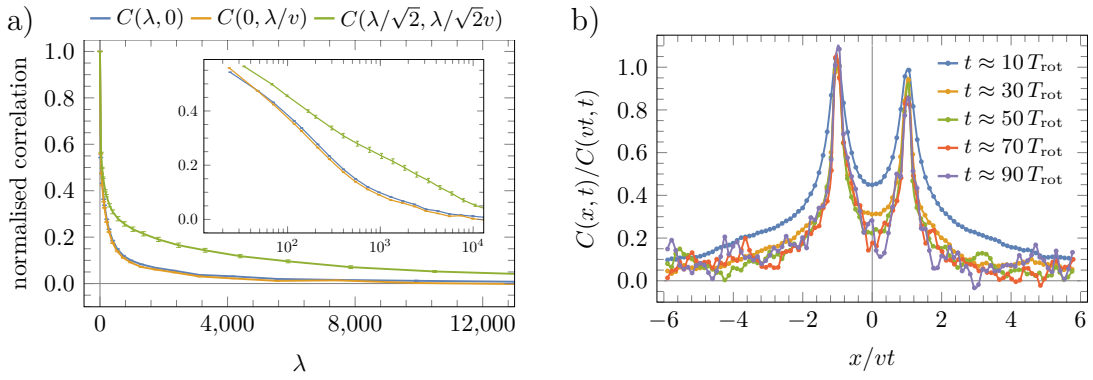

Figure 3.13: Different cuts of the steady-state space-time correlations, shown in Fig. 3.12 at temperature $T = 0.349\,E_{\mathrm{DW}}$. Panel a) compares three different cuts in Fig. 3.12, equal-time correlations $C(\lambda, t = 0)$, equal-space correlations $C(x = 0, t)$ for $t = \lambda/v$ and the diagonal with $C(\lambda/\sqrt{2}, \lambda/\sqrt{2}v)$. $v \approx 0.135\,Ja$ is the velocity of a single domain wall and approximately 10 % faster compared to the system at zero temperature. Here, we defined $\lambda = \sqrt{x^2 + (vt)^2}$ as the distance to the origin to compare the three curves on an equal footing. Remarkably, the $C(\lambda, t = 0)$ and $C(x = 0, \lambda/v)$ are identical within the error bars. The decay is much slower along the diagonal, $C(\lambda/\sqrt{2}, \lambda v/\sqrt{2})$, in agreement with the statement that this corresponds to the moving domain walls, which stretch out much further along that direction. The inset shows it on a linear-log scale to highlight the similarities and differences mentioned. Panel b) displays horizontal cuts in Fig. 3.12 normalised by the value of the diagonal $C(x,t)/C(vt,t)$ as a function of $x/(vt)$. This confirms that the peaks scale with velocity v and also shows that for long times, the width has the same scaling.

the corresponding diagonal line through the magnetisation, the average length of a domain is enhanced. This geometric argument is the same for $-v$. In turn, the correlation length along those lines is increased compared to other directions. Thus, we can use the space-time correlation data to give a more precise estimate of the value of the velocity under the influence of thermal fluctuations. The value provided above is approximately 10.2% larger compared to the system at zero temperature ($v \approx 0.1226$).

Additionally, we can use a scaling plot of time-cuts from Fig. 3.12 to confirm that the scaling, up to possible subleading corrections, is set by the moving domain walls. The result is shown in Fig. 3.13b), where space is scaled by the velocity and the space-time correlation value is normalised by $C(vt, t)$. The curves at late times fall exactly on top of each other, while the peaks are at $\frac{x}{vt} = \pm 1$, confirming the estimated value for the velocity. Furthermore, this also shows that the width of the peaks scales with vt.

Moreover, we can compare the space-time correlations with the space correlations and the time correlations. These are the diagonal sections, horizontal sections and vertical sections in Fig. 3.12. To make a reasonable comparison, we define $\lambda = \sqrt{x^2 + (vt)^2}$ as the distance from the origin. This enables us to measure the

three different correlations on an equal footing. The result for equal-time $C(\lambda, 0)$, equal-space $C(0, \lambda/v)$ and space-time $C(\lambda/\sqrt{v}, \lambda/\sqrt{2}v)$ correlations are shown in Fig. 3.13a). The inset shows the same data on a linear-log scale.
Surprisingly, the equal-space and equal-time correlations match within the small error bars. Meanwhile, the space-time correlations are roughly five times larger. This behaviour is observed at other temperatures as well.
Throughout this section, we confirmed the initial estimate of the increased velocity, which gives another confirmation that the actively moving domain walls are stable at the finite temperatures shown.

3.5.2 Healing Mechanisms

Within this section, we want to discuss possible sources which can protect the ordered phase in the driven system. We will give an explanation for the strong resilience to thermal fluctuations, i.e., a substantial increase of correlations with temperature in comparison to the equilibrium system.
A necessary event to lower the correlation length due to thermal fluctuations is the frequent formation of a domain inside a domain with opposite magnetisation. This is for example visible in the bottom curve of Fig. 3.9c) for the non-driven system.
In the driven system, the two domains carry an opposite sense of rotation in the xy-plane. Thus, an apparent reason for the suppression of such events, i.e., defects in the ordered phase, is dynamical frustration at the domain walls.
Two different types of defects, type I and type II, arise from thermal fluctuations and can be seen in Fig. 3.9a) and Fig. 3.9b).
Type I defects are described by pairs of parallel moving domain walls, best seen for the lower temperature shown in Fig. 3.9a) by thin blue lines of up to a few hundred sites. They occur frequently, even at lower temperatures, but are not able to destroy the long-ranged order. This comes from the fact that they do not grow in size and vanish upon meeting another type I defect, which moves in the opposite direction. In particular, these collisions build an efficient healing mechanism since the domain walls and, thus, the type I defects only move with constant velocity either to the left or to the right and are equally nucleated in both directions. We give additional confirmation to this claim in a later section, Sec. 3.6, using numerical simulations of the effective model.
In contrast, type II defects are, in general, much more likely to destroy long-range order. They are characterised by two domain walls which move in opposite directions and thus give rise to growing domains. At first glance, these seem to be much more dangerous in the driven system due to the constant velocity of the walls. A few of these can be seen in Fig. 3.9b) at higher temperature or, e.g, in Fig. 3.9a)

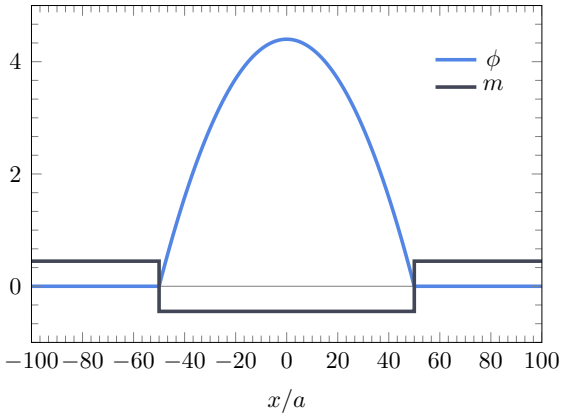

Figure 3.14: Illustration of the initial state used for the simulations shown in Fig. 3.15 and Fig. 3.16 with $L_{\text{init}} = 100$ and $s_{\text{init}} = 1$ from Eq. (3.53). The slope difference at the domain walls is chosen in such a way that the walls are initially propelled outwards. This is an artificial way to create an initially outward-moving type II defect.

at approximately $x \approx 35{,}000a$. Additionally, we show the very rare event of a type II defect, which grows to the size of the entire system in the appendix Fig. B.3 for lower temperatures. During the whole investigation, it was the only observation of such an incident.

This already shows that these defects are very rare and thus not as harmful as believed at first glance. To analyse the cause of this, we use simulations at $T = 0$ of a down-domain $-|m_0|$ initialised with size L_{init} inside of an up-domain with the corresponding $|m_0|$ value, Eq. (2.4). In order to mimic a developing type II defect, i.e., two domains moving in opposite directions, we use the following profile for the phase

$$\phi = \begin{cases} \left(\frac{L_{\text{init}}}{4} - \frac{x^2}{L_{\text{init}}}\right) \delta_0 s_{\text{init}} & \text{for} \quad |x| < \frac{L_{\text{init}}}{2}, \\ 0 & \text{for} \quad |x| \geq \frac{L_{\text{init}}}{2}, \end{cases} , \tag{3.53}$$

where $\delta_0 = 0.176$ is the slope difference at a single right-moving up-down domain wall taken from the data shown in Fig. 3.1b) and s_{init} is a factor to scale the initial magnitude. As before, we define $\phi = (\phi_e, \phi_o + \pi)$ for the microscopic model. This construction creates a smooth parabolic shape between the two domain walls and carries an initial slope of $\phi'(\pm\frac{L_{\text{init}}}{2}) = \mp\delta_0 s_{\text{init}}$ exactly at the domain walls, see Fig. 3.14. Therefore, the down-up domain wall at $x = \frac{L_{\text{init}}}{2}$ has a slope difference of $\Delta\phi' = (\phi'_R - \phi'_L) = \delta_0 s_{\text{init}} > 0$, which results in a positive velocity for the domain wall, compare to Eq. (3.5). Similarly, the up-down domain wall at $x = -\frac{L_{\text{init}}}{2}$ is equipped with a negative slope difference, which ends up giving it a negative initial velocity. In total, this yields an initially growing type II defect.

With this at hand, we can perform simulations for different values of the two control parameters s_{init} and L_{init} and create a phase diagram, displayed in Fig. 3.15, which

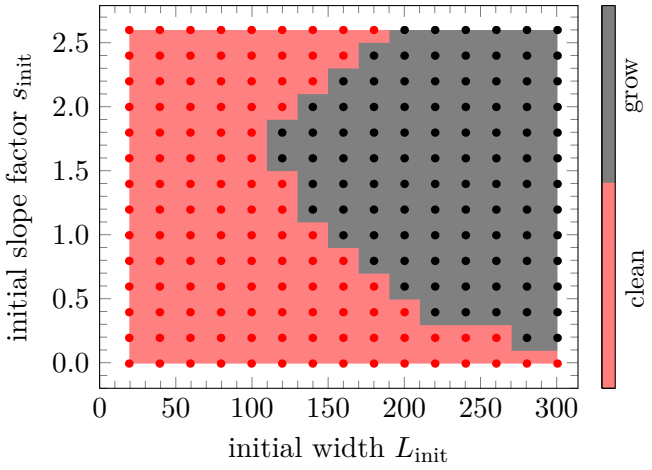

Figure 3.15: Phase diagram of type II defects as a function of L and s_{int}, which parametrise the initial state according to Eq. (3.53). Points denote data points, and the background is a guide to the eye. The red region assigned as clean is associated with final states where the down-domain vanishes. The two possible scenarios which we observe are displayed in Fig. 3.16(a,b) for a lower initial slope and in Fig. 3.16(e,f) for a higher initial slope. Only in the black region is the domain able to grow, with the only observed scenario shown in Fig. 3.16(c,d). For all initial slopes shown, only large domain sizes of $\gtrsim 100$ can grow. This explains why we rarely observe growing domains, even under thermal fluctuations. Parameters as in Fig. 3.1 for systems of 20,000 sites.

shows the final state. The grey colour denotes the area where the type II defect grows, with the data points shown as black points on top. The red colour shows the area where the ordered phase is recovered, for brevity we call it 'clean' at the colourbar. Before going into further details, we notice that the system is able to recover the ordered phase for all shown values of s_{init} if $L_{\text{init}} \lesssim 100$. Thus, we conclude that there has to be an effective, attractive interaction between the two domain walls, which decreases with distance. This is in agreement with the rare occurrence of type II defects in thermal simulations where fluctuations have to conspire over a long distance of $\mathcal{O}(100)$ to end up creating such defects.

Another noticeable feature of the phase diagram is that the 'clean'-phase first shrinks with increasing s_{int}, but then increases again above $s_{\text{int}} \gtrsim 1.8$. It turns out that there are three different regions in the phase diagram with different behaviour. To study the microscopic cause, we can look at one point in each of the three different regions visible in the phase diagram. These are shown in Fig. 3.16 with $(L_{\text{init}}, s_{\text{int}}) = (200, 0.4)$ for the self-annihilating type II defect in panels a) and b), $(220, 0.4)$ for the growing type II defect in panels c) and d) and $(100, 2.6)$ for the four domain wall self-annihilation in panels e) and f). Both the first and last mentioned fall into the class of cleaning mechanisms. All other points in the phase diagram belong to one of those three solutions.

Let us first focus on the first two, which are directly at a boundary between the two

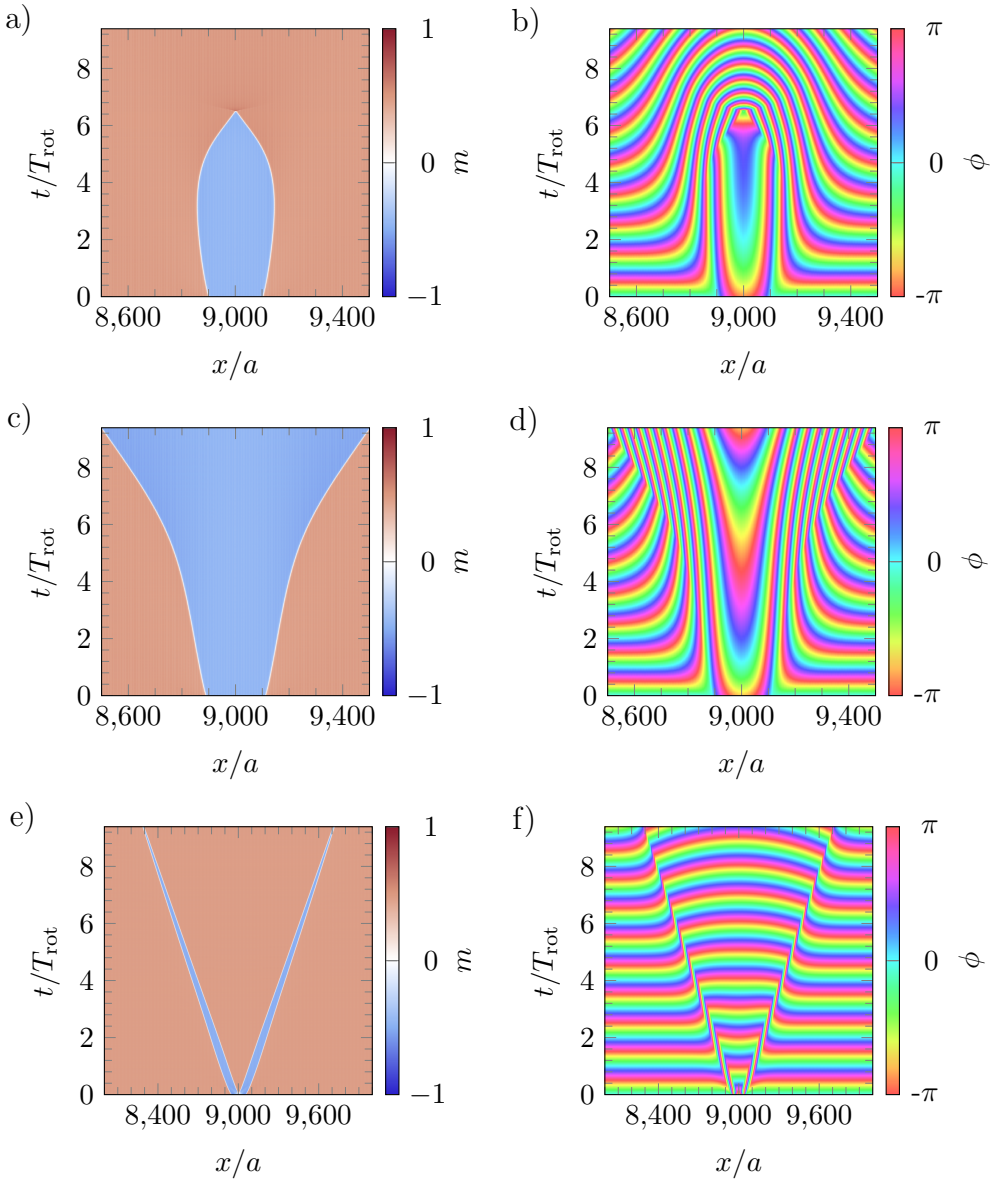

Figure 3.16: Simulation of an initially growing type II defect in the absence of thermal noise. The three initial states are given according to Eq. (3.53), which is visualised in Fig. (3.14). Afterwards, we track the evolution in time to measure if the defect manages to grow or if it annihilates. Within this figure, we show the three types of observed evolutions. Panels a) and b) show the magnetisation and phase for the shrinking domain at $(L_{\mathrm{init}}, s_{\mathrm{int}}) = (200, 0.4)$ in the phase diagram, Fig. 3.15. The domain starts moving outward at initial times but slows down and then shrinks for later times until the system is fully ordered. Panels c) and d) show the growing domain at $(220, 0.4)$, which picks up the final speed after approximately six rotations. The scenario is close to the previous scenario in the phase diagram but shows very different behaviour. Panels e) and f) are at $(100, 2.6)$ in the phase diagram and show another 'cleaning' mechanism. The initial slope is so large that the current pointing to the middle is large enough to flip the magnetisation, creating an up-domain inside the down-domain. The two outward-moving domains annihilate after roughly nine rotations. Parameters as in Fig. 3.1 for systems of 20,000 spins.

phases. The smaller of the two, Fig. 3.16(a,b), initially expands but then shrinks while building up a linear velocity, which is of the order of the usual velocity for the given parameters. At approximately $t = 6\,T_{\mathrm{rot}}$, the two domains meet and the ordered phase is recovered. For the slightly bigger one, Fig. 3.16(c,d), the domain grows and accelerates until it picks up the corresponding linear velocity after about $t = 6\,T_{\mathrm{rot}}$. To explain the shrinking of the smaller domains, we can again use the change in spin current, which is proportional to ϕ''. Since $\phi'' < 0$ inside the down-domain, spin currents flow to the centre of the domain. Therefore, the system favours an increase in magnetisation due to $\dot{m} \propto -\phi'' > 0$, which supports the shrinking of the down-domain and, thus, the recovery of the ordered phase. Since $\phi'' \propto \frac{1}{L\mathrm{init}}$ for our construction, the current is larger for small L_{init}. This is the reason why this mechanism is more efficient for smaller domains, which is in agreement with the numerical simulations.

Above a certain critical value of s_{int}, which depends on the value of L_{init}, another 'cleaning' mechanism takes over from the self-annihilation explained above: the four-domain domain-wall self-annihilation, see Fig. 3.16(e,f). Here, inward-pointing currents overcome the barrier to flip the magnetisation and create an up-domain inside the down-domain. All four domain walls move away from the centre, but each pair annihilates after $t \approx 9\,T_{\mathrm{rot}}$. Within the considered parameter regime, we have not observed any stable (non-annihilating) version of the four-domain wall process. However, even if this type stabilises under the influence of thermal fluctuations in certain parameter regimes, it is effectively the same as the creation of two type I defects which move in opposite directions.

Within this simplified approach of creating artificial type II defects, we found out that these are strongly suppressed via an effective, attractive force mediated by ϕ''. Additionally, type I defects show an efficient self-healing mechanism. Together, this explains the large correlation length of the driven system in comparison to the non-driven one.

3.6 Left and Right Movers

Within this section, we want to investigate if the moving domain walls created by thermal fluctuations undergo spontaneous symmetry breaking, i.e., if left- or right-moving domain walls dominate at a certain point in time. We have not yet observed clear evidence that this is the case. Only in Fig. 3.13b) can we notice that the peaks do not have equal height. However, this can also just be caused by a slight difference in the spatial distribution of the moving domain walls.

Nevertheless, we would like to investigate this with simulations from the effective

model, described in Eq. (2.43), with thermal fluctuations and finite driving $\iota \neq 0$. In this scenario, the driving term serves as an additional loss parameter since the domain walls move faster with increasing driving strength. I.e., collisions occur more frequently the larger ι gets compared to just the diffusive process from thermal fluctuations. On the other hand, we have thermal fluctuations, which can alter the magnetisation inside a domain, leading to the creation of two domain walls.
To identify domain walls, we have to use a filter due to the thermal fluctuations. The usual method of measuring the number of zero crossings in the raw data of m, as done for $T = 0$, does not work. As an initial filter, we use the digital filter method from the package DSP.jl [70]. The most common method is the Butterworth filter, which we use in fourth order with a lowpass filter, a cutoff frequency of $f_c = 1/10$, and a sampling frequency of $f = 1/300$. This choice eliminates small peaks on a local level but does not influence the general curve. An example of the non-driven system (with the highest domain wall density) is given in Fig. B.4 in the appendix. However, this initial filter is not sufficient to determine the domain walls. Therefore, we define a height cutoff h_c, so that every data point with $|m_i| > h_c$ is considered to be within a domain. On the other hand, every data point with $|m_i| < h_c$ is not part of a domain, i.e., it is part of the wall region. This simple approach might produce wall regions inside a domain. Thus, we correct this in the second step and identify wall regions that are inside a domain as part of the domain as well. Finally, we attribute the domain wall positions to the middle of each wall region. This gives us an estimate of the domain walls and their positions at a certain time. Doing this for many consecutive times gives an intuition of the direction of movement. This allows us to identify the left- and right-moving domain walls.
We choose the parameters in such a way that we get a sufficient amount of domain walls for the non-driven system, $\iota = 0$. Then, we repeat the measurement for several values of ι. The result is shown in Fig. 3.17, where panel a) shows the inverse domain wall density and panel b) the number of left- and right-moving domain walls. Each data point is averaged over five runs and multiple times in the stationary state. The two curves lie exactly on top of each other, within error bars. Thus, we conclude that there is no preferred direction and the domain walls created from thermal fluctuations move to the left and to the right at equal rates. We compare this to data extracted with the same parameters but larger system size and different cutoff h_c in Fig. B.5 in the appendix. The normalised curves are roughly identical. Naturally, we introduce a bias with the given filter. However, the bias should be the same for both types of moving domains.
The most simple ansatz to describe such loss and gain physics in the stationary state

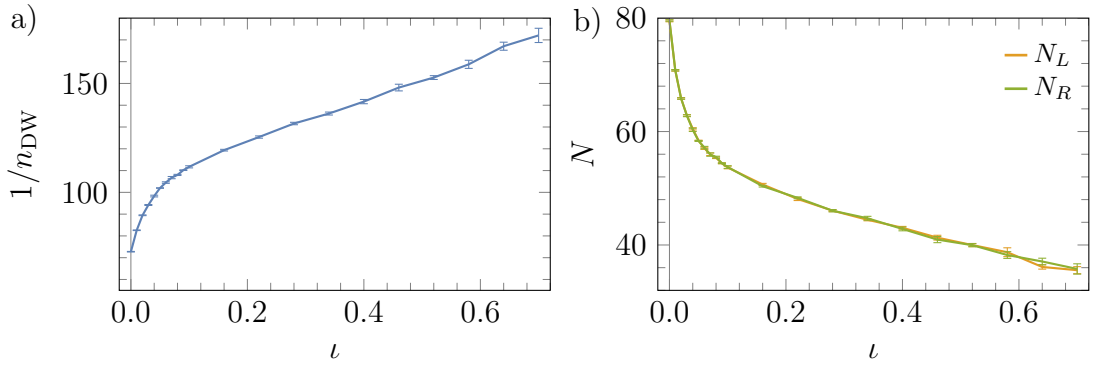

Figure 3.17: Number of domain walls and density, estimated as described in the text, deducted from simulations of the effective model. Panel a) shows the total inverse density. For large values of ι, the curve is approximately linear. Panel b) shows the number of left- and right-moving domain walls with N_L and N_R, respectively. The curves are identical within the error bars. Each data point is averaged over five runs and multiple times in the stationary state for a system of 15,000 sites. The error bars are the standard deviation of the mean. Parameters: $\alpha = 1, r = -0.1, u = 1, D_m = 1, D_\phi = 1, T = 0.01$ and $h_c = 0.15$.

is given by the following rate equation

$$\dot{n} = \Gamma_{\text{creation}} - \Gamma_{\text{annihilation}} = 0\,, \tag{3.54}$$

for the domain wall density. Γ_{creation} describes the creation rate of domain walls and $\Gamma_{\text{annihilation}}$ the annihilation of them. Since only the noise is capable of creating domains, the average creation rate is solely described by the noise, and thus constant for constant noise strength, $\Gamma_{\text{creation}} = \text{const.}$. Assuming that the loss rate is purely given by the driving part and supposing that only collisions of two domain walls exist, the average annihilation rate can be estimated as

$$\Gamma_{\text{annihilation}} \propto |v| n^2\,, \tag{3.55}$$

where v is the velocity of a single domain wall. Inserting this into the rate equations and solving for the density yields

$$n \propto \sqrt{\frac{\Gamma_{\text{creation}}}{|v|}}\,, \tag{3.56}$$

which scales like $n \propto \iota^{-1/4}$ for large enough driving strength. However, this simple argument cannot sufficiently describe the curves shown in Fig. 3.17. One explanation might be that the domain walls move faster with thermal fluctuations, as confirmed in Sec. 3.5.1. This effect is relatively stronger for smaller driving strength. Moreover, we neglected any interaction effects of noise and driving, as well as the influence of

noise on the annihilation rate.
While we could not give an analytical description, this section showed that there is no spontaneous symmetry breaking from moving domain walls created by thermal fluctuations.

3.7 The Localised Domain Wall

Above a critical driving field, the *localised* domain wall shows up. By this term, we characterise a domain wall which stays at the same position, i.e., does *not* move in the driven setup. We have already seen a glimpse of that in the velocity discussion in Fig. 3.2, where a drop to zero velocity signals this new behaviour. The rotation is still stable within this field ratio, i.e., ϕ rotates in opposite directions in up- and down-domains. Thus, we expect the dynamical frustration to show up and tension to build up at the centre of the domain wall. As the domain wall does not move, there must be another mechanism to lift this frustration. This section will investigate this very mechanism.
Fig. 3.18 shows the results of a microscopic simulation of a localised domain wall in a system with 40,000 spins and open boundary conditions. The domain wall at $x \approx 18{,}000\,a$ is far enough away from the boundary and thus, boundary effects are negligible. The initial state used consists of $\phi = 0$ and a sharp domain wall in m. Notice that this is an idealisation to isolate the main effects arising from the localised domain wall without spoiling them by influences such as slowly decaying phase gradients.
So much for the setup, but what happens to the localised domain wall under the effect of dynamical frustration? Let us have a closer look at the results. This time, we look at the phase first, see Fig. 3.18b). We can confirm that far away from the domain wall, the rotational frequency on the left and right sides is equal and opposite in orientation. The rotational speed is enhanced by $\sim 2\,\%$ compared to the value derived in Sec. 2.2, which arises due to the high field amplitude of $b_0 = 0.42$. At the centre, very close to the domain, we observe a region where the phase is constant in time. We can highlight this even more by using data which is averaged over a driving period, see Fig. 3.19.
From these simple observations, we can already deduce that there cannot be a smooth continuous solution of the phase, which connects the two regions consisting of a finite rotation in time and no rotation at all times. The discontinuities that show up as a consequence are also called space-time vortices [71]. To quantify this, the vorticity or winding number is a useful quantity. The simplest way of writing it

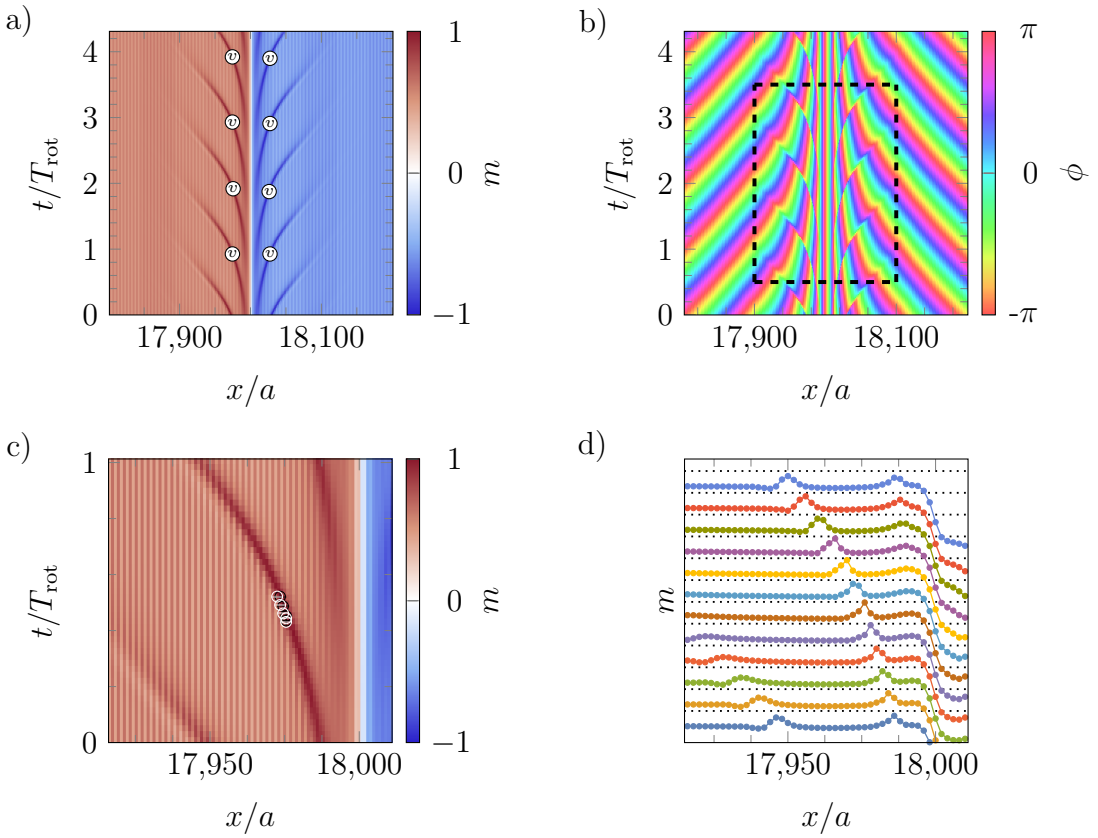

Figure 3.18: The localised domain wall which up at large driving amplitudes as a mechanism to lift the dynamical frustration. Panel a) shows m, where the vertical white line indicates the domain wall position. Instead of a moving domain wall, we observe the localised domain wall, which sends out pulses on the left and right sides at each rotation. Furthermore, space-time vortices, indicated with a v-symbol, show up wherever the pulses hit $m = 1$, indicated with a v-symbol on top of the pulses. Panel b) shows the phase ϕ. We observe a finite region around the domain wall where the phase does not rotate. Far away from the domain wall, the rotation frequency is equal and opposite. This explains why there is one vortex on each side per rotation period. Panel c) shows a zoom on a pulse from panel a). We find vortex-anti-vortex lines which have a total winding number of -1 for the up-down domain wall, and $+1$ for a down-up domain wall. Panel d) displays cuts from panel c) for $t = nT_{\mathrm{rot}}/12$, $n = 0, \ldots, 11$. For better visibility, the curves are shifted relative to each other by $1/8$. The black dotted lines serve as a guide, each corresponding to $m = 1$ for the curve below it. An example where the peak reaches $m = 1$ is at $x = 17{,}976\,a$ for the brown curve. This is the same location as the vortex-anti-vortex line in panel c). Parameters: $J = 1, \Delta = 0.8, \delta_2 = -0.6, \delta_4 = 1, g_1 = 1, g_2 = 0.1, \alpha = 0.1, B_0 = 0.42, \omega = 3.6$ with $T_{\mathrm{rot}} \approx 81$ for a system of 40,000 spins.

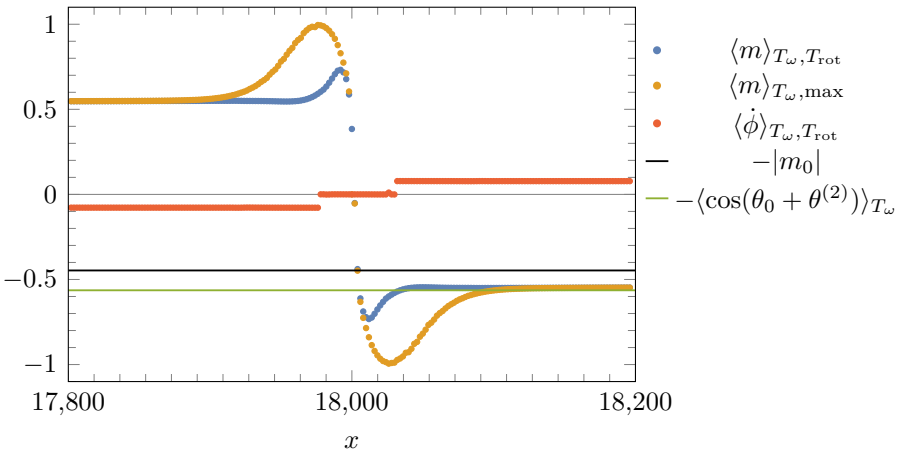

Figure 3.19: In contrast to most other figures, we show data averaged over the driving period, where we collected ten points per period. $\langle m\rangle_{T_\omega,T_{\rm rot}}$ is the time-independent profile, where we additionally averaged over one rotation period to remove the pulses. We compare the value away from the wall to our perturbative constant correction from the second-order calculation from Sec. 2.2, which becomes clearly visible. The deviation is roughly $\sim 2.5\%$. Close to the domain wall, the curve shows a peak. The averaged $\dot{\phi}$ is zero in the middle region between the vortices and jumps to a constant rotation value, $\sim \pm\omega_{\rm rot}$, to the left and right of the region. Comparing to the maximum in each rotation period $\langle m\rangle_{T_\omega,\max}$, we find another confirmation that the vortices appear when $m = 1$. Parameters as in Fig. 3.18.

down is in integral form

$$W = \frac{1}{2\pi}\oint_C \mathrm{d}\boldsymbol{l}\boldsymbol{\nabla}_l\phi\,, \tag{3.57}$$

with $\boldsymbol{l} = (t, x)$, $\boldsymbol{\nabla}_l = (\partial_t, \partial_x)$ where C is a closed loop in space-time, e.g., the dashed box in the figure. To find the exact position of the vortices, we determine the local winding number, which is given by the sum over the finite differences of four neighbouring sites. This alone does not yet match the integral representation, which translates to the smallest finite difference of the periodic phase between the sites. In order to account for that, we project each finite difference onto the interval of $[-\pi, \pi]$ before summing them up and dividing by 2π. The resulting winding numbers have one of the following three values $(-1, 0, 1)$, which stand for an anti-vortex, no vortex and a vortex, respectively. We calculate this quantity for the shown interval in Fig. 3.18b) and find vortex-anti-vortex lines, which occur every oscillation period $T_{\rm rot}$. The total vorticity of the lines is -1 in the shown case for an up-down domain wall and would be $+1$ for down-up domain walls. It is fixed by the topology. Each rotation period, one vortex has to be nucleated to compensate for the dynamical frustration. The different values for the two domain wall types show up due to the opposite sense of rotation on the left and right sides.

Next, we look at the magnetisation shown in Fig. 3.18a), where we mark the location

of the vortex-anti-vortex lines with a v-like symbol approximately in the middle of the line. Notice that two pulses on each side are emitted each rotation period close to the centre of the domain wall. These pulses move away from the centre, initially increasing until the maximum value of $m = 1$. Here, the full strength of the saturation magnetisation is reached, and the phase ϕ becomes ill-defined. This is the point where a discontinuity in ϕ can take place. And indeed, the vortex-anti-vortex lines sit exactly on the pulses shown in Fig. 3.18c), where the maximum in the magnetisation is reached. This turns out to be in an interval and not just at a single point in time. After this vortex region, the pulse decreases again and moves with a roughly constant velocity until it decays to zero. Fig. 3.18d) shows cuts from Fig. 3.18c), which are shifted vertically relative to each other for better visibility. The dotted lines correspond to the point where $m = 1$. At roughly $x = 17{,}976\,a$, the brown curve hits $m = 1$, which is exactly the region of the space-time vortices. Additionally, we show data averaged over a driving period T_ω and then also over a rotation period T_{rot} in Fig. 3.19, where the average over the rotation period was used to eliminate contributions from the pulses. We find the stationary m-profile to be different to the usual domain wall with peaks close to the centre. Furthermore, we show that the maximum in m is reached where the averaged $\dot{\phi}$ jumps, i.e., at the location of the vortex region. Moreover, we compare the domain value of m to our perturbative second-order correction, which becomes relevant (larger) at high enough driving fields. Similar to the rotation speed, the value deviates by about $\sim 2.5\%$.

Overall, we have uncovered the second mechanism to remove dynamical frustration. This consists of pulses in the magnetisation, which reach the maximum value of $m = 1$, accompanied by space-time vortices in the phase. We remark that this mechanism cannot be described by the effective theory, where the unique point of $m = 1$ does not exist.

4

Active Domain Walls in Two Dimensions

This chapter explores the nature of the active domain walls in two spatial dimensions. We want to utilise the knowledge gained about the one-dimensional domain walls in the previous chapter and compare the results. One main difference is that domain walls in two spatial dimensions can move even in the non-driven system at $T = 0$, known as coarsening. Another difference is that, due to the additional spatial dimension, not only can space-time vortices exist, but space-space vortices are also possible.

First, we recall the coarsening arguments known for the Ginzburg Landau theory in two dimensions. This is followed by studying the coarsening dynamics in the non-driven ferrimagnet via instantaneous quenches to zero and (high) subcritical temperature. The coupling to the staggered xy-order is observed to alter the expected coarsening exponent from the Ising type for a quench to $T = 0$.

A discussion on the coarsening in the driven ferrimagnet at $T = 0$ reveals the characteristic linear growth of correlation length. Afterwards, we provide a concise discussion of the shift to the position of the phase transition resulting from the driving. The ordered region extends to higher temperatures with increasing driving strength. A brief revision of type II defects in two dimensions gives one possible explanation for the shift.

The driven ferrimagnet at subcritical temperatures divides into two distinct parts. One behaves very similarly to the $T = 0$ quenches, and the other is solely ordered due to driving. This is followed by applying the Kibble-Zurek mechanism to the non-driven ferrimagnet, from which we conclude that the model belongs to the Ising class. After, we apply the mechanism to the driven ferrimagnet, where we cannot make a conclusive statement.

Finally, we briefly overview the different vortex dynamics in the two models without thermal fluctuations.

4.1 Coarsening in the Ginzburg Landau Theory

In one dimension without thermal fluctuations, a domain wall is stable and stationary within the Ginzburg Landau theory, see Sec. 1.6. Moreover, the energy cost of a domain wall is independent of system size. This changes in higher dimensions $d > 1$ since $\Delta F_{\text{wall}} \sim L^{d-1}$ and the ordered phase becomes stable for small but finite temperatures. A simple structure in two dimensions, which is smooth in space analogous to the one-dimensional domain wall in one dimension, is a circular domain wall, visualised in Fig. 4.1a). Starting with this structure, we want to understand how the increase in spatial dimension influences the dynamics of domain walls. The discussion about the circular domain wall is based on [72].
Due to the circular symmetry, the dependence of the magnetisation in space is only radial. We assume that without thermal fluctuations, $T = 0$, this symmetry always exists. Since we used r for the control parameter of the effective model, we denote the radial distance by ρ, i.e., $m(\boldsymbol{x}, t) = m(\rho, t)$. The equation of motion $\alpha \dot{m} = -\frac{\delta F}{\delta m}$ with $F[m(x)]$ given by Eq. (1.20) expands to

$$\alpha \dot{m} = -rm - um^3 + D_m \left(\partial_\rho^2 + \frac{1}{\rho} \partial_\rho \right) m \,, \tag{4.1}$$

where the last term on the RHS arises from the two-dimensional nature of the problem.
After all, we want to analyse the dynamics of this structure, which we assume to carry the circular symmetry, as well. We use the explicit ansatz

$$m(\rho, t) = m(\rho - R(t)) \,, \tag{4.2}$$

where $R(t) \gg \xi_0$ is the radius of the circular domain wall at time t and ξ_0 is the width. Inserting this into the equation of motion above yields

$$0 = -rm - um^3 + D_m \partial_\rho^2 m + \left(\frac{D_m}{\rho} + \alpha \dot{R} \right) \partial_\rho m \,. \tag{4.3}$$

To simplify this equation, we use a common trick. We multiply the equation with $\partial_\rho m$ and integrate over a region far away from the domain wall centre, i.e., $|x| \gtrsim \xi_0$. Here, we use that $m(|x| \gtrsim \xi_0) = m_0$ and $m'(|x| \gtrsim \xi_0) = 0$ sufficiently far from the centre of the domain wall. Therefore, the first three terms vanish under the integral, and we are left with

$$0 = \int_{|x| \geq \xi} \left(\frac{D_m}{\rho} + \alpha \dot{R} \right) (\partial_\rho m)^2 \,. \tag{4.4}$$

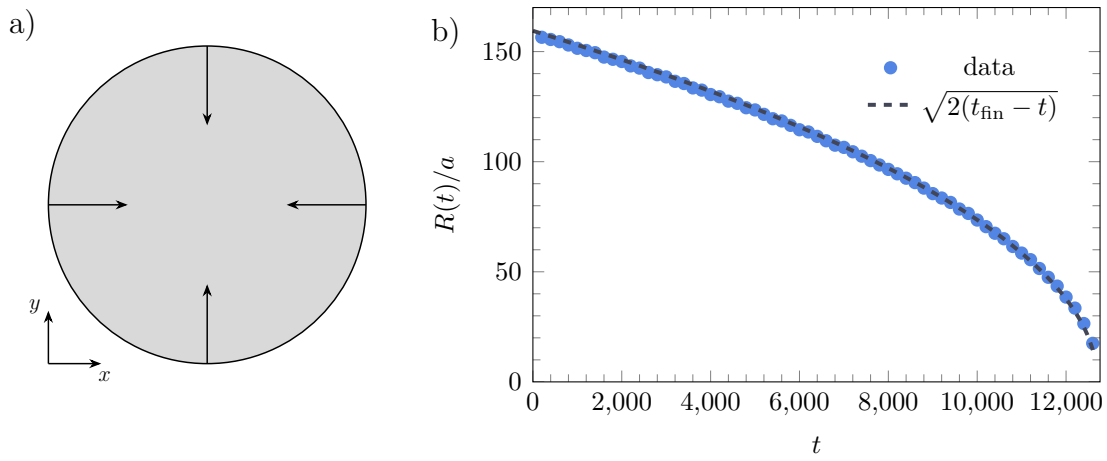

Figure 4.1: Panel a) illustrates a circular domain where the equal arrows indicate the shrinking direction and that the force on each point is the same. Panel b) compares data taken from simulations of a circular domain wall as shown in Panel a) using the time-dependent Ginzburg-Landau model for $D_m = 1$, $\alpha = 1$ to the analytical prediction given by Eq. (4.6). The agreement is excellent, validating that the exact form of the domain wall is not crucial and is entered only via small corrections.

To solve this, we make one more assumption, which is that the width of the domain wall is small compared to other length scales in the problem, i.e., the change of the magnetisation in space is approximately given by $m' \propto \delta(\rho - R)$. Using this inside of the integral in Eq. (4.4), yields

$$\dot{R} = -\frac{D_m}{\alpha R}\,. \tag{4.5}$$

This is in contrast to one dimension, as the circular domain wall is dynamic even in the non-driven case. In particular, it shrinks over time with increasing velocity. The decisive factor of the motion is the curvature in two dimensions, $\kappa = \frac{1}{R}$. In arbitrary dimensions $d \geq 2$, there is a prefactor in front of the LHS given by $(d-1)$. The solution of $R(t)$ for Eq. (4.5) is given by

$$R = \sqrt{2\frac{D_m}{\alpha}\,(t_{\text{fin}} - t)}. \tag{4.6}$$

From this equation, we can deduce directly that a circle of size $R(0) = R_0$ will vanish after a time $t_{\text{fin}} = \frac{\alpha R_0^2}{2D_m}$ so that $R(t \geq t_{\text{fin}}) = 0$ in agreement with power counting of Eq. (4.5). Fig. 4.1b) shows this theoretical prediction with numerical data. The agreement turns out very well.

We learned here that the simple structure of a circular domain wall always shrinks with respect to its curvature $\kappa = \frac{1}{R}$ in two dimensions for the Ginzburg Landau theory. This argument can be extended to an arbitrarily curved domain wall and

was derived by Allen and Cahn [73]. We will briefly discuss it here. To do so, we define $\hat{\boldsymbol{g}}$ as the unit vector normal to the domain wall in the direction of increasing m. We make the same assumption as before, i.e., that the dominating change happens exactly at the domain wall, and all other contributions can be neglected. Then, we can write the spatial derivatives as the directional derivative of m in the direction of $\hat{\boldsymbol{g}}$. Thus, $\nabla m = \frac{\partial m}{\partial g}\hat{\boldsymbol{g}}$ and $\nabla^2 m = \frac{\partial^2 m}{\partial g^2} + \frac{\partial m}{\partial g}\nabla \cdot \hat{\boldsymbol{g}}$, where $\frac{\partial}{\partial g}$ denotes the directional derivative in the direction of $\hat{\boldsymbol{g}}$. Additionally, we can write the time derivative as $\frac{\partial m}{\partial t} = -\frac{\partial m}{\partial g}\dot{g}$, where $\dot{g}$ is the velocity of the domain wall in the direction of increasing m. Plugging these relations into the equation of motion and using the same integral trick as before gives

$$\dot{g} = -\frac{D_m}{\alpha}\nabla \cdot \hat{\boldsymbol{g}}\,, \tag{4.7}$$

where the divergence of $\hat{\boldsymbol{g}}$ is nothing but the local curvature κ. Notice that for a circular domain, the expression is the same as above. It is important to note that the exact shape of the domain wall was not included in the discussion. Additionally, the velocity and its direction are purely given by the local curvature in the limit where the principal radii of the curvature are large compared to the wall thickness. The arguments above are only valid in a system where the scalar order parameter is not conserved, which is already encoded in the equation of motion, Eq. (4.1).
This effect of domain growth falls under the general topic of *coarsening*, also called ageing, of the system [74, 75]. Consider a rapid quench into the ordered phase, where after a short time, domains of the two phases form and a domain mosaic emerges. Since each domain is roughly at local equilibrium, the ordering kinetics is mostly described by the curvature-driven movement of domain walls. Larger curvature corresponds to less coarse domain walls, which move faster than more coarse walls. Thus, the structure becomes smoother, and one of the two phases grows, which increases the order and, consequently, the correlation length. However, the time needed for the system to order fully diverges with system size.
For late times, the dynamical scaling hypothesis holds and states that a single length-scale characterises the system, given by

$$R(t) \propto t^{\frac{1}{z_d}}\,, \tag{4.8}$$

which carries the time dependence, and z_d is a dynamical exponent that depends on the dynamics of the system. Relating this to the discussion above, we can find the dynamical exponent for the Ising class as $z_d = 2$ [76]. Notice that the exponent is, in general, different to the dynamical critical exponent, which is $z_{\text{eq}} \approx 2.17$ for the Ising model in two dimensions [77]. A fascinating study on the influence of long-range interaction on the coarsening dynamics in the long-range Ising model can be

found in [78].
Since only one characteristic length scale is involved, the system looks self-similar if length is scaled by $R(t)$. A direct consequence of this fact is that the equal-time correlation function can be written in the scaling form

$$C(\boldsymbol{x}, t) = f\left(\frac{x}{R(t)}\right). \tag{4.9}$$

A more experimentally accessible quantity is the Fourier transform of the equal-time correlation function, namely the structure factor, which has the scaling form

$$S(\boldsymbol{k}, t) = R(t)^2 g(kR(t)), \tag{4.10}$$

in two dimensions. Where f and g are scaling functions. This allows to estimate the dynamical exponent z_d and, with that, the scaling of the characteristic length scale $R(t)$ from a scaling plot of either $C(\boldsymbol{x}, t)$ or $S(\boldsymbol{k}, t)$ following the above expressions. Since the correlations are directly accessible to us, we will use this quantity in the following.
This type of scaling can also be applied to systems where the order parameter is conserved. The analogous equation to the time-dependent Ginzburg Landau equation is the Cahn-Hiliard equation for a scalar conserved order parameter, which then follows the theory by Lifshitz-Slyozov [79] with an exponent of $z_d = 3$ [75], which has been confirmed in the conserved Ising case [80].
The concept of dynamical scaling is very general, and thus coarsening is found in many different areas including, e.g., fluid dynamics [81], ferromagnetic condensates [82] and active matter systems [83].
In the following, we want to study the coarsening dynamics of the ferrimagnet, starting with the non-driven scenario. This is notable because, unlike the Ising class described above, the ferrimagnetic model also exhibits the staggered xy-order, which couples to the magnetisation in the z-direction.

4.2 Coarsening in the Non-Driven Ferrimagnet

A good strategy to study coarsening in a system is a quench from a disordered phase to an ordered one. Remember that we used this already in the one-dimensional case to study how order builds up in the *driven* system, Sec. 3.4. Again, we rely on an instantaneous quench so that there is no dependence on the exact protocol, and we can concentrate purely on the ordering dynamics. We make use of the same initial state with $\phi = 0$ and m randomly distributed in $(-0.1, 0.1)$, but now extended to two spatial dimensions. This corresponds to a state where ϕ is already in the ordered

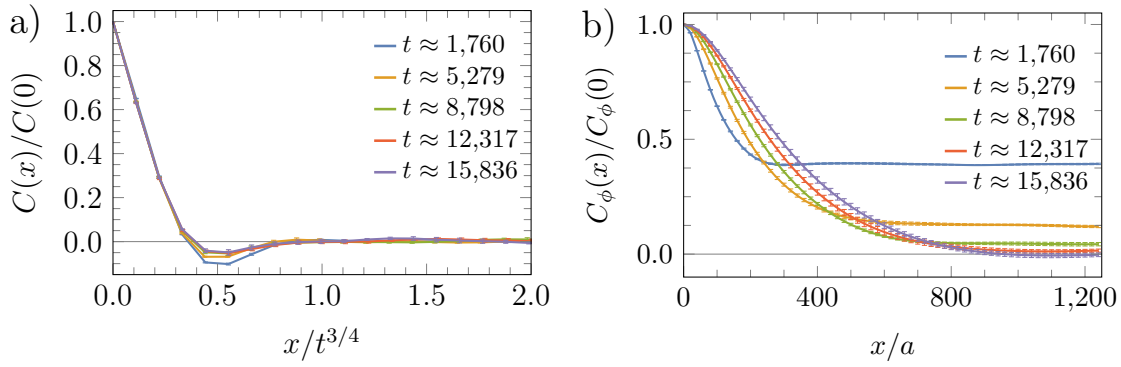

Figure 4.2: Panel a) shows the equal-time correlations of m for different times from a quench to $T = 0$ in a system of $10{,}000 \times 10{,}000$ sites. Each curve is averaged over five initial conditions. The spatial axis is scaled by $t^{3/4}$, which leads to a convincing data collapse of the curves. The small dip at $x \approx 0.5\, t^{3/4}$ decreases initially but saturates for later times. This coarsening exponent differs from the Ising exponent ($t^{1/2}$) arising from the long-range interactions through ϕ. Panel b) shows the ϕ-correlations, Eq. (4.12), for the same data. The initial state was completely ordered in ϕ. However, the correlations decrease over time, and the correlation length becomes finite. Parameters: $J = 1, \Delta = 0.8, \alpha = 0.1, \delta_2 = -1.2, \delta_4 = 2, b_0 = 0$.

phase, and we cross only the transition of the magnetisation in z-direction, where m becomes finite and ϕ starts to precess. Thus, as in the previous chapter, we do not expect effects from vortices in the chosen parameter regime. In fact, we have not observed any vortices in the data displayed in this section.

As earlier, we will use the correlation function as a measure. Within a scaling plot, we can then capture the time dependence of the characteristic length scale $R(t)$. As it is now two-dimensional, the correlations are calculated via

$$C(x) = \frac{1}{2}\langle m_{i+x,j} m_{i,j} + m_{i,j+x} m_{i,j} \rangle \,, \tag{4.11}$$

where $\langle \dots \rangle$ denotes an average over all even or odd sites i, j. Notice that this includes the assumption that a distance in the i direction is the same as in the j direction. Throughout this study, we have not observed a sizeable difference between the two, hence the above definition.

A plot of the normalised correlations for a system of $10{,}000 \times 10{,}000$ spins is shown for five different times after a quench in Fig. 4.2a). The negative dip at around $x \approx 0.5\, t^{\frac{3}{4}}$ decreases for earlier times but saturates to the same value for the last two times shown. The estimated errors from the five simulations presented above are of the order of the line width.

The coarsening exponent, which we read off from this scaling plot, is $z_d \approx \frac{4}{3}$ within the accuracy of the simulations. We used the interval before $C(x)$ hits zero for the first time to scale the curves on top of each other. The exponent is smaller than

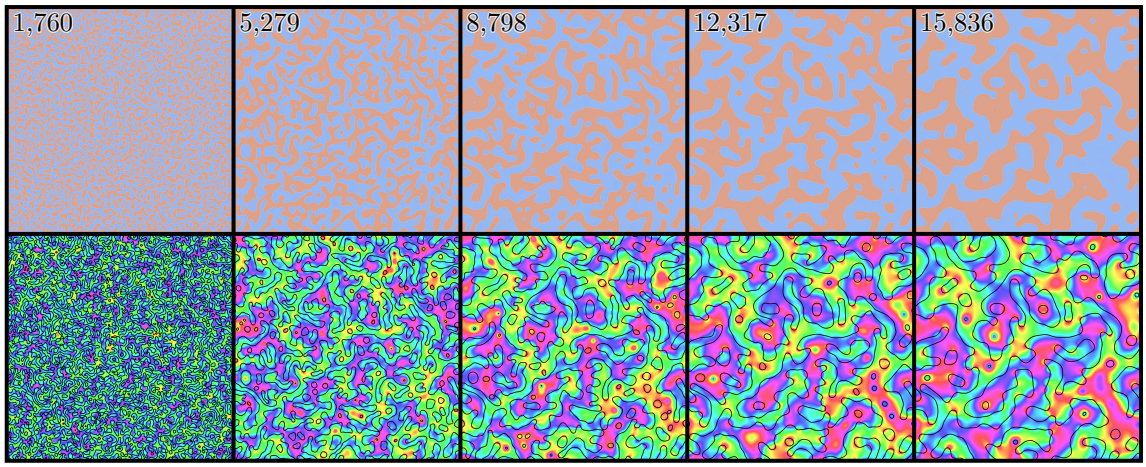

Figure 4.3: Snapshots form one simulation of a quench to $T = 0$. The top row shows the magnetisation in z-direction m, and the bottom row shows the staggered xy-order with the domain walls displayed as a top layer. The numbers in the upper right corner denote the time. While the snapshots of m do not show any noticeable feature different to coarsening in the Ising model, the snapshots in ϕ do. Gradient structures from the initial times freeze in, and additional gradients are produced near domain walls. These gradients feedback to m and give rise to the change in the coarsening exponent. Parameters as in Fig. 4.2.

the Ising class exponent of $z_d = 2$, i.e., the dynamics are faster in the ferrimagnet. A fundamental difference of the ferrimagnet compared to the Ising model is the coupling to the staggered xy-order ϕ. To get an intuition on how the coupling influences the domain wall dynamics, we show snapshots of one simulation in Fig. 4.3 for the same times as the correlation curves. To save space, the colour bars, which are the same for every snapshot, are omitted, but we use the same as before and after, see, e.g., Fig. 4.5. The top row in Fig. 4.3 shows m, and the bottom row shows ϕ where we additionally display the positions of the domain walls as black lines on top. These are simply determined by the locations where $m = 0$. The magnetisation exhibits the characteristic structure of curved domain walls, which shrink with respect to their curvature. These snapshots are indistinguishable from the Ising class without tracking their velocity. However, the staggered xy-order shows interesting features. One of them is that we can roughly read off the domain values of m, i.e., if it is an up- or down-domain, from the ϕ plots. This results from the fact that we start with a state which is completely ordered in ϕ. At initial times, $\dot{\phi} \propto \dot{m}$ because the gradients vanish, and thus, similar domains emerge in ϕ. Again, these structures slowly decay on a time scale much larger than the change in the domain wall profile. And therefore, they influences the domain walls throughout the coarsening process.

Another feature is that finite but small gradients build up behind moving walls. Even though those are small compared to the previously discussed driven one-dimensional

case (and as we will see later to the driven two-dimensional one), we know that any finite difference in ϕ does impose a spin current on m. The difference of those at the domain walls directly influence their velocity. The steepest slopes emerging from this effect are near the domain walls with the greatest curvature, which move the fastest. Notice that sections where the walls are approximately straight do barely move.

Even though we cannot pinpoint the exact mechanism responsible for the change in the coarsening exponent, we can infer that it is caused by a feedback effect from the two stated features in ϕ onto the domain walls in m.

For completeness, we also determine the correlations in the staggered xy-order given by

$$\begin{aligned} C_\phi(x) &= \frac{1}{2}\langle m^x_{i,j} m^x_{i+x,j} + m^x_{i,j} m^x_{i,j+x} + m^y_{i,j} m^y_{i+x,j} + m^y_{i,j} m^y_{i,j+x} \rangle \\ &= \frac{1}{2}\Big\langle \sqrt{1-m^2_{i,j}}\sqrt{1-m^2_{i+x,j}}\cos(\phi_{i,j}-\phi_{i+x,j}) \\ &\quad + \sqrt{1-m^2_{i,j}}\sqrt{1-m^2_{i,j+x}}\cos(\phi_{i,j}-\phi_{i,j+x})\Big\rangle , \end{aligned} \tag{4.12}$$

where m^x and m^y denote the magnetisation in x- and y-direction, respectively. Remember that we denote the magnetisation in z-direction simply by m. We call this also the ϕ-correlations, however, one should not confuse it with the ϕ-autocorrelations. The advantage of the cosine is that jumps of 2π in the angle are naturally taken into account. Fig. 4.2b) shows the correlations for the same data as the m-correlations. The initial state is fully ordered in ϕ, and we see that with time the correlation length becomes finite due to the approximate freeze in and build-up of gradients in ϕ from the domain walls. Compared to the magnetisation, correlations change in time much slower after the initial drop.

An example from literature where a structural feature alters the coarsening exponent for the special case of a quench to $T = 0$ is the three-dimensional Ising model, where sponge-like structures freeze in during the coarsening process. In contrast, the two-dimensional case shows the predicted Ising class exponent even for a quench to $T = 0$ [84]. There is an ongoing debate regarding the exact nature of the coarsening exponent for the three-dimensional model, but the latest study with large-scale simulations suggests super-diffusive scaling $z_d < 2$[85]. This behaviour is neither observed in the corresponding time-dependent Ginzburg Landau equation [86], nor for a quench to finite (high) subcritical temperatures $T < T_c$ [87], nor in experiments with Cu_3Au [88]. The term (high) subcritical temperature describes temperatures not close to zero but still below the critical temperature. In all these cases, values like or close to the theoretically predicted $z_d = 2$ exponent were reported. Thus characterising it as a unique behaviour for quenches to $T = 0$ and temperatures

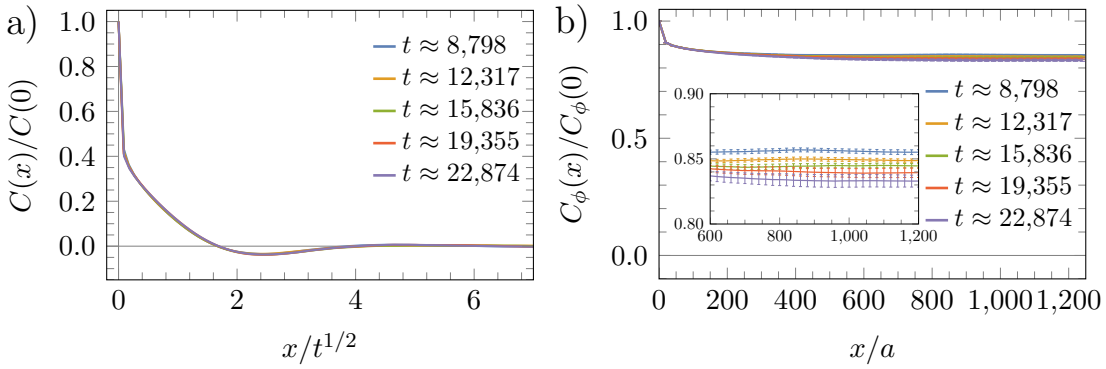

Figure 4.4: Panel a) shows the equal-time correlations for m for a quench to temperature $T_f =$ for 10 initial conditions and 2,500 × 2,500 sites. The scaling of distance with $t^{1/2}$ results in a collapse for all times. Thus, a quench to (high) subcritical temperatures falls into the Ising class for coarsening dynamics in contrast to the quench to $T = 0$. Panel b) shows the correlations in ϕ, Eq. (4.12), for the same data. The system stays completely ordered, and there is only a small decrease in the plateau value with time, as shown in the inset. Therefore, ϕ is approximately constant and does not affect the ordering dynamics in m. Parameters as in Fig. 4.2 but with $T_f = 0.1077$.

close to this value. Here, we have found a similar case where structures form that alter the dynamics.

Notice that there is one additional difference to the model of the ferrimagnet. The xy-order can show a temperature-dependent exponent as found in the XY-model, nicely explained in [89]. For a conclusive argument, one needs extensive numerical simulations to determine the exponent for many different temperatures in the range $0 < T < T_c$. This is out of the scope of this study, and we rather follow the example of the three-dimensional Ising model, i.e., we study the scaling of the non-driven ferrimagnet at a (high) subcritical temperature in the following subsection.

4.2.1 Coarsening Under Thermal Fluctuations

The different coarsening exponent, as compared to the Ising model at $T = 0$, results from gradients in the xy-order between the domain walls and the resulting feedback effect on m. Unlike in the driven system, these gradients are not strongly protected by the active domain wall propulsion or similar effects. Thus, the gradients might vanish at (high) subcritical temperatures. A brief discussion on the influence of the drive on the phase transition will be discussed later in Sec. 4.5 where we roughly estimate $T_c \approx 0.1111$ in the non-driven case.

The strategy stays the same as above, but instead of a quench to $T = 0$, it is now up to a finite temperature below T_c. The correlations of m for ten initial conditions with 2,500 × 2,500 sites and similar time scales as before are shown in Fig. 4.4a) for a final temperature of $T_f = 0.1077$. We observe a clear scaling with $z_d = 2$

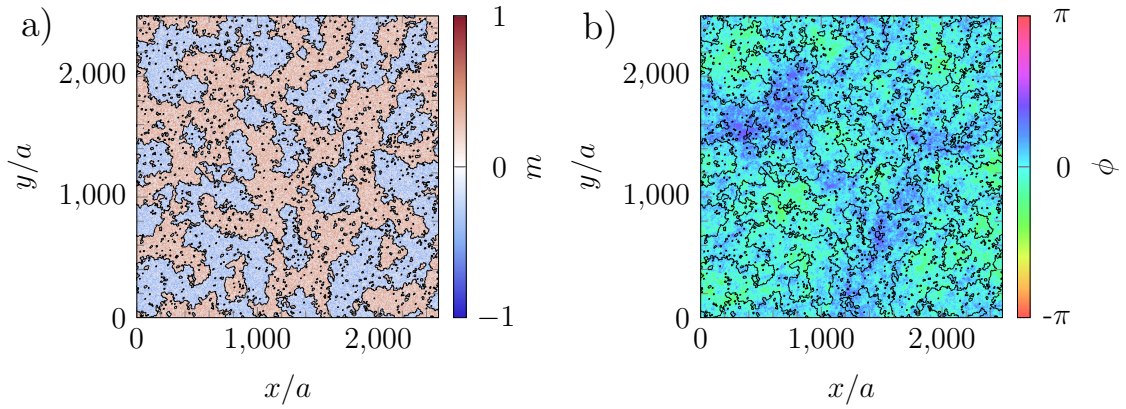

Figure 4.5: Snapshots from one simulation of a quench to $T_f < T_c$ at time $t \approx 12317$. Panel a) shows m with the domain walls displayed as black lines on top. Those were determined by a majority filter explained in the text. Thermal fluctuations lead to the generation of domains and the roughening of the domain walls. Panel b) shows ϕ for the same data, where we also show the domain walls as a top layer. The value of ϕ is approximately constant throughout the system, and there is no noticeable connection to the domain walls. Parameters as in Fig. 4.4.

where all curves fall exactly on each other. Again, the error is of the line width size and thus omitted. The scaling and the form changed. On short-scaled length, the correlations drop quickly, as expected, due to the thermal fluctuations. Only after this drop does a slower tail over several length scales arise. In fact, at (high) subcritical temperature, the exponent reverts to the expected coarsening exponent for the Ising class. The thermal fluctuations destroy the build-up of the slope in ϕ, which makes it irrelevant to the dynamics. Thus, the coarsening is, up to small corrections, purely characterised by the curvature of the domain walls.

This observation can also be seen in the ϕ-correlations shown in Fig. 4.4b). The system stays completely ordered in ϕ, building a constant plateau in the correlations. The inset shows that the plateau value decreases slowly with time while error bars increase. We do, however, expect that the plateau saturates and the system stays very ordered in ϕ with a correlation length exceeding the system size.

One possible cause for the different behaviour at finite temperatures could be free vortices in the staggered xy-order, which arise at high enough temperatures for the vortex anti-vortex unbinding [24, 25]. However, within the range of parameters we are looking at, this transition is at higher temperatures than the transition in m. Thus, we are not surprised that we do not find any free vortices in our simulations.

Snapshots for the time $t \approx 12317$ are shown in Fig. 4.5. Similar to the simulations for $T = 0$, we determined the position of domain walls and displayed them as a top layer. Due to the thermal fluctuations, this is not as trivial as before. To solve this issue, we apply a simple filter. In each application, the filter considers the neigh-

bouring values of each site and conducts a majority vote. If the majority is in the up-state, the average value of the neighbouring up-sites is assigned. Similarly, it assigns the average value of the neighbouring down-sites in case of a down majority. In case of a tie, the value remains unchanged. For the data shown, five iterations of the filter were sufficient to achieve a decent result. Fig. 4.5a) shows the determined domain walls on top of the magnetisation data with excellent agreement. There might be false detections on the scale of tiny domains, but these are irrelevant at larger scales.
In comparison to before, ϕ shown in Fig. 4.5b) has an almost constant value up to small slopes of the order of $\sim 10^{-3}$. The variance around it is small and approximately given by $\sim \frac{1}{2\pi}$. In addition, there is no strong visible dependence on domain wall positions. Therefore, we conclude that ϕ does not affect the coarsening dynamics at finite (high) subcritical temperatures. The two features observed for a quench to $T = 0$ are strongly suppressed.
We can confirm that the coarsening significantly differs for $T = 0$ and (high) subcritical temperatures. However, more extensive simulations are needed to determine whether there is a crossover with a smooth change between the different exponents or a sudden jump.
These findings will be relevant later in the section about the Kibble-Zurek mechanism, Sec. 4.8, where we will also observe $z_d \approx 2$ for slow protocols.

4.3 Parameter Choice and Changes for the Driven Ferrimagnet in Two Dimensions

Before we begin the study of the driven system, we want to consider reasonable parameter choices which might allow for a comparison with the one-dimensional case. For this think of a *straight* domain wall in two dimensions which is parallel to the y-axis. In the absence of thermal fluctuations the derivative in this direction drops out and the solution is quasi one-dimensional. Thus, we expect the wall to move in the direction perpendicular to y, parallel to the x-axis. The velocity should then be approximately given by Eq. (3.7) which is mostly determined by the rotational speed Eq. (2.11) for not too small values of the driving amplitude. But we cannot just use the same parameters as in the one-dimensional case. Due to the dimension-dependent shift in the value of the spin/magnetisation, Eq. (2.4), the transition in m shifts with respect to the spatial dimension, in particular with the number of couplings on the hypercube. Here, one has to make a choice as of which parameter set to adjust so that the straight two-dimensional domain wall has the same speed and domain value as its one-dimensional analogue. The simplest way

would be to absorb the dimension into the interaction strength J. However, our argument against this choice is that J is a natural way to set a scale. Thus, we take a different approach and adjust the parameters according to the following rules:

- $\delta_2^{2D} = 2 \cdot \delta_2^{1D}$ and $\delta_4^{2D} = 2 \cdot \delta_4^{1D}$ so that $m_0^{2D} = m_0^{1D}$
- $\omega^{2D} = 2 \cdot \omega^{1D}$ and $b_0^{2D} = \sqrt{2} \cdot b_0^{1D}$ so that $|\omega_{\mathrm{rot}}^{2D}| = |\omega_{\mathrm{rot}}^{1D}|$

While this choice nicely sets the two most important quantities for us to the same values as in the one-dimensional scenario, one characteristic quantity of the domain wall changes. The equilibrium domain wall width becomes $\xi_0^{2D} = \frac{\xi_0^{1D}}{\sqrt{2}}$ for the straight domain wall in two dimensions. For the velocity regime we will be looking at, this correction does not play a role. In addition, most of the coarsening physics does not depend on the exact shape of the domain wall, i.e, this correction to the width will only give rise to a small correction.
In fact, we have observed stripe solutions in simulations of smaller systems where the quench simulations were performed as long as needed to arrive at a stationary state. This state was the fully ordered state in most of the cases. However, in rare situations we would find a stripe characterised by two straight parallel domain walls. An example is shown in Fig. C.1 in the appendix. This also takes place throughout coarsening of the Ising model. In particular, $\frac{1}{3}$ of the final states in the two-dimensional Ising model were found to be a stripe state [90, 91].
We compared the velocity of these stripes with the corresponding one-dimensional velocity following the above rules with excellent agreement. Thus, we will stick with this choice of parameters in the following. This gives us the opportunity to compare to the corresponding one-dimensional velocity, Fig. 3.2.

4.4 Coarsening in the Driven Ferrimagnet

After setting the parameters in the previous section, we can start studying the driven ferrimagnet at $T = 0$, particularly its coarsening dynamics with an instantaneous quench. However, similar to the one-dimensional case, see Fig. 3.8, there is a certain number of rotations needed until the final long-time dynamics sets in, ~ 20 rotations. This is the time needed for the domain walls to pick up the corresponding speed. While it was numerically feasible to go for up to $t \approx 256\, T_{\mathrm{rot}}$ in one dimension, this is not the case in higher dimensions. The effective simulation costs scale with the number of sites. Thus, the effective length a domain wall can travel before going through the system decreases greatly when the dimensions are increased while keeping the number of sites fixed. In case of the one-dimensional discussion in Sec. 3.4 simulations with 500,000 and $v \approx 0.1226$ and $T_{\mathrm{rot}} \approx 612$ were performed.

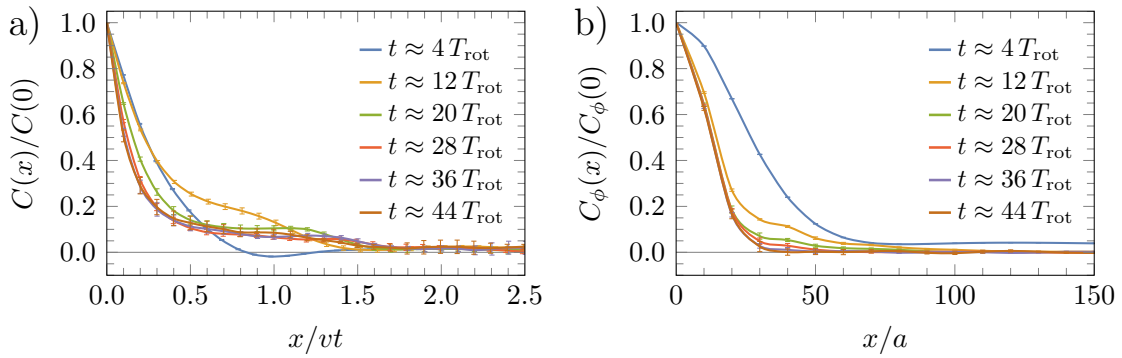

Figure 4.6: Panel a) shows the scaling plot of the equal-time correlations of the magnetisation in z-direction m for a system of 10,000 × 10,000 sites averaged over five initial configurations after a quench to $T = 0$. The scaling is linear in time, where the scaling factor is given by the velocity of a straight domain wall $v \approx 0.163$. In the long-time limit, the curves collapse on each other, and the linear scaling is fulfilled. Furthermore, we can read off the maximum speed as roughly $x \approx 1.7\,vt$, which is smaller than the speed of two straight domain walls moving apart. Panel b) shows the equal-time ϕ-correlations for the same data as Panel a). There is a drop from the completely ordered initial state to a small correlation length. However, this corresponds to slopes which build up in ϕ due to the domain wall propulsion. Parameters: $J = 1, \Delta = 0.8, \alpha = 0.1, \delta_2 = -2{\cdot}0.6, \delta_4 = 2, b_0 = \sqrt{2}{\cdot}0.2, \omega = 2{\cdot}3.6$ and thus $T_{\mathrm{rot}} \approx 344.7$.

It follows that one domain wall needs roughly $t \approx 3{,}332\,T_{\mathrm{rot}}$ to run once through half the system. In two dimensions, for the same total number of sites, we have approximately 707 × 707 sites for the square lattice. The maximum length one domain wall can travel is given by the diagonal $\sqrt{2} \cdot 707$. To travel half of that length with the given velocity takes roughly $t \approx 6.7\,T_{\mathrm{rot}}$, i.e., significantly smaller in comparison.

To reach a reasonable amount of rotations above ~ 20 without exceeding the size of the system, we can use the following estimate. The goal is to minimise the average distance travelled per one rotation of a straight domain wall since this will allow us to go to the maximum number of rotations for a given system size. The rotation frequency scales with $\omega_{\mathrm{rot}} \sim b_0^2$ and thus the rotation period with $T_{\mathrm{rot}} = \frac{2\pi}{\omega_{\mathrm{rot}}} \sim \frac{1}{b_0^2}$. We can approximate the velocity for large enough driving amplitudes via $v \sim \sqrt{\omega_{\mathrm{rot}}} \sim b_0$ and the average distance of a straight domain wall travelled during one rotation by

$$\bar{x} \sim v \cdot T_{\mathrm{rot}} \sim \frac{1}{b_0}\,. \tag{4.13}$$

Therefore, we can, in principle, maximise the number of rotations that we can observe for a given finite system, i.e., before the correlation length exceeds the system size, by increasing b_0. However, this does not work for arbitrary large field amplitudes. In fact, above a certain critical field, vortices show up similar to those in the one-dimensional analysis. This means that the system releases a part of

the built-up dynamical frustration by creating vortices which influence the speed of domain walls. A brief discussion of the vortex dynamics in two dimensions in comparison to the effective model is given in Sec. 4.9.
Here, we want to focus on the dynamics without vortices. Thus, we use $b_0 = \sqrt{2}\cdot 0.2$, which is the largest field amplitude for which we do not observe any vortices. We follow the same strategy as in the non-driven case and calculate the correlations. The results are shown in Fig. 4.6 for a system of $10{,}000 \times 10{,}000$ sites averaged over five initial states. Again, we show the m-correlations as a scaling plot where we use the velocity of a straight domain wall, i.e., the corresponding one-dimensional velocity, $v \approx 0.163$, as a scaling factor in Fig. 4.6a). Additionally, we show the ϕ-correlations, calculated via Eq. (4.12), without scaling in Fig. 4.6b).
Similar to the one-dimensional case, the main characteristic length scale in the m-correlations changes linearly in time, $R(t) \propto vt$. As anticipated, it takes, again, roughly 20 rotations before the true long-time scaling is revealed and the curves collapse in the scaling plot. The agreement within the error bars is very good. However, the form of the curve is different to the curve for one dimension. At short-scaled distances, the correlations fall off quickly, but a plateau shows up at around $x \approx 0.5\,vt$. This spans until the correlations drop to zero at roughly $x \approx 1.7\,vt$ from which, similar to the one-dimensional case, we can read off the maximum velocity as $1.7v$. It is slower than two straight domain walls moving in opposite directions. The plateau drops off very slowly compared to the initial short-scale drop. While these two distinct length scales exist in the problem, they both scale linearly in time.
The ϕ-correlations show, as in the one-dimensional case, a short correlation length. For late times, the ϕ-correlations do not show a visible change with time. Although we have observed finite correlation length in the non-driven system, see Fig. 4.2b), the correlation length in the driven case is more than one order of magnitude smaller. This is unsurprising as we know that every driven domain wall carries a constant slope of ϕ behind itself, which still holds in two dimensions.
In Fig. 4.7, we show snapshots of one simulation as an example. As before, the top row shows m and the bottom row ϕ for a similar range of times as for the correlations. The first main observation is that, although the times shown are similar to those for the non-driven ferrimagnet, the changes from one to the next image in m are drastic. Remember that without drive the structures looked well connected from one image to another. Thus, it is already visible on a macroscopic level that we are not dealing with purely curvature-driven motion. This can also be noted from the sharp corners even in the last image shown, $\sim 44\,T_{\mathrm{rot}}$, which cannot exist at late times for only curvature-driven forces. In the ϕ-pictures, we can see the characteristic build-up of gradients behind the walls, as in one dimension. However, due to the additional space dimension, the dynamics become more complicated since there are now many

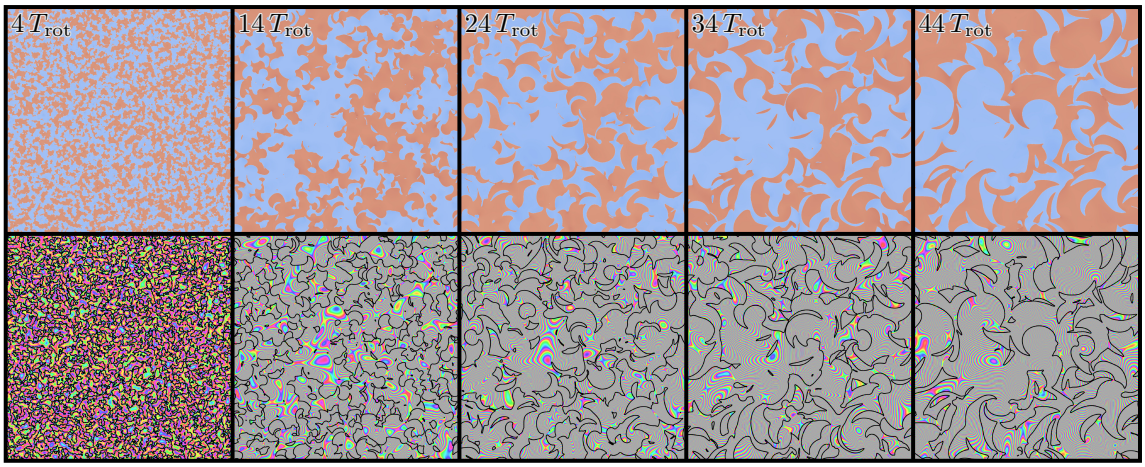

Figure 4.7: Snapshots from one simulation of a quench to $T = 0$. The top row shows m, and the bottom row ϕ with the domain walls displayed as a top layer for five different times. The numbers in the upper right corner denote the time. It is visible in m that the main characteristics do not occur from a curvature-driven motion. One of the distinctive features is given by very sharp corners, even in the last image after 44 rotations. Furthermore, the typical feature of a strong build-up of gradients in ϕ resulting from domain wall propulsion is clearly visible. Parameters as in Fig. 4.6

more directions to move than just left and right. This allows for situations where a part from one domain can separate or domains can merge. Moreover, the influence of $\nabla^2\phi$ on domain walls is evident from the shown pictures. The hydrodynamic long-range interaction still exists. However, while in one dimension, the influence could either reverse or slow down the domain wall, bending in various directions also turns up. This large variety makes the dynamics much more complex. Fig. 4.8a) shows a zoom on ϕ, from the last time shown in Fig. 4.7. At first glance, the slopes in ϕ around the curved domain wall in the centre do not seem to follow the same trend as in one dimension. The distances between the ϕ =const. lines have different spreads and orientations. However, subtracting the constant slope in the middle of the circular-like shape, approximately given by $\nabla\phi_{\mathrm{mid}} \approx (-0.15, -0.3)$, reveals the gradient's true nature. This is shown in Fig. 4.8b) with Φ given by $\nabla\Phi = \nabla\phi - \nabla\phi_{\mathrm{mid}}$ up to a constant shift. Here, the Φ =const. lines around the domain wall follow the shape and also show a circular trend further away. The slope is approximately constant inside the circular domain wall due to the subtraction. This resembles the one-dimensional case, where a characteristic slope difference was found at the domain wall. At each point on the circular domain, this is now approximately fulfilled. We conclude that the circular shapes of many visible domains are thus highly influenced by $\nabla\phi$. As before, this can interpreted as a conserved quantity that puts long-range hydrodynamic interactions on the domain walls. The sharp corners can be seen as a side product of the driven motion and the imprinted circular shape. Notice that

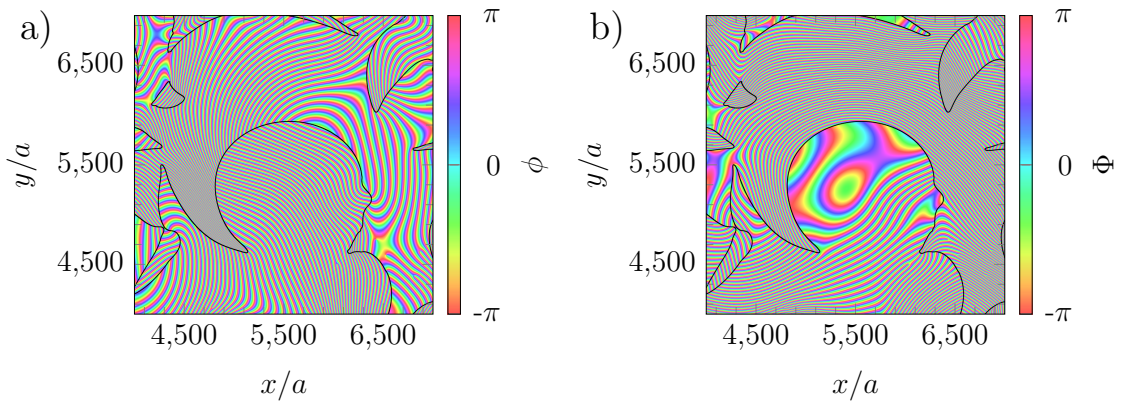

Figure 4.8: ϕ shown from a zoom in the middle of the last time shown in Fig. 4.7. Panel a) shows the raw data with a circular domain wall in the middle. This zoom highlights the large build-up of slopes in ϕ. Panel b) shows the same data but we subtracted the slope from the middle of the circular domain wall. We estimate this as $\nabla\phi_{\text{mid}} \approx (-0.15, -0.3)$ and $\nabla\Phi = \nabla\phi - \nabla\phi_{\text{mid}}$ determines the shown Φ up to a constant shift in the two directions. With this, the slope in the middle is approximately constant, which reveals the characteristic slope difference at the domain wall. Further away from the domain, the Φ =const. still show a circular shape. Parameters as in Fig. 4.6

the circular domain wall shown in Fig. 4.8 moves outwards. Due to other earlier domain wall movements, a gradient landscape has formed. For the one-dimensional scenario, we looked at a flat ϕ-profile where the domain wall carried the slope behind itself. Here, the domain wall enters a slope landscape and adjusts the slope behind itself so that the characteristic slope difference is still fulfilled.
Given the correlations discussed in the beginning, Fig. 4.6, we can now think about the two length scales. The short scale at the initial drop can be linked to the sharp corners. The larger one at the end of the plateau can be attributed to the long curved side of a domain. In this spirit, the drop from the plateau is a reasonable length to look at when thinking about the growth of the walls.
Before turning to the quench to a finite (high) subcritical temperature similar to the non-driven case, we briefly examine the phase transitions.

4.5 Shift of the Phase Transition

In this section, we want to look at the position of the phase transition in m. In a broad sense, the knowledge was already utilized in Sec. 4.2.1, where we used (high) subcritical temperatures, for which we needed at least a rough estimate of the transition temperature. Furthermore, we expect an influence due to the driving field on the position of the transition. Thus, the two parameters to map out the phase diagram are given by the temperature T and the field amplitude b_0.
Notice that the simulations with up to 10,000 × 10,000 sites were done for instan-

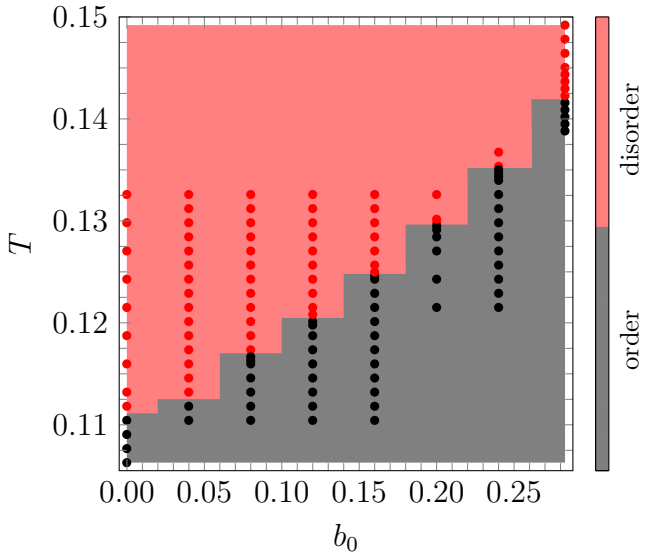

Figure 4.9: Phase diagram for transition in m as function of temperature T and driving amplitude b_0 for the microscopic system. The points are the data points where we estimate if the system is in an ordered or disordered state. For that, we used the plateau value C_{plateau} in the correlations with a threshold value of ~ 0.005. More details are explained in the text. Red denotes the disordered phase, and grey denotes the ordered phase, the background serves as a guide to the eye. We find an approximately linear relation between the transition temperature and the driving amplitude for small fields and without $b_0 = 0$. The data shown for the highest field amplitude is for $b_0 = \sqrt{2} \cdot 0.2$ as the maximum field where we did not observe vortices. A vertical cut at $b_0 = 0.16$ is shown in Fig. C.2. Parameters: driving amplitude b_0 and temperature T given on the axes, other parameters as in Fig. 4.6 for systems of 500×500 sites.

taneous quenches, which we simulated maximally until the correlation length got larger than the system size. This happens once the correlations do not fall off to zero and a roughly constant plateau builds out in the centre. Here, we want to use precisely this plateau value C_{plateau} in the stationary state to estimate if the state is ordered or disordered in m. However, since we need to simulate until the stationary state is reached, we are bound to smaller system sizes. We assume that the position of the phase transition determined with the smaller system size is close to the one with larger system sizes, i.e., the same up to small corrections.

The plateau value is calculated from the normalised correlations. Thus, $C_{\text{plateau}} = 1$ would be the completely ordered state and $C_{\text{plateau}} = 0$ disordered. However, due to small deviations in the numerics, the value will not be exactly zero but just very small. To compensate for that, we define a threshold value of ~ 0.005, slightly larger than the fluctuations around zero in the disordered phase. Any value below this threshold is counted as disordered in m, and any value above is counted as ordered. This characterisation leads to the phase diagram shown in Fig. 4.9. The points denote the data points for which we determined the plateau value, and the

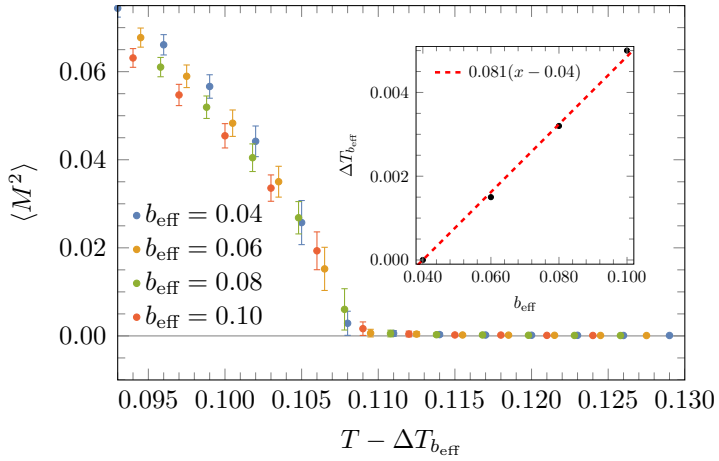

Figure 4.10: Square of the average magnetisation on the lattice averaged over multiple times for different effective magnetic fields around the phase transition. The curves are shifted by $\Delta T_{b_{\text{eff}}}$ so that the curves lie approximately on top orientated on the curve with the lowest value of b_{eff}. The shifts in temperature are shown in the inset and have an approximately linear relation as a function of the field amplitude. The transition in the effective model arises slightly earlier than in the microscopic counterpart. However, the effective model shows qualitatively the same behaviour as the microscopic model, Fig. 4.9. Parameters: $r = -0.4, u = 2, D_m = 0.8, D_\phi = 1, \alpha = 0.1$ for systems of 250×250 sites

background serves as a guide to the eye. Red represents the disordered phase, while black represents the ordered phase. We observe an almost linear relation between the critical temperature and the field amplitude for small field amplitudes, $0 < b_0 \lesssim 0.2$. The transition shifts to higher temperatures with increasing field amplitude. This means the ordered phase becomes more stable against thermal fluctuations, similar to the one-dimensional case. For the non-driven system, $b_0 = 0$, we estimate the critical temperature to be roughly at $T_c \approx 0.1111$, given by the midpoint between the two data points around it. A pessimistic error estimate using half the distance from T_c to the two neighbouring values yields $\sim \pm 0.0004$. A plot of a vertical cut for $b_0 = 0.16$ in Fig. 4.9 is shown in Fig. C.2 in the appendix. It shows a nice transition from the ferrimagnetic state with finite m to the xy-ordered state with $m = 0$.
Before going to the next section, where we reuse the notion of type II defect discussed for the one-dimensional case, we want to compare it to the effective model. We perform similar simulations for parameters following the translation rules, Eq. (2.47), and with a slightly smaller system size. Again, we use the relation from the microscopic model to determine an effective field amplitude b_{eff} from ι. In this case, we use $\langle M^2 \rangle$ where $\langle \dots \rangle$ denotes an average over multiple times and M is the average magnetisation at that point in time, $M = \frac{1}{N_{\text{tot}}} \sum_{i,j} m_{i,j}$. In Fig. 4.10, we show the numerical results where we shifted all curves on the curve with the lowest field amplitude in the area around the phase transition. The inset shows the shifts that lie roughly on a straight line, i.e., we observe an approximate linear shift for small field

amplitudes. Comparing the transition point of the two models for $b_0 = 0.04 = b_{\text{eff}}$, we see that the transition happens slightly earlier in the effective model. However, the effective model includes only the leading order terms, even for the noise strength. Considering this, we are not surprised that there is a small deviation. However, the qualitative agreement is still very nice, and we observe the linear shift of the transition in both models. Notice that the shift is much smaller than a possible shift by ι itself.

4.6 Circular Growing Domain Walls - Type II Defects Revisited

An emerging question is if we can adapt the idea about type II defects in one dimension, Sec. 3.5.2, and create a growing circular domain, as the analogue, in the absence of thermal fluctuations. The difference in the one-dimensional case as compared to the two-dimensional one is that there exists an additional force inwards from the local curvature which works against a growing domain and is stronger the smaller the radius R is, $\kappa = \frac{1}{R}$, see the beginning of this chapter. However, for large enough radii this effect should become negligible.
We can use the same profile, Eq. 3.53, but rotate it around the centre. This creates a circular domain with an initial diameter of L_{init} and an initial ϕ-profile which forces the circular domain wall to grow at the beginning.
With the initial state at hand, we can create the corresponding phase diagram of the two-dimensional type II defects. This is shown in Fig. 4.11. It turns out that we see the same solutions as in the one-dimensional case, see Fig. 3.16, but, similar to the initial state, spanned out into two spatial dimensions by rotating around the centre axis of the figures. This explains in the same way, why we find a very similar phase diagram. The size of the area, where the domain wall grows first, increases with increasing s_{init} but then decreases again for even higher values of s_{init}. This comes about because of the former four domain wall cleaning mechanism, which relies on a large magnetisation current flowing to the centre, mediated by the large slope difference in ϕ. At a certain strength, this flips the magnetisation in the centre and creates a domain with opposite sign inside the domain. However, in the two-dimensional picture this construction has only a total number of two circular domain walls. Nevertheless, the process shows the same behaviour where the outer wall is slightly slower than the inner wall which ultimately leads to annihilation. The other cleaning mechanism at lower s_{init} is the more trivial one where the circle shrinks and the circular domain wall annihilates itself. In the growth regime, only one solution exists which is the growing circular domain, i.e., the type II defect.

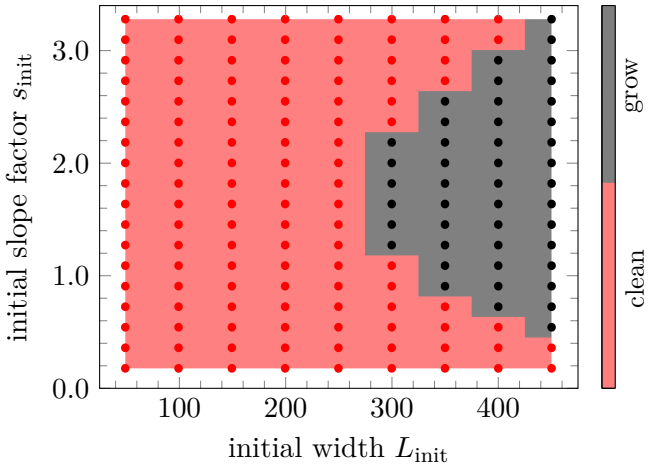

Figure 4.11: Phase diagram of type II defects in two spatial dimensions, a growing circular domain, at $T = 0$. The background serves as a guide to the eye and the points denote the data points. The red region is linked to final states where the circular down-domain vanishes, and is denoted by clean in the legend. The possible scenarios for this region are the analogues from the one dimensional case, see Fig. 3.16. The black region denotes the area where the domain is able to grow. For all values of initial slope and width shown in this plot, only large domains of ≥ 250 sites can grow. Parameters: $J = 1, \Delta = 0.8, \alpha = 0.1, \delta_2 = -2 \cdot 0.6, \delta_4 = 2, b_0 = 2 \cdot 0.15, \omega = 2 \cdot 3.6$

Thus, we observe solely the analogues of the solutions from the one-dimensional analysis, i.e., there are no additional solutions arising. However, as anticipated at the beginning of this section, the point of transition shifts to larger L_{init} in Fig. 4.11 although, we used a slightly larger field amplitude and thus a larger corresponding one-dimensional velocity. This can be explained by the fact that the curvature-driven motion which drops off with $\sim \frac{1}{R}$ enhances the area where the system is able to heal the defect and end up in the fully ordered state. In total, this might be one explanation, why the ordered phase in the driven system is more resilient to noise and therefore, why the position of the transition shifts to larger temperature values. Note that this is just a minimal modelling without thermal fluctuations.

4.7 Coarsening Under Thermal Fluctuations in the Driven Ferrimagnet

Previously, in Sec. 4.4, we investigated the coarsening of the driven ferrimagnet in the absence of thermal fluctuations. After briefly discussing the position of the phase transition and its shift, we will now explore the coarsening behaviour of the ferrimagnet at (high) subcritical temperatures (as done before for the non-driven scenario).
We use the same initial state, which is fully ordered in the phase, $\phi = 0$, and ran-

dom in m, drawn from a uniform distribution in the range of $(-0.1, 0.1)$. First, we perform quenches to the same (high) subcritical temperature as for the non-driven scenario, $T_f = 1077$. We use again the field amplitude of $b_0 = \sqrt{2} \cdot 0.2$ to reach the maximum amount of rotations. The correlations are calculated as before, Eq. (4.11), and shown in Fig. 4.12(a,b). We observe the same characteristics as in Fig. 4.6 for a quench to $T = 0$. The growth scales linearly in time, and a plateau builds out, consisting of a first initial drop and a second slower decay at a later rescaled position. And ϕ shows short correlations which roughly saturate for the last times shown. However, there are also some differences. The most important observation is that the plateau value decreased, and at the same time, the point of maximum velocity shifted to a larger value of $2.1v$. Therefore, we can only show data for 32 rotation periods before exceeding the system size. We assume that this change in the plateau value is continuous with temperature. Snapshots of the raw magnetisation data for one simulation at $t = 24\,T_{\mathrm{rot}}$ are shown in Fig. 4.12(c,d). It is nicely visible that the large domains, which still have a spherical shape, have many fluctuations inside. Although those fluctuations cannot nucleate a growing domain with opposite magnetisation, i.e., growing type II defects are rare, they do lower the correlations. The higher the temperature, the higher the strength of those fluctuations and the lower the plateau value. The domain walls are strongly protected by the gradients in ϕ, see Fig. 4.12d). Thus, the domain walls are not as strongly influenced as in the non-driven case for the same temperature, Fig. 4.5. However, we have not verified the claim of a continuous change of the plateau value with temperature as it requires a large amount of those heavy simulations for several temperatures, which exceed the scope of this study.

Next, we can see what happens for a quench into the ordered region, which solely exists because of driving the system. We perform quenches with the same initial conditions as before but now to $T_f = 0.1353$, which is in the upper-right half of Fig. 4.9. The results are shown in Fig. 4.13 where panels a) and b) show the two correlations and panels c) and d) a snapshot after $t = 24\,T_{\mathrm{rot}}$. The correlations look very different. In the correlations of m, no plateau is visible on the same scale as before. The inset in panel a) shows a zoom on small y-axis values where we can see a small plateau-like shape. However, the values are tiny, and the curves do not collapse at the plateau on one line within the range of times shown. Instead, the values at short-scaled distances grow faster than the ones further away, and the plateau-like shape becomes skewed over time. Notice that the time until the system size is reached, i.e., when the correlations do not go to zero any more, is reached again earlier than for the quench to lower temperature (here, after approximately 28 rotation periods). The ϕ-correlations shown in Fig. 4.13b) stretch out over approximately three times as large distances even for the last times shown. Furthermore,

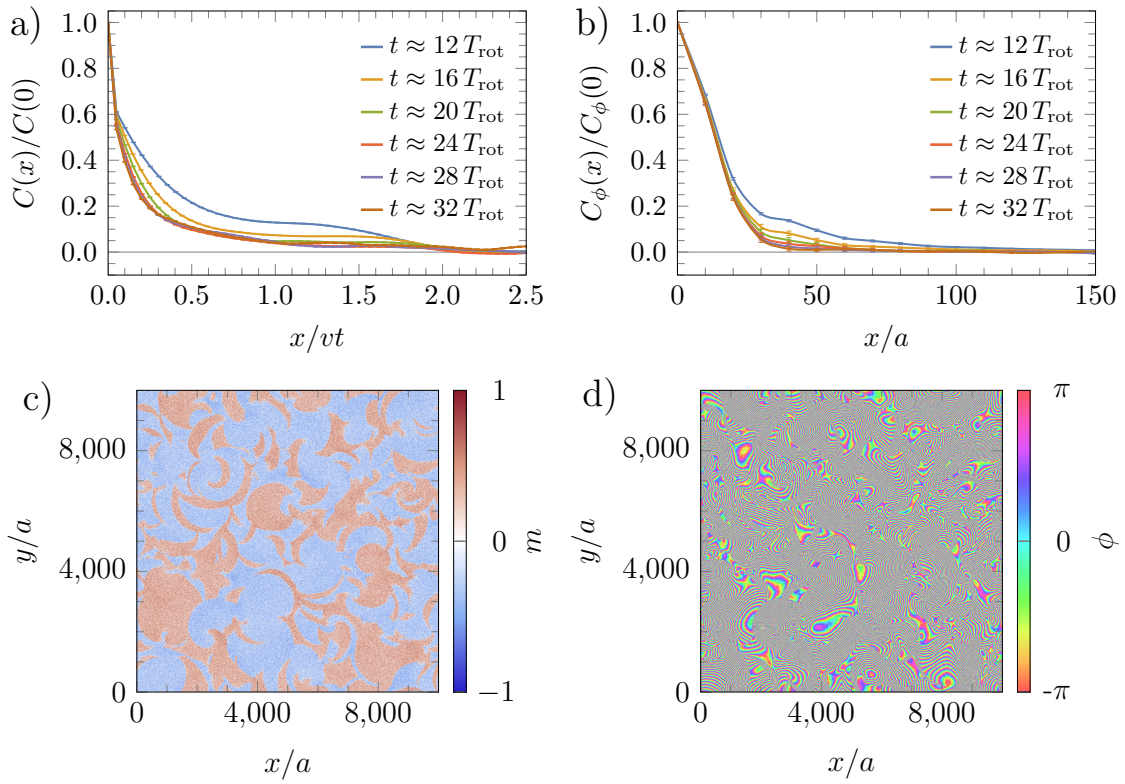

Figure 4.12: Panel a) shows the the equal-time correlations in m for a system of 10,000 × 10,000 sites averaged over five initial configurations after a quench to $T_f \approx 0.1077$. The scaling is linear in time, see the scaled positions, as before for the quench to $T_f = 0$, Fig. 4.6. The scaling factor is again the velocity of a straight domain wall, $v \approx 0.163$. However, the plateau value decreased, and the maximal speed increased to $2.1v$. Panel b) shows the ϕ-correlations for the same data as panel a). The curve looks very similar to the one with $T_f = 0$, Fig. 4.6, and saturates at a small correlation length for the last times shown. Panel c) displays the bare magnetisation data of one simulation at $t = 24\,T_{\mathrm{rot}}$. The image looks very similar to the one without thermal fluctuations, Fig. 4.7. Large domains have circular boundaries and sharp corners. Compared to the non-driven simulations for a quench to the same temperature, Fig. 4.5, we only encounter a few minor domains, in agreement with the discussion in the previous section. And the boundaries are much less affected by thermal fluctuations. However, inside the domains, we see many fluctuations that cause the plateau value to be lowered in panel a). Panel d) shows the phase for the same data as panel c). We refrain from determining the domain wall positions to draw them on top of the phase due to the large system size combined with thermal fluctuations. However, it is clearly visible that the gradients in ϕ, which build up in the driven system, are robust at the given temperature and protect the domain walls from a strong influence of thermal fluctuations. Parameters as in Fig. 4.6 but for quenches to $T_f \approx 0.1077$.

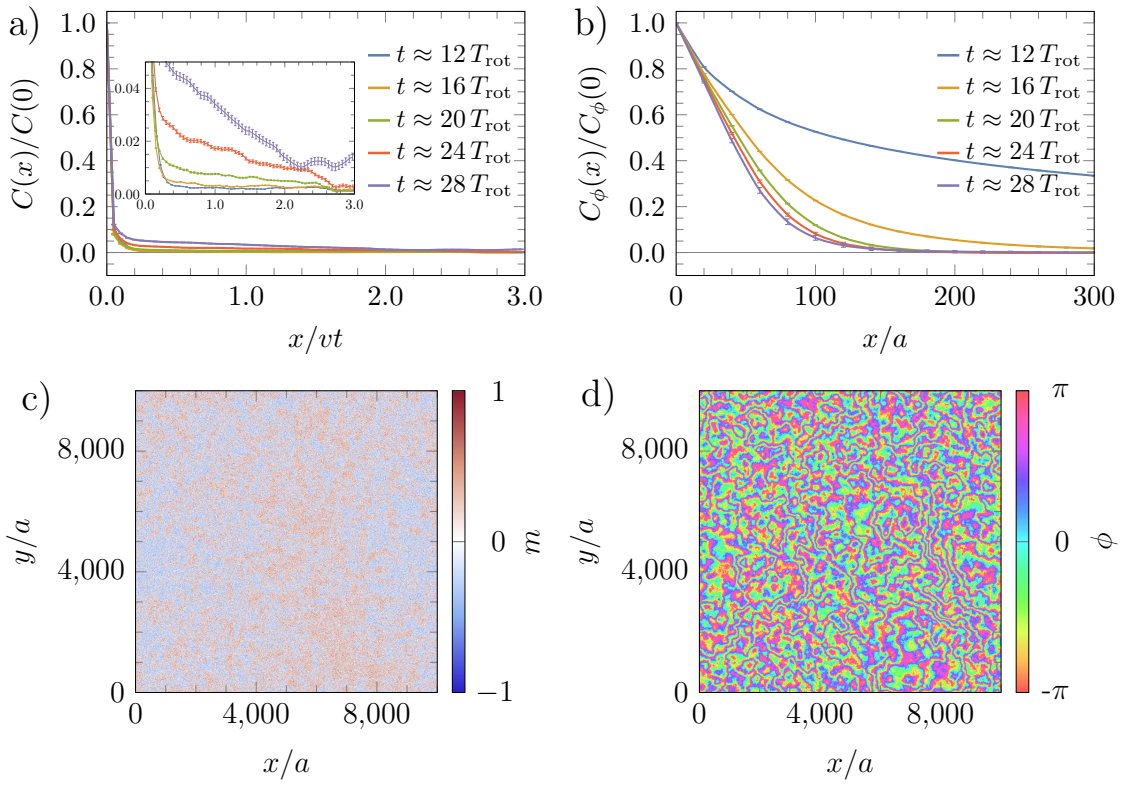

Figure 4.13: Panel a) shows the correlations in m, again averaged over five different simulations but for a quench to $T_f = 0.1353$ which is inside the region that solely becomes ordered because of the driving. The form is very different from before, and only with zoom, see inset, are we able to identify a plateau-like shape. However, this plateau becomes skewed, indicating a scaled distance-dependent correlation growth. The ϕ-correlations shown in panel b) stretch out over about three times as large distances as before, and the saturation is slower. Panel c) displays the snapshot of the raw magnetisation of one of the simulations after 24 rotations. The shape of domains is very different, and the boundaries are smoothed out. In panel d), we show the corresponding ϕ-data. Much less gradient piles up, leading to a lower protection of the domain walls against the fluctuations. While we can confirm that the maximum speed is again larger than compared to smaller or zero temperatures, we are not able to quantify this since the plateau value becomes tiny. Parameters as in Fig. 4.6 but quench to $T_f = 0.1353$.

the saturation happens more slowly.
Looking at the snapshot of the magnetisation after 24 periods displayed in Fig. 4.13c), it becomes evident that many smaller domains exist. Additionally, the boundaries are smoother and less clear than at lower temperatures. Also, the spherical shape of the walls is mainly gone. This is a hint that the walls are not as protected as at lower temperatures. This proves to be true from Fig. 4.13d), which shows ϕ for the same data. The build-up gradients are much lower, and thus, the domain walls are less protected against thermal fluctuations. However, as mentioned at the beginning, we do not observe any vortices and ϕ is still much more stable against fluctuations than m.
This is an exciting observation. While the driving is capable of shifting the position of the phase transition over more than 25% for the chosen parameters, the domains do not attain the same structure as outside of this stretched-out region. Moreover, one can argue that the plateau still exists but in a slightly different form since all curves go to zero at the same point in the inset of Fig. 4.13a). However, resolving this point is not feasible due to the small values, which makes it very difficult to define a reasonable quantity to track the time evolution of order in the system. Unfortunately, we could not identify an effective method for quantifying this parameter. Moreover, we cannot make a conclusive statement about this region. Similarly, this will be problematic in the next section, where we apply the Kibble-Zurek mechanism to our ferrimagnet.

4.8 Kibble-Zurek Mechanism

Within this section, we want to make use of the Kibble-Zurek mechanism, which was first developed by Kibble for the cosmological phase transition [92, 93] and then refined by Zurek for condensed matter systems [94, 95]. Before starting with its application, let us briefly recap what this phenomenological approach is about. The following discussion is based on [96]. So far, we have only considered instantaneous quenches. In the framework of the Kibble-Zurek mechanism, a finite quench rate is used to go through a second-order phase transition from a symmetric phase into the symmetry-broken phase. In the simplest approximation, a linear ramp is implemented. For the temperature, we can define

$$\Delta T = \frac{T(t) - T_c}{T_c}, \text{ with } \quad T(t) = T_c \left(1 - \frac{t}{\tau_Q}\right) , \tag{4.14}$$

as a protocol, where τ_Q is the time used to run through the transition, and the critical point is reached at $t = 0$. Notice that any control parameter can be used.

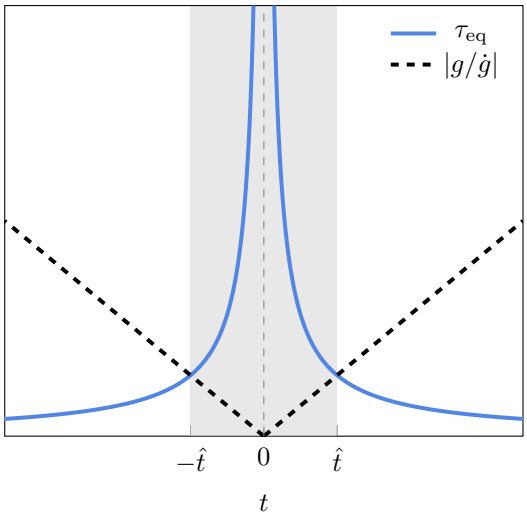

Figure 4.14: An illustration of the Kibble Zurek mechanism. The system is assumed to evolve adiabatically until $-\hat{t}$, then the dynamics freeze in due to the divergence of the relaxation time. After $\hat{t}$, it is assumed to return to an adiabatic evolution. The grey area highlights the freeze-out regime, and the dashed lines denote the inverse quench rate. The crossing point defines $\hat{t}$.

However, we will focus on temperature.

The crucial point is to use the equilibrium scaling theory to describe the effect of the dynamics across the transition. Close to the phase transition, critical slowing down takes place, and the correlation length and relaxation time diverge. From scaling laws, we can write down the following relations

$$\xi_{\rm eq}(\Delta T) = \frac{c_\xi}{|\Delta T|^\nu}, \qquad \tau_{\rm eq}(\Delta T) = \frac{c_\tau}{|\Delta T|^{\nu z_{\rm eq}}}, \tag{4.15}$$

where ν and $z_{\rm eq}$ are the equilibrium critical exponents and c_ξ, c_τ some constants which depend on the microscopic details. The subscript denotes that we are discussing the equilibrium correlation length and relaxation time, i.e., the one at ΔT after the stationary state is reached and not within the protocol, Eq. 4.14. Far away from the transition $\tau_{\rm eq}$ is of the order of the microscopic time. For very slow quenches, i.e., very large τ_Q, this means that the system evolves adiabatically and remains in equilibrium. However, this breaks down at some point when reaching the transition as the protocol has a finite rate, but $\tau_{\rm eq}$ diverges. The non-adiabatic regime is often referred to as the freeze-out regime. A lower bound for that is given by $-\hat{t} = \tau_{\rm eq}(-\hat{t})$, which is the point where the relaxation time becomes equal to the time remaining to the transition. A visualisation is shown in Fig. 4.14 where the freeze-out regime is highlighted by the grey area. Due to the symmetric shape, we

can equivalently determine $\hat{t}$ by

$$\hat{t} = \left(c_\tau \tau_Q^{\nu z_{\mathrm{eq}}}\right)^{\frac{1}{1+\nu z_{\mathrm{eq}}}} . \tag{4.16}$$

After the transition, the adiabatic evolution returns at $\hat{t}$. The simplest approximation is that the system is fully frozen in the non-adiabatic regime. Therefore, the correlation length does not change from $-\hat{t}$ to $\hat{t}$ so that

$$\xi(-\hat{t}) = \xi(\hat{t}) = c_\xi \left(\frac{\tau_Q}{c_\tau}\right)^{\frac{\nu}{1+\nu z_{\mathrm{eq}}}} . \tag{4.17}$$

This expression allows us to estimate the scaling of the correlation length with the quench time *at* $\hat{t}$ purely from the equilibrium critical exponents. Thus, this approach allows information about the phase transition to be gained. It is often referred to as the defect density, which is directly related to the correlation length. However, depending on the problem, only an effective defect density exists, just like domain walls.

While this approach follows simple assumptions, it was confirmed in many experiments for classical and quantum systems [97–103]. However, this discussion does not cover the evolution after $\hat{t}$. The evolution after $\hat{t}$ depends on the problem at hand, and for domain growth, coarsening is expected. This can be intuitively explained by the fact that the domain walls freeze in throughout the protocol, but once the relaxation time reduces again, the system can evolve. As we learned earlier, the domain wall evolution inside the ordered phase is dominated by coarsening. A nice discussion on the importance of coarsening can be found in [104]. The authors showed that the coarsening dynamics spoil the dynamics of the Kibble-Zurek mechanism, i.e., not close to the transition the coarsening exponent is observed.

We use the abovementioned approach to our ferrimagnet in the following, starting with the non-driven case.

4.8.1 Kibble-Zurek in the Non-Driven Ferrimagnet

Here, we want to apply the Kibble-Zurek mechanism to our non-driven ferrimagnet. At first, we have to remind ourselves that the transition is roughly at $T_c \approx 0.1111$. We use a linear quench protocol with

$$T(t) = T_i + (T_f - T_i)\frac{t}{\tau_Q} , \tag{4.18}$$

where T_i is the initial temperature at the beginning of the quench, and T_f is the final temperature. For the simulations shown here, we start at $T_i = 0.1229$ and

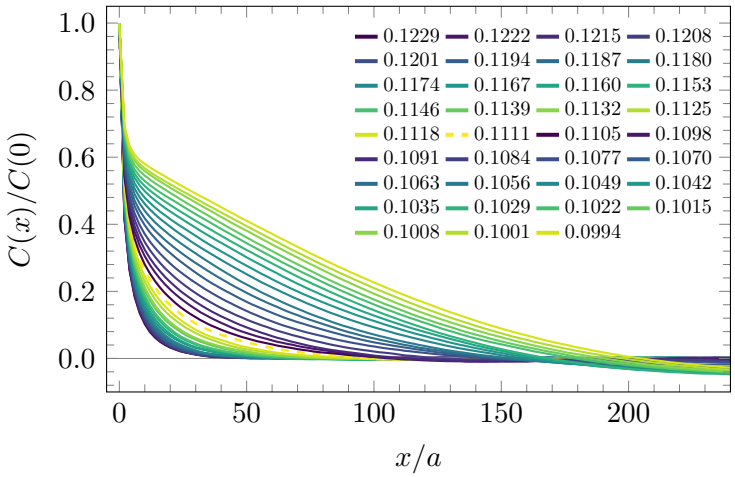

Figure 4.15: Equal-time correlations for a quench following the linear protocol of Eq. (4.18) for $\tau_Q \approx 26{,}392$ for the non-driven ferrimagnet. The legend denotes the temperature at the time when the correlations were conducted and should be read from left to right and top to bottom. The initial state was conducted from one simulation at $T_i = 0.1229$ until the stationary state was reached. The curve at the approximate transition temperature is highlighted with a thicker dashed line. Distances between consecutive curves are small at the beginning and become large towards the end, mostly after the transition. This is an imprint of coarsening which sets in beyond the immediate vicinity of the transition. Parameters as in Fig. 4.2 for a system of $2{,}500 \times 2{,}500$ sites.

stop at $T_f = 0.1015$. As in the general discussion, τ_Q is the total time used for the quench, i.e., until the temperature reaches the final value. However, the time when the transition takes place is not at $t = 0$ to simplify the numerical simulations. In the simulations, we have to approximate the linear protocol with a step-like shape. This equals a straight line for infinitely small steps. For practical reasons, we can only choose a small but finite step. We use ~ 0.176, which is much smaller than one full rotation period but larger than the numerical solver step.

Another technical remark is that to start the system at T_i, we first have to run a long simulation that reaches the stationary state at that temperature. An advantage of this approach is that we can perform the long simulations just once for the chosen parameters and reuse the last state of that simulation as an initial state for all the quench simulations with different τ_Q.

As a quantity of interest, we use again the equal-time correlations in m as defined in Eq. (4.11). The results of one simulation with $\tau_Q \approx 26{,}392$ are shown in Fig. 4.15 where each line corresponds to one time or equivalently one temperature value, see the legend where the temperatures are organised in order from left to right and top to bottom. We can clearly see that the change between consecutive curves is small for the first curves and becomes larger at later times or lower temperatures. The largest changes happen after T_c, highlighted with a thicker dashed line exactly

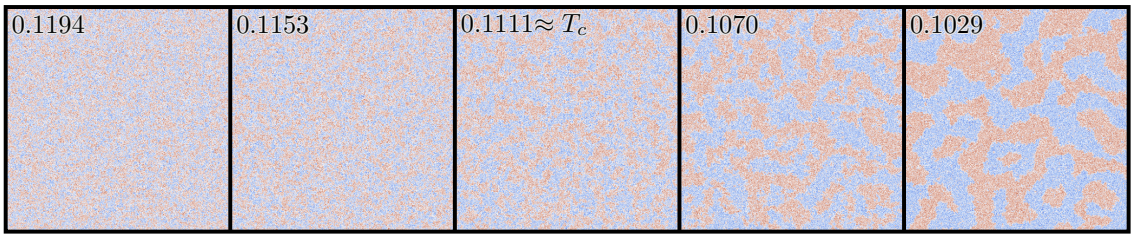

Figure 4.16: Snapshots taken from the same simulations as Fig. 4.15. The two snapshots before the transition only show a tiny increase in correlation length, i.e., domain sizes. However, the last two show coarsening characteristics. The colour bar is omitted for brevity but is the same as in all other colour plots of m.

where the gradient colour-scale restarts. This is in accordance with the assumption that coarsening hits in, significantly increasing the correlations even after $\hat{t}$. Notice that we do not show the curves until half of the system, i.e., until $x = 1{,}125\,a$, for better visibility of the spread between the curves. Thus, the small negative dip at the end of the shown frame is not an overlap effect due to finite system size. The correlations drop off quickly at small distances, and roughly all curves lie on each other. The curves only separate at about $C(x)/C(0) = 0.6$, and thus, the simple definition of the drop to half the maximum is not a good one for the correlation length.

In Fig. 4.16, we show snapshots from the same simulation. The number in the upper-left corner denotes the temperature, which, due to the linear protocol, corresponds one to one to a time throughout the quench. Before the transition, in the disordered phase, the size of domains only grows very little. At the transition, we see a mosaic-like shape with many domains. However, the evolution from the second last to the last image has characteristics of coarsening, where large domains become broader with time. This is in agreement with the observations from the correlations. For a more quantitive analysis, we follow [104] and conduct a scaling plot for the typical correlation length. Since the common definition of the drop to half the maximum is insufficient. As we noticed for instantaneous quenches, the first zero crossing of the correlations can serve as a value corresponding to the maximum domain size R, which is directly related to the maximum correlation length. However, small deviations get larger at the zero crossing, making it less feasible. As a workaround, we use a cut at $C(R)/C(0) = 0.02$, which is very close to the zero crossing. The result with the imposed scaling from Kibble-Zurek, see Eq. 4.15, is shown in Fig. 4.17. The scaling is performed with $\nu = 1$ [105] and $z_{\mathrm{eq}} \approx 2.17$ [106] the critical exponents from the Ising class. Notice that we shifted the time values so that the transition happens at $t = 0$ for each of the curves, making them comparable in the shown setting. Close to the transition, the curves collapse within the accuracy of the simulations. While we are unable to provide definitive proof that these are the correct exponents, our

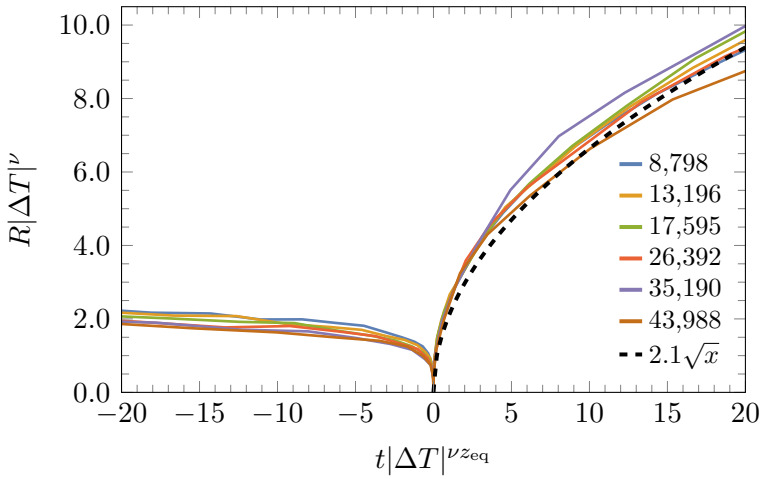

Figure 4.17: Scaling-plot of the estimate of the domain size R via $C(R)/C(0) = 0.02$. Each curve is averaged over three runs. The scaling is performed with Ising critical exponents, $\nu = 1$ and $z_{\mathrm{eq}} \approx 2.17$, according to the relations from Eq. 4.15. The curves collapse close to the transition within the accuracy of the simulations. Additionally, we find the coarsening-like shape for positive times, highlighted by a black dashed line as a guide to the eye. Parameters and protocol are the same as in Fig. 4.15 but different quench times τ_Q which are shown in the legend.

analysis serves as a preliminary confirmation that, despite the differing behaviour for quenches to $T = 0$, the non-driven ferrimagnet still falls into the Ising class for finite temperatures close to the transition.

We also find an approximate square-root growth, as for Ising class coarsening, at positive times, for which the dashed line serves as a guide to the eye. This shows that we cannot neglect coarsening effects beyond the close vicinity of the phase transition, as stated in [104] for the Ising model.

To stress this point even more and give further evidence, we show the value of R at two different temperatures for the different values of τ_Q in Fig. 4.18. One temperature, $T = 0.1001$, is far from the transition and compares well to the coarsening scaling with $\tau_Q^{1/2}$, which is the same as for the Ising class and the same as we observed for the instantaneous quench at (high) subcritical temperatures, see Sec. 4.2.1. The other one, $T = 0.1091$, is close to the transition and fits very well with the scaling proposed by Kibble-Zurek, Eq. (4.17) with the Ising critical exponents $\nu = 1$ and $z_{\mathrm{eq}} \approx 2.17$. This fits with the discussion in [104].

Thus, we conclude that the non-driven ferrimagnet falls under the Ising class regarding the transition in m for the parameters and ranges analysed within this discussion. However, this is not a definite proof due to the numerical limitations. Nevertheless, the agreement is very good based on our numerical simulations.

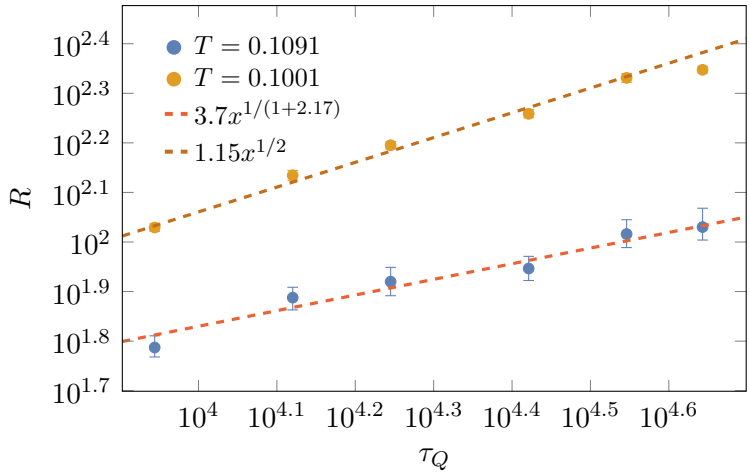

Figure 4.18: Domain size R estimated from $C(R)/C(0) = 0.02$ for the same data as shown in Fig. 4.17 but as function of the quench time τ_Q for two different temperatures, see legend. The temperature close to the transition, $T_c \approx 0.1111$ agrees with the prescriptions made by Kibble-Zurek, Eq. (4.17), for the Ising class. The temperature further away from the transition also follows the Ising class but for coarsening. The errors are estimated from varying the cutting level, in particular, the upper error ΔR_+ corresponds to $C(R + \Delta R_+)/C(0) = 0.015$ and the lower one ΔR_- to $C(R - \Delta R_-)/C(0) = 0.025$. The lines are not fitted curves but serve as a guide to the eye.

4.8.2 Kibble-Zurek in the Driven Ferrimagnet

After the successful application of the Kibble-Zurek mechanism on the non-driven ferrimagnet, we want to turn to the driven system. However, already in Sec. 4.7 about quenches to temperatures closer to the transition, the behaviour turned out very subtle and we could not draw a general conclusion. Nevertheless, we want to see if we can learn something about the transition in this subsection.

For the analysis presented here, we use $b_0 = 0.16$ instead of $\sqrt{2} \cdot 0.2$ for two reasons. One is that the dynamics due to the drive, e.g., the speed of the domain walls, is slower, allowing for slower quenches, i.e., larger quench times for the same system size. This works also better with the step-like linear protocol. Notice that we are again bound to smaller system sizes compared to the instantaneous quenches due to the initial state preparation. The other reason is that the elongated ordered region emerging due to the drive is smaller, and we can perform simulations with reasonable quench times up to temperatures near the transition of the non-driven system. We use the same linear temperature protocol but with an initial state prepared at $T_i = 0.1381$ in a system of $2{,}500 \times 2{,}500$ sites and a final temperature of $T_f = 0.1105$. This means that we quench slightly below the transition of the non-driven system. The transition for the used field amplitude is at approximately $T_c \approx 0.1250$.

Another drawback is that, while we scale quasi-linearly in time through the temperatures, we also have to consider the period of the drive T_ω. Then again, we want to

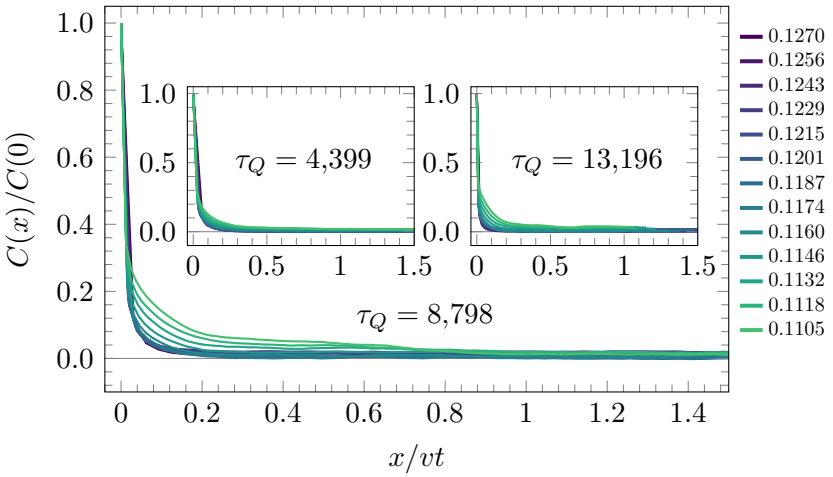

Figure 4.19: Equal-time correlations of the magnetisation shown at different temperatures throughout the quenches. The quench time is given in each of the figures, and the linear protocol goes from $T_i = 0.1381$ to $T_f = 0.1105$. Distances are scaled with the velocity of a straight domain wall given by $v \approx 0.0915$. For the fastest quench, left inset, we do not observe a significant change in the correlations. The intermediate quench, the main image, shows characteristics similar to the instantaneous quenches for low temperatures, which agrees with the assumption that coarsening plays a role further away from the transition. For the slowest quench, this is not as clearly visible, and finite-size effects start to set in. The curves around the transition and for higher temperatures show no visible variation, making it impossible to attain information about the transition itself. Parameters as in Fig.4.6 but with $b_0 = 0.16$ and $T_{\text{rot}} \approx 1077.2$.

extract the data at the same temperatures for the different quench times to make them comparable. It turns out that the step size of the protocol, with 0.176, is very close to a fifth of the driving period, which is approximately less than one percent off. Thus, for simplicity, we use the same procedure as before.

The correlations for three different quench times are shown in Fig. 4.19 where the x-axis of each is scaled with the velocity of a straight domain wall taken from the one-dimensional data, Fig. 3.2. Each curve is averaged over three different runs. For the quench time shown in the main image, we see a plateau-like structure for the last three temperatures shown. The drop to zero of those three curves happens at the same point at roughly $x \approx 0.72\,vt$, and we can deduce a linear time-dependence similar to the instantaneous quenches. Moreover, there is an additional shift in the height of the plateaus, which is strongest for short scaled distances. Here, we have to recall that we are changing the temperature in time and that earlier, for the instantaneous quenches, the plateau showed a dependence on temperature. Thus, we can attribute this shift to the change in temperature. For the faster quench, in contrast, we do not observe any plateau or significant shift in height at any of the temperatures (times) shown. On the other hand, for the slower quench, only a small sign of a plateau is visible. However, the shift in height for small scaled distances is

evident. Due to the longer times combined with the scaled distances, some of the curves do not extend to the end of the plot range, and overlap effects become visible. This leaves us with a much smaller range of possible quench times compared to the non-driven case. Additionally, we show the correlations of an even slower quench, where the correlation length clearly exceeds the system size, and the fully ordered state is acquired, in Fig. C.5 in the appendix. As an orientation, we can look at the distance a straight domain wall moves on average during one rotation for the given parameters. This length is $\bar{x}_{\mathrm{rot}} = v \cdot T_{\mathrm{rot}} \approx 98.6$. This means that a domain wall needs roughly 13 rotation periods to travel through half the system. Future efforts with larger system sizes might give better insights since this would allow for slower quench times.

So far, the discussion was purely about the slower quenches further away from the transition, where the dynamics are mostly dominated by the moving domain walls with constant velocity. However, we are not able to draw any conclusions from the data closer to the transition. The curves for temperatures near the transition and higher fall roughly on each other. The change, even for non-scaled distances, is small and slightly oscillatory. The latter could be an effect of the not exact stroboscopic measure and the low amount of averaging. Alternatively, it could also come from the transition itself. In [34], it was shown that the transition in the effective theory is rendered first-order under the drive. Thus, it could be that we observe a metastable state. One possible direction for further studies would be to increase the number of samples to average on and measure much more values in the early regime around the transition for quench speeds similar as in Fig. 4.19. An alternative approach could also include changing the quench protocol, e.g., to a function that spends less time close to the phase transition itself.

As a last point in this discussion, we show snapshots from one simulation with $\tau_Q = 8{,}798$ in Fig. 4.20. Notice that we only show snapshots from after the transition. This is simply because there is no visible difference between the images before that point, which agrees with the fact that the correlations do not show many variations in this regime. However, at lower temperatures, the coarsening with clearly recognisable moving domain walls sets in. This turns in at the same time as the plateau-like structure in the correlations. Thus, the earlier conclusion to identify the shape again as a result of the moving domain walls can be confirmed.

To conclude this subsection, we want to emphasise that the slow quench behaviour at temperatures further away from the transition shows the expected behaviour in agreement with the instantaneous quenches up to the accuracy of the simulations. However, we are unable to reach definitive conclusions regarding the behaviour of the phase transition.

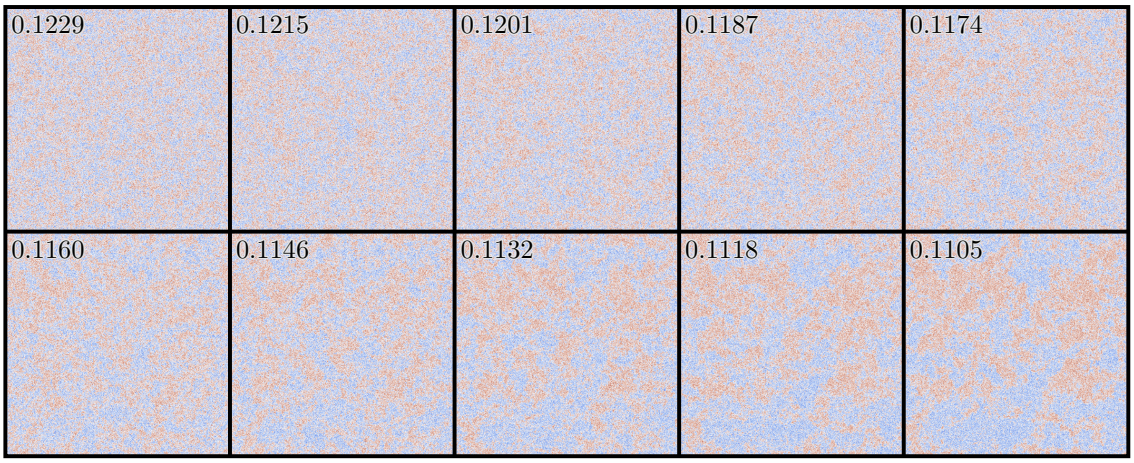

Figure 4.20: Snapshots from one simulation following the Kibble Zurek mechanism in the driven system for a quench time of $\tau_Q = 8{,}798$. The transition is at roughly $T_c \approx 0.1250$, and we show only snapshots from after the transition. The temperatures of the protocol at the time of the snapshots are shown in the upper-left corner of each image. The images above the temperatures shown do not show much variations. For low temperatures, bottom row, we observe moving domains which grow in size in accordance with the instantaneous quenches. Parameters as in Fig. 4.19.

4.9 Vortices in the Two Models

In the previous sections, we focused solely on the regime without vortices, where the effective model can qualitatively describe the physics of the microscopic model. Here, we want to briefly study the effect of vortices in two dimensions and examine the differences between the two models in the absence of thermal fluctuations.

We start with the microscopic ferrimagnet with one example simulation at higher fields and our usual parameter choice. Snapshots of the simulation are shown in Fig. 4.21 for a bit more than one rotation period. The vortices are marked with dots in blue for a winding number of -1 and in red for $+1$. We calculated them similarly to the one-dimensional case, Sec. 3.7, but now not in space-time but in space-space. Nevertheless, this also hides an aspect. In contrast to the one-dimensional case, where the vortices showed up at a specific point in space-time, they now exist until they annihilate again. At each vortex, the magnetisation peaks to its maximum of $m = 1$, as before. Therefore, the vortices would be visible even without our emphasis on red and blue dots due to the strongly increased magnetisation value precisely at the vortex core. However, we are also interested in the winding number, which would not be visible from the peaks in m.

In the upper half, close to the middle of each snapshot in Fig. 4.21, we find a nice example of an area where several vortices get created over the time range shown. Notice that due to topology, only vortex pairs can be created. We can compare this to the one-dimensional case and observe that, near the domain wall, there is a line

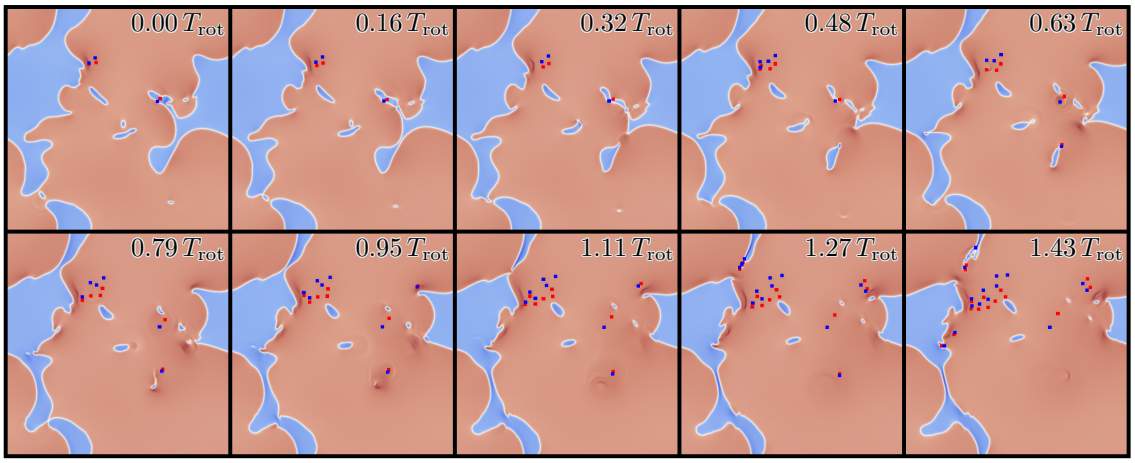

Figure 4.21: Snapshot from a simulation of the microscopic model with vortices. It is nicely visible that a line of enhanced magnetisation near the domain is the source of the vortices, similar to the one-dimensional case. However, this source is only on one side, and the domain is still moving. The vortices do not annihilate quickly and can thus influence the coarsening process. Parameters: $J = 1, \Delta = 0.8, \alpha = 0.1, \delta_2 = -2 \cdot 0.6, \delta_4 = 2, b_0 = 0.5, \omega = 2 \cdot 3.6$ and thus $T_{\mathrm{rot}} \approx 110.3$ for a system of 500×500 sites.

with enhanced magnetisation. This serves as a point of creation for the vortices. In one dimension, we found a similar enhanced profile in space very close to the point where the vortices emerged for the time-averaged data shown in Fig. 3.19. Nevertheless, in two dimensions, it extends into a line and is present only on one side of the domain, specifically, the side opposite to the direction of movement. Moreover, this is an additional difference: the wall is not localised but moves slower. Moreover, the line of enhanced magnetisation can have vortices at several points. This simple observation explains why more than one vortex pair can be created per rotation period. We observe this behaviour at every other point where vortices are created. Furthermore, the vortex pairs show a long lifetime even when they stay close after their creation. This comes from the gradients in ϕ, which only decay slowly far away from the domain walls. Due to this long lifetime, the vortices created by one domain wall can influence the dynamics of another further away and influence the coarsening process. We have found several similarities to the one-dimensional localised wall but with some changes due to the different geometry.

The story is very different for the effective model. Notice that here, we do not have the constraint that the magnetisation vector is normalised, and the mechanism described above does not exist in this model. However, we can still tune the system in a regime where vortices show up by adjusting the drive, even without thermal fluctuations. Snapshots from one of those simulations are shown in Fig. 4.22. The vortices are marked in the same way as for the microscopic model. However, the picture is very different. We do observe semi-stable straight domain walls, which are

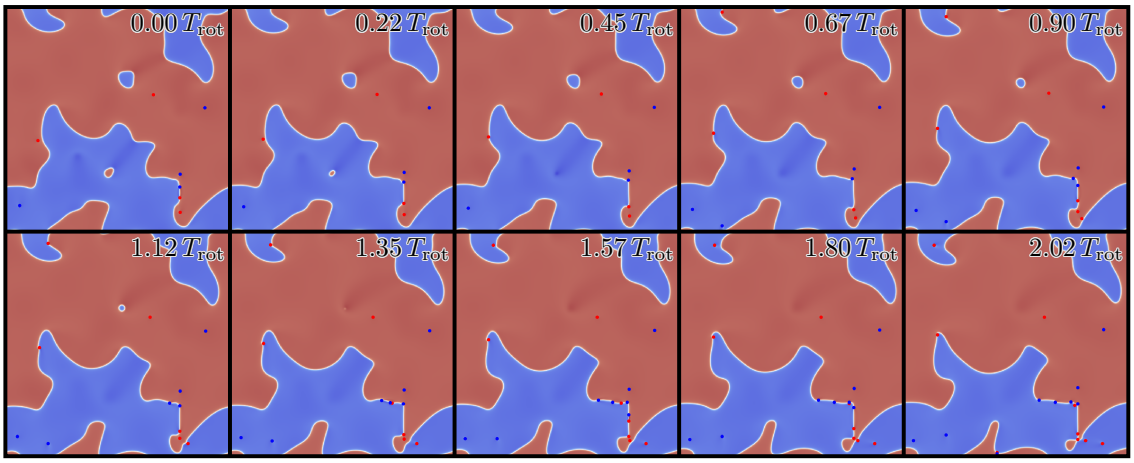

Figure 4.22: Snapshot from a simulation of the effective model with vortices. In fact, semi-stable straight-domain walls are a source of vortices. The point of creation is roughly in the centre of the line, and the oppositely charged vortices move in opposite directions along the wall until they reach the ends. Parameters: $r = -0.5, u = 1, D_m = 1, D_\phi = 1, \alpha = 1, \iota = 0.1$ for a system of 600×600 sites.

the source of vortices. Within the effective model, the vortex pairs are created at the domain walls and move along the wall in opposite directions. When the wall curves, the vortices move into the domain and stop following the wall. Furthermore, the vortices are created approximately in the middle of the straight part of the domain wall. This process happens roughly every rotation period. It follows the story where the tension which builds up due to the dynamical frustration is exactly at the wall, in contrast to the microscopic model, where a finite region around the wall does not rotate, and the tension builds up close but not at the wall. The process in the effective model comes from the fact that the system is discretised with a finite lattice spacing a and the energy to separate a pair scales with $\sim \ln\left(\frac{\Delta\rho}{a}\right)$ where $\Delta\rho$ is the final separation distance. Under the effect of the drive, the system uses this route to dissipate energy and lift the dynamical frustration.

While we do not have an analytical theory for either of the models of the vortex regimes, our numerical analysis gives important insight into the differences and causes of the observed phenomena.

5

Phase Transition in the Three-Dimensional Ferrimagnet

While our previous discussions have primarily focused on the characteristics of domain walls and only lightly touched upon the phase transition, this chapter delves into the phase transition in three dimensions in a brief exploration.
Here, we refer to existing literature that has investigated a transition between a static order and a rotating order [34]. In the study, a non-perturbative approach based on Dyson-Schwinger equations for non-equilibrium $O(2)$ models has been used. The authors find that the fluctuations diverge so strongly below the upper critical dimension, $d < d_c = 4$ that they can give rise to a fluctuation-induced first-order transition. As an important insight for us, they show that the effective model of the ferrimagnet can be mapped to the class of models they studied. Thus, they reveal that the ferrimagnetic transition is rendered first order upon driving the system out of equilibrium. We will now briefly discuss the mapping and the limit to which the first-order transition is expected within our choice of notation. For this discussion, we follow mostly Sec. VII. of [34]. Our goal in this chapter is to investigate this transition numerically.
To stay close to the discussion in [34], we use the non-shifted version of the effective equations, Eq. (2.41), instead of the ones directly comparable to the microscopic system, Eq. (2.43). To improve readability, we state them here again with

$$\begin{aligned} \alpha\dot{\phi} &= -\alpha\iota m + D_\phi \nabla^2 \phi + \dot{m} + \eta_\phi \,, \\ \alpha\dot{m} &= -rm - um^3 + D_m \nabla^2 m - \dot{\phi} + \eta_m \,. \end{aligned} \tag{5.1}$$

Notice that there are also some differences in the signs compared to the expressions given in [34] which relates back to the fact that the effective equations stated above are based on a description with magnetisation while the paper relies on the spin system. The two vector-valued quantities point in opposite directions. However,

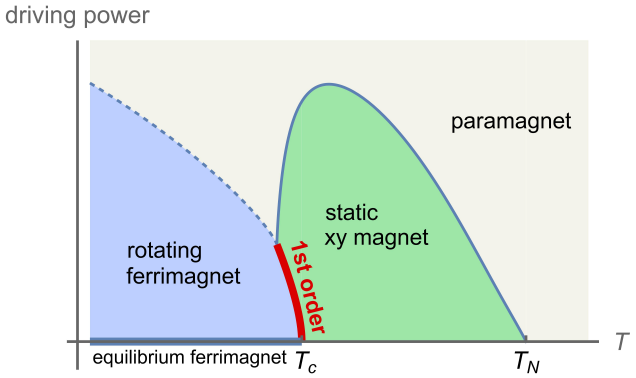

Figure 5.1: Phase diagram of the ferrimagnet where the equilibrium ferrimagnet is assumed to have the transition in m at $T_c < T_N$. T_N denotes the transition of in the xy-order, ϕ. The transition for the driven ferrimagnet is predicted to be a first-order transition. Above a certain driving power estimated by Eq. (5.3), the xy-order breaks down after the transition, and the transition arises between the paramagnetic and the rotating phases. Figure taken from [34].

the differences do not influence the conclusions for the transition. For any non-zero value of ι, a finite average value of m leads to a rotating phase in the xy-order, ϕ. Thus, it creates a transition between a rotating and a non-rotating phase. A phase diagram taken from [34] is shown in Fig. 5.1. For not too large values of the driving power, $\sim \iota$, the transition between the rotating phase and the static phase of ϕ is of a first-order nature. Above, the static xy-order breaks down, and the transition is between the disordered (paramagnetic) phase and the rotating phase, which has a possible non-equilibrium universality class.
The effective theory used to investigate the first-order transition is given by

$$\left(\partial_t^2 + (\delta - Z\nabla^2)\partial_t - v^2\nabla^2\right)\phi + \frac{g}{6}(\partial_t\phi)^3 + \eta = 0\,, \tag{5.2}$$

for the transition in $O(2)$ models. To map our effective model to this one-field equation, the first assumption is that η_ϕ is suppressed in the first equation. This is true for length and time scales larger than $(\alpha\iota)^{-1}$. Additionally, we assume that the damping parameter is small and keep only leading order terms in α. Next, we use the first equation to eliminate m in the second equation. For small frequencies and large wavelengths corresponding to the limit of long times and large distances, we arrive at the effective theory stated above, Eq. (5.2). The control parameter of the phase transition is $\delta = \frac{\iota\alpha(r-\iota)}{r}$ and thus, the transition occurs at $r = \iota$. Close to the transition, the other parameters fulfil the following relations within our choice of notation and signs: $Z = \frac{D_\phi}{\alpha}, v^2 = D_\phi\iota, g = \frac{6u\alpha}{\iota^2}$ and $\eta = \iota\alpha\eta_m$. Note that the coefficient labelled by v can be identified as the velocity of the domain walls, compare to Eq. (3.6).

From this mapping, we can adjust the criterion given in [34] for the first-order transition in our notation to

$$\frac{6u\alpha^2}{\iota} \gg 1\,. \tag{5.3}$$

For the opposite limit, the xy-order is said to break down, giving rise to the transition between the rotating and the paramagnetic phases. From this, we can estimate that large driving power is reached when $\iota \sim 6u\alpha^2$ above which the xy-order breaks down.

With these insights, we now move to the numerical study of the transition. Although some of the claims are also true in two dimensions, we use the three-dimensional case to avoid possible issues from quasi-long range order and logarithmic corrections. In order to scale through the phase transition, we want to use a Landau paradigm for which $r \sim T - T_c$ gives the control parameter in mean-field theory, where the transition takes place at $r = 0$. Beyond mean-field theory, there is an additional shift in the transition point. In general, the shift can be estimated via the linearised equations in a self-consistent approach, see, e.g., [107] for the Ginzburg Landau framework for superconductors. However, we do not need to approach this here for our coupled equations. In addition, there is a shift from the driving. Therefore, we anticipate the transition not at $r = 0$ but at a non-zero value of $r = r_c$.

For accessibility reasons, we use $M = \frac{1}{L^3}\sum_{i,j,k} m_{i,j,k}$ as the order parameter. We assume that a signature of the first-order transition is also visible in this quantity due to the relation from the drive in the first equation.

In general, more information about the phases and the transition is in the distribution function of the order parameter. However, the distribution function itself is often difficult to obtain, but information about it can be extracted from higher moments of the order parameter. A quantity which has become very useful to analyse phase transitions is the Binder cumulant [108] given by

$$U_B = 1 - \frac{\langle M^4\rangle}{3\langle M^2\rangle^2}\,. \tag{5.4}$$

Here, $\langle \dots \rangle$ denotes a statistical average. For a Gaussian distribution, the fourth moment in the thermodynamic limit becomes $\lim_{L\to\infty}\langle M^4\rangle = 3\langle M^2\rangle^2$, following Wick's theorem [109], and thus, $U_B = 0$. This is a good description of the disordered phase of m, where its average value is zero. Conversely, in the ordered phase, the system predominantly exists in a single-domain state, with the order parameter close to its maximum value. Thus, the distribution sharply peaks around this value, and the fourth moment is very close to the second moment. Consequently, the Binder cumulant takes a value of $U_B = \frac{2}{3}$ deep in the ordered phase, $T \ll T_c$, in the thermodynamic limit.

So how does the Binder cumulant behave for the two different types of transitions, and can we use it as a quantity to detect them? For a continuous phase transition, the scaling is given by

$$U_B = g((r - r_c)L^{\frac{1}{\nu}}), \tag{5.5}$$

where g is a universal scaling function, L the linear system size and ν the critical exponent. Certainly, for a finite-size system, all quantities are dependent on the system size. For the two moments in the Binder cumulant, $\langle M^4 \rangle$ and $\langle M^2 \rangle^2$, the scaling is exactly the same at the transition. This leads to a crossing point for curves with different system sizes, which can be used to determine the critical point r_c. An advantage of the Binder cumulant is thereby that the usage of different system sizes and of two higher-order cumulants substantially reduces finite size effects compared to only one cumulant or the order parameter itself [110]. Scaling and crossing points can be used to identify whether the transition is of a second-order nature. Furthermore, one can perform a crossing point analysis as nicely described in the supplement of [111]. However, this is only feasible for very high-quality data. For a first-order transition, in contrast, there is no unique crossing point and close to the critical point within the disordered phase, the Binder cumulant can attain very large negative values. The scaling of the negative peak goes by L^d [112]. This arises due to the double peak structure in the order parameter distribution. This can be used to identify if the transition is of a first-order nature.
Thus, the Binder cumulant serves as a good quantity to identify the nature of the transition. An example where this has been used to detect a first-order transition is a modified version of the Vicsek model with self-propelled particles [113].
In Fig. 5.2, we show the Binder cumulant for different system sizes up to $L = 40$, which is the upper limit of what we can reasonably simulate. Due to the slowing down near the transition, which increases with system size, each increase in system size is linked with an increase in the time needed to be simulated. Both a longer time to simulate and larger system sizes increase the runtime. We simulated $(1.35, 1.89, 2.57, 3.51, 4.93, 6.75) \cdot 10^6$ for the linear system sizes $(20, 24, 28, 32, 36, 40)$, respectively, to compensate for the slowing-down near the transition. The time distance between the data points follows the same trend with $(210.0, 294.0, 399.0, 546.0, 766.5, 1050.0)$. For all sizes smaller than 20, the same time values as those for 20 sites were used. To support this choice, we show equal-space time-correlations of m in Fig. D.1 in the appendix for the two different system sizes $L = 20$ and $L = 40$. Although the time steps between the correlation points shown are ten times larger than the distance between the data points in this chapter, we see nicely that it instantly drops, and neighbouring points are quasi-uncorrelated. This gives us at least ~ 600 independent data points per time series of M to average over for each point

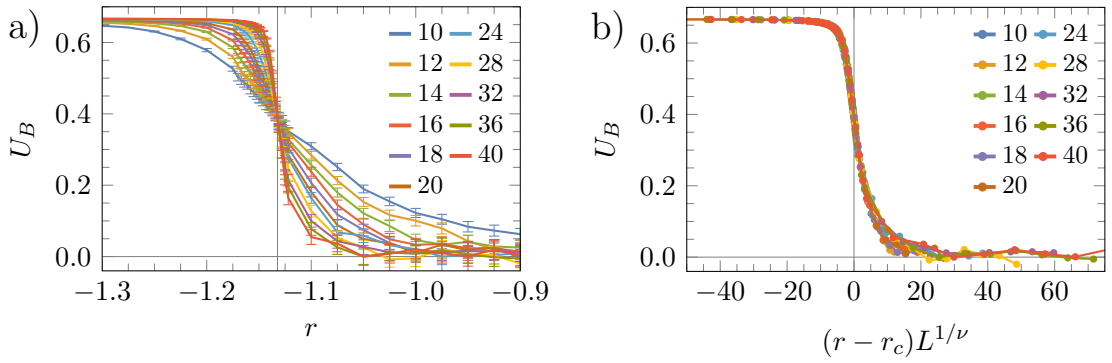

Figure 5.2: The Binder cumulant is shown as a function of the control parameter, Eq. (5.4), for 11 different system sizes where each point is averaged over time and three different runs. Panel a) shows the unscaled data. We observe a distinct crossing point at $r_c \approx -1.1323(4)$ determined from the mean from the different crossing pairs $(L, 2L)$. There is no signature of a negative peak corresponding to a first-order transition. Panel b) shows the same data in a scaling plot following Eq. (5.5) with $\nu \approx 0.63$ from the Ising class. We archive a nice data collapse. Parameters are $\alpha = 0.1, u = 3, D_m = 0.8, D_\phi = 1, \iota = 0.04$ and $T = 0.5$.

in the graph. The parameters we used are based on the conversion rules and roughly correspond to those used in the previous two chapters. A larger temperature was chosen, once because of the increase in spatial dimension and thus in the number of couplings and second to enhance the critical regime where fluctuations become important.

Fig. 5.2a) shows the unscaled data. First to notice is that we do not observe any signature of a negative peak related to a first-order transition. Then again, there is a unique crossing of all curves. We estimate the critical point as $r_c \approx -1.1323(4)$ from the mean of the crossing points of the different pairs $(L, 2L)$ and the error from the standard deviation. The solid vertical line highlights this critical value. In Fig. 5.2b), we show the same data but in a scaling plot following Eq. (5.5). A good data collapse is reached for $\nu \approx 0.63$ which is the same critical exponent as for the Ising class. Visible deviations are only present in the disordered phase, where the Binder cumulant becomes small.

We also show the second moment alone in Fig. 5.3a) around the transition. Further away from the ordered phase, we find a nice data collapse. Notice that we did not apply any scaling. This is an imprint of mean-field behaviour where fluctuations are negligible. In this limit, the fluctuations of the order parameter are much lower than the average value of the order parameter over the same volume. This criterion was first estimated for the Ginzburg Landau theory by Levanyuk [114] and reformulated by Ginzburg [115]. Hence, it is often only referred to as the Ginzburg criterion. A detailed explanation can be found in [116]. Closer to the transition, fluctuations become important, and the curves become sharper with increasing sys-

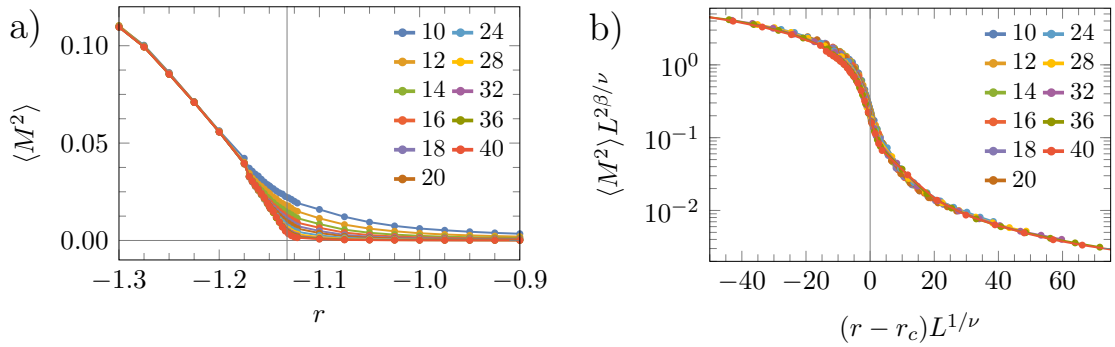

Figure 5.3: The second moment of the order parameter is shown as a function of the control parameter for the same data as in Fig. 5.2. Panel a) shows the data without any scaling. The curves initially converge into a single line and then spread closer to the transition. This shows nicely the point where fluctuations become important. Panel b) shows a scaling plot of the same data following Eq. (5.6) with the same value for the critical point as in Fig. 5.2, $r_c \approx -1.1323(4)$, and $\nu \approx 0.63$ and $\beta \approx 0.326$ from the Ising class. Again, a nice data collapse is achieved, with slight deviations from finite-size effects. Parameters as in Fig. 5.2.

tem size, showing a spread between them. Similar to the Binder cumulant, there is also a scaling relation for the order parameter given by

$$M = L^{-\frac{\beta}{\nu}} f((r - r_c)L^{\frac{1}{\nu}}) \,, \tag{5.6}$$

where f is a universal scaling function and β the critical exponent. Fig. 5.3b) shows the same data for the second moment, as before, but within a scaling plot. Since the order parameter is squared, the scaling exponent gets an additional factor of 2. Notice that we used a log scale to enhance the small values near the transition visually. Again, we imposed the Ising exponents with $\beta \approx 0.326$. This assumption gives a nice data collapse with only small deviations related to finite-size effects.
Within this investigation, all characteristics fit a second-order transition with Ising exponents. Our data is, however, not sufficient to perform a full crossing point analysis to fit the critical exponents and extrapolate to the thermodynamic limit. Nevertheless, we confirmed scaling behaviour and found a unique crossing point in the Binder cumulant. One could argue that we are not at the best limit to resolve the first-order transition from the criterion Eq. (5.3) with a value of $4.5 > 1$. However, the correlations in the xy-order never drop below $\sim 86\%$ of the maximum, and we do not observe any free vortices throughout the study, i.e., the xy-order is stable at all values shown. Nevertheless, in the appendix, we show data for a much smaller driving power, $\iota = 0.001$, in Fig. D.1. We keep the other parameters the same, and thus, the criterion is now $180 \gg 1$. Much lower driving power is not feasible because of numerical resolution. Although we drastically changed the criterion, a good data

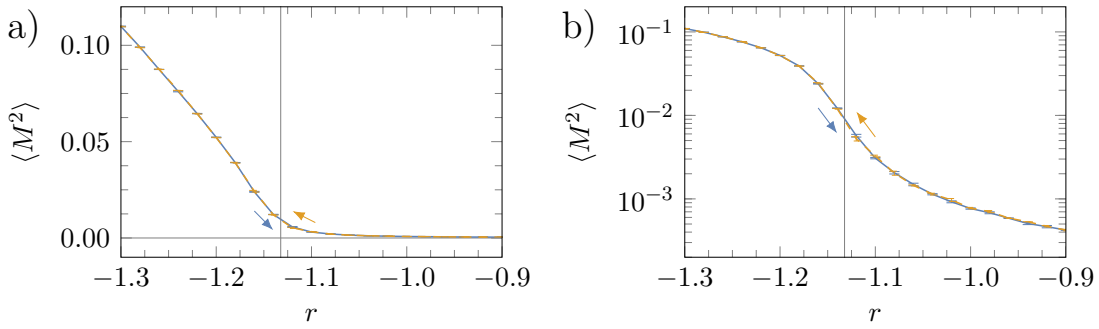

Figure 5.4: Data from hysteresis loops performed as written in the text where each point is the average of three runs, and the curves serve as a guide to the eye. The arrows denote the direction of the curves. The spread between the curves, particularly around the transition, is of the order of the error determined by the standard deviation of the mean. Parameters as in Fig. 5.2.

collapse is still archived for Ising exponents. In contrast to before, the critical point is shifted to lower values.

As an additional source of information, we want to use what is called hysteresis, another feature of a first-order transition. This phenomenon appears when cycling through the critical point. By tuning through the transition, once from the disordered phase and once from the ordered phase, it is possible to map out the regime where the two states coexist. In the case of a second-order transition, such a coexistence regime does not exist, and thus, no hysteresis is observed. For a more detailed discussion on hysteresis, we refer to [117] for equilibrium transitions. A study of a first-order transition in a driven-dissipative Bose-Hubbard model is presented in [118]. In [119] a discussion on the observability of hysteresis in equilibrium and non-equilibrium transitions is shown. We will now not delve further into hysteresis phenomena and will focus on applying it to our transition.

Fig. 5.4a) shows the result of a hysteresis protocol for a system of 20^3 sites averaged over three different runs. Again, we use the second moment of the order parameter as a measure. The arrows denote the protocol direction, the orange curve goes from $r = -0.9$ to $r = -1.3$, and the blue one is in the opposite direction. We use a step-wise function to scale through the r-values with a step size of $\Delta r = 0.02$. Each step takes a time of $1.6 \cdot 10^5$ to first relax to the stationary value, which is only a small amount of that $\sim 10^3$, and second, the rest to average over. Within the spirit of the hysteresis, we would expect the two directions to show a spread around the transition. However, this is not the case within the accuracy of the numerical data. Fig. 5.4b) displays the same data with a log scale to enhance the region around the transition. The small deviations near the transition are of the order of the error between the different runs. Thus, we do not observe the characteristic hysteresis of a first-order transition.

It is important to note that this analysis is by no means a definitive proof for a second-order transition. The transition is actually found to be weakly first order in [34]. This means the correlation length at the critical point becomes large but does not diverge. It is generally challenging to determine the nature of those types from numerical simulations. Within our data, the correlation length exceeds the system size at the transition. However, since we have no exact analytical prediction for the correlation length at the transition, we cannot declare if it is divergent or just larger than the system sizes we used. Since in a system smaller than the large value of the correlation length, the first-order signatures might not be visible, and the transition appears of a second-order nature. The study in [120] focuses on that question by analysing the two-dimensional Potts models, including $q = 5$, which is known to have a weak first-order transition where the exact correlation length at the transition point is known. With the help of the Binder cumulant, they find signatures such as systematic deviations from the data collapse at system sizes $N \sim \mathcal{O}(200)$ much below the correlation length $\xi \sim \mathcal{O}(2{,}500)$. Nevertheless, in their convention of the Binder cumulant, they also find the characteristic peak (in their convention positive instead of negative), with a small but visible scaling with system size. As explained before, we do not find those signatures in the scaling plots of the Binder cumulant.

A method proposed in [121], where a coupling to the order parameter is used to detect weak first-order transitions could be used for future investigations. While applied to quantum models, it should be possible to use a similar approach. The authors claim that moderate system sizes are sufficient for the detection, which might also reveal the signatures in our case. Furthermore, a stronger focus on $\dot{\phi}$ with a corresponding order parameter is a worthwhile consideration. Within our investigation, we did not succeed in defining a well-accessible order parameter for this quantity. However, it would be a more direct way to access the phase transition. In summary, within the limitations of the numerical simulations, e.g., regarding system size and runtime limits, we are not able to find signatures of the first-order transition.

Part II

Non-Equilibrium System with a Current

6

Current in a One-Dimensional Two-Particle Gas

The previous part focused on a magnetic system where the drive activated the Goldstone mode, which gave rise to physical properties where no equilibrium counterpart exists. Here, we want to study a simple particle model where a steady state current arises due to a drive. We also made efforts to induce a current in a driven Heisenberg model. However, we did not succeed. This is briefly described in App. E.

A system with a current is generally very different from one without a current. As an illustrative example, consider a lake and a river. The river has a steady state current in one direction, and if a blockage is placed at a certain point, the water piles up and particles much further away are influenced by the blockage. In the case of the river, only the particles in close proximity to the blockage are affected, while those located further away remain largely unaffected.

This simple consideration also raises the question of whether a system with a steady-state current can show true long-range order even in one dimension with short-range interactions. This is in contrast to the Mermin-Wagner theorem in equilibrium. The initial motivation behind our study was to investigate this question. For more general non-equilibrium scenarios, this has been confirmed for a harmonic chain driven out of equilibrium by athermal fluctuations in [122]. In this chapter, we develop a simple model with two particle types with steady-state current and draw similarities to existing studies, e.g., on anharmonic chains [123]. However, the proposed question remains unresolved and needs to be investigated further.

First, we explain the setup and its implementation, in particular, the way of driving and damping as part of an efficient framework. Then, we start with the study of just one particle type and find diffusive scaling in the moving frame of reference. Here, we use fluctuating hydrodynamics to make an analytical prediction, which has been very successful in the description of driven diffusive systems and their dynamical

Figure 6.1: Illustration of a part of the one-dimensional ring on which the particles of type A and B move. Each particle moves with a different velocity depending on its momentum and the driving protocol, which is displayed by arrows of different sizes. Interactions happen only upon collisions via elastic scattering.

universality classes [124]. Subsequently, we investigate the case with two particle types, where interactions play an important role. However, we do not manage to fully link it to the fluctuating hydrodynamic theory presented for similar works on discrete systems [123, 125].

6.1 Setup

Here, we want to explain the one-dimensional model used for the simulations and its implementation. The simulations are based on a code in C++ built upon an earlier version developed by Jonathan Lux [126]. It was already adapted to encounter for time-dependent hopping terms and tunnelling as well as periodic boundary conditions within a study of quenches to investigate the entropy production [127, 128]. For the current investigation, we want to add a mechanism to constantly drive the system, which also requires a cooling mechanism, to get a stationary state and avoid heating up to infinite temperature. First, we explain the model, including driving and damping, and then we briefly discuss the implementation. Within the model, the only conservation law is particle number conservation.

6.1.1 Model

The model consists of two different particle types, which we call type A and type B which move on a one-dimensional ring with different velocities. An illustration of a part of the ring is shown in Fig. 6.1. We assume an energy dispersion of the form

$$\epsilon_{A,B}(k,t) = -2J_{A,B}\cos(k + \phi_{A,B}(t))\,, \tag{6.1}$$

where $J_{A,B}$ denotes the hopping of an underlying Hamiltonian, here interpreted as a mass term, and k is the momentum. Notice that k is only defined modulo 2π for this dispersion. We confine the k-values to the range of $(-\pi, \pi)$ and use umklapp scattering when the momentum goes out of this range,i.e., we fold it back into the range by a shift of 2π. Thus, momentum is, in general, not conserved. To drive the system, we add a time-dependent contribution $\phi_{A,B}(t)$ to the momentum. The exact form will be explained in more detail later in this section. The velocity of each

particle is given by the group velocity defined by

$$v_{A,B}(k,t) = \frac{\partial \epsilon_{A,B}(k,t)}{\partial k} = 2J_{A,B}\sin(k+\phi_{A,B}(t))\,. \tag{6.2}$$

The evolution from time t_0 to time t is then simply described by the time given by $x_{A,B}(t) = x_{A,B}(t_0) + \int_{t_0}^{t} v_{A,B}(k,s)ds$. The only complexity of this integral comes from the driving. However, we choose a stepwise function, and within every step, $\phi_{A,B}(t)$ attains a constant value. Thus, assuming that t and t_0 are in the same step, i.e., $\phi_{A,B}(t) = \phi_{A,B}(t_0)$, the position formula simplifies to

$$x_{A,B}(t) = x_{A,B}(t_0) + v_{A,B}(k,t)(t-t_0)\,. \tag{6.3}$$

With this, we can describe the driven movement of the particles.
The interaction is given by classical elastic two-particle scattering. For identical particles (same mass, i.e., hopping) in one dimension, the momenta are only exchanged. Therefore, the momentum distributions remain the same. For distinct particles, the total momentum and energy are conserved during the scattering event. Assuming we have a particle with momentum k_1 and a particle of the other type with momentum k_2, we can write two conditions,

$$\begin{aligned} k_1 + k_2 &= p_1 + p_2\,, \\ \epsilon_1(k_1,t) + \epsilon_2(k_2,t) &= \epsilon_1(p_1,t) + \epsilon_2(p_2,t)\,, \end{aligned} \tag{6.4}$$

where p_i denotes the final momenta. We use the labels 1 and 2 for the dispersion, where one of the two is of type A and the other is of type B. A crucial point in one dimension is that this set of equations has a unique solution which we can determine. The trivial solution is the transmission case where the momenta remain unchanged, $p_1 = k_1$ and $p_2 = k_2$, and the particles *tunnel* through each other. The non-trivial solution is given by

$$p_1 = 2\arctan\left(\frac{J_2\sin\left(\frac{\tilde{k}_1}{2}+\tilde{k}_2\right) - J_1\sin\left(\frac{\tilde{k}_1}{2}\right)}{J_2\cos\left(\frac{\tilde{k}_1}{2}+\tilde{k}_2\right) + J_1\cos\left(\frac{\tilde{k}_1}{2}\right)}\right), \qquad p_2 = k_1 + k_2 - p_1\,, \tag{6.5}$$

for $J_1 \neq J_2$. For brevity, we used $\tilde{k} = k + \phi_{A,B}(t)$. If the momenta exceed the interval of $(-\pi,\pi)$, we fold them back by adding or subtracting 2π which characterises the umklapp scattering. Notice that the special case of $k_1, k_2 = \pm\frac{\pi}{2}$, which leads to zero total energy and transmission as the only solution, is never reached exactly within the numerical precision. With this, we have completed the discussion of the interactions between the different types.

For the damping mechanism, we also use elastic scattering with a third particle type, bath particles. We assume that our one-dimensional ring, on which the particles of types A and B are confined, lies in a three-dimensional space in which the bath particles move. Eventually, a bath particle crosses the ring and scatters with one of the A, B-particles. Due to the confinement to the ring, the momentum exchange happens only in the ring direction, and we can use the same formula as before, Eq. (6.5). After the collision, the bath particle moves away from the ring due to the momenta in the other two spatial directions. Furthermore, the bath particles' momentum distribution is assumed to remain at the same temperature with the same thermal distribution. This assumption holds in the limit of a much larger number of bath particles. If the bath temperature is now lower than the one in the system, energy is dissipated via the scattering and the system is cooled down. The level of cooling is thereby directly proportional to the number of bath scatterings in a certain time interval. We define τ_{bath} to be the average time between scattering events with bath particles. Thus, we provided a simple method which relies on the same type of interactions to cool the system.
The part of interest is certainly the driving protocol which finally leads to a non-zero current in the system. This is a state very different from any equilibrium counter part. To ensure better traceability while still initiating a current in the system, we set the following three requirements for the driving protocol: (i) A stepwise protocol to simplify the numerical implementation. (ii) A periodic shape for stable time dynamics. (iii) The breaking of time reversal symmetry in the system, which together with (ii) can give rise to a steady-state current.
Those requirements are fulfilled by the protocol shown in Fig. 6.2a) which will be used throughout the study. It is stepwise and periodic since a shift of 2π results in the same outcome due to the defined energy dispersion. In addition, time-reversal symmetry is broken due to the different times at which the values change from one step to the next in combination with scattering events. However, the bath particles already satisfy this condition, and even if there is just a single particle type, a current can emerge.

6.1.2 Implementation

A crucial point of the simulations is that we do not simulate the actual time evolution of each particle at each point in time but can calculate the scattering events directly and update the states, i.e., the times and positions of the particles, according to a time-sorted list. This is much more efficient and allows for larger system sizes and time scales. In the following, we will outline the general scheme of the simulations.

1. Initialisation: only performed once at the beginning

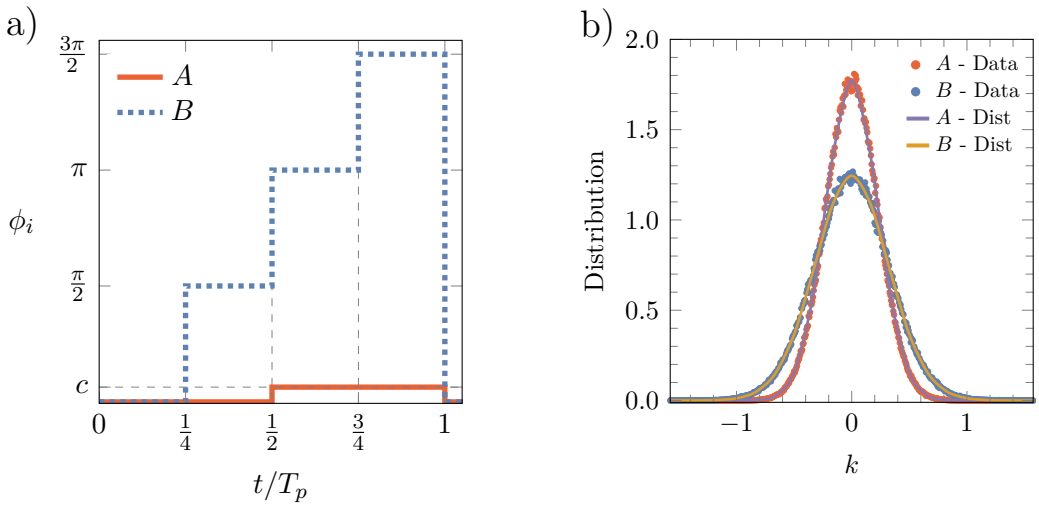

Figure 6.2: Panel a) The driving protocol is shown for one driving period T_p. The particle types A and B are driven by different magnitudes, and changes do not always occur at the same point. $c = 0.2$ denotes the height of protocol for type A particles. The protocol for type B particles is in steps of $\frac{\pi}{2}$ which ensures that a four-step protocol is still periodic with respect to the energy dispersion, Eq. (6.1). Panel b) displays the momentum distribution of the two particle types for an equilibrium simulation, $\phi_{A,B}(t) = 0\ \forall t$, averaged over 600 different times in the stationary state. The dots denote the data, and the lines denote the expected equilibrium distribution at the bath temperature. Data and theory are in very good agreement. Parameters: $N_A = 5{,}000 = N_B, N = N_A + N_B, J_A = 2, J_B = 1, T_{\text{ini}} = 1, J_{\text{bath}} = 0.2, T_{\text{bath}} = 0.2, \tau_{\text{bath}} = \frac{1.5}{N}$.

  - initial equilibrium state: draw $x \in (0, L)$ uniformly and $k \in (-\pi, \pi)$ Boltzmann distributed according to $\sim e^{-\frac{\epsilon(k)}{T}}$
  - initial scattering time list T^*: calculate t^* from $x_i(t^*) = x_j(t^*)$ from the analytical expression using Eq. (6.3) for all neighbouring pairs and store all potential scattering times, i.e., $t^* > 0$ in T^* which is a sorted list of the multimap class (keeps the list sorted in ascending order) in C++

2. Scattering loop: T^* and the position of all particles are updated every quarter of T_p to take into account the change in the driving, Fig. 6.2

  - bath scatterings: before the next scattering event, perform bath scatterings with an average time difference of τ_{bath} from a uniform distribution
    * uniformly randomly select a particle P on the ring to scatter with
    * erase all scattering events with P from T^*
    * draw a bath momentum k_{bath} from $\sim e^{-\frac{\epsilon_{\text{bath}}(k)}{T_{\text{bath}}}}$
    * update momentum of P according to Eq. (6.5) with $\tilde{k}_{\text{bath}} = k_{\text{bath}}$
    * calculate the updated scattering times of P and its neighbours and add them to T^*

- A, B scatterings: if the next bath scattering would take place later than the next normal scattering, carry out a normal scattering
  - take the first element of T^*
  - erase all scattering events with the two involved particles from T^*
  - update the momenta according to Eq. (6.5) or, if the tunnelling probability is non-zero, perform a transmission event
  - calculate the updated scattering times of the involved particles and their neighbours and add them to T^*
- go back to the start of 2. until the final time is reached

3. Check for errors: the particles should be in the order of their positions, i.e., $x_i < x_j$ where $j > i$

While we do not describe all the details here, this scheme explains the general idea, order and nature of the important steps in the simulation. Note that the described bath scatterings boil down to keeping the same distribution, i.e., the same temperature from which the momenta are drawn, and one additional random number to choose the particle to scatter with from. We confirm this damping mechanism by an equilibrium simulation shown in Fig. 6.2b), i.e., where the driving protocol is zero at all times. The data points from the stationary state are compared to the expected momentum distribution at the bath temperature, $\sim e^{-\frac{\epsilon(k)}{T_{\text{bath}}}}\Big|_{\phi_{A,B}=0}$ with excellent agreement. Thus, our implementation of the bath particles is sufficient to cool the system to a thermal state in the equilibrium case.
A further crucial point in the implementation is that the scattering list T^* is updated when the next step in the protocol is reached and the driving strength changes. Thus, within our approach, a stepwise protocol is required.
As a last remark from the technical side, we should mention that there is also some sort of geometric conservation law. This is the configuration of A and B particles which is not altered by elastic collisions given by Eq. (6.5). To prevent that, we make use of the trivial solution, which is the tunnelling process. In the simulations, we specify a non-zero probability with which the particles tunnel through each other to break the geometric conservation law. This is only relevant in the case of two different particle types.

6.2 One Particle Type - Driven Diffusion

At first, we concentrate on the simple case of only one particle type. This goes joint with just one conserved field, the particle number of said type. While this

in itself is interesting, it also serves as a benchmark for the implementation of the driving and damping process. For the following discussion, we choose type B with the stronger driving protocol, see Fig. 6.2. While this choice makes some signatures more prominent, it does not affect the general conclusions.
Since we have one conserved quantity, in our case, the particle number, we can write down a continuity equation for the coarse-grained particle density as

$$\partial_t \tilde{\rho}(x,t) + \partial_x J(x,t) = 0, \tag{6.6}$$

where $\tilde{\rho}$ is the particle density and J the corresponding current density. Let us first focus on the equilibrium case, i.e., without driving and thus without steady-state current through the system. From a hydrodynamic perspective, we can then expand the current in the small density fluctuations ρ in the system around the average density ρ_0, i.e., $\tilde{\rho} = \rho_0 + \rho$. In leading order, we get $J_{eq}(x,t) \approx -D\partial_t \rho - \eta$ for the equilibrium current density, reminiscent of Fick's law [129]. Here, we included stochastic fluctuations within a Gaussian white noise, η, where the sign is just a convention. This yields the usual form of the noisy diffusion equation,

$$\partial_t \rho = D\partial_x^2 \rho + \partial_x \eta\,, \tag{6.7}$$

for which it is known that the density-density correlations scale with $\langle \rho(0,0)\rho(x,t)\rangle = t^{-\frac{1}{2}} f(t^{-\frac{1}{2}}x)$. We only briefly cover the necessary parts for the discussion. For a deeper introduction to fluctuating hydrodynamics, we recommend [130].
Now, we can move on to the driven scenario, where an average current is generated in the stationary state. Here, the current in Eq. (6.6) gets an additional contribution to the equilibrium parts, which we call j. We again expand in powers of ρ with $j(\tilde{\rho}) \approx j(\rho_0) + j'(\rho_0)\rho + \frac{j''(\rho_0)}{2}\rho^2 + \dots$ where the dots denote possible higher-order terms. This gives us

$$\partial_t \rho + j'\partial_x \rho + \frac{j''}{2}\partial_x \rho^2 = D\partial_x^2 \rho + \partial_x \eta, \tag{6.8}$$

which has the form of a noisy Burgers equation. A crucial point is the term proportional to the second derivative in the current, $\propto j''$. It leads to the different scaling of the density-density correlations with $\langle \rho(0,0)\rho(x,t)\rangle = t^{-\frac{2}{3}} f(t^{-\frac{2}{3}}(x - j't))$ [131]. This scaling has been derived exactly for the TASEP, totally antisymmetric simple exclusion process, model [132], which is a simple and well-studied model. From the scaling relation, we find that the $\propto j'$ term has been absorbed by going to a moving frame with velocity j', this is also reminiscent in Eq. (6.8). Notice that it is possible to map the Burgers equation to a Kardar-Parisi-Zhang (KPZ) equation [133] and

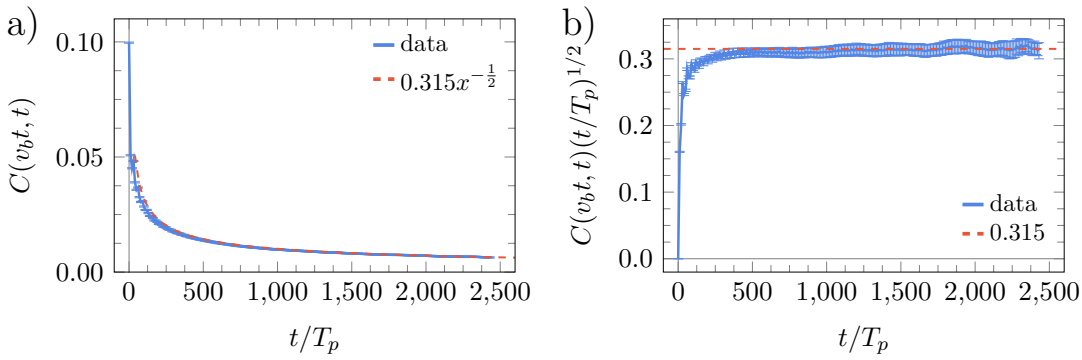

Figure 6.3: Diagonal space-time correlations according to Eq. (6.11) averaged over ten runs. Panel a) shows the data including a $\frac{1}{2}$-power-law decay as a guide to the eye. The error bars are the standard deviation of the mean. Panel b) shows the same data but in a scaling plot with the constant being the prefactor of the power-law in panel a). The agreement is very good, suggesting diffusive scaling within the long-time limit. Parameters: $L = 10{,}000, L_b = 1{,}000, N_A = 0, N_B = 10{,}000, N = N_B, J_A = 2, J_B = 1, T_{\text{ini}} = 1, J_{\text{bath}} = 0.2, T_{\text{bath}} = 0.2, \tau_{\text{bath}} = \frac{1.5}{N}$ and driving according to Fig. 6.2. The resulting velocity was measured as $v_b = 0.00812(3)$.

in fact, the scaling function for the TASEP model is the scaling function for KPZ growth, which is exactly given in [134].

However, this section focuses on only one particle density in the AB-model with elastic scatterings as interactions. Since the scattering events between the same particle type do not exchange momentum, the only true interaction happens with the bath particles. The steady-state current can be written in terms of the density and the velocity of the particles with $j = v\tilde{\rho}$ on average. Thus, $j'' = 0$ and $j' = v$. Therefore, we only expect diffusive scaling in the moving frame of reference, i.e.,

$$\langle \rho(0,0)\rho(x,t)\rangle = t^{-\frac{1}{2}} f(t^{-\frac{1}{2}}(x - vt)). \tag{6.9}$$

We now want to verify this with numerical data. To do so, we must define a particle density $\tilde{\rho}$ instead of a particle number N. In order to address this, we divide the one-dimensional strip of length L with periodic boundary conditions, i.e., a ring, into M_b equal boxes of length $L_b = \frac{L}{M_b}$. We label the position values of those boxes by x_b, which runs from 1 to M_b. Within each box, we average over the particle number within the box length, which yields a density. This resulting density can be used to calculate the density-density correlations and to compare to the expected diffusive scaling in the moving frame, Eq. (6.9). To determine the correlations, we use

$$\tilde{C}(x_b, t) = \frac{1}{N_p M_b} \sum_{s=1}^{N_p} \sum_{i=1}^{M_b} \tilde{\rho}_i(sT_p)\tilde{\rho}_{i+x_b}(sT_p + t) - \rho_0^2\,, \tag{6.10}$$

where we do not only average over all boxes M_b but also over many periods in the stationary state N_p. Notice that since we calculate the full density-density correlations, we subtract ρ_0^2 to be left with the correlations in the fluctuations. Before this step, the position was a continuous variable. However, the approach with the discrete boxes is necessary to define a density within a hydrodynamic picture. Nevertheless, it causes an artificial discreteness in the result. To arrive at a smoother result, we make a simple linear interpolation between the correlations of two neighbouring boxes via

$$C(x,t) = (1 - (x \bmod 1))\tilde{C}(\lfloor x \rfloor, t) + (x \bmod 1)C(\lfloor x \rfloor + 1, t) \tag{6.11}$$

where $\lfloor \dots \rfloor$ denotes the floor function, which takes a real number and gives an integer which is less or equal to that number.
In Fig. 6.3a), we show the diagonal correlations for $x = vt$ averaged over ten runs. We use a system of length $L = 10{,}000$ with an average density $\rho_0 = 1$, i.e, $N = 10{,}000$ of all type B particles and an average bath scattering time of $\tau_{\text{bath}} = \frac{1.5}{N}$ as for the equilibrium simulation, Fig. 6.2. For each run, the velocity is determined from the average velocity of the particles over time. The estimated velocity averaged over the different runs is $v = 0.0812(3)$ or $v_b = \frac{v}{L_b} = v_b = 0.00812(3)$ in units of the box length. For longer times after about 500 driving periods, we observe the diffusion scaling expected from the hydrodynamic argument given above, Eq. (6.9), with $C(vt, t) \sim \sqrt{t}$. This is better visualised by a scaling in Fig. 6.3b), where a constant value is attained for sufficiently large time values.
Another way of probing the scaling behaviour is via the shifted space correlations at different times. This is shown in Fig. 6.4a) for one of the runs used for Fig. 6.3. The velocity estimated for this run is $v \approx 0.0807$. The correlations have a similar form to a Gaussian distribution, and the maximum decreases over time while the correlations spread. The maximum stays at $x_b = 0$ in the plot due to the shift in the space component of the correlations. This confirms that the velocity determined is the correct velocity for the scaling function. Furthermore, we show a scaling plot in Fig. 6.4b) where, again, diffusive scaling was assumed. The data collapse is very good. This, in contrast to the diagonal correlations, does not only show that the maximum has a diffusive scaling but also that the spread of the correlations scales according to Eq. (6.9).
From this, we can conclude that the behaviour of the system with only one conserved quantity with a steady-state current is indeed well described by diffusive behaviour over large time scales in the stationary state.

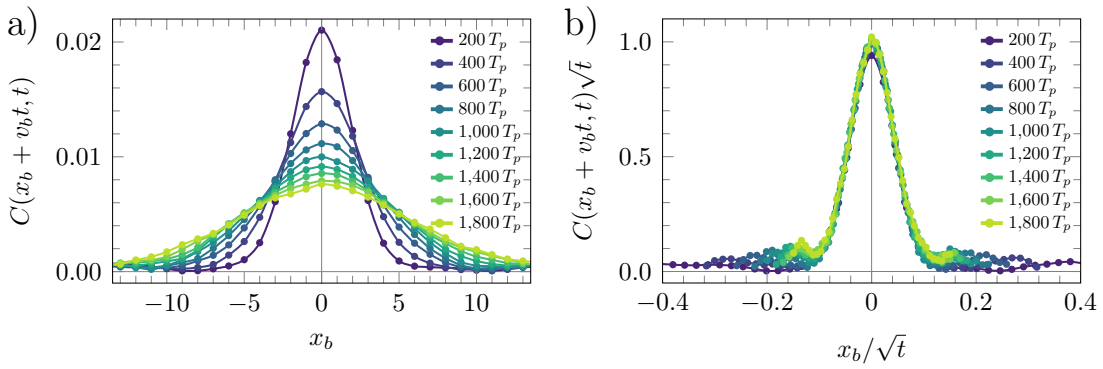

Figure 6.4: Space-time correlations shown as a function of space at different times determined via Eq. (6.11) from a single simulation. Note that the data becomes smooth due to the averaging performed according to Eq. (6.9). Panel a) shows the data with a shift of the position value in the correlations by $v_b t$ where $v_b \approx 0.00807$ is estimated as explained in the text. Since the maximum persists at $x = 0$, the correct value of the velocity is confirmed. The lines serve as a guide to the eye, and the dots show the data points. Over time, the correlations decay and the spread increases. Panel b) displays the same data but in a scaling plot following the hydrodynamic expectation, Eq. (6.9). The very good data collapse into one unified curve confirms the diffusive scaling. Parameters as in Fig. 6.3

6.3 Two Particle Types - Influences of a Current

After investigating the more straightforward case with just one particle type, we can now move to the case with the two different types with interactions upon them. Now, two quantities are conserved: The particle number of type A and the particle number of type B both follow the continuity equation given by

$$\partial_t \tilde{\rho}_\alpha(x,t) + \partial_x J_\alpha(x,t) = 0, \tag{6.12}$$

where $\alpha = A, B$. As in the previous section, we will first attempt to establish an analytic framework. For this, we assume the hydrodynamic limit where we can expand the current around small density fluctuations. The following discussion is adapted from [135]. We write the full density as a vector $\tilde{\boldsymbol{\rho}} = \boldsymbol{\rho}_0 + \boldsymbol{\rho}$ where the first entry is the density of type A and the second entry is the density of type B. The steady-state current gets the form

$$j_\alpha(\tilde{\boldsymbol{\rho}}) \approx j_\alpha(\boldsymbol{\rho}_0) + (Q\boldsymbol{\rho})_\alpha + \frac{1}{2}\boldsymbol{\rho}^T H^\alpha \boldsymbol{\rho} \tag{6.13}$$

up to second order, where $Q_{\alpha\beta} = \left.\frac{\partial j_\alpha}{\partial \rho_\beta}\right|_{\boldsymbol{\rho}=\boldsymbol{\rho}_0}$ is the Jacobian matrix and $H^\gamma_{\alpha\beta} = \left.\frac{\partial^2 j_\gamma}{\partial \rho_\alpha \partial \rho_\beta}\right|_{\boldsymbol{\rho}=\boldsymbol{\rho}_0}$ the Hessian matrix of j_α. ^{T} denotes transposition.

Adding the generalised Fick's law and fluctuations yields

$$\partial_t \rho_\alpha + \partial_x (Q\boldsymbol{\rho})_\alpha + \frac{1}{2}\partial_x(\boldsymbol{\rho}^T H^\alpha \boldsymbol{\rho}) = \partial_x (D\boldsymbol{\rho})_\alpha + \partial_x (K\boldsymbol{\eta})_\alpha \tag{6.14}$$

as the final equations. This is now much more complicated than in the case of just one conserved quantity due to the multiple coupling terms where both densities and prefactors occur. However, under certain conditions, it can be simplified.
The strategy is as follows: If Q has real eigenvalues and non-degenerate eigenvectors, we can define normal mode coordinates with $\boldsymbol{n} = R\boldsymbol{\rho}$ where R is the transformation matrix. This brings Q in the diagonal form $RQR^{-1} = \mathrm{diag}(v_{n_1}, v_{n_2})$ where v_{n_1} and v_{n_2} are the velocities of the normal modes. However, this is not yet a unique transformation since we can multiply R by any real number and still get the same diagonal matrix but not the same normal modes. To fix this choice, we first have to define the correlation matrix with entries $C_{\alpha\beta}(x,t) = \langle \tilde{\rho}_\alpha(0,0)\tilde{\rho}_\beta(x,t)\rangle - \langle \tilde{\rho}_\alpha\rangle\langle\tilde{\rho}_\beta\rangle$. This allows us to define the susceptibility matrix with $\chi_{\alpha\beta} = \sum_x C_{\alpha\beta}(x,t)$ for a system which is discrete in space. With this quantity at hand, we require that the normal modes are orthogonal in the steady state, which means that $R\chi R^{-1} = 1$. Together with the diagonalisation of Q, this yields a unique transformation up to a global sign.[123]
With the normal modes, Eq. (6.14) can be transformed into the normal mode basis. The crucial point is that if the velocities of the normal modes differ, i.e., $v_{n_1} \neq v_{n_2}$, the drift term dominates, and the dynamics separate on large scales in time and space. As we learned from the discussion with one conserved quantity, the correlations in space peaked around a mean value and moved with the velocity given by the drift term. If this is the case, only the diagonal parts of each term contribute, and the equations become

$$\partial_t n_i + \partial_x (v_i n_i) + \frac{1}{2}\partial_x(\tilde{H}^i_{ii} n_i^2) = \partial_x(\tilde{D}_i n_i) + \partial_x(\tilde{K}\eta_i)\,, \tag{6.15}$$

where the $\tilde{}$ denotes the basis change to normal modes for the previous terms in the equation, e.g., $\tilde{D} = RDR^{-1}$. Except for the slightly more complicated notation, the above equations are of the same form as the noisy Burgers equation for a single conserved field. Thus, we expect the same KPZ scaling behaviour for the two normal modes n_1 and n_2. However, in contrast to before, this is only true for long times and large distances if the velocities of the two modes differ.
After the extensive introduction, we would now like to apply the knowledge gained to the AB-model. At the outset, however, we must concede that these initial efforts were not as conclusive as we had hoped. Nevertheless, we will report on them to support future investigations.

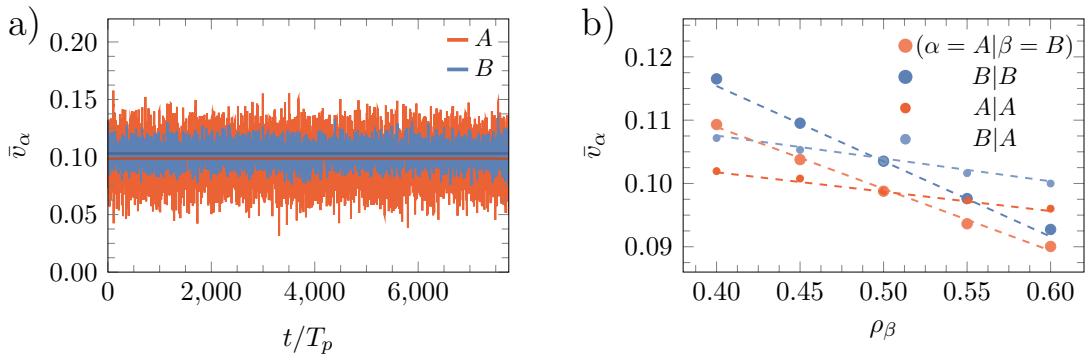

Figure 6.5: Panel a) shows the average velocities of the particles as a function of time for one simulation with $N_A = 5{,}000 = N_B$. The data has been averaged over a driving period, and an additional moving average over 8 periods was used to reduce the noise and make the trend more visible. The solid lines denote the mean value of the data shown. The two average velocities lie very close, which goes back to a lower transmission rate of 10%. The average velocity shows that our construction of a driven particle model leads to a steady state current. Panel b) shows the mean velocities as functions of the two different densities. The values of the linear fits are given in Eq. (6.17). Changing the density of type B has a more substantial effect on the velocities than a change in type A. This goes back to the stronger driving of type B particles. Parameters: $L = 10{,}000, L_b = 1{,}000, N = N_A + N_B, J_A = 2, J_B = 1, T_{\text{ini}} = 1, J_{\text{bath}} = 0.2, T_{\text{bath}} = 0.2, \tau_{\text{bath}} = \frac{1.5}{N}$.

At first, we track the velocities of the two different particle types to check if a stationary state is reached and whether our efforts to create a protocol that yields a finite steady-state current were successful. In Fig. 6.5a), we show the two average velocities from one simulation over many driving periods. Note that we performed a moving average to reduce the noise level. The solid lines show the average value over the shown scale. The values are $\bar{v}_A \approx 0.0987$ and $\bar{v}_B \approx 0.1031$, which are very close compared to the different strengths in the driving, Fig. 6.2. We see a finite average steady-state velocity in both particle types. Those correspond to a finite steady-state current in both particle densities. Due to the collisions, the velocity of one particle type depends on its own density and the density of the other type. Thus, we assume a form of

$$j_\alpha(\tilde{\boldsymbol{\rho}}) = v_\alpha(\tilde{\boldsymbol{\rho}})\tilde{\rho}_\alpha \,, \tag{6.16}$$

for the steady-state current. From this, we can now determine the Jacobian Q by varying the density of one of the types while keeping the other constant and vice versa. The result of the simulations is shown in Fig. 6.5b). We display the average velocities of the two types as a function of the two densities. The behaviour in all cases is approximately linear, and the dashed lines show a fit for each curve in the same colour. The slopes of the fitted curves and by using the product rule on

Eq. 6.16 the Jacobian, we get the following expressions

$$\left.\frac{\partial v_\alpha}{\partial \rho_\beta}\right|_{\boldsymbol{\rho}_0=(0.5,0.5)} = -\begin{pmatrix} 0.0977 & 0.0306 \\ 0.1189 & 0.0361 \end{pmatrix}, \qquad Q_{\alpha\beta} = \begin{pmatrix} 0.0500 & -0.0153 \\ -0.0595 & 0.0854 \end{pmatrix}. \quad (6.17)$$

This matrix has real-valued eigenvalues and is non-degenerate. We can diagonalise it and get two velocities, $v_n = (0.1027, 0.0327)$ and eigenvectors. The good news is that the values differ in magnitude, and the modes should be separated. However, a problem lies in determining the correlation matrix χ to utilise the second requirement for the normal modes, their normalisation. In fact, this matrix is always zero within the model for the particle densities. We tried to compensate for this by fitting the peak in each matrix entry with a Gaussian as an approximation. This neglects the negative dips and noise away from the peak. However, this did not give conclusive results at all times. In [136], a diagonal form with different strengths is assumed. In any way, this normalisation is just a rescaling of the normal modes and should only influence the magnitude. Direct use of the eigenvectors without additional correction with χ yields non-vanishing cross-correlations between the normal modes, which should not be the case from the hydrodynamic picture. Furthermore, the correlations of the normal modes do not move with the velocity from the eigenvalues. While parts of this might be possible to improve by averaging over more samples, the general drift of the peak and its velocity should not be significantly affected by that.

An issue within this approach is the determination of the current Eq. (6.16) including its derivative. Our approach relied on the assumption of Eq. (6.16). Another way could be the usage of current-density correlations, where one determines the current between the boxes and calculates the correlations with the densities. We implemented the measurements for the currents between boxes and confirmed that the continuity equations are fulfilled locally between the boxes. However, the calculation of the Jacobian remains open.

For completeness, we still show the actual correlations of the densities calculated with Eq. (6.11) in Fig. 6.6. The index denotes which densities are used to calculate the correlations. It is clearly visible that the autocorrelations have a very similar velocity, in the same way as the velocity of the particles is very similar. In contrast to a single conserved density, however, the curves do not fall on top of each other with the scaling of the particle velocities. This comes due to the non-vanishing cross-correlations, which also carry a velocity. Hence, a simple scaling plot similar to the previous section is not possible.

One further remark should be made. The results presented in this section have been simulated with a transmission rate of 10%. Increasing this rate will lead to a

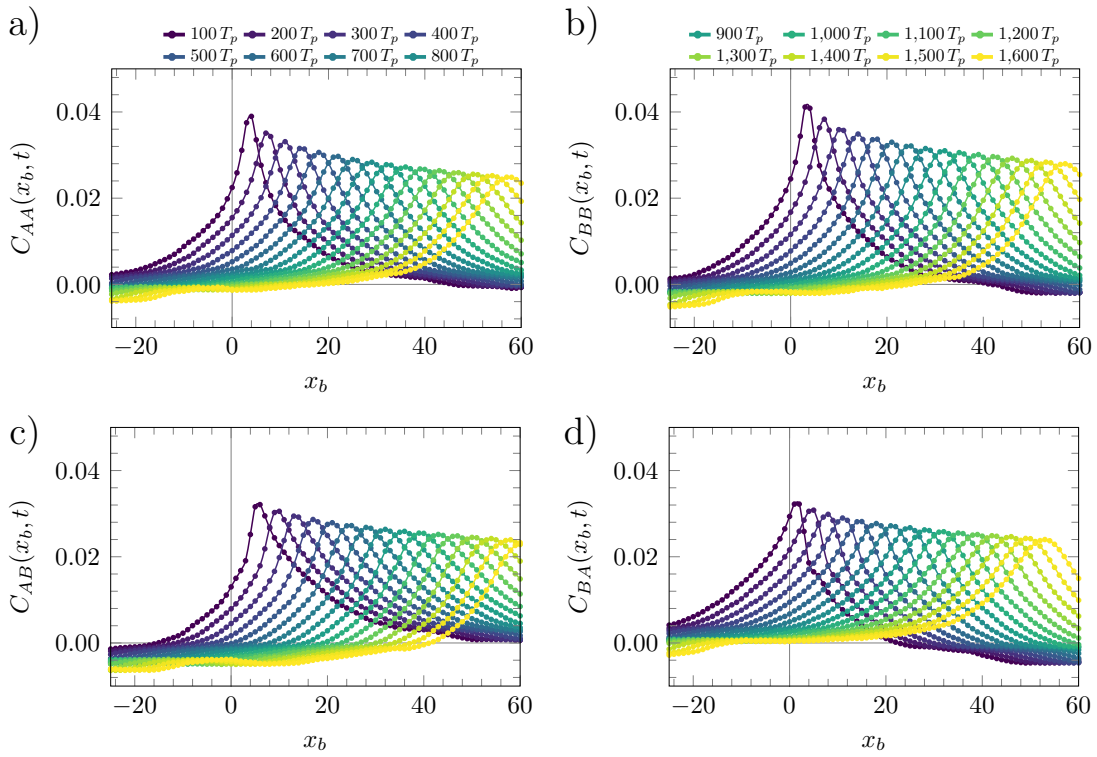

Figure 6.6: The equal-time correlations for the different density combinations as a function of space for different times. The colours in each plot show the same time, and the legend is split into panels a) and b) for compactness. Panels a) and b) show the auto-correlations, and panels c) and d) show the cross-correlations, which are finite due to the interactions via elastic scattering. We observe a movement in each of the correlations. Notice that the velocities are very similar, equivalent to the particles' velocities. However, the velocities are of the order of 10% of the actual velocity of the particles. This is an imprint from the coupling effects of the two densities via elastic scattering. Due to this, the hydrodynamic equations have a form like Eq. (6.14) where the contribution from the drift cannot be simply absorbed into the time coordinate. Parameters as in Fig. 6.5a)

larger difference in the velocities, which could be one way to separate the dynamics naturally. Another way could be to choose the hopping parameters such that one particle type is much 'heavier' than the other, leading to a larger difference in the velocities.

Although we have not managed to link the results with KPZ-scaling from fluctuating hydrodynamics, we strongly believe that this is possible within certain limits. Furthermore, the implementation of the simulations leads to very efficient modelling for non-equilibrium phenomena in a current-carrying medium. An example is that it is possible to change to a momentum-conserving representation by adjusting the energy dispersion. This could replace particle conservation with momentum conservation or increase the number of conserved quantities.

Conclusion

Now that we have navigated through the maze of data and arguments, let us bask in the light of our conclusions. This includes a summary of our findings and an outlook for future tasks.

Our journey started by introducing the ferrimagnetic model consisting of a ferromagnetic coupling in the z-component, an antiferromagnetic coupling in the xy-plane, and a uniaxial anisotropy in the z-component. We found analytically that a staggered oscillating magnetic field is sufficient to activate the Goldstone mode, which is a rotation of the magnetisation in the xy plane. A crucial point is that the direction of the rotational frequency ω_{rot} depends on the sign of the magnetisation in the z-direction m with $\omega_{\mathrm{rot}} \propto -m$. This gives rise to dynamical frustration at a domain wall. We also introduced an effective theory that considers only the most relevant terms and can qualitatively describe the dynamics over a large parameter space.

In one dimension, a domain wall cannot remain static under dynamical frustration, and we found that domain walls move with a constant velocity in a broad parameter regime. We determined the velocity analytically, with $v \propto \pm\sqrt{|\omega_{\mathrm{rot}}|}$ (within the framework of the effective theory) for small velocity and magnetic field amplitude values. A comparison of the analytical formula to numerical data showed good agreement over a wide range of field amplitudes. The drive does not imprint the movement direction. Instead, the direction originates from spontaneous symmetry breaking, and the domain wall moves either left or right. These characteristics show strong similarities to the field of active matter, which describes systems consisting of autonomous units that convert energy into movement, giving rise to various complex collective dynamics. In our case, the domain walls act as the fundamental units that transform the energy pumped in by the oscillating magnetic field into movement, facilitated by the rotation of the Goldstone mode and the dynamical frustration. The emergent collective behaviour is further explained in the following.

Both numerical data and analytical arguments revealed a characteristic difference in the spatial gradient of the rotating xy-order ϕ at a domain wall. This characteristic difference is dependent on ω_{rot} by topology. A domain wall alters the gradient in ϕ on the side opposite the movement direction to achieve the characteristic value. Going to the multi-domain wall picture, we used instantaneous quenches in the ordered phase. We found that the gradients in ϕ give rise to a long-range hydrodynamic interaction, which alters the ordering dynamics. This interaction leads to a linear

growth in the correlation length $\xi \propto t$, which differs from $\xi \propto \sqrt{t}$ for a minimal model without interactions. Our numerical studies of the steady state showed that the driven ferrimagnet is also much more resilient to thermal fluctuations. The correlation length grows faster with the inverse temperature than in a purely thermal process. On the same scale, the correlation length in the non-driven ferrimagnet showed only a tiny change. We also characterised the two defect types that can potentially destroy the ordered phase. Through minimal simulations, we demonstrated that these defects are suppressed by effective healing mechanisms, which lead to enhanced resilience against thermal fluctuations.

Above a critical field amplitude, the domain walls become localised and cease to move. Here, the formation of space-time vortices lifts the dynamical frustration. One vortex is created a short distance from the domain wall in each period and on each side. This can be explained by the finding that a region around the domain wall does not rotate. The vortices emerge exactly where this region meets the rotating region. The vorticity is -1 for an up-down domain and $+1$ for a down-up domain. Furthermore, we found that pulses in m are sent out and hit $m = 1$ precisely when the vortices are created. At this point, the magnetisation becomes fully z-polarised, and ϕ becomes ill-defined. This makes it an efficient way of lifting the dynamical frustration.

While we understand the propelled domain walls and the interactions in one dimension on a deep level, an analytical understanding of the pulses after the non-analytic vortex regime of the localised domain wall is still open. Furthermore, we have not focused on the non-driven ferrimagnet and the consequences of the coupling to ϕ on the dynamics. Due to the feedback effect, this might reveal interesting dynamics at low temperatures.

In two dimensions, domain walls generally move with respect to their local curvature. This is often referred to as coarsening. For the non-driven ferrimagnet, we found that those dynamics in m combined with the coupling to ϕ, particularly the spatial gradients of ϕ, influence the ordering dynamics. The correlation length grows with $\xi \propto t^{3/4}$ for an instantaneous quench to $T = 0$. However, for a quench to higher subcritical temperature, ϕ is approximately constant and irrelevant for the dynamics in m. We observed the Ising class growth with $\xi \propto t^{1/2}$. We confirmed this via the Kibble-Zurek mechanism, where we determined $\xi \propto \tau_Q^{1/(1+2.17)}$ for slow quench times τ_Q to shortly after the transition. On the other hand, for slow quenches deeper into the ordered phase, coarsening sets in and $\xi \propto \tau_Q^{1/2}$. Both scaling laws are in line with the Ising class. In the case of the driven system, the growth is again linear in time. Similarly to one dimension, gradients build up from the domain wall propulsion, giving rise to a long-range hydrodynamic interaction. We confirmed the linear scaling for instantaneous quenches to $T = 0$ and higher subcritical temperature. However,

we also discovered that the phase transition shifts approximately linear to higher temperatures as a function of the field amplitude, i.e., the ordered phase expands. In other words, the system is more resilient to thermal fluctuations. As for the one-dimensional case, we identified the two defect types and found analogous healing mechanisms. We could not confirm the linear growth for instantaneous quenches for temperatures closer to the transition inside the extended ordered region. We found that far fewer gradients build up, so the domain walls are less well protected against thermal fluctuations, which spoils the identification. The same problem occurred when we applied the Kibble-Zurek mechanism to the driven system. The signatures were too subtle to draw definite conclusions.

One open task is the characterisation of the extended ordered phase, which solely exists due to the driving field. With a better understanding of this phase, it might be possible to revise our approach to the Kibble-Zurek mechanism and gain more insights into the transition. A denser grid of instantaneous quenches throughout the extended ordered region may suffice.

For three dimensions, we focused purely on the phase transition of the driven system in the framework of the effective theory. Existing literature analytically predicts that the transition is rendered first-order under driving. We investigated the transition numerically using the Binder cumulant and hysteresis simulations. Despite our comprehensive efforts, we only found signatures of a second-order transition that agreed with Ising class exponents. Here, the small system sizes are a bottleneck. Extending the numerical solver of the effective theory to GPUs may give the relevant scaling factor. Moreover, a term coupling to the order parameter, which is extrapolated to zero, might reveal the first-order nature even at lower system sizes.

In the final, we numerically studied a model with two particle types driven out of equilibrium via a periodic change in the dispersion. This was done to study a simple non-equilibrium system which carries a steady-state current. We successfully implemented reasonable damping and driving to activate a steady-state current in a very efficient numerical framework. For only one particle type, we accomplished the mapping to fluctuating hydrodynamics, allowing for an analytical understanding of the density-density correlations. However, for the model with two particle types, we have yet to map the numerical data to fluctuating hydrodynamics successfully. Going to more drastic parameter regimes might separate the dynamics more clearly and allow for the mapping.

Much like our restless domain walls and relentless steady-state current, may the conclusions of this thesis only mark the beginning of an ever-evolving journey of discovery.

Bibliography

[1] Aristotle. "On the Soul". In: *The Complete Works: The Rev. Oxford Translation*. Ed. by J. Barnes. Princeton University Press, 1984, pp. 641–692.

[2] L. D. Landau and E. Lifshitz. "On the theory of the dispersion of magnetic permeability in ferromagnetic bodies". In: *Phys. Z. Sowjet.* 8 (1935), p. 153. URL: http://cds.cern.ch/record/437299.

[3] T. L. Gilbert. "A Lagrangian Formulation of the Gyromagnetic Equation of the Magnetization Field". In: *Physical Review D* 100 (1955), p. 1243. URL: https://api.semanticscholar.org/CorpusID:197507556.

[4] T. Gilbert. "A phenomenological theory of damping in ferromagnetic materials". In: *IEEE Transactions on Magnetics* 40.6 (2004), pp. 3443–3449. DOI: 10.1109/TMAG.2004.836740.

[5] D. Stancil and A. Prabhakar. *Spin Waves: Theory and Applications*. Springer US, 2009. ISBN: 9780387778655. URL: https://books.google.de/books?id=ehN6-ubvKwoC.

[6] K. Yang and J. O. Hirschfelder. "Generalizations of classical Poisson brackets to include spin". In: *Phys. Rev. A* 22 (5 1980), pp. 1814–1816. DOI: 10.1103/PhysRevA.22.1814.

[7] R. Skomski. *Simple Models of Magnetism*. Oxford University Press, 2008. ISBN: 9780198570752. DOI: 10.1093/acprof:oso/9780198570752.001.0001.

[8] M. Coey and P. S. *Handbook of Magnetism and Magnetic Materials*. Springer, 2021. ISBN: 9783030632083. DOI: https://doi.org/10.1007/978-3-030-63210-6.

[9] M. Henkel, H. Hinrichsen, and S. Lübeck. *Non-Equilibrium Phase Transitions: Volume 1: Absorbing Phase Transitions*. Theoretical and Mathematical Physics. Springer Netherlands, 2008. ISBN: 9781402087653. URL: https://books.google.de/books?id=OKbtkq4A-1EC.

[10] L. D. Landau. "On the theory of phase transitions. I." In: *Phys. Z. Sowjet.* 11 (1937), p. 26. URL: http://cds.cern.ch/record/480039.

[11] L. P. Kadanoff. *Critical behavior, universality and scaling, proceedings of the 1970 Varenna summer school on critical phenomena, edited by MS Green.* 1971.

[12] P. C. Hohenberg and B. I. Halperin. "Theory of dynamic critical phenomena". In: *Rev. Mod. Phys.* 49 (3 1977), pp. 435–479. DOI: 10.1103/RevModPhys.49.435.

[13] V. L. Ginzburg and L. D. Landau. "On the Theory of Superconductivity". In: *On Superconductivity and Superfluidity: A Scientific Autobiography.* Berlin, Heidelberg: Springer Berlin Heidelberg, 2009, pp. 113–137. ISBN: 978-3-540-68008-6. DOI: 10.1007/978-3-540-68008-6_4.

[14] D. Tong. "Statistical field theory". In: *Lecture Notes* (2017). URL: http://www.damtp.cam.ac.uk/user/tong/sft.html.

[15] Y. Elskens and H. L. Frisch. "Annihilation kinetics in the one-dimensional ideal gas". In: *Phys. Rev. A* 31 (6 1985), pp. 3812–3816. DOI: 10.1103/PhysRevA.31.3812.

[16] J. Krug and H. Spohn. "Universality classes for deterministic surface growth". In: *Phys. Rev. A* 38 (8 1988), pp. 4271–4283. DOI: 10.1103/PhysRevA.38.4271.

[17] W. R. Inc. *Mathematica, Version 14.* Champaign, IL, 2024. URL: https://www.wolfram.com/mathematica.

[18] E. Ben-Naim, S. Redner, and P. L. Krapivsky. "Two scales in asynchronous ballistic annihilation". In: *Journal of Physics A: Mathematical and General* 29.22 (1996), p. L561. DOI: 10.1088/0305-4470/29/22/002.

[19] D. Tong. *The Standard Model.* URL: http://www.damtp.cam.ac.uk/user/tong/standardmodel.html.

[20] J. Goldstone, A. Salam, and S. Weinberg. "Broken Symmetries". In: *Phys. Rev.* 127 (3 1962), pp. 965–970. DOI: 10.1103/PhysRev.127.965.

[21] C. F. Tejero and M. Baus. *Equilibrium Statistical Physics: Phases, Phase Transitions, and Topological Phases.* Springer, 2021.

[22] N. D. Mermin and H. Wagner. "Absence of Ferromagnetism or Antiferromagnetism in One- or Two-Dimensional Isotropic Heisenberg Models". In: *Phys. Rev. Lett.* 17 (22 1966), pp. 1133–1136. DOI: 10.1103/PhysRevLett.17.1133.

[23] P. C. Hohenberg. "Existence of Long-Range Order in One and Two Dimensions". In: *Phys. Rev.* 158 (2 1967), pp. 383–386. DOI: 10.1103/PhysRev.158.383.

[24] V. L. Berezinsky. “Destruction of long range order in one-dimensional and two-dimensional systems having a continuous symmetry group. I. Classical systems”. In: *Sov. Phys. JETP* 32 (1971), pp. 493–500.

[25] J. M. Kosterlitz and D. J. Thouless. “Ordering, metastability and phase transitions in two-dimensional systems”. In: *J. Phys. C* 6 (1973), pp. 1181–1203. DOI: 10.1088/0022-3719/6/7/010.

[26] M. Fruchart et al. “Non-reciprocal phase transitions”. In: *Nature* 592.7854 (2021), pp. 363–369. ISSN: 1476-4687. DOI: 10.1038/s41586-021-03375-9.

[27] Z. You, A. Baskaran, and M. C. Marchetti. “Nonreciprocity as a generic route to traveling states”. In: *Proceedings of the National Academy of Sciences* 117.33 (2020), pp. 19767–19772. DOI: 10.1073/pnas.2010318117.

[28] I. Buttinoni et al. “Dynamical Clustering and Phase Separation in Suspensions of Self-Propelled Colloidal Particles”. In: *Phys. Rev. Lett.* 110 (23 2013), p. 238301. DOI: 10.1103/PhysRevLett.110.238301.

[29] J. Toner, Y. Tu, and S. Ramaswamy. “Hydrodynamics and phases of flocks”. In: *Annals of Physics* 318.1 (2005). Special Issue, pp. 170–244. ISSN: 0003-4916. DOI: https://doi.org/10.1016/j.aop.2005.04.011.

[30] T. Grafke, R. Grauer, and T. Schäfer. “The instanton method and its numerical implementation in fluid mechanics”. In: *Journal of Physics A: Mathematical and Theoretical* 48.33 (2015), p. 333001. DOI: 10.1088/1751-8113/48/33/333001.

[31] N. del Ser, L. Heinen, and A. Rosch. “Archimedean screw in driven chiral magnets”. In: *SciPost Phys.* 11 (2021), p. 009. DOI: 10.21468/SciPostPhys.11.1.009.

[32] K. Shimizu et al. “Emergent electric field from magnetic resonances in a one-dimensional chiral magnet”. In: *Phys. Rev. B* 108 (13 2023), p. 134436. DOI: 10.1103/PhysRevB.108.134436.

[33] N. del Ser and V. Lohani. “Skyrmion jellyfish in driven chiral magnets”. In: *SciPost Phys.* 15 (2023), p. 065. DOI: 10.21468/SciPostPhys.15.2.065.

[34] C. P. Zelle et al. “Universal Phenomenology at Critical Exceptional Points of Nonequilibrium O(N) Models”. In: *Phys. Rev. X* 14 (2 2024), p. 021052. DOI: 10.1103/PhysRevX.14.021052.

[35] A. Vansteenkiste et al. “The design and verification of Mumax3”. In: *AIP Advances* 4.10 (2014), p. 107133. DOI: 10.1063/1.4899186.

[36] R. Doostani. “Flying Domain Walls in a Driven Ferrimagnet”. Master’s thesis. Universität zu Köln, 2024.

[37] https://mumax.github.io/api.html. [Accessed 10-02-2025].

[38] J. D. Clercq, J. Leliaert, and B. V. Waeyenberge. "Modelling compensated antiferromagnetic interfaces with MuMax3". In: *Journal of Physics D: Applied Physics* 50.42 (2017), p. 425002. DOI: 10.1088/1361-6463/aa8601.

[39] J. Leliaert et al. "Adaptively time stepping the stochastic Landau-Lifshitz-Gilbert equation at nonzero temperature: Implementation and validation in MuMax3". In: *AIP Advances* 7.12 (2017), p. 125010. ISSN: 2158-3226. DOI: 10.1063/1.5003957.

[40] L. M. Sieberer et al. "Lattice duality for the compact Kardar-Parisi-Zhang equation". In: *Phys. Rev. B* 94 (10 2016), p. 104521. DOI: 10.1103/PhysRevB.94.104521.

[41] W. Rüemelin. "Numerical Treatment of Stochastic Differential Equations". In: *SIAM Journal on Numerical Analysis* 19.3 (1982), pp. 604–613. DOI: 10.1137/0719041.

[42] P. E. Kloeden and E. Platen. *Numerical Solution of Stochastic Differential Equations*. Stochastic Modelling and Applied Probability. Springer Berlin Heidelberg, 2011. ISBN: 9783540540625.

[43] K. Itô. "Stochastic integral". In: *Proceedings of the Imperial Academy* 20.8 (1944), pp. 519–524. DOI: 10.3792/pia/1195572786.

[44] R. L. Stratonovich. "A New Representation for Stochastic Integrals and Equations". In: *SIAM Journal on Control* 4.2 (1966), pp. 362–371. DOI: 10.1137/0304028.

[45] R. Kubo and N. Hashitsume. "Brownian Motion of Spins". In: *Progress of Theoretical Physics Supplement* 46 (1970), pp. 210–220. ISSN: 0375-9687. DOI: 10.1143/PTPS.46.210.

[46] W. F. Brown. "Thermal Fluctuations of a Single-Domain Particle". In: *Phys. Rev.* 130 (5 1963), pp. 1677–1686. DOI: 10.1103/PhysRev.130.1677.

[47] S. Pöllath et al. "Dynamical Defects in Rotating Magnetic Skyrmion Lattices". In: *Phys. Rev. Lett.* 118 (20 2017), p. 207205. DOI: 10.1103/PhysRevLett.118.207205.

[48] M. te Vrugt and R. Wittkowski. "A review of active matter reviews". In: 2024. URL: https://api.semanticscholar.org/CorpusID:270045240.

[49] T. Sugi, H. Ito, and K. H Nagai. "Collective pattern formations of animals in active matter physics". In: *Biophys Physicobiol* 18 (2021), pp. 254–262.

[50] T. Vicsek et al. “Novel Type of Phase Transition in a System of Self-Driven Particles”. In: *Phys. Rev. Lett.* 75 (6 1995), pp. 1226–1229. DOI: 10.1103/PhysRevLett.75.1226.

[51] D. Helbing. “Traffic and related self-driven many-particle systems”. In: *Rev. Mod. Phys.* 73 (4 2001), pp. 1067–1141. DOI: 10.1103/RevModPhys.73.1067.

[52] C. Wolgemuth et al. “How Myxobacteria Glide”. In: *Current Biology* 12.5 (2002), pp. 369–377. ISSN: 0960-9822. DOI: https://doi.org/10.1016/S0960-9822(02)00716-9.

[53] L. Blanchoin et al. “Actin Dynamics, Architecture, and Mechanics in Cell Motility”. In: *Physiological Reviews* 94.1 (2014). PMID: 24382887, pp. 235–263. DOI: 10.1152/physrev.00018.2013.

[54] R. Niu and T. Palberg. “Modular approach to microswimming”. In: *Soft Matter* 14 (37 2018), pp. 7554–7568. DOI: 10.1039/C8SM00995C.

[55] W. Wang et al. “Small power: Autonomous nano- and micromotors propelled by self-generated gradients”. In: *Nano Today* 8.5 (2013), pp. 531–554. ISSN: 1748-0132. DOI: https://doi.org/10.1016/j.nantod.2013.08.009.

[56] H. Šípová-Jungová et al. “Nanoscale Inorganic Motors Driven by Light: Principles, Realizations, and Opportunities”. In: *Chemical Reviews* 120.1 (2020), pp. 269–287. ISSN: 0009-2665. DOI: 10.1021/acs.chemrev.9b00401.

[57] J. Toner and Y. Tu. “Long-Range Order in a Two-Dimensional Dynamical XY Model: How Birds Fly Together”. In: *Phys. Rev. Lett.* 75 (23 1995), pp. 4326–4329. DOI: 10.1103/PhysRevLett.75.4326.

[58] A. P. Solon and J. Tailleur. “Revisiting the Flocking Transition Using Active Spins”. In: *Phys. Rev. Lett.* 111 (7 2013), p. 078101. DOI: 10.1103/PhysRevLett.111.078101.

[59] A. P. Solon and J. Tailleur. “Flocking with discrete symmetry: The two-dimensional active Ising model”. In: *Phys. Rev. E* 92 (4 2015), p. 042119. DOI: 10.1103/PhysRevE.92.042119.

[60] S. Heckel et al. “An Account on BiVO4 as Photocatalytic Active Matter”. In: *Accounts of Materials Research* 5.4 (2024), pp. 400–412. DOI: 10.1021/accountsmr.3c00021.

[61] K. Villa et al. “Visible-Light-Driven Single-Component BiVO4 Micromotors with the Autonomous Ability for Capturing Microorganisms”. In: *ACS Nano* 13.7 (2019), pp. 8135–8145. DOI: 10.1021/acsnano.9b03184.

[62] D. Hardt et al. “Propelling ferrimagnetic domain walls by dynamical frustration”. In: *Nature Communications* 16.1 (2025), p. 3817. ISSN: 2041-1723. DOI: 10.1038/s41467-025-58920-1.

[63] E. B. Sonin. “Spin currents and spin superfluidity”. In: *Advances in Physics* 59.3 (2010), pp. 181–255. DOI: 10.1080/00018731003739943.

[64] S. K. Kim and Y. Tserkovnyak. “Interaction between a domain wall and spin supercurrent in easy-cone magnets”. In: *Phys. Rev. B* 94 (22 2016), p. 220404. DOI: 10.1103/PhysRevB.94.220404.

[65] P. Upadhyaya, S. K. Kim, and Y. Tserkovnyak. “Magnetic Domain Wall Floating on a Spin Superfluid”. In: *Phys. Rev. Lett.* 118 (9 2017), p. 097201. DOI: 10.1103/PhysRevLett.118.097201.

[66] M. Jin et al. “Domain-wall motion driven by a rotating field in a ferrimagnet”. In: *Phys. Rev. B* 104 (18 2021), p. 184431. DOI: 10.1103/PhysRevB.104.184431.

[67] A. Mougin et al. “Domain wall mobility, stability and Walker breakdown in magnetic nanowires”. In: *Europhysics Letters* 78.5 (2007), p. 57007. DOI: 10.1209/0295-5075/78/57007.

[68] H. Chaté et al. “Collective motion of self-propelled particles interacting without cohesion”. In: *Phys. Rev. E* 77 (4 2008), p. 046113. DOI: 10.1103/PhysRevE.77.046113.

[69] F. Thüroff, C. A. Weber, and E. Frey. “Numerical Treatment of the Boltzmann Equation for Self-Propelled Particle Systems”. In: *Phys. Rev. X* 4 (4 2014), p. 041030. DOI: 10.1103/PhysRevX.4.041030.

[70] S. Kornblith et al. *JuliaDSP/DSP.jl: v0.7.9*. Version v0.7.9. Sept. 2023. DOI: 10.5281/zenodo.8344531.

[71] L. He, L. M. Sieberer, and S. Diehl. “Space-Time Vortex Driven Crossover and Vortex Turbulence Phase Transition in One-Dimensional Driven Open Condensates”. In: *Phys. Rev. Lett.* 118 (8 2017), p. 085301. DOI: 10.1103/PhysRevLett.118.085301.

[72] A. J. Bray. “Theory of phase-ordering kinetics”. In: *Advances in Physics* 43.3 (1994), pp. 357–459. DOI: 10.1080/00018739400101505.

[73] S. M. Allen and J. W. Cahn. “A microscopic theory for antiphase boundary motion and its application to antiphase domain coarsening”. In: *Acta Metallurgica* 27.6 (1979), pp. 1085–1095. ISSN: 0001-6160. DOI: https://doi.org/10.1016/0001-6160(79)90196-2.

[74] G. Biroli. "A crash course on ageing". In: *Journal of Statistical Mechanics: Theory and Experiment* 2005.05 (2005), P05014. DOI: 10.1088/1742-5468/2005/05/P05014.

[75] A. J. Bray. "Coarsening Dynamics of Phase-Separating Systems". In: *Philosophical Transactions: Mathematical, Physical and Engineering Sciences* 361. 1805 (2003), pp. 781–792. ISSN: 1364503X. URL: http://www.jstor.org/stable/3559175 (visited on 12/07/2024).

[76] E. T. Gawlinski et al. "Growth of unstable domains in the two-dimensional Ising model". In: *Phys. Rev. B* 31 (1 1985), pp. 281–286. DOI: 10.1103/PhysRevB.31.281.

[77] M. P. Nightingale and H. W. J. Blöte. "Dynamic Exponent of the Two-Dimensional Ising Model and Monte Carlo Computation of the Subdominant Eigenvalue of the Stochastic Matrix". In: *Phys. Rev. Lett.* 76 (24 1996), pp. 4548–4551. DOI: 10.1103/PhysRevLett.76.4548.

[78] H. Christiansen et al. "Aging in the Long-Range Ising Model". In: *Phys. Rev. Lett.* 125 (18 2020), p. 180601. DOI: 10.1103/PhysRevLett.125.180601.

[79] I. M. Lifshitz and V. V. Slyozov. "The kinetics of precipitation from supersaturated solid solutions". In: *Journal of Physics and Chemistry of Solids* 19.1 (1961), pp. 35–50. ISSN: 0022-3697. DOI: https://doi.org/10.1016/0022-3697(61)90054-3.

[80] S. Majumder and S. K. Das. "Domain coarsening in two dimensions: Conserved dynamics and finite-size scaling". In: *Phys. Rev. E* 81 (5 2010), 050102. DOI: 10.1103/PhysRevE.81.050102.

[81] S. Ahmad, S. K. Das, and S. Puri. "Kinetics of phase separation in fluids: a molecular dynamics study". en. In: *Phys Rev E Stat Nonlin Soft Matter Phys* 82.4 Pt 1 (Oct. 2010), p. 040107.

[82] L. A. Williamson and P. B. Blakie. "Universal Coarsening Dynamics of a Quenched Ferromagnetic Spin-1 Condensate". In: *Phys. Rev. Lett.* 116 (2 2016), p. 025301. DOI: 10.1103/PhysRevLett.116.025301.

[83] F. Dittrich et al. "Growth and aging in a few phase-separating active matter systems". In: *Phys. Rev. E* 108 (2 2023), p. 024609. DOI: 10.1103/PhysRevE.108.024609.

[84] N. Vadakkayil, S. Chakraborty, and S. K. Das. "Finite-size scaling study of aging during coarsening in non-conserved Ising model: The case of zero temperature quench". In: *The Journal of Chemical Physics* 150.5 (2019), p. 054702. ISSN: 0021-9606. DOI: 10.1063/1.5052418.

[85] D. Gessert, H. Christiansen, and W. Janke. "Superdiffusion-like behavior in zero-temperature coarsening of the d=3 Ising model". In: *Scientific Reports* 13.1 (2023), p. 13270. ISSN: 2045-2322. DOI: 10.1038/s41598-023-39328-7.

[86] G. Brown and P. A. Rikvold. "Numerical confirmation of late-time $t^{1/2}$ growth in three-dimensional phase ordering". In: *Phys. Rev. E* 65 (3 2002), p. 036137. DOI: 10.1103/PhysRevE.65.036137.

[87] J. Midya, S. Majumder, and S. K. Das. "Aging in ferromagnetic ordering: full decay and finite-size scaling of autocorrelation". In: *Journal of Physics: Condensed Matter* 26.45 (2014), p. 452202. DOI: 10.1088/0953-8984/26/45/452202.

[88] R. F. Shannon et al. "Time-resolved x-ray-scattering study of ordering kinetics in bulk single-crystal Cu_3Au". In: *Phys. Rev. B* 46 (1 1992), pp. 40–54. DOI: 10.1103/PhysRevB.46.40.

[89] M. Kardar. *Statistical Physics of Fields*. Cambridge University Press, 2007.

[90] V. Spirin, P. Krapivsky, and S. Redner. "Freezing in Ising ferromagnets". In: *Phys. Rev. E* 65 (1 2001), p. 016119. DOI: 10.1103/PhysRevE.65.016119.

[91] P. Sundaramurthy and D. L. Stein. "Zero-temperature dynamics of 2D and 3D Ising ferromagnets". In: *Journal of Physics A: Mathematical and General* 38.2 (2004), p. 349. DOI: 10.1088/0305-4470/38/2/005.

[92] T. W. B. Kibble. "Topology of cosmic domains and strings". In: *Journal of Physics A: Mathematical and General* 9.8 (1976), p. 1387. DOI: 10.1088/0305-4470/9/8/029.

[93] T. Kibble. "Some implications of a cosmological phase transition". In: *Physics Reports* 67.1 (1980), pp. 183–199. ISSN: 0370-1573. DOI: https://doi.org/10.1016/0370-1573(80)90091-5.

[94] W. H. Zurek. "Cosmological experiments in superfluid helium?" In: *Nature* 317.6037 (1985), pp. 505–508. ISSN: 1476-4687. DOI: 10.1038/317505a0.

[95] W. Zurek. "Cosmological experiments in condensed matter systems". In: *Physics Reports* 276.4 (1996), pp. 177–221. ISSN: 0370-1573. DOI: https://doi.org/10.1016/S0370-1573(96)00009-9.

[96] T.-C. Ma et al. *Universal Critical Holography and Domain Wall Formation*. 2024. arXiv: 2406.05167 [cond-mat.stat-mech].

[97] C. Bäuerle et al. "Laboratory simulation of cosmic string formation in the early Universe using superfluid 3He". In: *Nature* 382.6589 (1996), pp. 332–334. ISSN: 1476-4687. DOI: 10.1038/382332a0.

[98] V. M. H. Ruutu et al. “Vortex formation in neutron-irradiated superfluid 3He as an analogue of cosmological defect formation”. In: *Nature* 382.6589 (1996), pp. 334–336. ISSN: 1476-4687. DOI: 10.1038/382334a0.

[99] G. Lamporesi et al. “Spontaneous creation of Kibble–Zurek solitons in a Bose–Einstein condensate”. In: *Nature Physics* 9.10 (2013), pp. 656–660. ISSN: 1745-2481. DOI: 10.1038/nphys2734.

[100] S. Ulm et al. “Observation of the Kibble–Zurek scaling law for defect formation in ion crystals”. In: *Nature Communications* 4.1 (2013), p. 2290. ISSN: 2041-1723. DOI: 10.1038/ncomms3290.

[101] A. Keesling et al. “Quantum Kibble–Zurek mechanism and critical dynamics on a programmable Rydberg simulator”. In: *Nature* 568.7751 (2019), pp. 207–211. ISSN: 1476-4687. DOI: 10.1038/s41586-019-1070-1.

[102] M. Anquez et al. “Quantum Kibble-Zurek Mechanism in a Spin-1 Bose-Einstein Condensate”. In: *Phys. Rev. Lett.* 116 (15 2016), p. 155301. DOI: 10.1103/PhysRevLett.116.155301.

[103] W. Wen et al. “Generalized Kibble-Zurek mechanism for defects formation in trapped ions”. In: *Science China Physics, Mechanics & Astronomy* 66.8 (2023), p. 280311. ISSN: 1869-1927. DOI: 10.1007/s11433-023-2119-8.

[104] G. Biroli, L. F. Cugliandolo, and A. Sicilia. “Kibble-Zurek mechanism and infinitely slow annealing through critical points”. In: *Phys. Rev. E* 81 (5 2010), p. 050101. DOI: 10.1103/PhysRevE.81.050101.

[105] L. P. Kadanoff. “Scaling laws for ising models near T_c”. In: *Physics Physique Fizika* 2 (6 1966), pp. 263–272. DOI: 10.1103/PhysicsPhysiqueFizika.2.263.

[106] Z. Liu et al. “Critical dynamical behavior of the Ising model”. In: *Phys. Rev. E* 108 (3 2023), p. 034118. DOI: 10.1103/PhysRevE.108.034118.

[107] A. I. Larkin and A. A. Varlamov. “Fluctuation Phenomena in Superconductors”. In: *Superconductivity: Conventional and Unconventional Superconductors*. Ed. by K. H. Bennemann and J. B. Ketterson. Berlin, Heidelberg: Springer Berlin Heidelberg, 2008, pp. 369–458. ISBN: 978-3-540-73253-2. DOI: 10.1007/978-3-540-73253-2_10.

[108] K. Binder. “Finite size scaling analysis of ising model block distribution functions”. In: *Zeitschrift für Physik B Condensed Matter* 43.2 (1981), pp. 119–140. ISSN: 1431-584X. DOI: 10.1007/BF01293604.

[109] G. C. Wick. “The Evaluation of the Collision Matrix”. In: *Phys. Rev.* 80 (2 1950), pp. 268–272. DOI: 10.1103/PhysRev.80.268.

[110] J. C. Pillay and I. P. McCulloch. "Cumulants and scaling functions of infinite matrix product states". In: *Phys. Rev. B* 100 (23 2019), p. 235140. DOI: 10.1103/PhysRevB.100.235140.

[111] H. Shao, W. Guo, and A. W. Sandvik. "Quantum criticality with two length scales". In: *Science* 352.6282 (2016), pp. 213–216. DOI: 10.1126/science.aad5007.

[112] K. Vollmayr et al. "Finite size effects at thermally-driven first order phase transitions: A phenomenological theory of the order parameter distribution". In: *Zeitschrift für Physik B Condensed Matter* 91.1 (1993), pp. 113–125. ISSN: 1431-584X. DOI: 10.1007/BF01316713.

[113] M. Durve and A. Sayeed. "First-order phase transition in a model of self-propelled particles with variable angular range of interaction". In: *Phys. Rev. E* 93 (5 2016), p. 052115. DOI: 10.1103/PhysRevE.93.052115.

[114] A. P. Levanyuk. "Contribution to the theory of light scattering near the second-order phase-transition points". In: *Sov. Phys. JETP* 9.3 (1959), 571–576.

[115] V. Ginzburg. "Some remarks on phase transitions of the second kind and the microscopic theory of ferroelectric materials". In: *Soviet Phys. Solid State* 2 (1961), pp. 1824–1834.

[116] P. Hohenberg and A. Krekhov. "An introduction to the Ginzburg–Landau theory of phase transitions and nonequilibrium patterns". In: *Physics Reports* 572 (2015). An introduction to the Ginzburg–Landau theory of phase transitions and nonequilibrium patterns, pp. 1–42. ISSN: 0370-1573. DOI: https://doi.org/10.1016/j.physrep.2015.01.001.

[117] V. Basso et al. "Hysteresis and Phase Transition Kinetics in Magnetocaloric Materials". In: *physica status solidi (b)* 255.2 (2018), p. 1700278. DOI: https://doi.org/10.1002/pssb.201700278.

[118] D. Huybrechts and M. Wouters. "Dynamical hysteresis properties of the driven-dissipative Bose-Hubbard model with a Gutzwiller Monte Carlo approach". In: *Phys. Rev. A* 102 (5 2020), p. 053706. DOI: 10.1103/PhysRevA.102.053706.

[119] G. S. Agarwal and S. R. Shenoy. "Observability of hysteresis in first-order equilibrium and nonequilibrium phase transitions". In: *Phys. Rev. A* 23 (5 1981), pp. 2719–2723. DOI: 10.1103/PhysRevA.23.2719.

[120] S. Iino et al. “Detecting Signals of Weakly First-order Phase Transitions in Two-dimensional Potts Models”. In: *Journal of the Physical Society of Japan* 88.3 (2019), p. 034006. DOI: 10.7566/JPSJ.88.034006.

[121] J. D’Emidio, A. A. Eberharter, and A. M. Läuchli. “Diagnosing weakly first-order phase transitions by coupling to order parameters”. In: *SciPost Phys.* 15 (2023), p. 061. DOI: 10.21468/SciPostPhys.15.2.061.

[122] H. Ikeda. “Harmonic chain far from equilibrium: Single-file diffusion, long-range order, and hyperuniformity”. In: *SciPost Phys.* 17 (2024), p. 103. DOI: 10.21468/SciPostPhys.17.4.103.

[123] H. Spohn. “Nonlinear Fluctuating Hydrodynamics for Anharmonic Chains”. In: *Journal of Statistical Physics* 154.5 (2014), pp. 1191–1227. ISSN: 1572-9613. DOI: 10.1007/s10955-014-0933-y.

[124] G. M. Schütz. “Fluctuations in Stochastic Interacting Particle Systems”. In: *Stochastic Dynamics Out of Equilibrium*. Ed. by G. Giacomin et al. Cham: Springer International Publishing, 2019, pp. 67–134. ISBN: 978-3-030-15096-9.

[125] G. Cannizzaro et al. “From ABC to KPZ”. In: *Probability Theory and Related Fields* (2024). ISSN: 1432-2064. DOI: 10.1007/s00440-024-01314-z.

[126] J. Lux. “Fluctuations in and out of equilibrium: Thermalization, quantum measurements and Coulomb disorder”. PhD thesis. Universität zu Köln, 2016. URL: https://kups.ub.uni-koeln.de/6791/.

[127] P. S. Weiß, D. Hardt, and A. Rosch. “Entropy production for quasiadiabatic parameter changes dominated by hydrodynamics”. In: *Phys. Rev. A* 103 (3 2021), p. 033309. DOI: 10.1103/PhysRevA.103.033309.

[128] D. Hardt. “Hydrodynamics, Entropy Production and Long-Time Tails”. Master’s thesis. Universität zu Köln, 2020.

[129] A. Fick. “Ueber Diffusion”. In: *Annalen der Physik* 170.1 (1855), pp. 59–86. DOI: https://doi.org/10.1002/andp.18551700105.

[130] P. S. Weiß. “Quantum Fluctuations and Hydrodynamic Noise in Low Dimensions”. PhD thesis. Universität zu Köln, 2020. URL: https://kups.ub.uni-koeln.de/11817/.

[131] H. Spohn and G. Stoltz. “Nonlinear Fluctuating Hydrodynamics in One Dimension: The Case of Two Conserved Fields”. In: *Journal of Statistical Physics* 160.4 (2015), pp. 861–884. ISSN: 1572-9613. DOI: 10.1007/s10955-015-1214-0.

[132] J. Baik, P. L. Ferrari, and S. Péché. "Convergence of the Two-Point Function of the Stationary TASEP". In: *Singular Phenomena and Scaling in Mathematical Models*. Ed. by M. Griebel. Cham: Springer International Publishing, 2014, pp. 91–110. ISBN: 978-3-319-00786-1. DOI: 10.1007/978-3-319-00786-1_5.

[133] L. Gosteva et al. "Inviscid fixed point of the multidimensional Burgers–Kardar-Parisi-Zhang equation". In: *Phys. Rev. E* 110 (5 2024), p. 054118. DOI: 10.1103/PhysRevE.110.054118.

[134] M. Prähofer. "Tables to: Exact scaling functions for one-dimensional stationary KPZ growth". In: *Preprint, http://www-m5. ma. tum. de/KPZ* (2003).

[135] P. L. Ferrari, T. Sasamoto, and H. Spohn. "Coupled Kardar-Parisi-Zhang Equations in One Dimension". In: *Journal of Statistical Physics* 153.3 (2013), pp. 377–399. ISSN: 1572-9613. DOI: 10.1007/s10955-013-0842-5.

[136] V. Popkov, J. Schmidt, and G. M. Schütz. "Universality Classes in Two-Component Driven Diffusive Systems". In: *Journal of Statistical Physics* 160.4 (2015), pp. 835–860. ISSN: 1572-9613. DOI: 10.1007/s10955-015-1241-x.

[137] F. Lange. "Giant response to weak pumping in quantum systems with approximate symmetries". PhD thesis. Universität zu Köln, 2020. URL: https://kups.ub.uni-koeln.de/10708/.

[138] F. Lange, Z. Lenarčič, and A. Rosch. "Pumping approximately integrable systems". In: *Nature Communications* 8.1 (2017), p. 15767. ISSN: 2041-1723. DOI: 10.1038/ncomms15767.

Appendix A

Coefficients of the Responses

Within this appendix, we provide the full expressions of the first-order responses, the rotational frequency and the static second-order correction to the θ-angle which were left out of the main text to increase clarity. We still use the abbreviations $c_n = \cos(n\theta_0)$ and $s_n = \sin(n\theta_0)$.
The linear response coefficients to the ansatz Eq. (2.8) after solving the first-order equations of motion Eq. (2.7) are given by

$$\begin{aligned}
\phi^{(1)}_{e/o,\omega} &= \frac{1}{2} i b_0 \left(\frac{g_{e/o} + g_{o/e}}{den_1} - \frac{\omega \left(g_{o/e} - g_{e/o} \right)}{den_2} \right), \\
\theta^{(1)}_{e/o,\omega} &= \frac{1}{2} b_0 s_1 \left(-\frac{i\alpha \left(g_{e/o} + g_{o/e} \right)}{den_1} + \frac{\left(g_{o/e} - g_{e/o} \right) \left(4Jd + i\alpha\omega \right)}{den_2} \right),
\end{aligned} \tag{A.1}$$

where $\phi^{(1)}_{e/o,-\omega} = \left(\phi^{(1)}_{e/o,\omega} \right)^*$ and $\theta^{(1)}_{e/o,-\omega} = \left(\theta^{(1)}_{e/o,\omega} \right)^*$ with * denoting the complex conjugate. The denominators have the following form

$$\begin{aligned}
den_1 &= 2\left(1+\alpha^2\right)\omega - i\alpha\left(\delta_4 c_4 + c_2\left(2\delta_2 + \delta_4 + 4(1-\Delta)Jd\right)\right), \\
den_2 &= 16(1+\Delta)J^2d^2 - 4i\alpha Jd(3+\Delta)\omega - \left(\delta_4 c_4 + \left(2\delta_2 + \delta_4\right)c_2\right)\left(4Jd - i\alpha\omega\right) \\
&\quad - 2\left(1+\alpha^2\right)\omega^2 .
\end{aligned} \tag{A.2}$$

The full expression of the rotational frequency as a second order response can then be stated as

$$\omega_{\mathrm{rot}} = \frac{4b_0^2 (g_e - g_o)^2 Jd\omega^2 S_0^z}{den_2 den_2^*}, \tag{A.3}$$

where den_2 is the same as above.

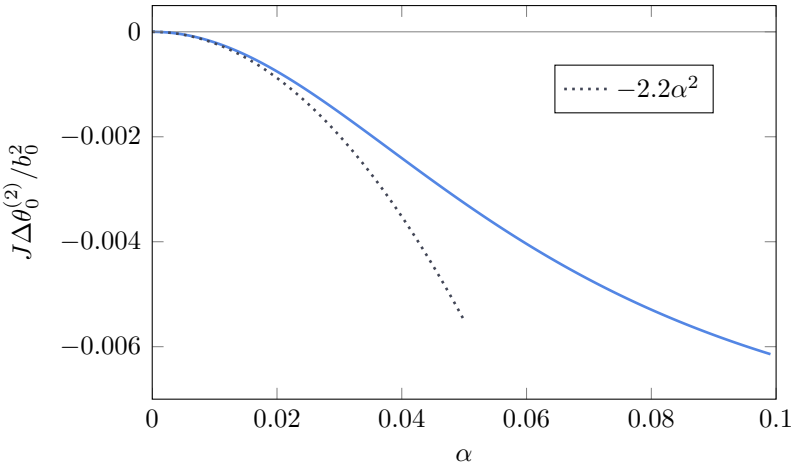

Figure A.1: The difference of the static corrections to $\theta_{e,o}$, Eq. (A.5) shown as a function of the damping parameter. The leading order is given by α^2 for small damping. Parameters are $d = 1, J = 1, \Delta = 0.8, \delta_2 = -0.6, \delta_4 = 1, \omega = 3.6, g_e = 1, g_o = 0.1, b_0 = 0.15$.

The second order static correction to $\theta_{e/o}$ is given by

$$
\begin{aligned}
\theta^{(2)}_{e/o,0} = \Bigg\langle \Bigg(& \left(2c_2\left(Jd(\Delta-1)-\delta_2\right)-\left(c_2+c_4\right)\delta_4+2Jd(\Delta+1)\right) \\
& \cdot \left(2c_1\theta^{(1)}_{e/o}\left(B_z g_{o/e}-2c_1 Jd(\Delta-1)\theta^{(1)}_{o/e}\right)\right. \\
& + c_2\left(\theta^{(1)}_{e/o}\right)^2\left(\left(4c_2+1\right)\delta_4 - Jd(\Delta-1)+2\delta_2\right) \\
& + c_2 Jd\left((\phi^{(1)}_{e/o}-\phi^{(1)}_{o/e})^2-(\Delta-1)\left(\theta^{(1)}_{o/e}\right)^2\right)-2c_1\theta^{(1)}_{o/e}\dot{\phi}^{(1)}_{o/e}\Big) \\
& - 2Jd\left(c_2(\Delta-1)-\Delta-1\right)\Bigg(2c_1\Bigg(B_z g_{e/o}\theta^{(1)}_{o/e} \\
& + c_1\Bigg(\left(\theta^{(1)}_{o/e}\right)^2\left(4c_2\delta_4 - Jd(\Delta-1)+2\delta_2+\delta_4\right)+Jd(\phi^{(1)}_{e/o}-\phi^{(1)}_{o/e})^2\Bigg)\Bigg) \\
& \left. - 2c_1\theta^{(1)}_{e/o}\left(2c_1 Jd(\Delta-1)\theta^{(1)}_{o/e}+\dot{\phi}^{(1)}_{e/o}\right)-c_2 Jd(\Delta-1)\left(\theta^{(1)}_{e/o}\right)^2\Bigg)\Bigg)\Bigg\rangle_T \\
& \Big/\Bigg(\left(-2c_2\delta_2-\left(c_2+c_4\right)\delta_4+4d(\Delta+1)J\right) \\
& \cdot\left(c_2\left(-4Jd(\Delta-1)+2\delta_2+\delta_4\right)+c_4\delta_4\right)\Bigg),
\end{aligned}
\tag{A.4}
$$

where we used the average over a driving period $T = \frac{2\pi}{\omega}$ to shorten the expression. $B_z(t) = b_0\cos(\omega t)$ as given in Eq. (2.5).
Compared to the rotational frequency, the difference in the shift of the spin-z-

component is different for even and odd sites. It can be stated in the form

$$\Delta\theta_0^{(2)} = \theta_{e,0}^{(2)} - \theta_{o,0}^{(2)} = \Bigg\langle \Bigg(2B_z c_1 \left(g_e \theta_o^{(1)} - g_o \theta_e^{(1)} \right) + 2c_1 \left(\theta_o^{(1)} \dot{\phi}_o^{(1)} - \theta_e^{(1)} \dot{\phi}_e^{(1)} \right) \\ - c_2 \left((4c_2 + 1)\,\delta_4 + 2\delta_2 \right) \left(\left(\theta_e^{(1)}\right)^2 - \left(\theta_o^{(1)}\right)^2 \right) \Bigg) \Bigg\rangle_T \\ \Big/ \left(4Jd(\Delta + 1) - 2c_2\delta_2 - (c_2 + c_4)\,\delta_4 \right), \tag{A.5}$$

again using the temporal average over a period. Fig. A.1 shows this difference as function of the damping constant. For small damping, the difference scales with $\sim \alpha^2$.

Appendix B

Additional Data for 1D Domain Walls

B.1 Velocity Distribution - Ordering Dynamics

Here, we present additional information on the ordering dynamics. Fig. B.1 shows the velocity distribution of the domain walls for three different times after a quench into the ordered phase without thermal fluctuations. From the three different times shown, we can nicely see that a finite time is needed for the domain walls to reach the final speed. This is connected to the phase gradients needing some time to build out the characteristic slope. It also explains the delay before the linear growth in correlation length sets in, see Fig. 3.8a).

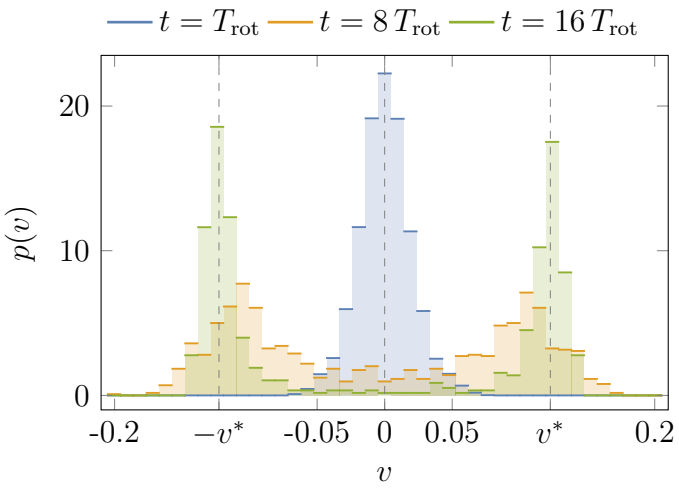

Figure B.1: The velocity distribution $p(v)$ of the domain walls shown for three different times of one simulation used for Fig. 3.8a). After about one rotation period, the velocity distribution is yet centred around zero. With time, two peaks show up, moving to larger velocities until their maximum is around $|v| = v^*$, for $t \gtrsim 16\,T_{\mathrm{rot}}$. This shows that it takes a certain time until the domain walls reach the final speed of $v^* \approx 0.1226$. Parameters are $J = 1, \Delta = 0.8, \delta_2 = -0.6, \delta_4 = 1, g_e = 1, g_o = 0.1, \alpha = 0.1, b_0 = 0.15, \omega = 3.6$ with $T_{\mathrm{rot}} \approx 612$.

B.2 Correlations in the xy-order in the stationary state

In Sec. 3.5, we focused mainly on the correlations in m. In this appendix, we give more information on the ordering in ϕ. Fig. B.2 shows the correlations of the xy-order calculated via

$$C_\phi(x) = \langle m_i^x m_{i+x}^x + m_i^y m_{i+x}^y \rangle \,, \tag{B.1}$$

after quenches to different temperatures. The data from the driven (NEQ) system is compared to the data of the non-driven (EQ) system. The correlation length in the driven system is lower, and the correlations drop faster. This comes from the fact that slopes build up in the xy-order in the different domains, which leads to a lower correlation. An exponential with a correlation length of 67 is shown as a guide to the eye. The correlations in the non-driven system follow this curve very well. Differences between the different temperature curves are small. This compares to large correlation lengths in the z-component of the magnetisation with decreasing temperature, see Fig. 3.10b).

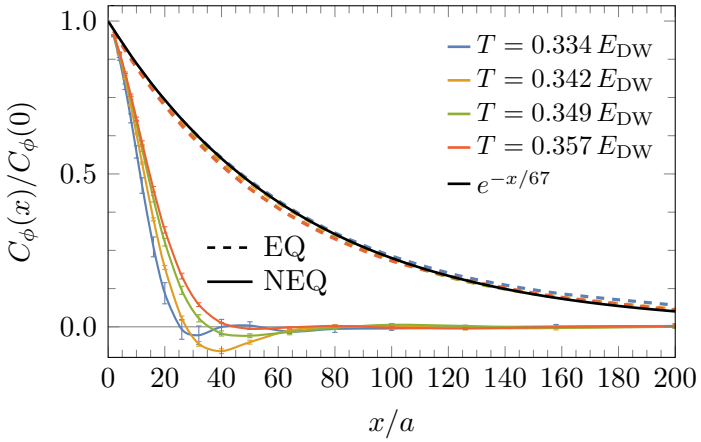

Figure B.2: Correlations of the xy-order calculated via Eq. (B.1) for the same data as used in Fig. 3.10b) for the quenches from an xy-ordered state, and compared to non-driven simulations for quenches to the same temperatures. The solid lines denote the driven case with much a shorter correlation length, and the dashed lines are the non-driven case with a larger correlation length. Additionally, an exponential function is displayed as a guide to the eye to show that the correlations in the non-driven case decay exponentially on a length scale of ~ 67 sites. The correlations in the driven system decay much faster and on a length scale of roughly ~ 20. Parameters as in Fig. B.1 but at finite temperature given in the legend.

B.3 Growing Type II Defect

Within this appendix, we report on a growing type II defect. Fig. B.3a) shows a defect that can reverse the magnetisation in the whole system. At first glance, these types seem very harmful to the ordered phase. However, they rarely occur due to an effective healing mechanism discussed in Sec. 3.5.2. The shown simulation was the only observation of a type II defect that grows to the size of the system during the entire investigation. This highlights highlights their rare nature. Fig. B.3b) shows a zoom-in on the nucleation. In addition to the growing type II defect, it shows many type I defects. These are described by parallel-moving domain walls that are nucleated by thermal fluctuations. Although there are many of them, they cannot destroy the ordered phase. Due to the constant velocity, either to the left or right, type I defects frequently annihilate. Overall, the driven system is much more resilient to thermal fluctuations.

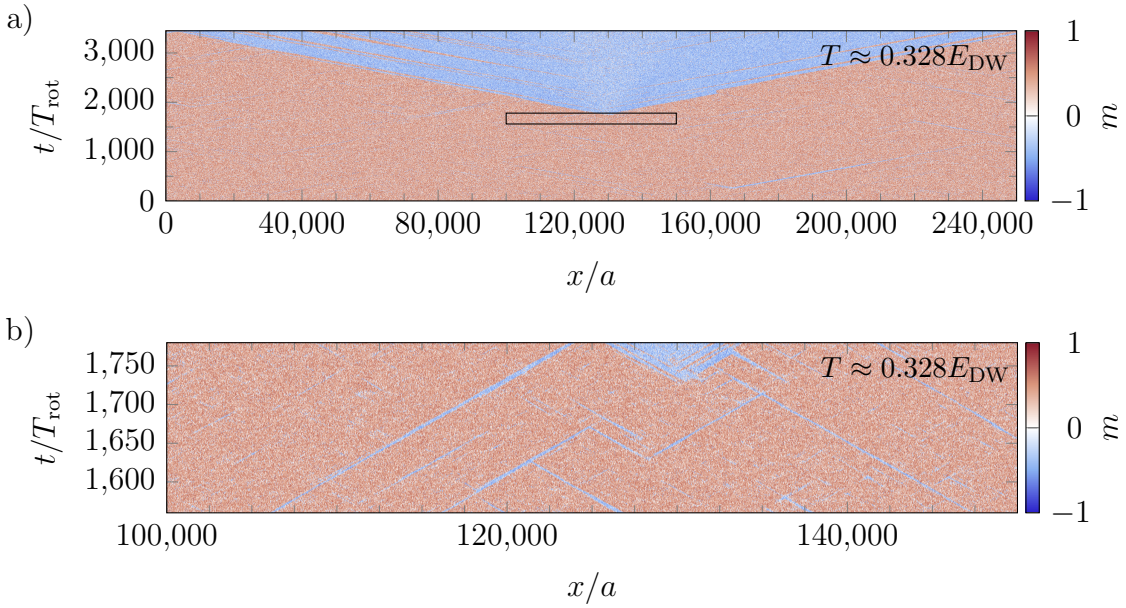

Figure B.3: Raw magnetisation data showing a growing type II defect, a growing domain, for 250,000 sites in one dimension after a quench into the ordered phase. Panel a) shows the wide view. After approximately $t \approx 1{,}725\, T_{\mathrm{rot}}$, a type II defect is launched. Panel b) shows a zoom on the area enclosed by the black rectangle in panel a). Frequent type I defects are also visible. However, only the type II defect can reverse the order in the system. The defect stretches out to the whole system size in the shown case. Parameters are $J = 1, \Delta = 0.8, \delta_2 = -0.6, \delta_4 = 1, g_e = 1, g_o = 0.1, \alpha = 0.1, b_0 = 0.15, \omega = 3.6$, i.e, $T_{\mathrm{rot}} \approx 612$ is the rotational period. $E_{\mathrm{DW}} = 0.076$ is the energy of a single domain wall measured from a non-driven simulation.

B.4 Domain Wall Identification

In Sec. 3.6, we used a filtering scheme to estimate the number of left- and right-moving domains in the effective model. Here, we want to give a better feeling for the digital filter and show that the height cutoff does not influence the general scaling with the driving parameter. Fig. B.4 shows a zoom on the bare magnetisation data from the effective model without driving, $\iota = 0$. On top of that, we display the corresponding curve after a Butterworth lowpass filter in fourth order. The filter is used to eliminate the fluctuations on a small scale and get a more smoothed-out signal. We used the non-driven system to define reasonable values for the filter parameters since it is the system with the largest number of domain walls.

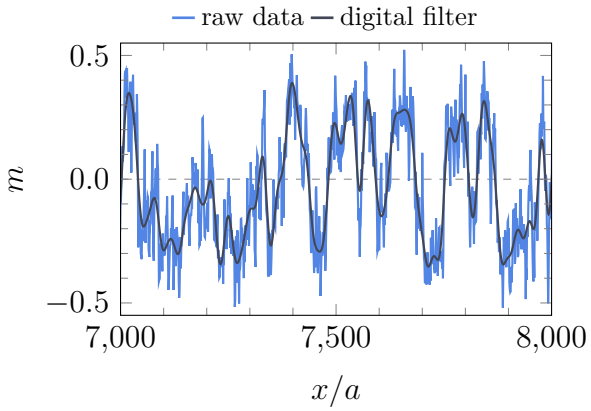

Figure B.4: Raw magnetisation data of a simulation of the effective model shown with a digital filter with a cutoff frequency of $f_c = 1/10$, and a sampling frequency of $f = 1/300$. The filter eliminates strong fluctuations on small scales. Parameters are $\alpha = 1, r = -0.1, u = 1, D_m = 1, D_\phi = 1, T = 0.01$ for the non-driven model, $\iota = 0$, for a system of 15,000 sites.

Fig. B.5 compares different values of the number of left- and right-moving domain walls, depending on system size and the height cutoff h_c explained in Sec. 3.6. The curves for different system sizes can be scaled to one another by the system size ratio. Also, the curves for the different height cutoffs show the same trend. Thus, we can conclude that the cutoff has little influence on the actual scaling with ι in the range of the two values. Notice that the value $h_c = 0.15$ is of the order of half of the domain value without thermal fluctuations, $m_0 = \sqrt{\frac{-r}{u}} \approx 0.316$. The most important point is that the number of left- and right-moving domain walls is always the same, i.e., there is no preferred direction of domain walls nucleated from thermal fluctuations.

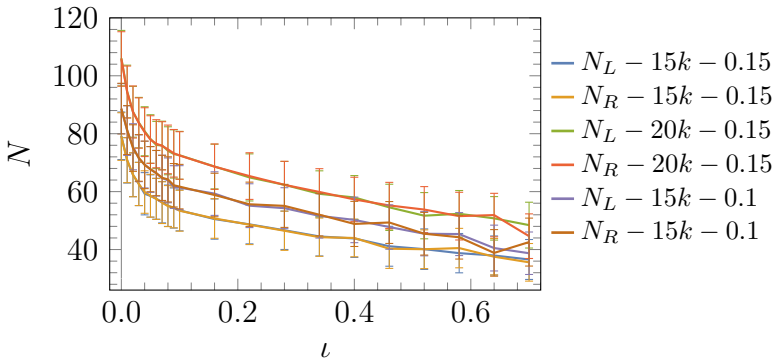

Figure B.5: Number of left- and right-moving domain walls as a function of the driving ι. All curves have a similar trend and can be scaled roughly on each other. The legend indicates the nature (left- or right-moving), the number of sites (15,000 or 20,000 sites) and the height cutoff h_c (0.1 or 0.15). The height cutoff h_c determines whether the data points belong to the up- or down-domain. Parameters as in Fig. B.4 for different values of ι with respect to Eq. (2.43). Thus, $m_0 = \frac{-r}{u} \approx 0.316$.

Appendix C

Additional Data for 2D Domain Walls

C.1 The Stripe Solution and Confirmation of Velocity

Fig. C.1 shows the build-up of a stripe solution in a system with 500×500 sites. At the last time shown, the stripe has fully built out and moves with a constant velocity. The velocity is measured as $v \approx 0.2275$. From Fig. 3.2, we can read off the corresponding one-dimensional velocity of a straight domain wall with $v^{1D}\left(\frac{0.4}{\sqrt{2}}\right) \approx 0.2222$. The two values match up to a small deviation, which confirms that our mapping for the parameters explained in Sec. 4.3 works.

Stripe solutions have also been reported on in the Ising model. In general, these states prevent the system from becoming fully ordered.

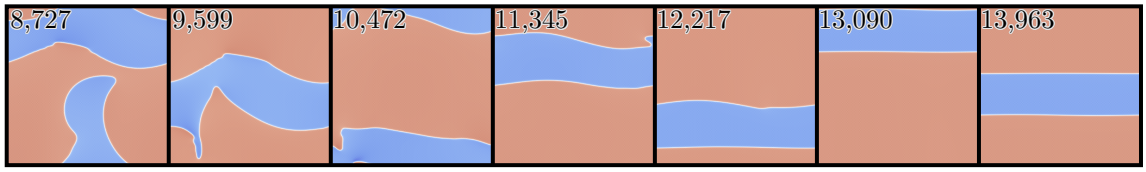

Figure C.1: Snapshots of the build-up of the stripe solution shown at seven different times in a system with 500×500 sites. After some time, the stripe moves with a constant velocity through the system. This velocity matches the corresponding one-dimensional velocity. Parameters: $J = 1, \Delta = 0.8, \alpha = 0.1, \delta_2 = -2 \cdot 0.6, \delta_4 = 2, b_0 = 0.4, \omega = 2 \cdot 3.6$ and thus $T_{\text{rot}} \approx 172.4$.

C.2 Phase diagram cut

Fig. C.2 shows a vertical cut of the phase diagram in Fig. 4.9 at $b_0 = 0.16$. C_{plateau} is the value of the plateau in the equal-time correlations of m in the stationary state. For $C_{\text{plateau}} = 0$ the system is assumed be in the disorder phase. From this, we can estimate the transition to be at approximately $T_c \approx 0.125$. The plateau value becomes finite for lower temperatures, and the system is in the ordered phase.

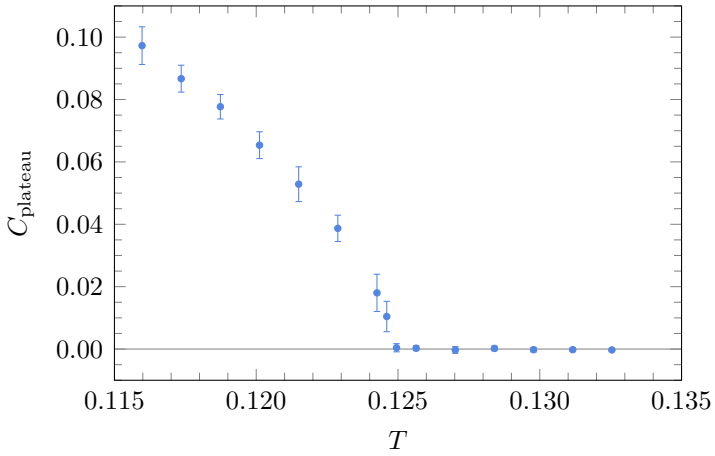

Figure C.2: Plateau value of the equal-time correlations in m for different temperatures around the transition. In the disordered phase, the value drops to zero. The data points show a nice curve without many fluctuations and allow for a rough estimate of the critical temperature, as $T_c \approx 0.125$. Parameters: $J = 1, \Delta = 0.8, \alpha = 0.1, \delta_2 = -2 \cdot 0.6, \delta_4 = 2, b_0 = 0.16, \omega = 2 \cdot 3.6$ and thus $T_{\text{rot}} \approx 1077.2$.

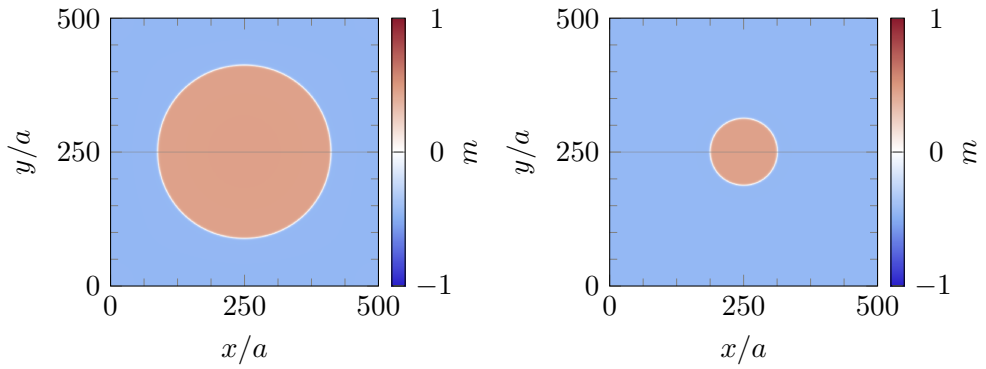

Figure C.3: The magnetisation shown at $t = 445$ (left panel) and $t = 6{,}903$ (right panel) for a circle geometry of the micromagnetic model in the non-driven case. The grey line at $y = 250$ shows the cuts for the space-time plots in Fig. C.4. Parameters are $J = 1, \Delta = 0.8, \alpha = 0.1, \delta_2 = -2 \cdot 0.6, \delta_4 = 2$.

C.3 Numerical Comparison of the Two Models

Here, we compare the dynamics of the effective model with those of the micromagnetic model. In order to do so, we choose the simple structure of a circular domain wall in two dimensions and use the conversion rules given in section 2.6.1 to run the simulations with approximately equal settings. Keep in mind that for the effective field theory, higher-order terms in the fields, e.g., $m^2\nabla^2\phi$, were neglected, so we do not expect a perfect match. But the mismatch should decrease the closer we go to the critical point where $m \to 0$.

We start by looking at the equilibrium setting, where we expect the enclosed domain to shrink with a speed proportional to the curvature.

Fig. C.3 shows the magnetisation in z-direction in space at two different times for the micromagnetic model. One shortly after the initial equilibration phase with $t = 445$ (left panel) and one not far from the completely ordered phase with $t = 6{,}903$ (right panel). The simulation was performed at a rather large magnetisation value of $m \approx 0.448$ and is better for visibility. To prove the point that the effective field theory converges to the micromagnetic model, we take cuts at $y = 250$ and show the (x, t) space-time behaviour in Fig. C.3. The left panel shows the two simulations with higher m, and the right panel shows the simulations with a lower value of m. The tendency is clearly visible. Note that we can scale the curves on top of each other by scaling the time of one of the theories. It turns out that the scaling factor is of the order of $1 - m^2$. As mentioned at the beginning of this section, this corresponds exactly to the next higher-order terms that we neglected for the effective theory.

Note that the step-like shape at final times comes from discretisation effects. Overall, the effective theory converges to the microscopic model for $m \to 0$. Nevertheless,

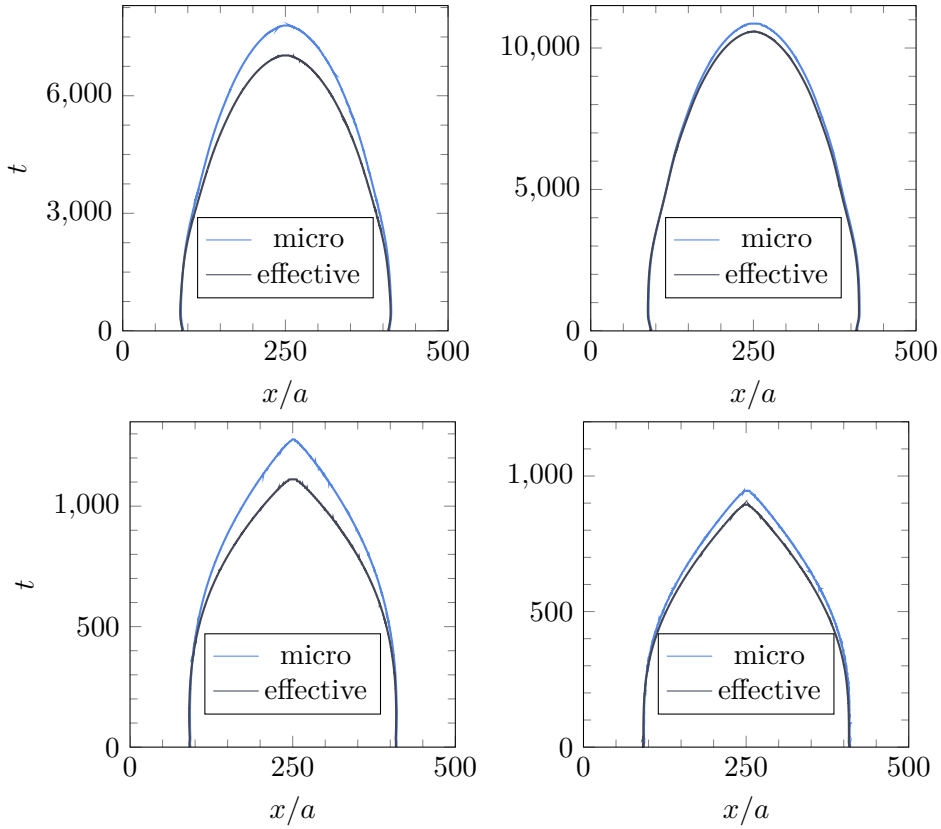

Figure C.4: Cuts of the shrinking circular domain for different scenarios. It is visible that the effective model converges to the microscopic one in the limits of small m. Parameters for the microscopic model are $J = 1, \Delta = 0.8, \alpha = 0.1, \delta_4 = 2$. For higher m (left side), $\delta_2 = -2 \cdot 0.6$ and for lower m (right side), $\delta_2 = -2 \cdot 0.45$. In the driven case (bottom) $b_0 = 0.3$. Parameters for the effective model are $\alpha = 0.1, u = 1, D_m = 0.8, D_\phi = 1$. For higher m (left side), $r = -0.4$ and for lower m (right side), $r = -0.1$. In the driven case (bottom), $\iota = 0.045853$.

the effective model also gives a good qualitative description at higher m.

C.4 Kibble-Zurek Driven System Fully Ordered

In Sec. 4.8.2, we used the Kibble-Zurek mechanism for the driven ferrimagnet. Fig. C.5 shows the equal-time correlations in m throughout the quench protocol with a much larger quench time. We observe that within the protocol, the correlation length becomes much larger than the system size and a precise plateau forms deep in the ordered phase. For slow enough quenches, the system relaxes every single time, and the same behaviour as in the stationary state is expected. Here, it also shows that due to the much faster dynamics, the system size limit is reached much earlier than in the non-driven system for a given system size. This is another argument that larger systems might be necessary to reach a better resolution with more significant quench times.

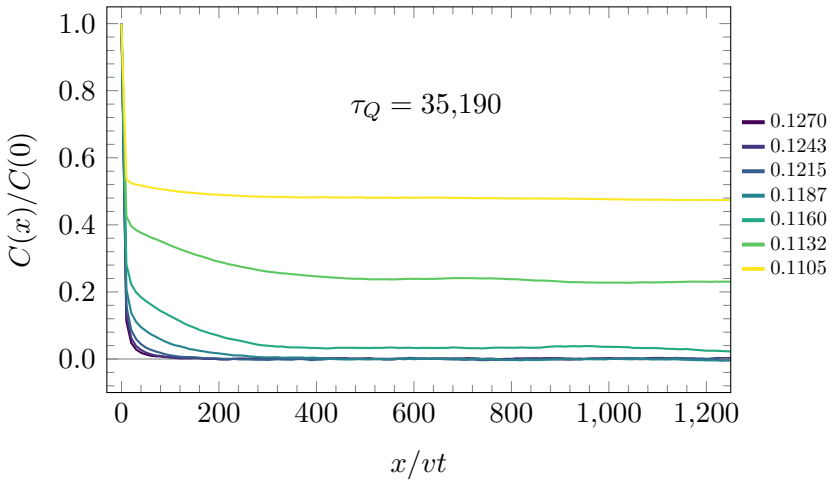

Figure C.5: Equal-time correlations in m throughout a quench according to the Kibble-Zurek mechanism. The protocol is the same as explained in Sec. 4.8.2. Due to the relatively large value of the quench time, the system becomes fully ordered. Parameters: $J = 1, \Delta = 0.8, \alpha = 0.1, \delta_2 = -2 \cdot 0.6, \delta_4 = 2, b_0 = 0.16, \omega = 2 \cdot 3.6$ and thus $T_{\text{rot}} \approx 1077.2$.

Appendix D

Additional Data on Phase Transition in 3D

In Fig. D.1, we show the equal-space correlations for a system of linear system size $L = 20$ and 40. This is to estimate how much our measured time values are correlated. The step in time used in the plots is ten times larger than the time difference between the data points used for the average for the second and the fourth moment in Ch. 5. In both cases, the correlations drop to zero very quickly and show only fluctuations around it. The legend shows different values around the transition. At all values, the fluctuations and the drop are similar. This confirms that our choices of time values give a reasonable number of independent points to average over.

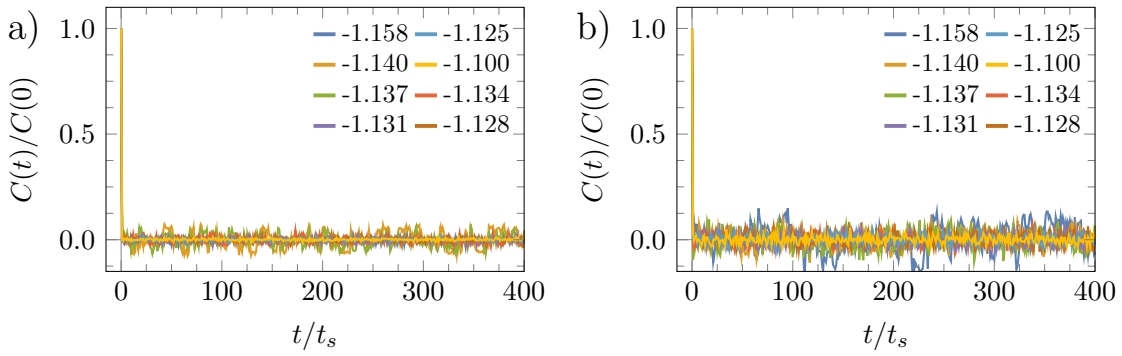

Figure D.1: Equal-space correlations in m shown as a function of time for a linear system size of $L = 20$ in panel a) and $L = 40$ in panel b). $t_s = 2{,}100$ and $t_s = 5{,}460$ for the two system sizes, respectively. The correlations drop very quickly, with some fluctuations around zero. Parameters are $\alpha = 0.1, u = 3, D_m = 0.8, D_\phi = 1, \iota = 0.04$ and $T = 0.5$.

Here, in Fig. D.2, we show the scaled Binder cumulant and the scaled second moment for simulations with much smaller driving compared to Ch. 5. With $180 \gg 1$, the criterion Eq. 5.3 should be fulfilled. However, we also do not find any signature for a first-order transition in this more drastic parameter regime.

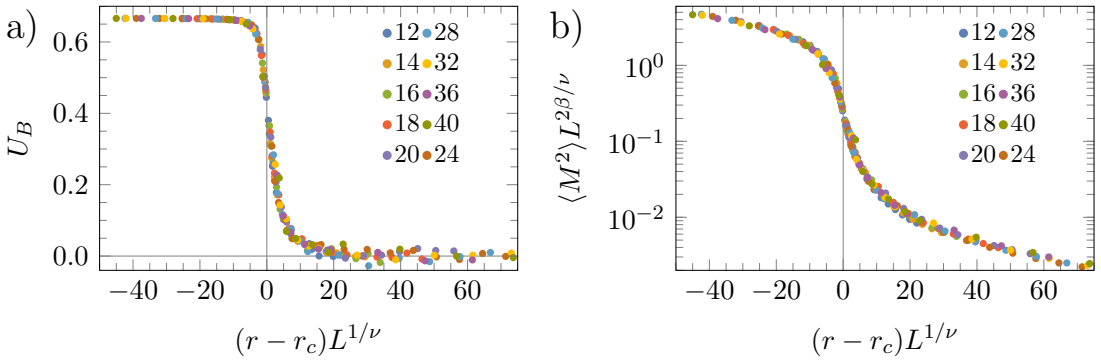

Figure D.2: Panel a) shows the Binder cumulant as a function of the control parameter, Eq. (5.4), for ten different system sizes where each point is averaged over time and three different runs. Notice that this is already the scaling plot with good agreement for Ising exponents, $\nu \approx 0.63$ and $\beta \approx 0.326$. The critical point was estimated from the mean of the different crossing pairs $(L, 2L)$ with $r_c \approx -1.189(1)$. There is no signature of a negative peak corresponding to a first-order transition. Panel b) shows the second moment of the order parameter in a scaling plot as a function of the control parameter. Again, Ising exponents give a nice data collapse. Parameters are $\alpha = 0.1, u = 3, D_m = 0.8, D_\phi = 1, \iota = 0.001$ and $T = 0.5$.

Appendix E

Current in a Heisenberg Chain

Here, we report on a negative result. The goal was to numerically achieve a heat current in a driven classical Heisenberg chain. This was inspired by a work of Florian Lange [137], where a similar setting for the XXZ model has been used as an example of an efficient heat and spin pump. However, in the approach, the quantum version of the model was utilised.
The full Hamiltonian for the one-dimensional chain with classical spins is given by

$$H = \sum_i \left[J\boldsymbol{S}_i\boldsymbol{S}_{i+1} - BS_i^z - \Delta J(-1)^i \boldsymbol{S}_i\boldsymbol{S}_{i+1}\sin(\omega t) + \Delta B(-1)^i S_i^z \cos(\omega t) \right], \quad \text{(E.1)}$$

where we assume antiferromagnetic coupling, $J > 0$, and a constant magnetic field B. The last two terms are the time-dependent driving terms. Similar to the ferrimagnet, these are a perturbation of the static model and thus ΔJ and ΔB are considered to be small compared to J. Following [137], the specific form of the drive is needed to break the necessary symmetries. The staggeredness of the two driving terms ensures that all spatial reflection symmetries are broken. The staggered magnetic field breaks the symmetry of rotations by π around the x- and y-direction, and it has to be phase-shifted to the other driving term. The static magnetic field breaks the combination of a rotation around the x- and y-direction and the spatial bond-centred mirror symmetry. This, in total, should allow a spin current and a heat current.
Let us first get an intuition on the static case where the driving terms are zero. Due to the antiferromagnetic coupling in the Heisenberg term, the spins fully anti-align for $B = 0$. However, at a finite magnetic field, canting takes place in the direction of the magnetic field. To describe this, we use again an even and odd sublattice with the simple normalised spin parametrisation given in Eq. (2.3). Minimising the energy yields

$$S_e^z = \cos(\theta_e) = \frac{B}{4J} = \cos(\theta_o) = S_o^z, \qquad \phi_e = \phi_o + \pi, \quad \text{(E.2)}$$

which gives the canting angles θ_e, θ_o as function of the field and coupling. To guarantee reasonable values for the spin components, $-4J < B < 4J$ sets a bound on the static magnetic field value.

In principle, we could now follow the same approach as for the Goldstone mode activation of the ferrimagnet and use a perturbative expansion in ΔB and ΔJ to determine the responses from the LLG Eq. (1.7). However, this was not the goal of this study, and it is already clear at this point that it will not reveal a heat current on this level. The formula for the heat current in the presence of a magnetic field is given by

$$J_h = \sum_i \left[J^2 (\boldsymbol{S}_i \times \boldsymbol{S}_{i+1}) \boldsymbol{S}_{i+2} - BJ(\boldsymbol{S}_i \times \boldsymbol{S}_{i+1})_z \right], \tag{E.3}$$

where the second term is just BJ_s with J_s being the spin current [138]. Due to the even and odd structure of the Hamiltonian Eq. (E.1) and the sum in the current formula, the current always vanishes for a configuration where every second spin is the same. This is the case for an even and odd structure, hence no heat current. While this holds for the given equations, it is not necessarily true at finite temperatures, where each spin is subjected to a slightly different noise field.

We extended a code developed within [137] to study this behaviour numerically. The code is based on Heun's method as a solver. This solver does not necessarily conserve the spin length. An additional step is added at each time step to ensure that the length of the spin is conserved at all times. In this step, the result is projected back onto a solution with said spin length. For details of the solver, we refer to [137]. However, while keeping the noise term untouched, we changed the used damping to the usual Gilbert damping explained in Sec. 1.1. In addition, we added open boundary conditions with the motivation to study a heat current flowing from one end to another. Note that one limitation of this code is that it is running on CPUs, and the projection algorithm at each time step results in much smaller system sizes, $\mathcal{O}(100)$, than we were used to with the ferrimagnet and Mumax3 in one dimension. As mentioned at the beginning of this appendix, we could not obtain a finite average heat current despite all our efforts. We scaled through different values of the parameters, in particular, the strengths of the driving terms as well as for the frequency and the static field, but the even and odd structure persisted on average for all values, leading to vanishing heat and spin current.

We also added a next-nearest neighbour driving field $\sim \Delta J_2 \boldsymbol{S}_i \boldsymbol{S}_{i+2}$ in an attempt to break this even and odd structure. But we did not succeed.

While the staggered time-dependent ΔJ-term is not straightforward to add in Mumax3, it should be possible to calculate the effective field of said term and add it to the external field $\boldsymbol{B}_{\text{ext}}$. This would allow much more extensive system sizes. In ad-

dition, one could add a static component to the ΔJ-term, which would add a more direct influence on the couplings, and eventually, one could use a staggered version with slightly different prefactors as for the driving in the ferrimagnet. However, this is open for future investigations.

Acknowledgements

The time has come to express my deep appreciation to everyone who has been part of this journey, both professionally and personally.
First and foremost, I would like to express my deepest gratitude to my advisor, Prof. Dr. Achim Rosch, for his guidance, support, and encouragement since my Master's. His genuine enthusiasm for physics, strong intuition, and ability to connect various perspectives on a problem have both fascinated and inspired me. I am deeply appreciative of the vast amount I have learned from him.
I would also like to give a big thank you to my thesis advisory committee members and examiners Prof. Dr. Sebastian Diehl, Prof. Dr. Matteo Rizzi and Prof. Dr. Joachim Hemberger for their constructive feedback, patience and availability.
A heartfelt thanks go to the administrative staff Dr. Andreas Sindermann, Ute Grafenberger, Konstantinia Schäfer, Mariela Boevska for their invaluable support and dedication to keep the computer system, our contracts and everything else running. Special thanks to Dr. Petra Neubauer Günther, the managing director of the BCGS, whose significant contributions have greatly enhanced the wonderful atmosphere.
A special thanks to Nina, Yaren, Alla, Sagar, Julian and Marcel G., who generously dedicated their time and effort to proofread various parts of this thesis.
The camaraderie and support from my office mates and colleagues have been exceptional. I would like to explicitly mention a few: Philipp, Lukas, Vivek, Thomas B., Nina, Alla, Reza, Adrian, as well as Lasse and Sagar, who were just one office away. Special recognition goes to Reza and Adrian, whom I had the privilege to co-supervise during their Master's. Their determination and enthusiasm were truly inspiring and had a positive impact on me as well. A particular thanks go to Nina, who was not only one of the most fun office mates but also my swimming coach, a teacher in mastering long equations, and a great collaborator and friend.
During the challenging times of the COVID-19 pandemic, I want to especially thank Alla, Marcel, Thomas M., Nick, and Valentin for our various trips and hikes when not much else was possible. I am also grateful for the various Zoom sessions, including those of the buddy program.
I am deeply indebted to Robin, Joey, Michael, Marcel U. and Benjamin for their supportive, friendly, and fun company during my early studies.
My journey to this point would not have been the same without my school friends'

unwavering support and cherished friendships. A big thank you to the two groups, 'Clique' and 'Stammtisch', for the shared memories, honesty, encouragement and the many celebrations we had together. Together, they have brought me much joy and strengthened my character. I am particularly grateful to Pascal for his ongoing support and our strong bond.

I am profoundly grateful to my family for their unwavering support, love, and encouragement throughout my academic journey and life. To my parents, Birgit and Erik, thank you for always believing in me and for your countless sacrifices to help me succeed. To my sister, Alicia, your constant encouragement and understanding have been invaluable. I couldn't have done this without you. Your love and support have been the cornerstone of my success.

Finally, I want to express my deepest gratitude to my girlfriend, Yaren, for her endless support and love, especially during one of the most stressful periods of my life.

Erklärung zur Dissertation

Hiermit versichere ich an Eides statt, dass ich die vorliegende Dissertation selbstständig und ohne die Benutzung anderer als der angegebenen Hilfsmittel und Literatur angefertigt habe. Alle Stellen, die wörtlich oder sinngemäß aus veröffentlichten und nicht veröffentlichten Werken dem Wortlaut oder dem Sinn nach entnommen wurden, sind als solche kenntlich gemacht. Ich versichere an Eides statt, dass diese Dissertation noch keiner anderen Fakultät oder Universität zur Prüfung vorgelegen hat; dass sie - abgesehen von unten angegebenen Teilpublikationen und eingebundenen Artikeln und Manuskripten - noch nicht veröffentlicht worden ist sowie, dass ich eine Veröffentlichung der Dissertation vor Abschluss der Promotion nicht ohne Genehmigung des Promotionsausschusses vornehmen werde. Die Bestimmungen dieser Ordnung sind mir bekannt. Darüber hinaus erkläre ich hiermit, dass ich die Ordnung zur Sicherung guter wissenschaftlicher Praxis und zum Umgang mit wissenschaftlichem Fehlverhalten der Universität zu Köln gelesen und sie bei der Durchführung der Dissertation zugrundeliegenden Arbeiten und der schriftlich verfassten Dissertation beachtet habe und verpflichte mich hiermit, die dort genannten Vorgaben bei allen wissenschaftlichen Tätigkeiten zu beachten und umzusetzen. Ich versichere, dass die eingereichte elektronische Fassung der eingereichten Druckfassung vollständig entspricht.

Teilpublikationen:

Hardt, D., Doostani, R., Diehl, S., del Ser, N., & Rosch, A. (2025). Propelling ferrimagnetic domain walls by dynamical frustration. Nature Communications, 16(1), 3817. doi:10.1038/s41467-025-58920-1

Köln, den 04.06.2025

Dennis Christopher Hardt